IPP-Report

MAX-PLANCK-INSTITUT
FÜR PLASMAPHYSIK

Carl Friedrich Benedikt Zimmermann

Validation of Momentum Transport Theory in the Core Plasma of the ASDEX Upgrade Tokamak

IPP 2024-08
März 2024

Technische Universität München
TUM School of Natural Sciences

Validation of Momentum Transport Theory in the Core Plasma of the ASDEX Upgrade Tokamak

Validierung von Impulstransporttheorie im Plasmazentrum des ASDEX Upgrade Tokamaks

Carl Friedrich Benedikt Zimmermann

Vollständiger Abdruck der von der TUM School of Natural Sciences der Technischen Universität München zur Erlangung des Doktors der Naturwissenschaften (Dr. rer. nat.) genehmigten Dissertation.

Vorsitz: Prof. Dr. Bastian Märkisch

Prüfer der Dissertation:

1. Prof. Dr. Ulrich Stroth
2. Prof. Dr. Paolo Ricci

Die Dissertation wurde am 24.11.2023 bei der Technischen Universität München eingereicht und durch die TUM School of Natural Sciences am 08.03.2024 angenommen.

Abstract

This work implemented a methodology that can determine the contribution of diffusion, convection, and residual stress to momentum transport within the core of a tokamak plasma. The analysis is based on experiments with neutral beam modulation in the fusion experiment ASDEX Upgrade. The resulting perturbation of the plasma rotation is used to calculate Fourier profiles, which are utilized to deduce the transport coefficients. It is crucial to scale the momentum transport coefficients with the experimental ion heat diffusivity to compensate for the modulated turbulence amplitude due to the heating perturbation. The analysis is based on the TRANSP and NUBEAM codes to assess the torque from the neutral beams and the heat flux onto the ions. The momentum transport model is implemented in the ASTRA code. ASTRA solves the momentum transport equation based on an experimental boundary condition and a prescribed set of transport coefficients and predicts a consistent rotation profile. A statistical minimization algorithm iterates on the transport coefficients to fit the predicted rotation to the experimentally measured one. A statistical error analysis provides uncertainties for the fitting results. Furthermore, it shows that the obtained solution represents a global and unique minimum.

The modeling reproduces the experimental data with high accuracy. The determined values for the normalized diffusivity (Prandtl number) and convective velocity (pinch number) agree quantitatively with gyrokinetic prediction by the GKW code, resolving a long-standing mismatch between theory and measurement for this transport channel. It is shown that this mismatch was caused in previous works by neglecting the residual stress and the time dependence on the transport coefficients. The methodology is used to study the isotope dependence of the momentum transport coefficients. Agreeing with predictions, no significant isotope effect is found. An extensive database of gyrokinetic calculations was constructed to compare the predicted and measured parametric dependences of the transport coefficients. This database consists of data points corresponding to experimental data as well as isolated parameter scans, which avoid the cross-correlations of input parameters existing in experimental data. The Prandtl number is found in the gyrokinetic calculations and in the experiment to scale most clearly with the magnetically trapped particle fraction. The pinch number depends most strongly on the logarithmic density gradient and the magnetic shear, in agreement with the predictions from the Coriolis pinch. The residual stress produces an intrinsic torque that scales in the inner core with the logarithmic density gradient and in the outer core with the pressure gradient. This agrees with earlier experimental results and global, non-linear gyrokinetic predictions and suggests that different mechanisms are responsible for the production of residual stress in the inner and outer core. For the inner core, it is supposed that effects from profile shearing and turbulence intensity gradients are dominant, which can result in the observed sign reversal of the intrinsic torque. Towards the edge, the dependence on the $\mathbf{E} \times \mathbf{B}$ shearing is likely more important. While many of these results agree with earlier works, this is the first time such a coherent picture of this transport channel is presented for the core plasma. The assessed scaling laws are used to propose a reduced momentum transport model, which is validated on an additional data set. The successful reproduction of these experimental data shows that the reduced model catches the most important contributions to momentum transport in the core plasma. This allows for further applications, such as integrated modeling approaches or real-time control.

Overall, the theory validation and the assessed scaling laws open the door to first, physics-based predictions of the rotation profiles of future reactors. The next steps are to study the parametric dependence of the residual stress on the normalized gyro-radius, to extend this study to plasma conditions with more substantial electron heating, and to obtain a more complete understanding of the boundary conditions of the rotation in the plasma edge.

Zusammenfassung

In dieser Arbeit ist eine Methode entwickelt worden, um den Beitrag von Diffusion, Konvektion und Residual Stress zum Impulstransport im Zentrum eines Tokamak-Plasmas zu bestimmen. Die Analyse basiert auf der Auswertung von Experimenten mit Modulation der Neutralteilchenheizung am Fusionsexperiment ASDEX Upgrade. Die resultierende Modulation der Plasmarotation wird zur Berechnung von Fourier-Profilen verwendet, die dazu dienen, die Transportkoeffizienten zu bestimmen. Es stellt sich heraus, dass es entscheidend ist, die Impulstransportkoeffizienten mit der gemessenen Ionenwärmediffusivität zu skalieren, um die Modulation der Turbulenz zu kompensieren, die aus der Modulation der Heizung folgt. Die numerische Analyse basiert auf den Rechencodes TRANSP und NUBEAM, um das durch die Neutralteilchenheizung ausgeübte Drehmoment und den Wärmefluss der Ionen zu berechnen. Im Transportcode ASTRA wird die Impulstransportgleichung mithilfe experimenteller Randbedingungen und mit vorgegebenen Transportkoeffizienten gelöst. Ergebnis ist ein konsistentes Rotationsprofil. Ein statistischer Minimierungsalgorithmus iteriert über die Transportkoeffizienten, um die vorhergesagte Rotation an die experimentell gemessene anzupassen. Eine statistische Fehleranalyse liefert Unsicherheiten der Modellierung.

Die Modellierung reproduziert die experimentellen Daten mit hoher Genauigkeit. Die ermittelten Werte für die normalisierte Diffusivität (Prandtl-Zahl) und die Konvektionsgeschwindigkeit (Pinch-Zahl) stimmen quantitativ mit Vorhersagen des gyrokinetischen GKW-Codes überein, wodurch eine seit langem bestehende Diskrepanz zwischen Theorie und Experiment für diesen Transportkanal aufgelöst wird. Es wird gezeigt, dass die Diskrepanz in früheren Arbeiten durch die Vernachlässigung des Residual Stress und der Zeitabhängigkeit der Transportkoeffizienten verursacht worden ist. Bei der Untersuchung der Isotopenabhängigkeit der Impulstransportkoeffizienten wird, in Übereinstimmung mit theoretischen Vorhersagen, kein signifikanter Effekt festgestellt. Es ist eine umfangreiche Datenbank aus gyrokinetischen Berechnungen erstellt worden, um die vorhergesagten und gemessenen parametrischen Abhängigkeiten der Transportkoeffizienten zu untersuchen. Diese Datenbank besteht aus Werten, die einerseits auf experimentellen Daten basieren, sowie aus dedizierten Parameterscans, um eine Korrelation unter den Eingabeparametern zu vermeiden. Es ist festgestellt worden, dass die Prandtl-Zahl in den Vorhersagen und im Experiment am deutlichsten mit dem Anteil der magnetisch gefangenen Elektronen skaliert. Die Pinch-Zahl hängt am stärksten vom Dichtegradienten und der magnetischen Verscherung ab, in Übereinstimmung mit den Vorhersagen des Coriolis-Pinch. Der Residual Stress skaliert im inneren Plasmazentrum mit dem Dichtegradienten und im äußeren Plasmazentrum mit dem Druckgradienten. Dies stimmt mit früheren Ergebnissen und Vorhersagen überein und deutet darauf hin, dass unterschiedliche Mechanismen für die Erzeugung des Residual Stress verantwortlich sind. Damit wird erstmals ein schlüssiges Bild dieses Transportkanals für das Plasmazentrum präsentiert. Die ermittelten Skalierungsgesetze werden verwendet, um ein reduziertes Impulstransportmodell vorzuschlagen, das anhand eines zusätzlichen Datensatzes validiert wird. Die erfolgreiche Reproduktion dieser Experimentdaten zeigt, dass das reduzierte Modell die wichtigsten Beiträge zum Impulstransport im Plasmazentrum erfasst. Dies ermöglicht in Zukunft weitere Anwendungen für integrierte Modellierungsansätze oder Echtzeitkontrolle des Plasmas.

Insgesamt sind die erfolgreiche Validierung der Theorie und die gefundenen Skalierungsgesetze erste Schritte für Vorhersagen der Rotationsprofile in zukünftigen Fusionsreaktoren. Weitere offene Fragen betreffen die parametrische Abhängigkeit des Residual Stress vom normalisierten Gyroradius, die Ausweitung dieser Studie auf Plasmen mit stärkerer Elektronenheizung und ein tieferes Verständnis der Randbedingungen der Rotation am Plasmarand.

„Wir sollten lernen, dass auch die grössten technischen Leistungen, die grösste so genannte Tüchtigkeit, der Glaube, dass man alles tun kann, wenn es nur Erfolg verspricht, dass dies nicht die richtige Weltanschauung sein kann.

Wir müssen wieder Ehrfurcht vor dem Menschenleben haben.“

— Otto Hahn

In Gedenken an die Helden und Opfer von Tschernobyl

В память о героях и жертвах Чернобыля

Contents

Chapter 1

Introduction

"To boldly go where no man has gone before!"
— James Tiberius Kirk, Star Trek

As the world's population and living standard are constantly increasing, the demand for energy rises as well [1]. Moreover, the need to decarbonize the (primary) energy production to meet the challenge of climate change is one of the critical challenges of our generation [2]. Nuclear fusion is a promising way to provide baseload electrical power without the emissions of CO_2 (as with fossil fuels) and the risk of nuclear disaster or the problem of long-lived, dangerous, radioactive waste (as with nuclear fission). The proposed concept to exploit fusion opens the perspective for energy production for many thousands of years [3].

Nuclear fusion is the main energy source of the solar system, as the sun is burning 600 million tons of hydrogen to 596 million tons of helium every second. The mass deficit in these reactions converts into an immense energy of [4, p. 6]

$$E = mc^2 = 3.6 \times 10^{23}\mathrm{J}.$$

The proton-proton and CNO reactions in stars, however, are processes with low cross sections, which, on the one hand, ensures a long lifetime of our star, but, on the other hand, makes this reaction unsuitable for economical use on Earth.

Therefore, other fusion reactions need to be considered for a future fusion power plant. The reaction rates of the following proposed reactions [6]

$$\begin{aligned}
{}^2\mathrm{D} + {}^2\mathrm{D} &\rightarrow {}^3\mathrm{He}\,(0.82\,\mathrm{MeV}) + \mathrm{n}(\ 2.45\,\mathrm{MeV})\,[50\%] \\
{}^2\mathrm{D} + {}^2\mathrm{D} &\rightarrow {}^3\mathrm{T}\ \ (1.01\,\mathrm{MeV}) + \mathrm{p}(\ 3.05\,\mathrm{MeV})\,[50\%] \\
{}^2\mathrm{D} + {}^3\mathrm{He} &\rightarrow {}^4\mathrm{He}\,(3.71\,\mathrm{MeV}) + \mathrm{p}(14.64\,\mathrm{MeV}) \\
{}^2\mathrm{D} + {}^3\mathrm{T} &\rightarrow {}^4\mathrm{He}\,(3.52\,\mathrm{MeV}) + \mathrm{n}(14.06\,\mathrm{MeV})
\end{aligned}$$

are compared in Fig. 1.1. The D-T fusion process has the highest reaction rates below a fuel temperature of 1000 keV and high energy output. For such high temperatures, the fuel is in the plasma state, i.e., the gas is fully ionized, meaning the electrons are no longer bound to the atomic nuclei. The immense temperatures

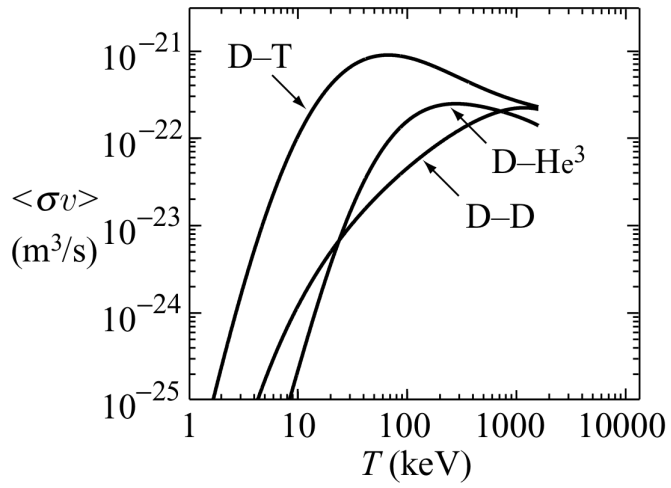

Figure 1.1: Reaction rates for multiple fusion reactions, calculated from cross-sections averaged over their velocity distribution. Figure adapted from [5].

at the peak of the reaction rates result from competing effects of the Coulomb repulsion between the ions and quantum tunneling. The basic principle of the relevant forces and a sketch of the connected potential energy as a function of distance between the particles is shown in Fig. 1.2.

In 1952, the Soviet physicists Tamm and Sakharov proposed and conducted experiments to confine such a hot plasma within a magnetic field. This concept is known as a tokamak, which is an acronym for "toroidal chamber with magnetic coils" (ТОроидальная КАмера с МАгнитными Катушками) [7–9]. Essentially, the tokamak concept involves a toroidal chamber that contains the plasma. The toroidal magnetic field required for confinement is generated by circular magnets arranged in a toroidal configuration, and the plasma itself carries a current that contributes to the overall magnetic field with a poloidal component. An induction process drives the current, utilizing a solenoid coil located at the center, where the plasma serves as the secondary winding of a transformer. The concept and basic geometry of the coil setup of a tokamak are shown in Fig. 1.3.

Due to the Lorentz force, charged plasma particles gyrate around the magnetic field lines and are, thus, confined by the magnetic field. A gradient in the thermal pressure of the hot plasma is sustained by the current and field in an equilibrium. This can be expressed as

$$\nabla p = \mathbf{j} \times \mathbf{B}, \tag{1.1}$$

with the current density $\mathbf{j}$ and magnetic field (flux density) $\mathbf{B}$. From this equation, it is understood that, in equilibrium, there cannot exist a pressure gradient along the magnetic field lines, resulting in nested magnetic flux surfaces on which the magnetic flux and the pressure are constant. The equation above can be applied to the tokamak geometry. This results in the famous Grad-Shafranov equation [10, 11]. Solving these equations, the *equilibrium reconstruction*, is a highly non-trivial but necessary part of understanding the magnetic configuration of a fusion device.

Present-day fusion experiments do not reach ignition, which means that the energy used for the auxiliary heating of the plasma is larger than the fusion power produced by the reactions.

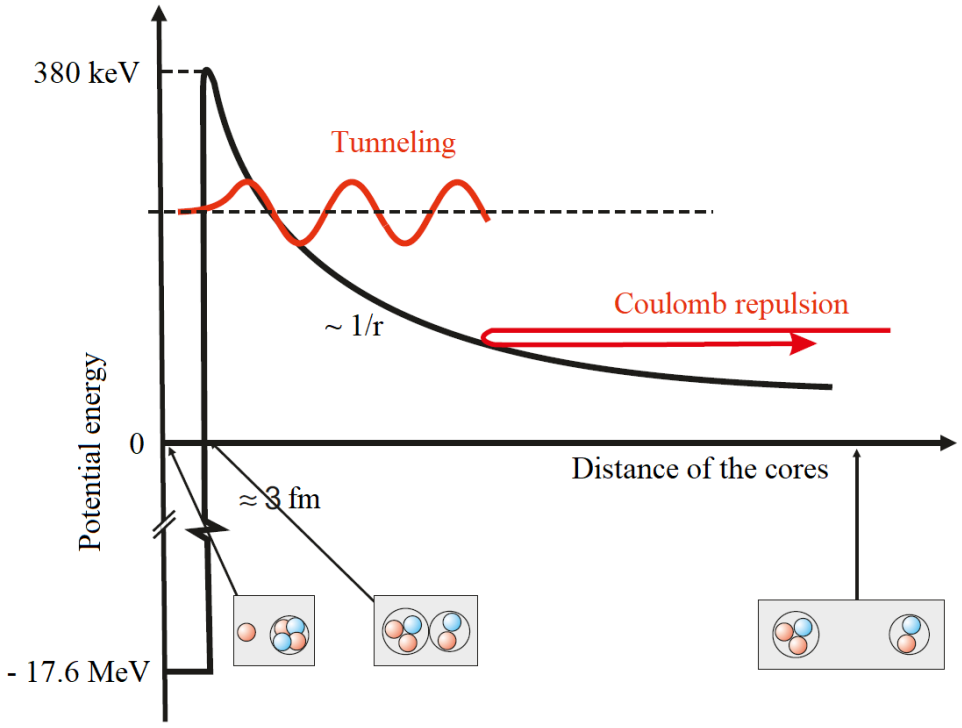

Figure 1.2: Sketch of the potential between the D (one blue neutron, one red proton) and the T core (two blue neutrons, one red proton). For large distances between the cores, the Coulomb repulsion dominates. The barrier can only be overcome with very large relative energies. Tunneling plays a crucial role by allowing the ions to get close, enabling the strong force to bring the D and T ions within the potential well, ultimately enabling fusion to occur. Figure adapted from [6].

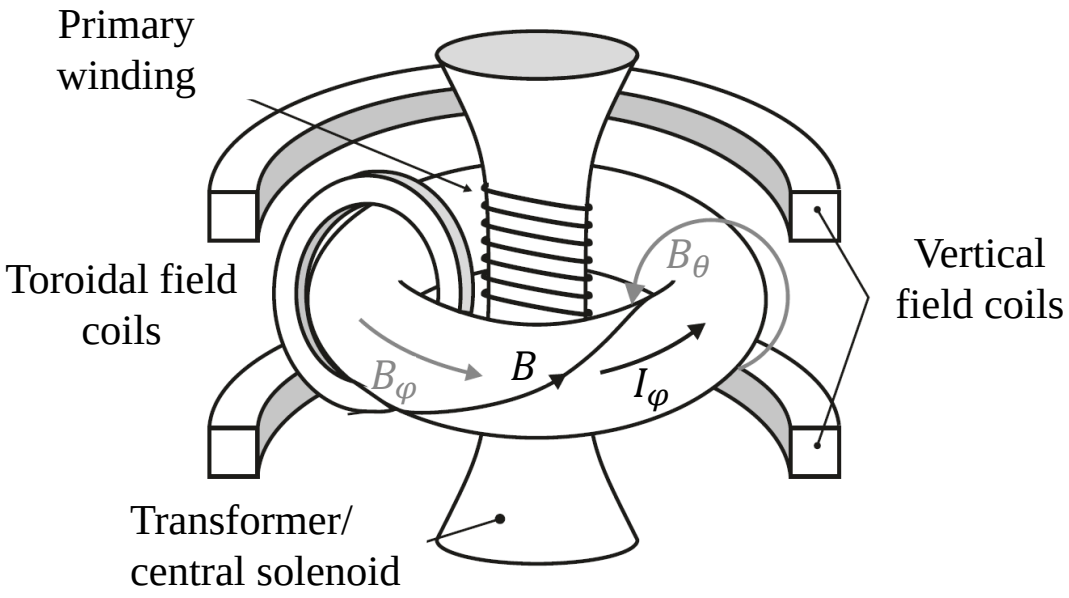

Figure 1.3: Basic coil concept of a tokamak. The magnetic field has a toroidal (B_φ) and a poloidal (B_θ) component, resulting from a toroidally induced plasma current I_φ. Figure adapted from [6].

To ignite a burning plasma, the Lawson criterion has to be met, which gives a lower boundary for the so-called triple product

$$n_e \, T_i \, \tau_E > 3 \times 10^{21} \text{ m}^{-3} \, \text{keV s}$$

with n_e the electron density of the plasma, T_i the ion temperature, and $\tau_E \sim W/P_{\text{loss}}$ the energy confinement time, with the plasma stored energy W and the power loss P_{loss} [12, 13].

The main loss of energy and degradation of confinement is caused by turbulence in the plasma, which leads to the transport of particles, heat, and momentum from the core to the edge of the plasma. This is illustrated in Fig. 1.4 together with the used coordinate system. This Figure shows the nested surfaces of constant magnetic flux and plasma pressure and the magnetic axis in the center at a minor radius $r = 0$. From the Grad-Shafranov equation, it is possible to derive in this geometry the effect of the Shafranov shift, which denotes the outwards displacement of the magnetic axis from its geometric center due to the pressure within the plasma.

In such a geometry, a normalized toroidal flux coordinate ρ_φ can be introduced, which is equal to 0 in the plasma center and 1 at the separatrix. The definition is given by $\rho_\varphi = \sqrt{(\Phi_0 - \Phi)/(\Phi_0 - \Phi_{sep})}$, where Φ_0 is the toroidal flux at the magnetic axis ($r = 0$) and Φ_{sep} at the separatrix (definition of ρ_ψ is similar with poloidal fluxes Ψ). The separatrix is the boundary between field lines closing on themselves after a given number of toroidal turns and open field lines that terminate on walls or other vessel components. Radial outward transport refers to a transport perpendicular to the flux surfaces from the core toward the edge of the plasma.

The radial transport of heat and plasma particles is well understood in the plasma core, i.e., its influence on confinement and plasma performance can be predicted to a good degree. Turbulent heat transport can be described as a diffusive process [17–22] and particle transport by a combination of diffusion and convection [23–25].

The transport of momentum in a plasma is more complicated and less understood. Present-day tokamak plasmas, in the presence of neutral beam heating, tend to exhibit a strong toroidal rotation and correspondingly large toroidal plasma momentum. The plasma rotation is an important quantity to describe the state of fusion plasma, as it influences the transport of plasma impurities [26–30], can stabilize turbulence and improve confinement [31–36]. Moreover, rotation can contribute to the mitigation and avoidance of harmful magnetohydrodynamic (MHD) events [37–42], which can severely damage fusion devices.

Because of its importance, considerable resources have been dedicated to advancing the theory of momentum transport [17, 43–49]. The experimental validation of these predictions, however, is still limited due to the complexity of the momentum transport: in addition to diffusive and convective mechanisms, it has a component not proportional to the rotation velocity (as a convection) or its gradient (as a diffusion). This phenomenon is usually referred to as residual stress flux [47, 49–51], which can result in an intrinsic torque. This torque can signif-

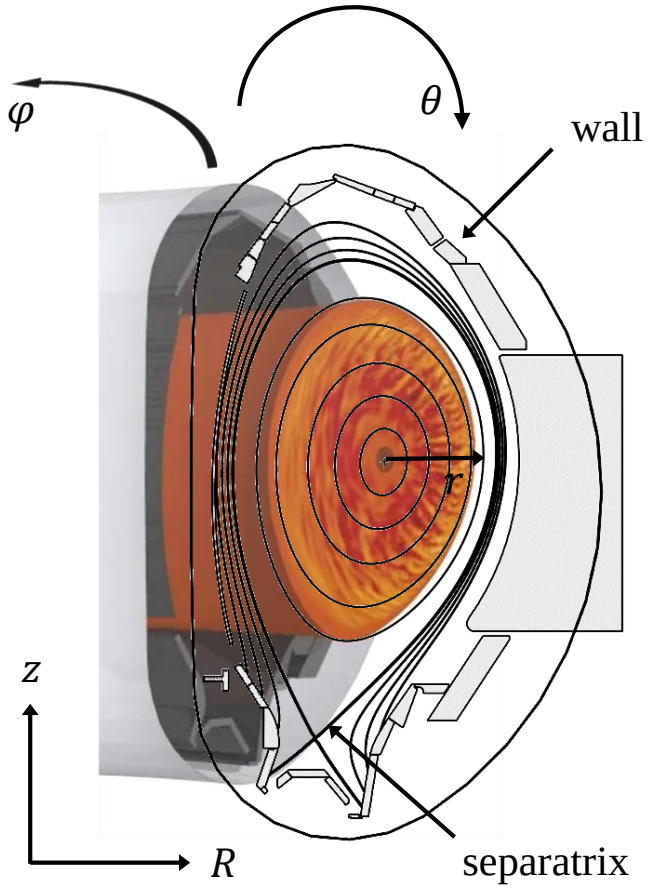

Figure 1.4: Cross section of a tokamak plasma. The basic coordinate system consists of φ the toroidal angle, θ the poloidal angle, z the vertical height, R the major radius from the center of the torus, and r the minor radius from the magnetic axis of the plasma to a given radial position in the plasma. Overplotted a sketch with the equilibrium reconstruction of the nested flux surfaces. In the background, a turbulence simulation from the GENE code is shown [14]. Figure adapted from [15, 16] for the ASDEX Upgrade tokamak.

icantly influence the plasma rotation and remains the largest uncertainty for the prediction of the toroidal rotation profiles in future devices.

A reliable prediction of the rotation profile requires a detailed understanding of momentum sinks, sources, and transport. In present-day devices, neutral beam injection (NBI) heating transfers not only heat to the plasma, but also a significant torque. In future tokamaks like ITER [52], given the larger size and inertia of the plasma, the direct torque from the beams may be insufficient to drive a strong toroidal rotation. Alternative mechanisms are needed to provide the desired level of rotation, such as inward convection of momentum or an intrinsic torque. A validated momentum transport theory is crucial not only for assessing rotation dynamics in present plasmas, but also for gaining insight into how rotation profiles can be optimized. Therefore, this knowledge is essential for achieving more favorable operational conditions in future devices.

In this doctoral thesis, a new analysis methodology is presented that is capable of uniquely, separately, and concomitantly determining the contributions of diffusion, convection, and residual stress to momentum transport within the core of the fusion plasma. It relies on NBI torque modulation experiments performed at the

Axial Symmetric Divertor Experiment (ASDEX) Upgrade tokamak. The aim is to understand the main parameter dependences of momentum transport and validate theory models with experimental data. This sets the basis for coherent, physics-based, and validated predictions of momentum transport for a prospective reactor scenario.

The work is organized as follows: In the second Chapter, the theory background of momentum transport is discussed, and the numerical basics and codes for the analysis are presented. Then, in Chapter 3, the ASDEX Upgrade experiment with its main diagnostic systems is introduced. In Chapter 4, the experimental scenario and its challenges are discussed in the context of the analysis of the reference plasma experiment. In Chapter 5, momentum transport is compared for different plasma isotopes. Detailed results of theory predictions on momentum transport are presented in Chapter 6. Experimental results on the parameter dependences of the transport mechanisms and a comparison of these results to theory are given in Chapter 7. The thesis concludes with a summary and an outlook.

Chapter 2

Theoretical Background

"When I meet God, I am going to ask him two questions: Why relativity? And why turbulence? I really believe he will have an answer for the first."

— Werner Heisenberg

In this Chapter, the basic theory of momentum transport is reviewed. First, the momentum transport equation is derived, and then the transport mechanisms will be discussed. Finally, the numerical codes used in this work are introduced.

2.1 Momentum Transport Equation

Toroidal angular canonical momentum is conserved for each plasma species [53, 54]. Assuming quasi-neutrality and summing over all species yields that the total angular momentum is a conserved quantity. Toroidal momentum can be transported radially, it can be driven externally, and be dissipated by neutral friction at the plasma edge and the scrape-off layer.

In a tokamak, the toroidal component of the angular velocity, Ω_φ, is constant on flux surfaces for sufficiently small poloidal velocity, which is a basic assumption in this work. In fact, the asymmetry in Ω on a flux surface can be used to calculate the poloidal rotation. It is found to be small in the plasma core [55]. The toroidal angular momentum density can be written as

$$L = mnR^2\Omega_\varphi, \tag{2.1}$$

with m the mass of the particles and n the particle density, which is in good approximation constant on flux surfaces. Due to their higher mass compared to electrons, the plasma main ions carry most of the momentum in the absence of a high impurity fraction, as is the case in this work. Since the angular momentum is a conserved quantity, a general continuity equation can be written as

$$\frac{\partial}{\partial t}\int L\,\mathrm{d}V = -\oint \mathbf{\Gamma}\cdot\mathrm{d}\mathbf{S} + \int S\,\mathrm{d}V, \tag{2.2}$$

with $\mathbf{\Gamma}$ the momentum flux, S the momentum sinks and sources. Using $\oint \mathbf{\Gamma} \cdot \mathrm{d}\mathbf{S} = \int \nabla \cdot \mathbf{\Gamma} \, \mathrm{d}V$ on Eq. 2.2, one obtains an equation for the torque density:

$$\frac{\partial}{\partial t} mn\langle R v_\varphi \rangle = -\langle \nabla \cdot \mathbf{\Gamma} \rangle + \langle S \rangle. \tag{2.3}$$

The toroidal plasma velocity is $v_\varphi = \langle R\Omega_\varphi \rangle$ with $\langle \cdot \rangle$ denoting the flux surface average. For the divergence of the flux, it is possible to write [56]

$$\langle \nabla \cdot \mathbf{\Gamma} \rangle = \frac{1}{V'} \frac{\partial}{\partial \rho} V' |\nabla \rho|^2 \, \Gamma_\varphi, \tag{2.4}$$

if the flux is in the radial direction. Here, V' is the flux surface area, ρ the radius in meters, and Γ_φ the radial momentum flux. Then, the equation can be written as:

$$m \frac{\partial}{\partial t} n\langle R v_\varphi \rangle = -\frac{1}{V'} \frac{\partial}{\partial \rho} V' \, |\nabla \rho|^2 \, \Gamma_\varphi + \langle S \rangle. \tag{2.5}$$

The source is due to the torque from the neutral beam injection. The radial flux of toroidal momentum can be split up into three components to describe the physical phenomena of diffusion, convection, and residual stress, written as

$$\Gamma_\varphi = -mnR\Big(\underbrace{\chi_\varphi \frac{\partial \, v_\varphi}{\partial \rho}}_{\text{Diffusion}} - \underbrace{V_\mathrm{c} \, v_\varphi}_{\text{Convection}} \Big) + \underbrace{\Pi_{\text{Rs}}}_{\text{Residual stress}}, \tag{2.6}$$

with χ_φ the momentum diffusivity, V_c the convective velocity, and Π_{Rs} the residual stress flux. In this picture, contributions related to particle fluxes are summed in the convective term of Eq. 2.6.

Finally, the momentum transport equation can be written as

$$m \frac{\partial}{\partial t} n\langle R v_\varphi \rangle = \frac{1}{V'} \frac{\partial}{\partial \rho} V' \, |\nabla \rho|^2 \left(mnR \left(\chi_\varphi \frac{\partial \, v_\varphi}{\partial \rho} - \, V_\mathrm{c} \, v_\varphi \right) - \Pi_{\text{Rs}} \right) + \langle S_{\text{NBI}} \rangle. \tag{2.7}$$

The total torque from NBI is given by the volume integral of the torque density:

$$\tau_{\text{NBI}} = \int S_{\text{NBI}} \, \mathrm{d}V. \tag{2.8}$$

The effective intrinsic torque can be calculated by multiplying the residual stress flux with the flux surface area through which it is flowing:

$$\tau_{\text{int}} = -V' \, |\nabla \rho|^2 \, \Pi_{\text{Rs}}. \tag{2.9}$$

In the following, the basic physical mechanisms and the various microscopic effects leading to transport will be discussed.

2.2 Classical and Neoclassical Transport

To derive *classical* and *neoclassical* transport mechanisms, the description herein mainly follows [5, 6]. Classical transport describes the effects of diffusion due to

thermal collisions of the plasma particles. According to Fick's law, the particle flux is given by

$$\Gamma = -D\nabla n.$$

For the diffusivity D, from a random walk ansatz with Δx the typical step size and Δt the typical time step, it is written:

$$D = \frac{\Delta x^2}{2\Delta t}.$$

To describe radial transport, a suitable Δx perpendicular to the flux surfaces has to be found. Due to the presence of a strong magnetic field $\mathbf{B}$, charged particles in a tokamak are influenced by the *Lorentz* force. Together with the centrifugal force, this leads to a gyromotion of the particle perpendicular to the field line with the *Larmor* radius:

$$\rho_L = \frac{mv_\perp}{|q||B|}.$$

For classical transport, the Larmor radius is used as the typical step size. Moreover, a collision frequency $\nu = 1/\Delta t$ needs to be defined, with Δt the time until a particle has undergone many small angle collisions equivalent to a 90° scattering. Classical transport predictions, however, underpredict the experimentally measured values for all transport channels.

For neoclassical transport, the effects of the magnetic field geometry are considered. For a particle confined in a magnet device, the magnetic moment $\mu \sim W_\perp/B$ and the energy $W = W_\perp + W_\parallel$ are conserved. If a particle moves in a region of a higher field, the parallel velocity decreases, and the perpendicular velocity increases until the point where the parallel motion is stopped and the particle is reflected. In a tokamak, due to the special magnetic field topology, the trapped particles move on so-called *banana* orbits. The *banana width* is the radial distance between the orbit in the toroidal direction and the orbit in the counter-toroidal direction. The banana width is mainly larger than the gyroradius. Assuming a Maxwellian velocity distribution of the particles, the fraction of trapped particles is given by

$$f_{\text{Tr}} \approx \left(\frac{2r}{R_0}\right)^{1/2} \approx \sqrt{2\epsilon}, \tag{2.10}$$

with the inverse aspect ratio $\epsilon = r/R_0$, therefore, the trapped particle fraction in a tokamak increases with the minor radius. The larger radial excursion of the banana orbits, compared to the gyroradius, leads to larger neoclassical transport coefficients for the trapped particles, as Δx for the calculation of the diffusion coefficient is set to the value of the banana width. The contribution of neoclassical effects to particle transport, however, is small, although it may have a minor impact on heat and impurity transport.

For toroidal momentum transport, neoclassical effects are found to be negligible. Due to the toroidal symmetry of the tokamak, the magnetic field is constant in the toroidal direction. This implies that the effects of particle trapping do not constrain the toroidal flow of the ions, but result in friction and damping of the poloidal flow. This does not hold for the toroidal rotation in non-axisymmetric geometry, such as a stellarator, or in the presence of 3D perturbations of the magnetic equilibrium (such as a magnetic ripple at the edge), where also in the toroidal direction the field varies. Such effects are discusses in more detail in [57, pp. 249] or [53, pp. 289].

In the experiment, however, a beam-heated plasma does not accelerate to arbitrarily high values, indicating that a non-zero radial momentum transport is present. Non-collisional contributions to the transport are referred to as *turbulent* transport.

2.3 Turbulent Transport

Transport of momentum in the tokamak core is dominated by turbulence. Therefore, in this work, the experimental measurements are compared to predictions from *gyrokinetic* turbulence codes, which are discussed in the next Section. A large number of different turbulent instabilities exist [6, pp. 455]. In the plasma regimes studied herein, micro-instabilities leading to turbulent eddies mainly emerge where gradients in the ion and electron temperature and density profiles exceed certain critical values [58]. The most dominant instabilities are the Ion Temperature Gradient (ITG) mode and the Trapped Electron Mode (TEM). An instability can also develop due to strong radial gradients of the parallel velocity above a certain threshold [59], which is not exceeded in the discharges considered in this work.

If only the fastest-growing instability (mode) is tracked and the interaction of different modes is neglected, the diffusion coefficients can be estimated as

$$D_{\text{turb}} \sim \frac{\Delta x^2}{\Delta t} \sim \frac{\gamma}{k_\perp^2}, \tag{2.11}$$

with γ the growth rate of the instability, and the wavenumbers $k_\perp = 2\pi/\lambda$ representing the perpendicular extent of the instability.

The ITG mode is found to have strong effects on momentum transport in the plasma core [59]. It also drives significant ion heat transport. The typical length scale is of the order of the ion Larmor radius ρ_i such that $k_\perp \rho_i \approx 0.1 - 1$. The following simplified picture can be made of the origin of this instability, and a more detailed explanation is given in [58, 60].

The effects of the Lorentz force on charged particles in a magnetic field have already been described. Additional forces can lead to drifts. Most important for this work is the $\mathbf{E} \times \mathbf{B}$-drift. The electric fields present in a tokamak can have various origins. A special role has the radial electric field E_r. For a stationary plasma, in the absence of external forces, Reynolds stress, and off-diagonal terms of the pressure tensor, it is possible to write [53]

$$E_r = \frac{\nabla p}{Zen} - v_\theta B_\varphi + v_\varphi B_\theta \tag{2.12}$$

where the first term is the diamagnetic contribution with the radial pressure gradient ∇p, and the second and third are the cross product of the poloidal and toroidal flow with the orthogonal magnetic field components.

The so-called ∇B-drift results from the inhomogeneous magnetic field in a tokamak device. Closely connected is the curvature-drift. Here, due to the toroidal

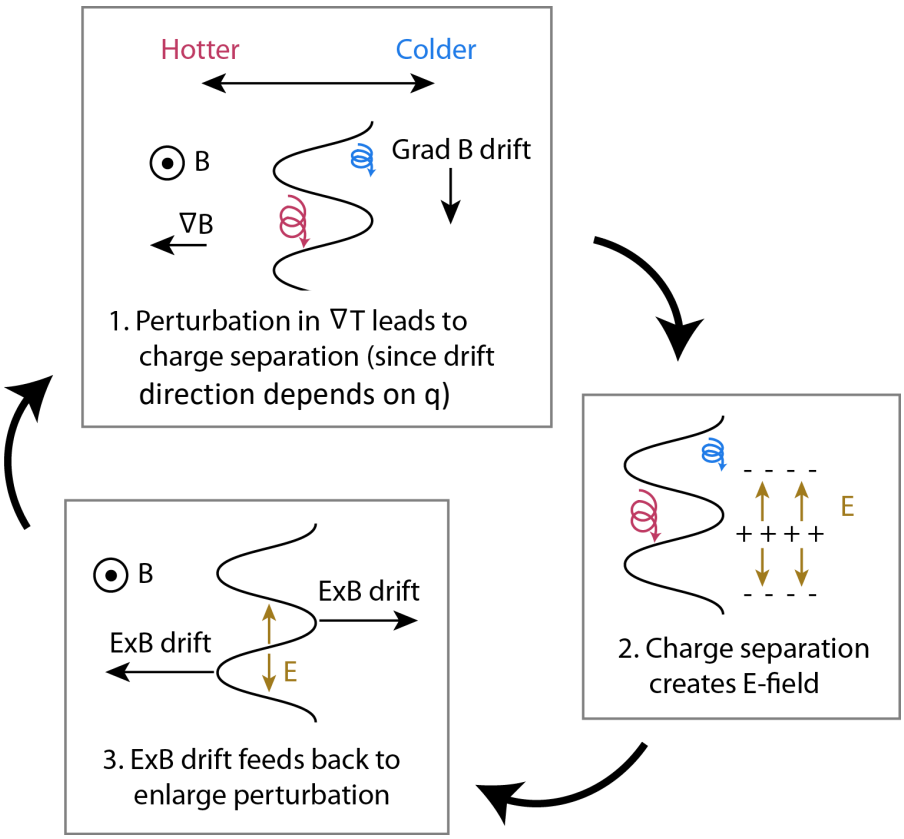

Figure 2.1: Growth mechanism of the ITG instability. Figure from [63].

geometry, a parallel velocity along the field lines is connected with a centrifugal force on the particles.

The ITG instability is related to both the curvature- and $\nabla\mathbf{B}$-drift, as well as the $\mathbf{E} \times \mathbf{B}$-drift. In the unfavorable curvature region on the low field side (for major radii R larger than the magnetic axis, see Fig. 1.4) is $\nabla T_i \parallel \nabla B$. It is assumed that T_i is constant on a flux surface until a perturbation occurs. Due to curvature- and ∇B-drift, this leads to a perturbation of the ion drift in the poloidal direction, resulting in a compression of the ions. The associated perturbed electric field leads, via the $\mathbf{E} \times \mathbf{B}$-drift, to a perturbed drift $\tilde{\mathbf{v}}_E$ in the radial direction. On the low field side, the colder volume of the fluctuation is transported to the region of lower temperature, i.e., radially outwards. This amplifies the perturbation, and the instability grows. The process is shown in Fig. 2.1. From simplified models, as well as from much more sophisticated full gyrokinetic models, a critical gradient $R/L_{T_i} = -R\nabla T_i/T_i$ is observed, which must be exceeded for an instability to grow. This is a very general feature of this kind of turbulence.

A different mechanism exists for electrons, leading to TEM turbulence and associated heat and particle transport. It results from trapped electron precession. This is discussed in more detail in [61, 62]. In reality, ITG and TEM co-exist, while in the linear calculations performed in this work, only the fastest-growing instability is tracked, and interactions are neglected.

2.4 Momentum Transport in the Gyrokinetic Formalism

The gyrokinetic formalism allows the computation of turbulence-induced fluctuations and transport on a microscopic scale. In statistical physics, the particle distribution function $\hat{f} = \hat{f}(\mathbf{r}, \mathbf{v}, t)$ defines the probability to find a particle at time t at location $\mathbf{r}$ with velocity $\mathbf{v}$ [6, pp. 219]. The 6-dimensional vector defines the position in the phase space.

To describe the interaction of many particles, an ensemble (e.g., $N \approx 10^{23}$) has to be implemented. If particles are not created or lost, the particle density is conserved in phase space, i.e., $d\hat{f}/dt = 0$. This time derivative has to be taken along the trajectory in phase space, this results in the *kinetic equation*:

$$\frac{d}{dt}\hat{f}(\mathbf{r}, \mathbf{v}) = \frac{\partial}{\partial t}\hat{f}(\mathbf{r}, \mathbf{v}) + \dot{\mathbf{x}} \cdot \nabla \hat{f}(\mathbf{r}, \mathbf{v}) + \dot{\mathbf{v}} \cdot \nabla_v \hat{f}(\mathbf{r}, \mathbf{v}) = 0. \tag{2.13}$$

With an electromagnetic forces $F = q(\mathbf{E} + \mathbf{v} \times \mathbf{B})$, $\dot{\mathbf{v}} = \mathbf{F}/m$ and $\dot{\mathbf{x}} = \mathbf{v}$, it becomes the *Vlasov equation*:

$$\frac{\partial}{\partial t}\hat{f}(\mathbf{r}, \mathbf{v}) + \mathbf{v} \cdot \nabla \hat{f}(\mathbf{r}, \mathbf{v}) + \frac{q}{m}(\mathbf{E} + \mathbf{v} \times \mathbf{B}) \cdot \nabla_v \hat{f}(\mathbf{r}, \mathbf{v}) = 0. \tag{2.14}$$

To solve the resulting system, the macroscopic fields and the microscopic interactions of the particles are separated. The microscopic interactions are summed in a collisional term added to the Vlasov equation:

$$\frac{\partial}{\partial t}\hat{f}(\mathbf{r}, \mathbf{v}) + \mathbf{v} \cdot \nabla \hat{f}(\mathbf{r}, \mathbf{v}) + \frac{q}{m}(\mathbf{E} + \mathbf{v} \times \mathbf{B}) \cdot \nabla_v \hat{f}(\mathbf{r}, \mathbf{v}) = \left(\frac{\partial \hat{f}(\mathbf{r}, \mathbf{v})}{\partial t}\right)_{\text{coll}}. \tag{2.15}$$

The l.h.s. of this equation only contains averaged mean-field quantities. The r.h.s. includes all microscopic, two-particle interactions. From here, the so-called *fluid picture* can be derived. This is done by taking moments of the kinetic equation and results in, among other things, the radial force balance Eq. 2.12. More details can be found in [6, pp. 235].

Herein, the *gyrokinetic formalism* is discussed that applies to magnetized plasmas. For sufficiently large magnetic fields, the gyromotion is much faster than the motion of the guiding center, so it is possible to average over the gyromotion to reduce the degrees of freedom of the problem. Therefore, the idea behind gyrokinetics [64–67] is to describe the evolution of the distribution function $\hat{f}$ of the gyro-centers in a 5-dimensional phase space.

The distribution function $\hat{f} = f + F$ can be split into a perturbed distribution f that is much smaller than the unperturbed background distribution F. This approximation is not applied in all gyrokinetic codes, but is very practical to reduce computational costs.

Then, for a local gyrokinetic equation, higher order terms in the expansion of the normalized gyroradius $\rho_* = m_i v_{th}/L_\perp e B_\varphi$ are neglected, with $v_{th} = \sqrt{2T/m}$ the thermal velocity, and $L_\perp$ the characteristic perpendicular length scale, e.g. the minor radius a [68]. The resulting gyrokinetic equation is used to solve the corresponding distribution function f.

To understand momentum transport, the symmetry properties of the gyrokinetic equation are investigated with respect to $v_\parallel$ and s, with $v_\parallel$ the parallel velocity, and s the coordinate along the field lines. This is done in Section 2.6 in more detail for the momentum convection. For now, an overview of the symmetry properties is given.

If the gyrokinetic equation is symmetric under the change of sign of $v_\parallel$ or s, the perturbed distribution function f is symmetric, $f(v_\parallel, s) = f(-v_\parallel, -s)$. In such a situation, solutions of the distribution function $f(v_\parallel, s)$ and $f(-v_\parallel, -s)$ can grow with the same growth rates and cancel each other. On the contrary, an asymmetry in the gyrokinetic equation leads to an asymmetry of the perturbed distribution function $f(v_\parallel, s) \neq f(-v_\parallel, -s)$. Such an asymmetry can be interpreted as meaning that solutions (instabilities) of the distribution function $f(v_\parallel, s)$ and $f(-v_\parallel, -s)$ can grow with different growth rates and do not cancel each other. This results in transport.

With the distribution function, the equation for the radial flux of parallel momentum produced by the fluctuating $\mathbf{E} \times \mathbf{B}$-drift $\tilde{v}_E$ can be written as [69]

$$\Gamma_\parallel^r = \langle m_i 2\pi B \, \tilde{v}_E \cdot \nabla r \int v_\parallel f \, dv_\parallel \, d\mu \rangle, \tag{2.16}$$

where $\langle \cdot \rangle$ denotes the flux surface average and $\mu = m v_\perp / (2B)$ the perpendicular velocity component. The integral, which runs over the velocity space, is the parallel velocity moment. Without symmetry breakings, the flux Eq. 2.16 contains the product of a symmetric (even) function along the field lines (the perturbed $\mathbf{E} \times \mathbf{B}$-drift velocity $\tilde{\mathbf{v}}_E$) and an antisymmetric (odd) function along the field lines (the parallel velocity moment $\int v_\parallel f$). Flux surface averaging yields a momentum flux of zero.

If symmetry breakings occur, the parallel velocity moment becomes asymmetric, the flux averaging results in non-zero values, and transport is caused. More detailed investigations yield five relevant sources of such symmetry-breaking mechanisms in the gyrokinetic equation [59]:

- A finite background velocity gradient of the plasma, $\nabla\Omega \neq 0$,
- a finite background velocity of the plasma, $\Omega \neq 0$,
- a radial variation of the radial electric field, resulting in $\mathbf{E} \times \mathbf{B}$-shearing $\gamma_E \neq 0$,
- up-down asymmetries of the magnetic equilibrium, resulting in variation of the curvature- and ∇B-drift, and
- higher order terms in ρ_*, resulting in non-linearities in $v_\parallel$ and including effects of radial variation of profiles and turbulence intensity.

Perturbation theory is applied, and an expression for Eq. 2.16 is found which is linear in the terms of symmetry-breaking and clearly expresses the different transport mechanisms.

It is given, for simplicity, in a normalized form [48]:

$$\Gamma_\varphi^N = \underbrace{\chi_{\varphi\parallel}^N\, u' + \chi_{\varphi\perp}^N \gamma_E^N}_{\text{Diffusion}} + \underbrace{(V_c^N + \Gamma_n^N)\, u}_{\text{Convection}} + \underbrace{C_{\text{M}}^N \gamma_E^N + C_{\text{FS}}^N + \rho_* C_*^N}_{\text{Residual stress}}. \tag{2.17}$$

Here, it is possible to identify the three momentum mechanisms already discussed for Eq. 2.6:

- The first term results from the symmetry breaking via $\nabla\Omega \neq 0$ and denotes the diffusion. It scales with the diffusivity $\chi_{\varphi\parallel}^N$ and $u' = -R^2\nabla\Omega/v_{th}$ the normalized rotation gradient. The second term adds a diffusive component due to the $\mathbf{E}\times\mathbf{B}$-shearing.
- The third term results from the symmetry breaking via $\Omega \neq 0$ and denotes the convection. In the brackets, aside from the convective velocity V_c^N, there is an additional term Γ_n^N from the particle flux. The convection scales with the normalized rotation $u = R\,\Omega/v_{th}$.
- The three terms on the right contribute to the residual stress, with C_{M}^N contributions from the $\mathbf{E}\times\mathbf{B}$-shearing (first order in ρ_*), with C_{FS}^N the flux due to up-down equilibrium asymmetries (lowest order in ρ_*), and $\rho_* C_*^N$ due to effects of higher order in ρ_*.

Details of the three mechanisms and their modeling will be discussed in the following Sections. Please note that, due to $B_\theta < B_\varphi$, the approximation $v_\varphi \approx v_\parallel$ is justified. This connects the theoretically discussed parallel angular momentum with the physically conserved toroidal angular momentum.

2.5 Momentum Diffusion

Momentum diffusivity can be likened to the viscosity of fluids. It was predicted in early theoretical works to be close to the ion heat diffusivity [70]. The similarity results from the fact that the related fluxes are first and second-order moments of the perturbed velocity distribution function, see, for example, the first-order moment in the integral in Eq. 2.16. The ratio of the diffusivities defines the *Prandtl number* [45]:

$$Pr = \frac{\chi_\varphi}{\chi_i}. \tag{2.18}$$

In a number of theoretical works, this quantity was found to be of order unity [59, 71–75] and be weakly dependent on plasma parameters [45, 48]. The momentum diffusivity χ_φ consists of two contributions, one accounting for effects reflected in diagonal elements of the transport matrix ($\chi_{\varphi\parallel}$), and one connected to the dynamics of the $\mathbf{E}\times\mathbf{B}$-shearing ($\chi_{\varphi\perp}$), see Eq. 2.17. The second contribution, however, scales with B_θ/B_φ and is, in the core, mostly negligible, such that $\chi_\varphi \approx \chi_{\varphi\parallel}$. It is neglected in linear gyrokinetic calculations, as performed in this work.

The concept of the Prandtl number can be used in the modeling of experiments, allowing the experimental ion heat diffusivity to constrain the momentum diffusivity. The ion heat diffusivity can be calculated via the power balance

$$\chi_i = -\frac{Q_i}{n_i \nabla T_i}, \tag{2.19}$$

with Q_i the heat flux onto the ions. This equation, together with

$$\chi_\varphi = Pr(\rho_\varphi)\,\chi_i \tag{2.20}$$

is part of the modeling in this work, where the Prandtl number is assumed to be a function of the normalized flux coordinate ρ_φ. From linear gyrokinetic theory, the Prandtl number is one of the most robust predictions and is relatively independent of the turbulent fluctuation level [76].

2.6 Momentum Convection

For the convection, as an example, it is shown how the previously mentioned symmetry breakings manifest in the gyrokinetic equation. The symmetry breaking associated with momentum convection is connected to the Coriolis drift.

For the description of the Coriolis pinch, the co-moving system is used, in which the toroidal rotation is zero. The rotation, therefore, only enters the system through the Coriolis and centrifugal forces, where the latter is neglected in the following derivation. The Coriolis force

$$\mathbf{F}_\mathrm{C} = 2m\mathbf{v}_\parallel \times \mathbf{\Omega} \tag{2.21}$$

leads to a Coriolis drift velocity of

$$\mathbf{v}_{dc} = \frac{2mv_\parallel}{ZeB}\mathbf{\Omega}_\perp. \tag{2.22}$$

A qualitative description of the Coriolis pinch can be made in a fluid picture [43]. The Coriolis drift velocity scales with $v_\parallel$. At the low-field-side midplane, this drift points in the vertical direction. Therefore, it increases or reduces the curvature- and ∇B-drift. If one imagines a finite density perturbation taking place (with some part of the plasma flowing parallel to the field, some part of the plasma flowing anti-parallel to the field), then the flow parallel to the field will drift faster in the vertical direction than the anti-parallel part. Together with the fluctuating $\mathbf{E}\times\mathbf{B}$-convection, this leads to a different radial transport for the two volume elements. This transport acts as a convection of momentum (as the drift scales with the parallel velocity) and inherently depends on the density gradient (as it is connected to the density perturbation).

The Coriolis pinch can also be derived in a gyrokinetic picture as shown in more detail in [43, 48, 68]. The starting point is a very simplified gyrokinetic equation [43]

$$\frac{\partial f}{\partial t} + (\mathbf{v}_d + \mathbf{v}_{dc})\cdot\nabla f = -\mathbf{v}_E\cdot\nabla F_M - \frac{ZeF_M}{T}(\mathbf{v}_d + \mathbf{v}_{dc})\cdot\nabla\langle\phi\rangle, \tag{2.23}$$

with $\mathbf{v}_d$ the curvature- and ∇B-drift, F_M the unperturbed Maxwell distribution, $\mathbf{v}_E$ the $\mathbf{E}\times\mathbf{B}$-velocity, and $\langle\phi\rangle$ the perturbed, gyro-averaged potential. The Coriolis pinch enters on both sides as the other drifts. The corresponding terms can be written with the Coriolis drift velocity as

$$\frac{\partial f}{\partial t} + \frac{2mv_\parallel}{ZeB}\Omega_\perp\cdot\nabla f + ... = ... - \frac{2mv_\parallel}{ZeB}\Omega_\perp\cdot\nabla\langle\phi\rangle\frac{Ze}{T}F_M. \tag{2.24}$$

Calculating the first moment of this equation with respect to the parallel velocity yields [48]

$$mn\frac{\partial w}{\partial t} + \frac{2m\Omega_\perp}{ZeB} \cdot \nabla p_\parallel + ... = ... - 2nm\Omega_\perp \cdot \nabla\langle\phi\rangle/B, \tag{2.25}$$

with w the perturbed velocity and $p_\parallel$ the perturbed parallel pressure. The second term on the l.h.s. is connected to the Coriolis force due to the perturbed diamagnetic velocity. The term on the r.h.s. results from the Coriolis force connected to the perturbed $\mathbf{E} \times \mathbf{B}$-velocity.

The perturbed pressure can be replaced by a sum of perturbed density and perturbed temperature, and a set of coupled equations for the density, temperature, and parallel velocity can be derived, as shown in more detail in [77, 78]. These equations show that the Coriolis drift couples even moments of the perturbed distribution (as density and temperature) and velocity perturbations. This is the reason why parallel velocity fluctuations can be driven by density and temperature perturbations. The fluctuating $\mathbf{E} \times \mathbf{B}$-velocity leads then to a finite flux of toroidal momentum.

So far, the contributions from a finite parallel wavenumber have been neglected. It was shown previously [77], that a symmetry-breaking/deformation of complex electrostatic potential along the field line can result in a finite parallel wavenumber, which can affect the calculated Coriolis pinch. The same work demonstrated that only gyrokinetic calculations with kinetic electrons can produce a finite Coriolis pinch, while in an adiabatic description, without trapped particles, parallel wave vectors occur that balance the equilibrium flow and cancel the Coriolis pinch effect. Therefore, even with kinetic electrons, the Coriolis pinch scales with the trapped electron fraction. In this context, this is known as a *compensational* effect of the passing particles.

The parameter dependences of the momentum pinch were studied via linear gyrokinetic calculations in [48, 79], where the strongest scalings were found with the density gradient and the magnetic shear $s = r/q\, dq/dr$. Here, $q = r/R\, B_\varphi/B_\theta$ is the safety factor, which can also be interpreted as the ratio of numbers of poloidal to toroidal turns of the field lines before they close.

The *pinch number* $-RV_c/\chi_\varphi$ is one of the main results for momentum transport from the gyrokinetic calculation, as the ratio of fluxes allows, at least partly, canceling the potential fluctuations of the turbulence simulation. For the modeling of momentum transport, the convective velocity is defined via the pinch number as

$$V_c = -\frac{\chi_\varphi}{R} h(\rho_\varphi), \tag{2.26}$$

where $h(\rho_\varphi)$ is a dimensionless function describing the radial variation of the pinch number. It could contain, e.g., dependences on gradients or other plasma parameters. Including a scaling with the experimental χ_i via χ_φ (compared Eq. 2.19 and 2.20) serves as a crucial proxy for an experimental, time-varying correlation with the intensity of turbulence [80, 81]. This will be discussed later, together with the experimental scenario in Section 4.1.

The particle flux, which can lead to additional convective momentum flux, is predicted to be small compared to the Coriolis pinch [48] because the particle source

in the core is small in the analyzed AUG scenario [82]. In this work, it will not be separated explicitly. Both the predictions of gyrokinetic theory and the experimental results contain the particle flux, allowing for a direct comparison between them.

2.7 Residual Stress and Intrinsic Torque

There is a variety of symmetry-breaking mechanisms that neither scale with the rotation nor its gradient. Usually, their sum is referred to as *residual stress* flux. The residual stress can also be considered as an *intrinsic torque*, which can spin up the plasma from rest and results in an *intrinsic rotation*. In the following, a number of residual stress generating mechanisms is discussed.

In general, the effects can be separated by their order in ρ_*. First, there are effects of the up-down asymmetry of the equilibrium, which are of the lowest order in ρ_* and are kept in a linear gyrokinetic picture. Second, the first-order contributions in ρ_* with non-linear effects break the symmetry by a finite average radial wavenumber. Third, effects of higher order in ρ_*, which have to be considered in a global, non-linear gyrokinetic picture.

First, asymmetries in the equilibrium break the symmetry along the field lines, resulting in a flux of toroidal momentum [50, 83] and a correlation of the generated intrinsic rotation with the degree of up-down asymmetry. Physically, the generation mainly results from asymmetries in the curvature- and ∇B-drifts and their interaction with the perpendicular turbulent wave vector structure along the field lines. Only modes that are largely extended along the field lines can cover regions with different asymmetry, therefore, mainly modes with small $k_\perp \rho \approx 0.1$ are affected. The flux shows weak dependences on the temperature and density gradients, but drops for the transition from ITG to TEM, being a factor of 4 smaller in TEM [50]. Again, a strong dependence on trapped particles is seen: kinetic electrons lower the flux. The sign of this flux (inward or outward, co-current or counter-current) depends on the direction of the magnetic field and plasma current. Overall, these asymmetries mainly exist towards the plasma edge, see the shape of the flux surfaces in Fig. 1.4, so this effect is small in the plasma core [48, 83] and much smaller than the following contributions.

Second, an important, non-linear effect is the shearing of the $\mathbf{E} \times \mathbf{B}$-drift velocity, the so-called $\mathbf{E} \times \mathbf{B}$-shearing. This shearing produces a finite perpendicular wavenumber $k_\perp$, which damps the turbulence and stabilizes the modes [84]. Furthermore, the sheared velocity front rotates the eddy structure of the turbulent modes away from the outboard midplane, breaking the symmetry $r \to -r$ around the midplane, and the fluxes do not compensate anymore for s and $-s$. The tilting is shown in Fig. 2.2. While the toroidal flow part of the radial electric force balance gives an apparent diffusive component via E_r, see Section 2.5, the diamagnetic and poloidal terms result in a residual stress. From theory, it is not expected that the corresponding fluxes change sign with the transition from ITG to TEM, because the $\mathbf{E} \times \mathbf{B}$-shearing rate does not change its sign [85]. This kind of non-linear gyrokinetic effects were studied in [76, 86–88].

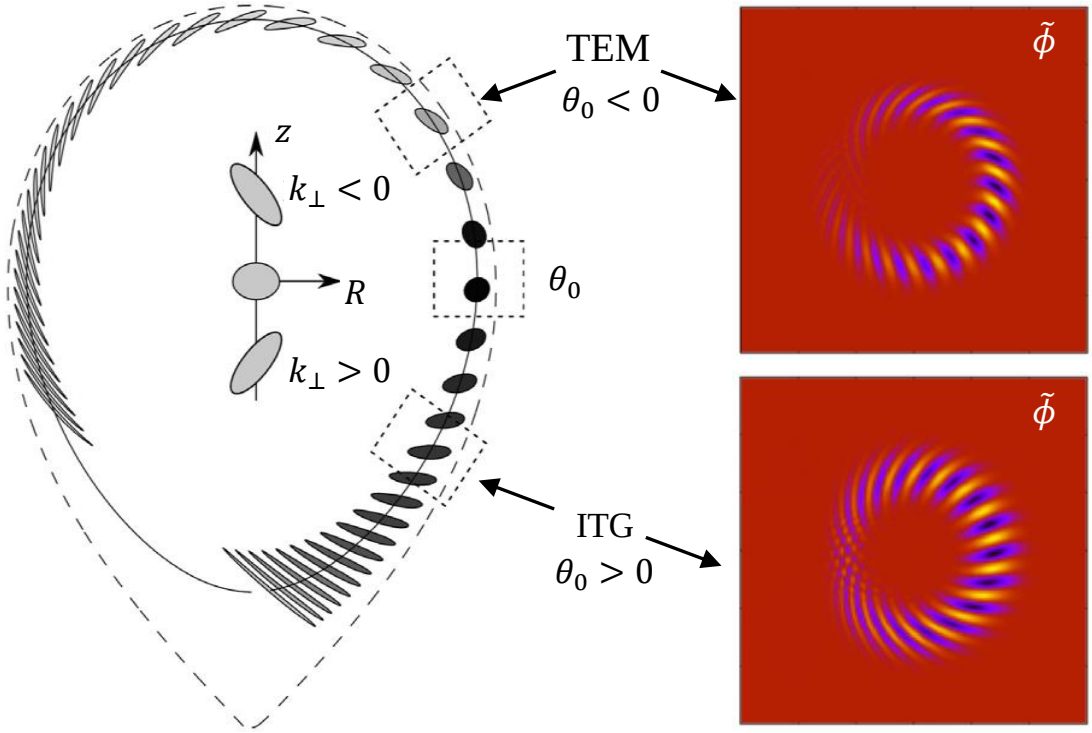

Figure 2.2: L.h.s.: tilting of eddy structure due to the $\mathbf{E} \times \mathbf{B}$ velocity shear or profiles shearing. Figure adapted from [89]. R.h.s.: electrostatic potential fluctuations obtained from global gyrokinetic calculations for TEM and ITG instabilities. The sign change of the tilt angles leading to a sign change of the induced radial flux is observed. Figure adapted from [51].

If a non-linear gyrokinetic picture with terms of higher order in ρ_* is considered, there are no symmetries left and a zoo of different effects arise as investigated, for example, in [47, 51, 85, 90–94]. As a detailed review of all these works is beyond the scope of this thesis, the brief discussion herein focuses on the effects of profile shearing [51, 85] and the radial variation of turbulence intensity. Comparably to the tilting eddy effect described before for the $\mathbf{E} \times \mathbf{B}$-shearing, here, the radial variation of the profiles leads to finite radial wave vectors and can tilt the eddies. These radial wave vectors then couple with the curvature- and ∇B-drifts and induce a flux. Studying the influence of the first-order derivatives of the profiles, it is seen that the tilts of the eddies and the connected flux are oriented in different directions for ITG (co-current, inward) and TEM (counter-current, outward), suggesting a sign reversal of the connected residual stress [51]. Including also the second order derivatives, e.g., for density and temperature profiles, this sign change cannot anymore be clearly attributed to the change of the turbulence regime [85]. The inclusion of such higher-order derivatives makes an experimental validation of such scalings very challenging. Altogether, the magnitude of the fluxes is found to be on the order of the diffusive flux [85].

Besides the residual stress mechanisms already discussed, there are a number of other effects, which can modify the toroidal rotation and could appear as an intrinsic torque in an experimental analysis. They are not directly related to gyrokinetic calculations for the confined plasma with an unperturbed magnetic equilibrium.

Prominent examples are MHD effects such as sawteeth that redistribute particles and their momentum [6, pp. 401], ion orbit losses [95], magnetic ripple [96, 97],

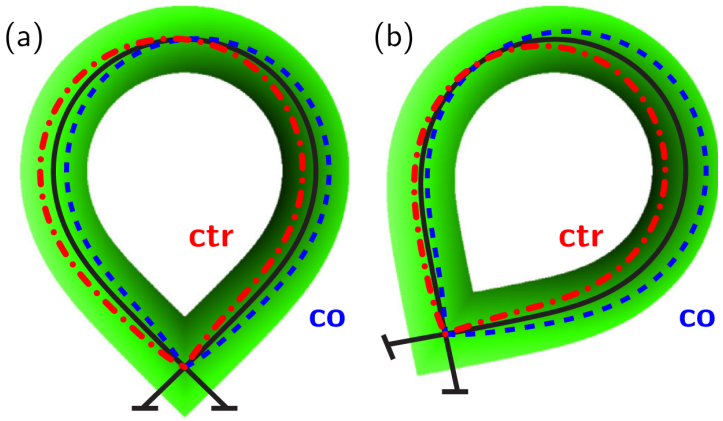

Figure 2.3: Trajectory (orbits) of counter- (red) and co-current (blue) passing ions. Panel (a) shows an equilibrium with an X-point radially aligned with the magnetic axis. In Panel (b), an equilibrium with an X-point shifted to the high-field side is shown. The darker the color, the higher the local diffusion. Figure reproduced from [49].

neutral drag [98, 99], neoclassical toroidal viscosity [100, 101], and the various effects of momentum loss to the wall of the machine.

Another model that has undergone experimental validation is the analytical, theory-based Stoltzfus-Dueck model, which predicts the pedestal top intrinsic torque based on ion orbit losses, scrape-off layer flows, and turbulence intensity gradients [49, 102–104]. It assumes a purely diffusive turbulent transport, which acts spatially inhomogeneously. Furthermore, parallel acceleration is neglected, and the excursion of the drift orbits of passing ions in the edge and SOL is maintained. Following the analytical derivation, it is found that the drift orbits of co-current moving ions are displaced outwards along the major radius. Vice versa, counter-current ions are displaced inwards along the major radius. If a turbulent diffusion with a typical gradient length is assumed, then, together with the tilt of X-point, see Fig. 2.3, this leads to a larger diffusion of counter-current than co-current particles. This results in an apparent co-current residual stress.

The net torque of these effects is given as a boundary condition at the edge of the plasma core, approximately at the pedestal top, but the model cannot predict the precise location. The intrinsic torque at the pedestal top by the Stoltzfus-Dueck model is given via

$$\tau_{\text{int,SD}} \approx 1.38\,(1-f_{\text{Tr}})\,(\bar{R}_X - d_c/2)\,\frac{(A_i/2)\,qR}{Z_i B_\varphi L_\phi}\,Q_i\ [\text{N m}], \tag{2.27}$$

with f_{Tr} the trapped particle fraction, Q_i the heat flux in MW, and L_ϕ the decay length of the potential fluctuations in the pedestal, which can be approximated by L_{T_e}. In this formula, q is used for the ratio of the thermal passing-ion drift-orbit width to the ion gyroradius and can be approximated as $q = [B_\varphi(R_{\text{out}} - R_{\text{in}})]/(2B_\theta R)$. d_c is an in-out-transport asymmetry factor ranging from $+2$ (all transport occuring at the low-field-side midplane) to -2 (all transport occuring at the high-field-side midplane). Estimates, relying on outboard ballooning modes, give values around $d_c \approx 1$. $\bar{R}_X = [2R_X - (R_{\text{out}} + R_{\text{in}})]/(R_{\text{out}} - R_{\text{in}})$ is the normalized major radius of the X-point, with R_{in} and R_{out} the inner- and outer-most major radii of the last closed flux surface (LCFS), and R_X the major radius of the X-

point. $\bar{R}_x$ then ranges from -1 (X-point at the high-field-side edge of the LCFS, as shown in Fig. 2.3b) to $+1$ (X-point at the low-field-side edge of the LCFS). The model is used in the integrated modeling approach by Luda *et al.* [105–107]. The implementation in this work is comparable to the one in that work, but the precise calculation of the gradient length, the passing particle fraction, and the heat flux differs.

A very flexible approach to model the residual stress from all these effects is to add an additional flux in the momentum transport equation, which is Π_{Rs} in Eq. 2.7 and 2.9:

$$\Pi_{\text{Rs}} = m_i n_i \, \chi_\varphi \, c_s \, g(\rho_\varphi), \tag{2.28}$$

with c_s the sound speed, m_i the main ion mass, n_i the main ion density, and $g(\rho_\varphi)$ is a dimensionless function describing the radial shape of the residual stress. Again, the scaling with the diffusivity is used to include a possible time-dependent turbulence intensity via χ_i, as already done for the momentum convection.

2.8 Momentum Sources via Neutral Beam Injection

The dominant source term in the momentum transport equation is the torque applied to the plasma via NBI. This heating technique relies on the acceleration of ions to high energies of up to tens of keV, their neutralization, and injection into the plasma. There, they are ionized by collisions and confined by the magnetic field. Via Coulomb collisions, they transfer their energy to the plasma bulk [5, pp. 540]. This is not only connected with a rise of ion and electron temperature, but can drive a plasma current and induce a strong torque [108].

There is a nearly instantaneous transfer of momentum from particles that are injected into regions of the plasma where they are ionized and, together with their radial movement, lead to a $\mathbf{j} \times \mathbf{B}$-force that acts on the background plasma as a torque. This happens on time scales of the order 10^{-5} s. These effects can be calculated analytically [109]. Furthermore, the fast particles transfer their momentum via collisions with bulk ions and electrons, acting as a torque onto the bulk plasma. This takes place on collisional time scales of hundreds of ms. The contribution of the collisions can be calculated by solving a Fokker-Planck equation [110].

Utilizing Monte Carlo models to calculate these contributions was proposed, for example, in [111, 112]. In such simulations, test particles are injected and tracked as they interact, while the torque is derived from momentum conservation. These models are the method of choice in this work, as explained in the next Section when describing the `NUBEAM` code. The torque from the NBI is included in the momentum transport modeling as the source term S_{NBI} in Eq. 2.7.

2.9 Applied Transport Codes and Models

The heat fluxes and torque in the plasmas analyzed in this work were calculated with the `TRANSP` code, which is developed and hosted at Princeton Plasma Physics

Laboratory (PPPL) [113–115]. TRANSP is generally employed for calculating particle and energy transport in tokamaks by analyzing conservation equations. It offers access to local quantities that may not be directly measurable in experiments, such as fluxes, based on realistic plasma input data, the plasma geometry, information about the auxiliary heating, et cetera. The input to TRANSP is documented in Appendix A.1.

TRANSP is a full transport code, however, for this work, only the modules for the calculation of heat fluxes and torque were employed. For the electron cyclotron resonance heating, the TORBEAM code [116] is used. As mentioned in the previous Section, Monte Carlo codes are the method of choice to calculate the effect of NBI. To this end, the NUBEAM code is utilized [117]. It is capable of simulating the power deposition, current drive, fueling, and torque fluxes in a tokamak due to NBI. NUBEAM includes effects of collisions, ion-neutral interaction (ionization, charge exchange, excitation), diffusion of fast ions, magnetic ripple, effects of the equilibrium (fast ion banana orbits), and finite Larmor radius effects (fast ion guiding center drifts). As Monte Carlo models are based on a statistical approach, significant parallel computing power is required. In the calculations performed herein, particle numbers between 50,000 and 200,000 are used to reduce the statistical noise.

The results from TRANSP, specifically the perpendicular and parallel fast ion pressures, the power to the ions (P_i) and electrons (P_e), the torque density from the NBI (S_{NBI}) and the radiated power (P_{Rad}) are then transferred to the ASTRA code, which is the second transport code applied in this work in an interpretative approach [118, 119]. Documentation of the input to ASTRA is given in Appendix A.2. ASTRA solves the transport equations for a tokamak plasma, in particular, the ion heat power balance and the momentum transport equation.

ASTRA is denoted as a 1.5-dimensional transport code. The “1.5 dimensions” are related to the fact that it is assumed that the main plasma quantities are constant on a flux surface such that the transport equations can be solved on the basis of the normalized toroidal flux coordinate ρ_φ, while the equilibrium reconstruction [120] is solved in 2 dimensions in the poloidal plane, assuming the axial symmetry of the tokamak.

In contrast to the TRANSP code, ASTRA is an interactive platform for tokamak transport modeling and allows the simulation of a plasma almost in real-time. It can be flexibly run with analytical expressions for the transport coefficients, which can be easily input by the user. Therefore, ASTRA can be efficiently used in an iterative approach to optimize transport coefficients and model experimental data.

Within ASTRA, the momentum transport equation was implemented by Fable [80]. It allows the specification of the following momentum transport coefficients:

- Radial diffusivity of parallel momentum

$$\texttt{XUPAR} = \chi_{\parallel} = Pr(\rho_\varphi)\,\chi_i \tag{2.29}$$

  in $\mathrm{m}^2\,\mathrm{s}^{-1}$, with a radially dependent Prandtl number, see Section 2.5.

- Convective velocity of parallel momentum transport

$$\texttt{CNPAR} = V_{\parallel} = V_c - \chi_{\parallel} \frac{\nabla I_\theta^N}{I_\theta^N} = -\chi_{\parallel}/R\, h(\rho_\varphi) - \chi_{\parallel} \frac{\nabla I_\theta^N}{I_\theta^N} \tag{2.30}$$

  in $\mathrm{m\,s^{-1}}$. Here, V_c is the convective velocity, see Eq. 2.26, which is modified by a correction term depending on the normalized poloidal current I_θ^N to account for the difference between toroidal and parallel field intensity. The radially dependent pinch number, here $h(\rho_\varphi)$, can be used to modify the radial shape of the pinch. In this work, a cubic polynomial is used. Thereby, the constant term is neglected to enforce continuity at $\rho_\varphi = 0$.

- Residual stress flux

$$\texttt{RUPFR} = \frac{\Pi_{\mathrm{Rs}}}{10^{19}\, m_p} = \frac{m_i n_i}{10^{19}\, m_p}\, \chi_\varphi\, c_s\, g(\rho_\varphi) \tag{2.31}$$

  in $\mathrm{s^{-2}}$, with Π_{Rs} as defined in the momentum transport Eq. 2.7. The residual stress flux proposed in Eq. 2.28 can be used. The dimensionless, radially dependent function $g(\rho_\varphi)$ allows the modification of the radial shape. In this work, a cubic polynomial is used. Again, the constant term is neglected to enforce continuity at $\rho_\varphi = 0$.

- Torque density from NBI

$$\texttt{TTRQ} = \frac{S_{\mathrm{NBI}}}{10^{19}\, m_p} \tag{2.32}$$

  in $\mathrm{m^{-1}\,s^{-2}}$, with the torque density S_{NBI} from TRANSP in $\mathrm{N\,m\,m^{-3}}$.

In ASTRA, the momentum fluxes are normalized by a factor $m_p \times 10^{19}$ with m_p the proton mass in kg. This results in the normalization of the residual stress flux and torque density. The ion heat diffusivity χ_i is calculated via a power balance, see Eq. 2.19. Based on these momentum transport equations and a boundary condition given by the experimental toroidal rotation at the edge of the calculation domain, ASTRA solves the time-dependent toroidal rotation consistent with the momentum transport coefficients given via $Pr(\rho_\varphi)$, $h(\rho_\varphi)$, and $g(\rho_\varphi)$. By comparing the modeled toroidal rotation profile to the experimentally measured, the quality of the used momentum transport coefficients can be assessed.

In ASTRA, the radial transport of parallel momentum transport is calculated. The parallel velocity is approximated by the toroidal velocity. Due to $B_\theta < B_\varphi$, this approximation is justified.

2.10 Applied Gyrokinetic Code

The gyrokinetic code GKW [68] was used to simulate turbulent transport. This results in predictions for the Prandtl and the pinch number, which can then be compared with experimentally assessed transport coefficients. The code solves the gyrokinetic equations, see Section 2.4, and includes kinetic electrons, electromagnetic effects, collisions, and a realistic reconstruction of the plasma equilibrium.

Quantity	GKW parameter	Comment
$k_y\rho_i$	`kthrho = ...`	poloidal wave vector
ϵ	`eps = ...`	inverse aspect ratio
	`geom_type= 'chease'`	use an experimental Hamada equilibrium
	`eqfile= '...'`	specify the path of the Hamada input file
β_{ref}	`beta_ref = ...`	$2\mu_0 nT/B^2$, for normalization
		for the first `SPECIES`, ions
R/L_{T_i}	`rlt = ...`	ion temp. gradient
R/L_{n_i}	`rln = ...`	ion density, approx. with R/L_{n_e}
		for the second `SPECIES`, electrons
m_e/m_p	`mass = ...`	mass ratio between electrons and ions
T_e/T_i	`temp = ...`	temperature ratio
R/L_{T_e}	`rlt = ...`	electron temp. gradient
R/L_{n_e}	`rln = ...`	electron density
u'	`uprim = ...`	rotation gradient
u	`vcor = ...`	rotation
		for the `COLLISIONS`
R	`rref = ...`	major radius
T_i	`tref = ...`	ion temp. for normalization
n_e	`nref = ...`	electron density for normalization
Z_{eff}	`zeff = ...`	effective charge of the plasma

Table 2.1: Most relevant input parameters to `GKW`.

Furthermore, it includes the effects of the plasma rotation, which makes it suitable to study the Coriolis momentum pinch [68].

Global, non-linear calculations are computationally expensive and inappropriate for the analysis of large databases, as done in this work. Therefore, only residual stress fluxes can be assessed that result from the up-down-asymmetry of the equilibrium. These are, by far, not the dominant contributions, compared, for example, with the finite ρ_* or profile shearing effects. Examples of global non-linear calculations are shown in [121–124].

For this work, local, linear calculations were performed. Experimental inputs and the most import settings in `GKW` are shown in Tab. 2.1. It is necessary to select which flux surface to consider (via ϵ and R), to give the corresponding experimental quantities, and to set a normalized binormal wavenumber/poloidal wave vector $k_y\rho_i$ to be studied.

The code is used with the time integration scheme for the identification of the micro-instability with the highest growth rate only. The convergence of the growth rate γ and real frequency ω_r of the fastest-growing mode as a function of the computed time is presented in Fig. 2.4(a). The sign convention for ω_r yields a positive sign for mode propagation in the ion diamagnetic direction (e.g., ITG) and a negative sign for a mode in the electron diamagnetic direction (e.g., TEM). In Panel (b), the resulting momentum flux is shown. The asymmetries of the potential and velocity distributions are shown in Panels (c) and (d). As already explained in Section 2.4, a symmetry breaking in the eigenfunctions leads to a non-zero momentum flux.

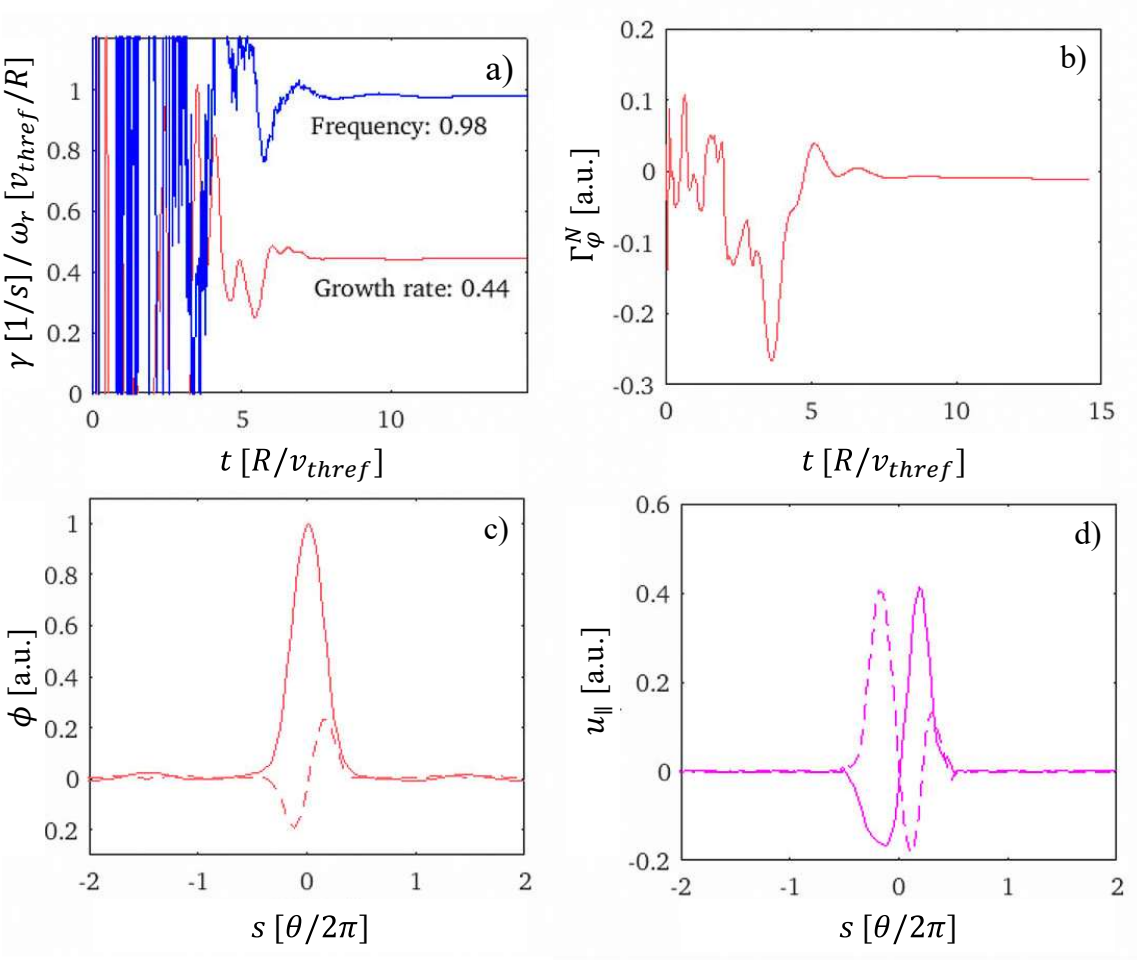

Figure 2.4: Typical output of a GKW calculation. Panel (a) shows the growth rate and the frequency of the fastest-growing instability converging over the computational time. Panel (b) shows the momentum flux, which also converges over the computational time. Panel (c) shows the potential fluctuation, with the real part as a solid line, and the imaginary part as a dotted line. Panel (d) shows the perturbed velocity distribution of the ions, $u_\parallel = \int v_\parallel f d^3v/n_i$, with the real part as solid line, and the imaginary part as dotted. Clearly visible are the asymmetries for $s \to -s$.

For the prediction of the Prandtl and pinch numbers, in general, three gyrokinetic simulations need to be performed for each wavenumber $k_y\rho_i$:

1. with $u' = u = 0$, this results in the residual fluxes (three last terms) of Eq. 2.17,
2. with $u' = 0$, $u = 0.15$, this results in the convective flux $\Gamma_{\varphi,V}$, third term of Eq. 2.17, and the residual fluxes, and
3. with $u' = 0.5$, $u = 0$, this results in the diffusive fluxes $\Gamma_{\varphi,D}$, first and second term of Eq. 2.17, and the residual fluxes.

The values $u = 0.15$ and $u' = 0.5$ can, in principle, be replaced by any small, finite number as they do not affect the turbulence calculation [76]. All three calculations give the ion heat flux Q_i. The residual fluxes (obtained in the first calculation) can be extracted from the second and third calculation to isolate the fluxes due to diffusion and convection only. The fluxes are weight-averaged over a spectrum of five binormal wavenumbers between $0.2 < k_y\rho_i < 0.9$ to include the contributions of

modes at different wavelengths in the spectrum, the index k denotes the different $k_y\rho_i$ used. As different tested wavenumbers grow with different growth rates γ_k, they are further weighted by a spectral amplitude that depends on the ratio of the growth rates to the perpendicular wavenumber squared.

First, the diffusivities and the convective velocity are calculated from the fluxes.

$$\begin{aligned}\chi_{i,k}/R &= -Q_{i,k}/\nabla T_i \\ \chi_{\varphi,k}/R &= -\Gamma_{\varphi,\mathrm{D},k}/u' \\ V_{c,k} &= \Gamma_{\varphi,\mathrm{V},k}/u\end{aligned}$$

Then, the binormal wavenumbers

$$\sqrt{2}\,k_y\rho_i = [0.21, 0.31, 0.44, 0.64, 0.92]$$

together with some practical knowledge weighting w_k give $k_\perp$:

$$k_\perp = k_y\, w_k.$$

The potential fluctuation can be assumed as

$$|\Phi|^2 = \gamma_k/k_\perp^2.$$

Then, it is possible to average via

$$\begin{aligned}\chi_i/R &= \int \frac{\chi_{i,k}}{R}\,|\Phi|^2 dk_\perp \\ \chi_\varphi/R &= \int \frac{\chi_{\varphi,k}}{R}\,|\Phi|^2 dk_\perp \\ V_c &= \int V_{c,k}\,|\Phi|^2 dk_\perp\end{aligned}$$

and to calculate the Prandtl and pinch numbers:

$$\begin{aligned}Pr &= \frac{\chi_\varphi}{R}\,\frac{R}{\chi_i} \\ -R\,V_c/\chi_\varphi &= -\frac{V_c}{\chi_\varphi/R}.\end{aligned}$$

It is important to mention that the fluxes in a linear calculation increase during the calculation with the growing potential fluctuation $|\Phi|^2$. Therefore, only ratios of fluxes, e.g., χ_i/χ_φ and $-RV_c/\chi_\varphi$, can be compared to the experimental results presented later in this work.

Chapter 3

Experimental Background

"A scientist in his laboratory is also a child confronting natural phenomena that impress him as though they were fairy tales."

— Marie Curie

In this Chapter, the experimental setup, the most relevant measurement diagnostics, and analysis techniques are presented that enable the modeling of momentum transport in the ASDEX Upgrade tokamak.

3.1 The ASDEX Upgrade Tokamak

The Axial Symmetric Divertor Experiment (ASDEX) Upgrade is a tokamak fusion experiment located at the Max Planck Institute for Plasma Physics in Garching, close to Munich. First experiments were performed in March 1991 [125].

The machine parameters are listed in Tab 3.1. Figure 3.1 shows a sketch of the machine. In the center, there is the transformer coil, which is capable of driving currents of up to 1.6 MA in the plasma. The plasma is produced in the vacuum vessel. Most of the plasma-facing components (PFC) are tungsten coated or are made of solid tungsten. During a so-called *boronization*, glow discharges with a mixture of He and B_2D_6 are performed to cover the PFCs with a thin layer of

Typical discharge length	10 s
Major radius	$R = 1.65$ m
Minor radius	$r = 0.5$ m
Plasma current	$I_p = 0.3$ – 1.4 MA
Toroidal magnetic field	$B_\varphi = 1$ – 3.5 T
Plasma volume	up to 14 m^3
Total available heating power	up to 30 MW
Plasma fuel	H, D, He

Table 3.1: Main machine parameters of the ASDEX Upgrade tokamak [125].

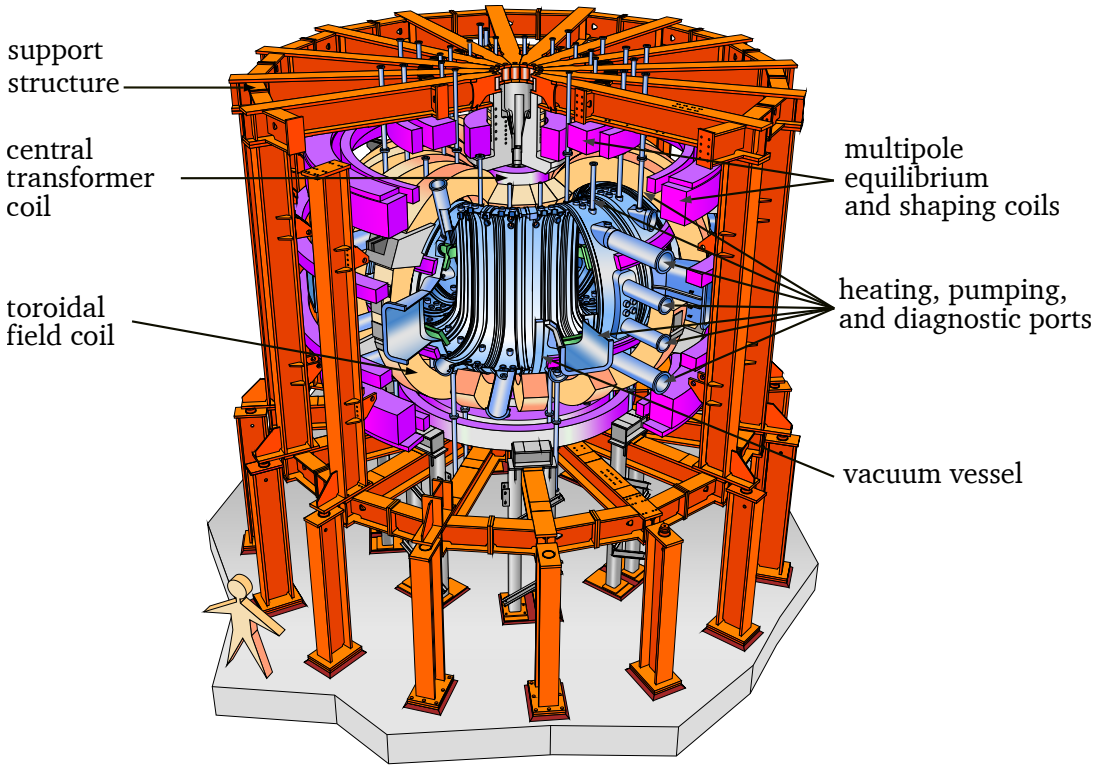

Figure 3.1: Sketch of the ASDEX Upgrade tokamak. Figure adapted from [126].

boron [127]. This reduces the tungsten influx, enabling low-density operation. This makes boron and helium the main impurities in the absence of additional impurity gas puffing.

The vessel is composed of 16 sectors. This can be seen in the schematic top-down view of the machine, given in Fig. 3.4. The vacuum vessel has several heating, pumping, and diagnostic ports. Around the vessel, shown in orange in Fig. 3.1, there are 16 D-shaped toroidal field coils. They can produce a toroidal magnetic field up to 3.5 T. The poloidal field and shaping coils are shown in magenta, and in red, the steel support structure is shown. As the toroidal field coils are made from copper, the joule heat limits the discharge length to approximately 10 s.

The fueling of the plasma takes place from various valves within the vacuum vessel. AUG can be operated with H, D, and He as main ions. The divertor systems, placed at the top and the bottom inside the plasma vessel, allow control of the exhaust of particles and power from the main plasma. The lower divertor, which was used for the experiments in this work, can be pumped via a cryopump.

The plasma heating can be composed of ohmic heating through the current drive, neutral beam injection heating (20 MW), ion cyclotron resonance heating (6 MW), and electron cyclotron resonance heating, short ECRH (6.4 MW).

The NBI has two injection boxes, one in sector 15 and another one in sector 7, as shown in Fig. 3.4, on opposite sides of the torus. Both boxes have four beam sources. NBI box 2 features higher extraction voltages of up to 90 keV, while

box 1 is operated with 60 keV. The standard operation for the beams is with D ions. They are produced by an arc source (box 1) and via a radio-frequency-driven plasma source (box 2). These ions are accelerated and neutralized to be able to enter the strong magnetic fields.

From the radio frequency heating systems, in the experiments presented in this work, only the ECRH was used. The basic principle of this heating technique is to launch microwave beams of the same or a multiple frequency as the electrons' gyration frequency. As the gyration frequency depends on the local magnetic field, a very localized heat deposition is feasible. The standard frequency is 140 GHz, which allows for central heating of the plasma at a magnetic field of 2.5 T on the magnetic axis. This corresponds to the second harmonic of the Larmor frequency in the so-called X-mode (inciting electric field vector $\mathbf{E} \perp \mathbf{B}$) heating scheme.

3.2 Main Diagnostic Techniques

The ASDEX Upgrade experiment provides a large number of measurement systems to diagnose various plasma parameters. This Section focuses on electron density and temperature measurements, as well as equilibrium reconstruction. Figure 3.2(a) shows a picture of a poloidal cut of the torus with the measurement positions of the most important diagnostics plotted over an equilibrium reconstruction.

Thomson Scattering

Thomson scattering (TS) is the well-known effect of scattering of induced electromagnetic waves on charged particles, which then act as dipoles and oscillate [128, 129]. In a plasma, due to the lighter mass, mainly electrons are involved, while ions are weakly affected by the induced electric fields. The scattered light is Doppler-shifted due to the movement of the electrons with respect to the incoming wave and the lines of sight.

In the application as a plasma diagnostic, a strong, pulsed laser is used to introduce the electromagnetic wave. As the overall scattered emission is very low, highly sensitive polychromators are used to measure the scattered light. If the Debye length, which is the distance up to which the plasma can screen induced electric fields with its free charges, is much larger than the wavelength of the incident electromagnetic wave, the scattering is called *incoherent*. Then, the Doppler shift correlates directly with the velocity distribution of the plasma electrons. The resulting spectrum is Gaussian with a half-width of $\sqrt{T_e}$. With an absolute calibration, the electron density can be measured via the intensity of the scattered light [130]. The advantage of the TS is to measure electron temperature and density simultaneously in the same plasma volume.

At ASDEX Upgrade, Thomson scattering systems routinely diagnose the plasma core and edge using Nd-YAG lasers. The exact localization of the measurement is shown as red squares in Fig. 3.2(a). The pulses are short, around 10 ns, the repetition rate is 20 Hz. The radial resolution is around 25 mm for the core TS and

3 mm for the edge measurements. Calibration is performed via Raman scattering in nitrogen [131, 132].

Electron Cyclotron Emission

Another approach to measuring the temperature profiles of the electrons is the electron cyclotron emission (ECE) [13, pp. 518]. In a magnetic field, which mainly has a toroidal component, the local magnetic field can be approximated via $B_\varphi = B_0 R_0 / R$. Charged particles emit cyclotron radiation with a frequency corresponding to multiples N of their Larmor frequency

$$\omega_N = N \frac{e B_0 R_0}{m_e R}.$$

For small N waves, the plasma is optically thick, and the intensity can be approximated as black body radiation. The Rayleigh-Jeans law can be applied:

$$I_N(\omega) = \frac{\omega^2 k_B}{8\,\pi^3\,c^2} \cdot T_e.$$

From this formula, the electron temperature can be derived directly from the intensity of the cyclotron emission. The frequency of the emission depends on the local magnetic field, and this feature is used to radially localize the measurements. Due to cutoffs, the strongest intensity outside of the plasma is measured for the second harmonic in X-mode ($\mathbf{E} \perp \mathbf{B}$) and fundamental frequency in O-mode ($\mathbf{E} \parallel \mathbf{B}$).

At ASDEX Upgrade, the second harmonic of the X-mode is measured via a 60-channel heterodyne radiometer [133]. It is sensitive to radio emission between 85 – 185 GHz, which corresponds to magnetic fields from 1.6 to 3.4 T. It has a radial resolution of about 5 mm, and a time resolution below a μs. The measurement antenna is placed slightly above the midplane and diagnoses the plasma from the low-field side. The measurement localization is shown in green symbols in Fig. 3.2(a). The system is calibrated by means of black-body radiation measurements [134, 135].

Lithium Beam

Lithium-beam spectroscopy (LIB) can be used to diagnose the plasma edge and derive density profiles. The use of an active beam allows the localization of the measurement in the edge region, which features very steep gradients.

The injected lithium atoms are accelerated to high kinetic energies. As these atoms penetrate the plasma edge, they undergo various collisional processes resulting in emission, which allows the detection of the Li I spectral line along the path of the beam. The most relevant process is the excitation of the lithium atoms by electron impact [136, 137]. The balance equation of impact excitation and spontaneous emission is solved in forward modeling to reconstruct the electron density profiles [138].

At ASDEX Upgrade, the lithium ions are extracted from a beta-eucryptite emitter and are accelerated to energies of up to 60 keV. The neutralization is done by means of a sodium neutralizer cell, and the beam is injected from the low-field side, shown in magenta circles in Fig. 3.2(a). Two optical heads are used to observe the emission. The data acquisition system is based on interference filters and photomultiplier tubes and has a high time resolution of 50 μs [139]. As discussed in [140], probabilistic data analysis can be used to assess density profiles from the Li I emission profile with a high spatial and temporal resolution of 5 mm and 50 μs.

Laser Interferometry

In a plasma, when an electromagnetic wave passes through, it undergoes not only scattering, but also experiences refraction and reflection. For the case of a collisionless plasma, in which the electric wave vector is parallel to the magnetic field, the refraction index for a wave traveling in a plasma is [13, pp. 506]

$$\mu = \sqrt{1 - \frac{\omega_{pe}^2}{\omega_0^2}}$$

with the plasma frequency

$$\omega_{pe} = \sqrt{\frac{n_e e^2}{\epsilon_0 m_e}}.$$

For $\omega_0 \gg \omega_{pe}$, it is possible to write

$$\mu \approx 1 - \frac{\omega_{pe}^2}{2\omega_0^2} = 1 - \frac{e^2}{2\epsilon_0 m_e \omega_0^2} \cdot n_e.$$

This connects the refraction index with the electron density. The refraction results in a phase shift of

$$\Delta\phi \approx \frac{e^2}{2c\epsilon_0 m_e \omega_0} \int n_e \mathrm{d}l,$$

with ω_0 the original frequency of the electromagnetic wave.

As a diagnostic technique, a laser traveling through the plasma can be compared with a second wave from the same source traveling outside the plasma. The interference of both waves is then used to measure the phase shift. This measurement principle is called interferometry, and it provides measurements of the line-integrated electron density along the line of sight of the laser [141].

At ASDEX Upgrade, a deuterium cyanide laser (DCN) with a wavelength of 195 μm is used. This laser is split up into 6 paths. 5 of them have distinct and well-characterized LOS through the plasma, shown in cyan in Fig. 3.2(a). One is used as a reference. A phase-modulated Mach-Zehnder interferometer measures the phase shift.

A phase shift of 2π corresponds here to a density of 5.72×10^{18} electrons/m^2. Dividing the result by the length of the line of sight through the plasma gives a line-averaged density in m^{-3}. The time resolution of these measurements is about 300 μs [141].

These four diagnostic systems estimate the electron temperature and density in various regions of the plasma with differing time bases. The measurements are combined to obtain a coherent and reliable picture of the electron density and temperature at high spatial and temporal resolution.

At ASDEX Upgrade, this is done by means of the Integrated Data Analysis (IDA), which relies on Bayesian inference [143]. The idea behind Bayesian inference is to use forward models for each included diagnostic to set up likelihood distributions based on the uncertainties of the diagnostic measurements. With d the measured data, the likelihood distribution function $p(d|T_e, n_e)$ can be calculated. This function can be imagined as a weighting factor discretizing how much to believe the specific measurement T_e and n_e from a certain diagnostic. Additionally, a prior $p(T_e, n_e)$ with additional knowledge and boundaries on the behavior of the physical quantities is set up. This ensures the physical validity of the results. In Bayes' theorem, the posterior probability density function is

$$p(x, y|d) = \frac{p(d|x, y)p(x, y)}{p(d)}.$$

The additional normalization can be neglected as it is not relevant to the parameter estimation in this application.

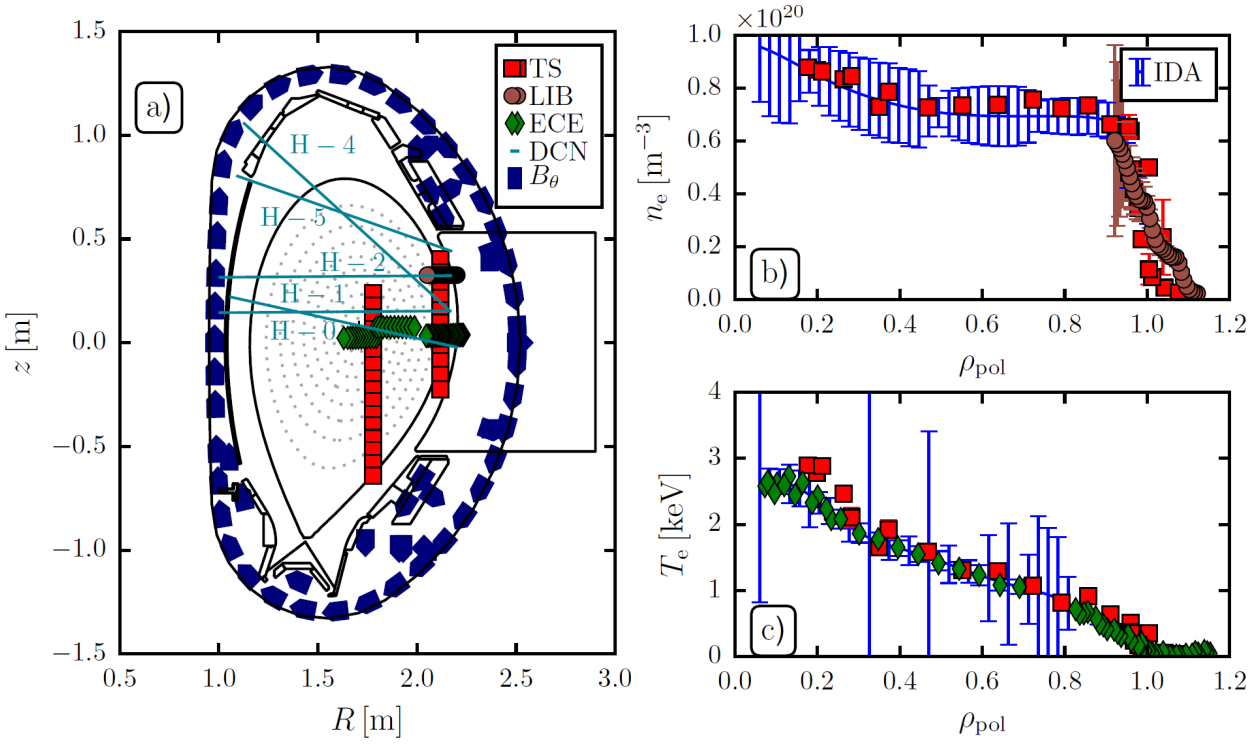

Figure 3.2: (a) Poloidal cut through AUG showing the measurement localizations of Thomson scattering (TS, red squares) in the edge and the core, the lithium beam (LIB, magenta circles), the electron cyclotron emission (ECE, green diamonds) and the lines of sight of the interferometry (DCN, cyan). The dotted points show the equilibrium reconstruction based on the poloidal field coils (dark blue). The solid black line is the last closed flux surface. In Panels (b) and (c), the resulting IDA modeling is shown in blue, compared to the raw data. Figure reproduced from [142] for a generic AUG H-mode discharge.

The posterior probability density function is then

$$\begin{aligned} p(n_e, T_e | d_{\text{LIB}}, d_{\text{DCN}}, d_{\text{ECE}}, d_{\text{TS}}) \propto & \, p(d_{\text{LIB}} | n_e, T_e) \\ & \times p(d_{\text{DCN}} | n_e) \\ & \times p(d_{\text{ECE}} | n_e, T_e) \\ & \times p(d_{\text{TS}} | n_e, T_e) \\ & \times p(n_e, T_e), \end{aligned}$$

and combines all probability distributions for the two quantities from all used diagnostics. With optimization routines, this function is maximized, and the combined electron temperature and density profiles can be extracted.

The uncertainty of these combined quantities is calculated by means of the χ^2-binning method [140]. For this, small subsets of the forward modeled data $X_{t,r}$ for given (n_e, T_e) profiles are increased or decreased until the χ^2 cost function for a certain time point t and radial channel r,

$$\chi^2(t, r) = \sum_{\text{diag}} \frac{(x_{t,r,diag} - X_{t,r})^2}{\sigma^2_{t,r,diag}},$$

is estimated to vary by more than 1. Here, $x_{t,r,diag}$ is the real measurement value from the diagnostic with its absolute uncertainty $\sigma_{t,r,diag}$. This, however, mathematically strictly speaking, does not result in a Gaussian distributed error. In Fig. 3.2(a), the measurement positions of the TS, the LIB, the DCN, and the ECE are shown. In Panel (b), the resulting `IDA` reconstruction is shown next to the measurement points.

Equilibrium Reconstruction

The correct reconstruction of the plasma equilibrium (see Fig. 3.2(a), dotted lines) is important for coherent modeling of the plasma. At ASDEX Upgrade, there are different levels of sophistication in the assessment of the plasma equilibrium. All of them are based on solving the Grad-Shafranov equation [10, 11], which can be derived from Eq. 1.1.

An important experimental input for the equilibrium reconstruction comes from the magnetic pick-up coils. They are used to locally measure the magnetic field at various positions around the plasma. Physically, the measurement principle relies on the Maxwell-Faraday equation. The induced voltage in a pick-up coil with N windings and area A is given by

$$U = -NA \frac{\partial B}{\partial t}.$$

From this, the local magnetic field perpendicular to the plane of the coils is calculated. For the equilibrium reconstruction, there exist poloidal coil arrays, see the dark blue symbols in Fig. 3.2(a). Furthermore, the poloidal coils can be used to assess the plasma current via Ampere's law or to measure the voltage of the transformer onto the plasma.

Based on this information, the `CLISTE` code is used (CompLete Interpretive Suite for Tokamak Equilibria) to reconstruct the equilibrium [144, 145]. Routinely, this

reconstruction does not include the effects of fast ions on the pressure and current drive [146] and is not constrained by the measured thermal pressure. CLISTE could, in principle, include such effects. The calculated equilibrium is stored in the EQH shotfile with a time resolution of 1 ms to provide fast, reasonably accurate, high-time resolution reconstruction. Reconstructed scalar quantities like the loop voltage u_{loop} or the plasma current I_p are stored in the FPC and FPG shotfiles.

More sophisticated effects are routinely included in the Integrated Data analysis Equilibrium (IDE) [147]. IDE constraints the ∇p term in the Grad-Shafranov equation by pressure profiles consisting of the sum of thermal electron and ion pressure (via IDA) and fast-ion pressure calculated (via TRANSP or RABBIT [148]). In addition to the pressure constraint, it is coupled with the neo-classical current diffusion equation. Practical differences of the EQH and IDE equilibrium reconstruction with respect to the methodology and discharges presented in this work are discussed in Section 4.1.

3.3 Charge Exchange Recombination Spectroscopy

Charge Exchange Recombination Spectroscopy (CXRS) is the most important diagnostic to measure the impurity temperature and rotation in this work. These quantities are assessed via the analysis of the Doppler broadening and shift of spectral lines emitted from the plasma impurity ions.

Charge Exchange Reactions

The measured spectral lines are emitted by ions ($\mathrm{A}^{\mathrm{Z+}}$) that capture an electron into an excited state, which de-excites subsequently[149, 150]. The electron comes from a fast neutral beam atom (D^0):

$$\mathrm{A}^{\mathrm{Z+}} + \mathrm{D}^0 \rightarrow \mathrm{A}^{\mathrm{(Z\text{-}1)+*}} + \mathrm{D}^+ \rightarrow \mathrm{A}^{\mathrm{(Z\text{-}1)+}} + h\nu + \mathrm{D}^+.$$

The charge exchange reaction leaves the ion in an excited state (denoted by a star), which decays through photon emission ($h\nu$). The emission energy of the photon is discrete and corresponds to a specific wavelength λ. In this work, charge exchange with fully stripped impurities in the plasma is considered.

Measurement Principles

The impurities analyzed in this work are boron and nitrogen, which have distinct spectral lines in the visible range that are suitable for spectroscopy with present spectrometers, optical lenses, and fibers. Furthermore, due to their low Z, they are fully ionized across the full plasma minor radius on the low-field side (LFS). This allows the utilization of a single spectral line over the entire measurement domain. In this work, the NBI, see Section 3.1, provides a source of neutrals.

In the analysis of charge exchange spectra, it is distinguished between *active* and *passive* lines. Active lines result from charge exchange reactions with the injected

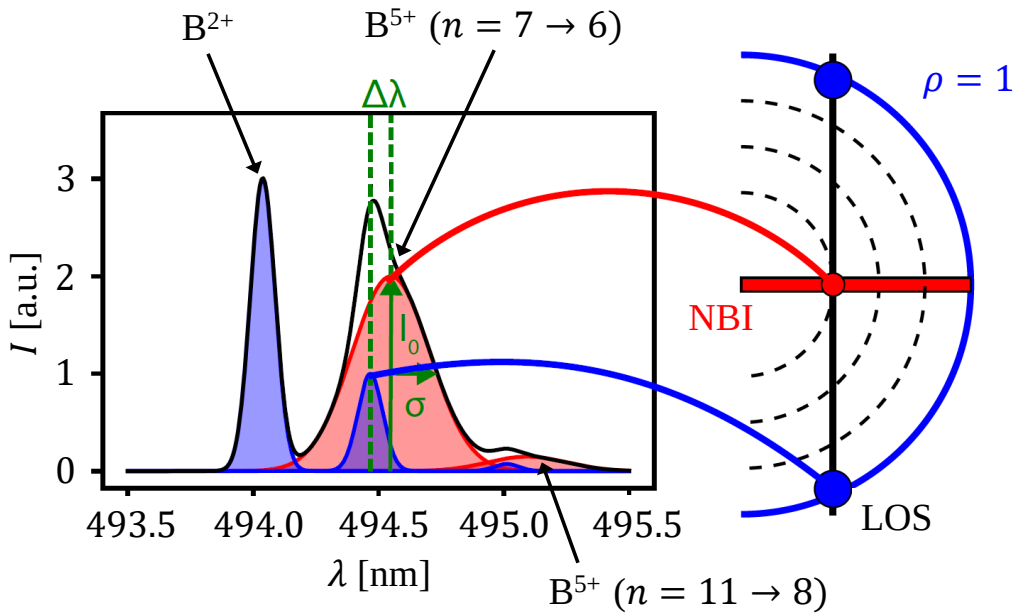

Figure 3.3: Basic composition of the boron charge exchange spectrum for a typical AUG discharge. Passive lines are shown in blue, emerging from the edge of the plasma. Active lines are shown in red, resulting from the charge exchange reaction with the neutral beams. In black, the total measured signal is shown. Figure adapted from [142, p. 42].

neutrals. They are well localized as they originate at the intersection between the collimated diagnostic lines of sight (LOS) and the collimated neutral beam path. Passive lines are produced by electron or ion impact excitation of the $\mathrm{A}^{(Z-1)+}$ or charge exchange with the thermal neutrals generated in the edge of the plasma.

The resulting measured spectrum is shown in Fig. 3.3. On the l.h.s., a typical boron spectrum is shown consisting of the B^{2+}, B^{5+} ($n = 7 \rightarrow 6$), and B^{5+} ($n = 11 \rightarrow 8$) lines. The actual measurement is the black envelope curve. It consists of passive (blue, from the edge of the plasma) and active contributions (red, due to the neutral beam). Focusing on the B^{5+} ($n = 7 \rightarrow 6$) line in the middle, it is shown, in green, the shift of the central line $\Delta\lambda$ due to the Doppler shift, the standard deviation σ of the Gaussian due to the Doppler broadening, and the maximum intensity I_0. To distinguish between the active and passive contributions, either a modulation of the neutral beams is necessary to subtract the passive contribution, or all contributions need to be fit simultaneously in the data analysis.

By describing the Doppler broadening with a Gaussian line shape, the implicit assumption of a Maxwellian velocity distribution is made. Under these conditions, the intensity can be described as [142, p. 43]

$$I_{\mathrm{CX}}(\lambda) = I_0 \cdot \exp\left\{-\frac{m_\alpha c^2}{2\,T_\alpha}\frac{(\lambda - \lambda_0 - \Delta\lambda)^2}{\lambda_0^2}\right\}. \tag{3.1}$$

Here, m_α is the mass of the ion, T_α its temperature, c the speed of light, and λ_0 the expected central wavelength in rest, which can be obtained from databases such as the Atomic Data and Analysis Structure (ADAS) [151] or calculated from the energy differences of the quantum shells. From the measured standard deviation

of this Gaussian, the ion temperature can be easily calculated via

$$T_\alpha = \frac{m_\alpha c^2}{\lambda_0}\,\sigma^2. \tag{3.2}$$

This work assumes that the impurity temperature is representative of the main ion temperature, $T_i = T_\alpha$. This approximation is justified due to very short thermal equilibration times between these species, which are on the order of µs [152], and, thus, much shorter than the transport time scales.

The Doppler shift of the active line, $\Delta\lambda$, results from the flow velocity of the ion species $\mathbf{v}_\alpha$. With $\mathbf{u}_{\mathrm{LOS}}$, the unit vector along the LOS, it is possible to derive [153, p. 35]:

$$\frac{\Delta\lambda}{\lambda_0}\,c = \mathbf{v}_\alpha \cdot \mathbf{u}_{\mathrm{LOS}}. \tag{3.3}$$

As already discussed in Section 2.1, the poloidal flows are neglected in this work. Therefore, the flow velocity is assumed to be in the toroidal direction. Furthermore, the LOS have only a very small vertical component and, therefore, are not sensitive to poloidal velocity contribution. Herein, the impurity rotation is assumed to be equal to the main ion rotation, i.e., neoclassical corrections are not applied. In principle, the neoclassical flows [154] can be calculated, for example, by the NEOART code [155, 156]. Calculations for a typical discharge have shown corrections of the order of a few km/s and that this results mainly in an offset of the rotation profiles [157].

The assessment of absolute impurity densities is not the focus of this work. The impurity density can be calculated from the measured intensities, together with knowledge about the charge exchange cross-sections and the absolute neutral density, which can be obtained from beam attenuation codes. For more details on these measurements, see, for example, [158].

The CXRS Suite at ASDEX Upgrade

The CXRS diagnostics at AUG are comprised of several different optical heads that focus on specific spacial domains of the plasma [159, 160]. Figure 3.4 shows a top-down view of AUG. This work uses the NBI sources from box 1 (sector 15) for heating and diagnostic purposes. The beam paths are shown in red and magenta. The used CXRS systems are the `CMR` for edge measurements (sector 16) and the `CER` for core measurements (sector 13). The diagnostic LOS are shown in black. The systems related to NBI box 2 are not used in this work.

The `CMR` features optical heads in the plasma vessel, which consist of aspherical, plano-convex lenses to focus the LOS. Shutters protect these lenses during glow discharges or boronizations. The optics of the `CER` are placed outside the plasma vessel and view the plasma via a mirror and a window that can be protected by a shutter. In the optical heads, multiple fibers are connected to the spectrometers outside of the experimental hall. Multiple fibers are used for simultaneous measurement of different LOS and, thus, at different radial locations.

The precise 3-dimensional geometry of the LOS is determined by backlighting the fibers and measuring the light cone at multiple positions in the vessel via a robotic

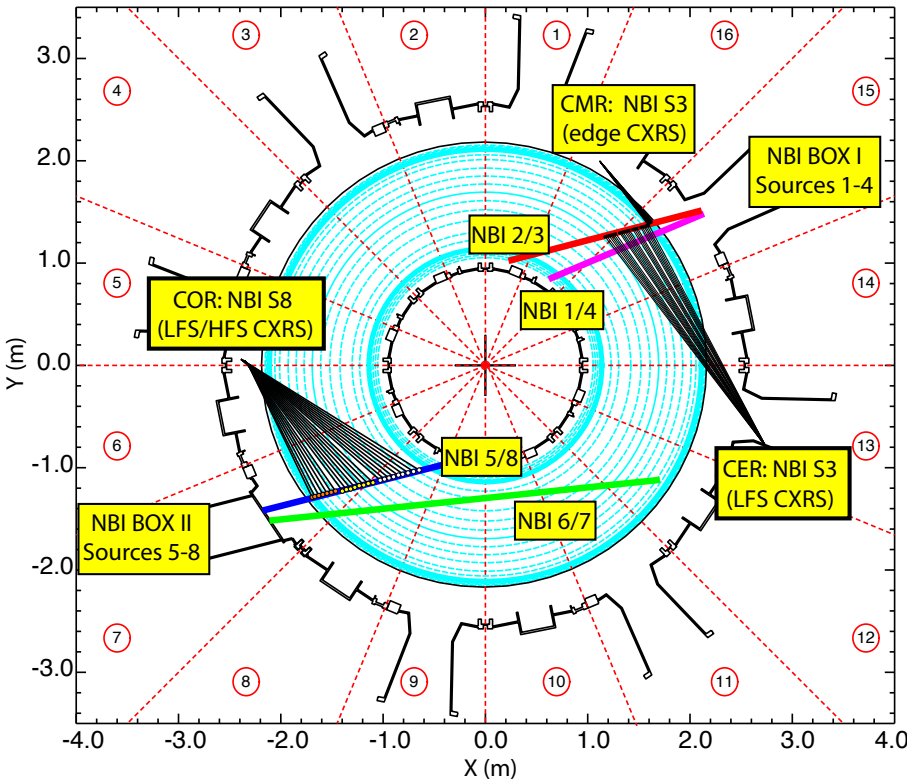

Figure 3.4: Geometry of the CXRS systems and the NBI at ASDEX Upgrade. Figure reproduced from [159].

arm. Depending on the diagnostic, the finite spot size of the light cone and the related uncertainty of the localization of the measurement can be up to $\approx \pm 1 - 2$ cm for the core CER and $\approx \pm 2 - 3$ mm for the edge CMR diagnostics. The beam sources have different injection axes, which are consistently taken into account in the analysis. The uncertainties of the measurement positions are consistently included in the CXRS shotfiles and the analysis. While the measured data is mapped in the analysis onto the normalized toroidal flux coordinate corresponding to the location of the measurement, the measured values are not necessarily flux surface averaged values.

The spectrometers are placed outside the experimental hall. The basic setup of the used Czerny-Turner-like spectrometers is shown in Fig. 3.5 and described in more detail in [159, 160]. The light enters the spectrometer via the fiber bundle, and the variable entrance slit can be used to balance the intensity and the size of the natural line width. The imaging behavior of the slit is called instrument function. To parallelize the light onto the grating, an entrance lens is used. The sine drive of the grating is used to select the desired wavelength range. The diffracted light is refocused with the exit lens on the charged coupled device (CCD) camera. The 2-dimensional CCD sensor allows fitting light from multiple vertically stacked fibers to be imaged separately. The spectra (wavelength) are resolved horizontally (x-axis) on the sensor, while the LOS (channels) are resolved vertically (y-axis). The sensor has 512×512 16 µm pixels and is split vertically into 25 regions of interest, defined to correspond to the 25 fibers. While the CER is usually operated with 10 ms time resolution, the CMR is used with 2.5 ms time resolution. The readout rates of the sensors and cameras set a lower limit on the feasible integration time.

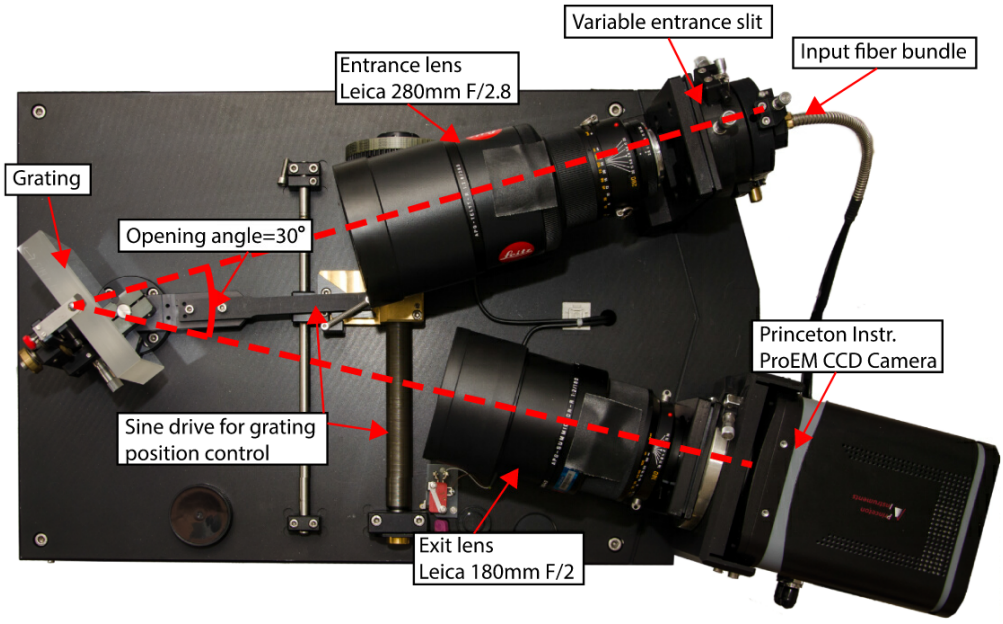

Figure 3.5: Typical spectrometer setup used at AUG, here shown for the COR system. Figure reproduced from [159].

Calibration

The calibration of the measurement system is required for the correct interpretation of the experimental data. The characterization of the measurement localization and its uncertainty has already been discussed. The following discussion of the calibration workflow is given in more detail in [159, 161].

When entering the spectrometer, the light passes a slit, usually set to 50 – 100 μm width. This results in a convolution of the entering Gaussian spectrum with the instrument function. This is shown in Fig. 3.6 for a low-temperature Ne pen lamp, which has a very thin Gaussian line shape. To ensure a precise interpretation of the velocity measurements, the total broadening effects connected to the measurement setup are defined in the instrument function for each channel explicitly as a wavelength-dependent function, determined using spectral lines from Ne pen lamps. However, the thermal Doppler broadening is much larger than the instrument function in the discharges analyzed in this work. Therefore, the Doppler broadening determines the measured width of spectral lines. In the CXRS analysis at AUG, a full deconvolution of the measured line shapes with the measured instrument functions is always performed. This procedure is essential for obtaining accurate rotation measurements, even though it is often unimportant for temperature measurements.

As the fibers at the spectrometer entrance are stacked vertically, they are vertically displaced from the optical axis of the system. This results in a parabolic distribution of the central wavelength, as shown in Fig. 3.7. This parabola function can be measured using well-defined spectral lines from a low-temperature Ne pen lamp. Furthermore, the dispersion relation, i.e., which $\Delta\lambda$ corresponds to how many pixels on the CCD chip, can be determined from such Ne spectra.

To compensate for small variations of the central wavelength and the wavelength

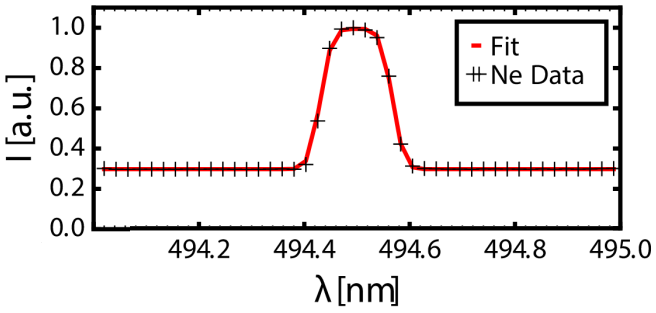

Figure 3.6: Typical instrument function, shown for the COR spectrometer at AUG. The Gaussian Ne line is convoluted with the instrument function. Figure adapted from [159].

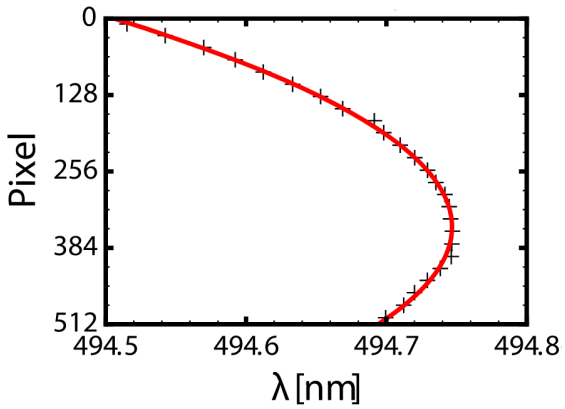

Figure 3.7: Typical parabola function, showing the deviation of the central wavelength (x-axis) for the vertical position on the CCD sensor (y-axis). Figure reproduced from [159].

range due to the sine drive of the grating, after every plasma discharge, a Ne pen lamp is recorded for one channel on the chip to determine the central wavelength for this specific channel. Based on the measured parabola function, the central wavelength can then be determined for all regions of interest [161].

As the knowledge of absolute intensities is unimportant to this work, the intensity calibration and the specifications of the sensor readout are not addressed here. For example, they are discussed for CXRS systems at AUG in [159].

Analysis and Corrections

At AUG, the CXSFIT tool is routinely used to analyze the CXRS spectra [162]. To fit a boron spectra, as shown in Fig. 3.3, 5 Gaussians are used, one for the passive B^{2+}, two for the active and passive of each of the B^{5+} ($n = 7 \rightarrow 6$), and B^{5+} ($n = 11 \rightarrow 8$) lines. The temperatures and rotation from the latter two lines come from the same ions and must be the same. This reduces the free parameters of the fitting problem. Furthermore, assumptions are made about the passive contributions, for example, limits on their temperatures, to separate them effectively from the active ones.

Depending on the studied experimental scenario, several corrections are applied in addition to the calibrations mentioned before. The most relevant ones are to correct for the Zeeman effect, which denotes the splitting of spectral lines into multiple components in the presence of a magnetic field [163, 164]. Furthermore, there is the fine structure splitting due to relativistic electron spin coupling. Each of these single lines is Doppler-broadened due to the ion temperature. However, the sum of these lines has an apparent broadening, which is larger than that of its single components. This leads, if not corrected, to an overestimation of the temperature (Zeeman effect) and misinterpretation of the rotation (fine structure). The Zeeman effect and the fine structure are routinely corrected via a database of corrections curves.

The analysis routine takes the characterization, calibration, and corrections into account and derives temporally resolved radial profiles of the impurity temperature and rotation.

Chapter 4

Developed Methodology

"Kinder, schafft Neues!"

— Richard Wagner

This Chapter delves into the details of the experimental scenario. The modeling technique is outlined, followed by a detailed discussion on the analysis of the reference discharge. Parts of this Chapter have already been published [165, 166].

4.1 Neutral Beam Injection Modulation Experiments

The discharges studied in this work were performed in standard conditions. They are type-I ELMy H-mode plasmas, with a toroidal field of $B_\varphi = -2.5$ T, and in a lower single null, favorable drift configuration. The deuterium reference discharge, #40076, has a plasma current of $I_\mathrm{p} = 0.8$ MA and a line-averaged core density of 6.4×10^{19} m^{-3}. The plasma was heated using 0.6 MW of ECRH and 4.8 MW of steady, on-axis NBI heating with an extraction voltage of $U_\mathrm{ex} = 53$ kV. Additionally, a torque perturbation was induced by injecting a neutral beam with a reduced power of 0.7 MW ($U_\mathrm{ex} = 50$ kV) at a modulation frequency of 5 Hz. For the torque perturbation, in the first phase (2.0 – 4.2 s), off-axis beam modulation is used, and in the second phase (4.2 – 6.4 s), on-axis beam modulation.

Modulating particle or heat sources is a common technique to investigate particle or heat transport in a tokamak [167, 168]. The problem of solving the transport equation is then transformed into a time-dependent one, and transport processes can be separated by their temporal dependences.

For the study of momentum transport, torque modulation experiments can be used to modulate the toroidal rotation and, thus, the momentum of the bulk plasma. Figure 4.1(a) shows the modulation of a reduced power neutral beam and the resulting modulation of the toroidal rotation. Panel (b) indicates that also the temperatures are modulated, while Panel (c) shows that the core density and the plasma stored energy are comparably stable. Aside from the modulation, the time traces are stable, which allows time-averaging them to obtain a steady-state pro-

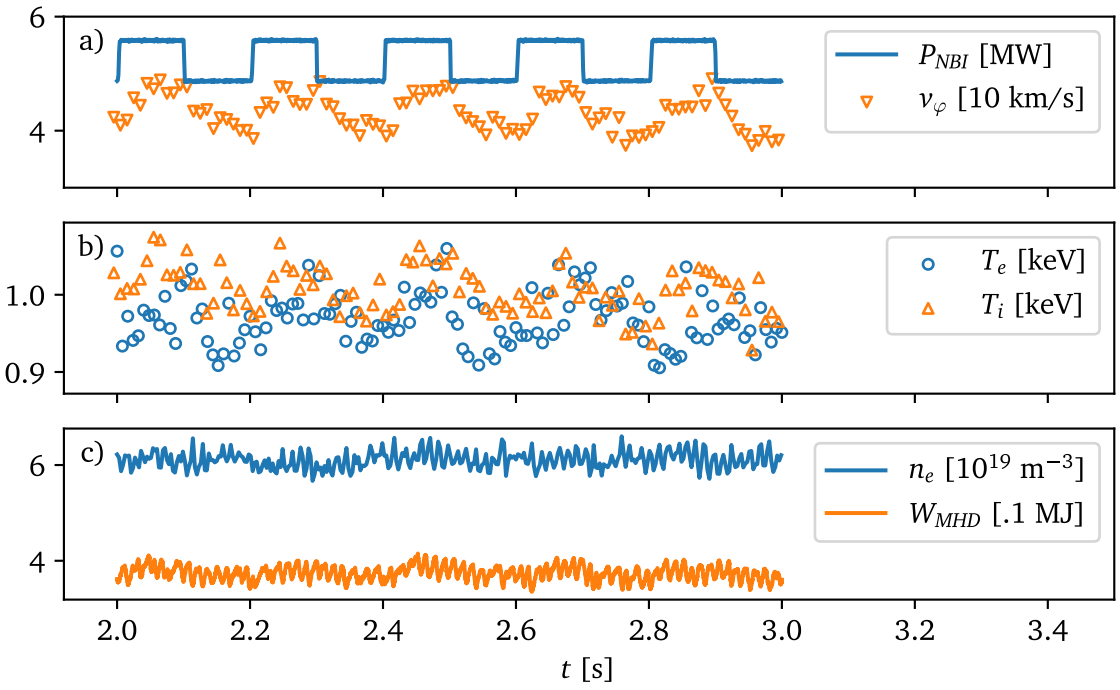

Figure 4.1: Plasma parameter time traces of the reference discharge #40076 (2.0 – 4.2 s). Toroidal velocity, temperatures, and density values are shown at $\rho_\varphi = 0.5$.

file, as shown in the left-hand column of Fig. 4.2. Calculating the Fourier amplitude and phase from the time traces of each radial position yields the amplitude and phase profiles as shown in the central and right-hand columns, respectively. In this work, the phases are shifted by their value at the boundary $\rho_\varphi = 0.8$ to allow for an easier comparison of the effective phase shifts. A negative phase value corresponds to a delay of the perturbation with respect to the boundary.

As already stated, the modulation is required to separate the three momentum transport processes: diffusion, convection, and residual stress. In a purely steady-state scenario, the time derivative on the l.h.s. of the momentum transport Eq. 2.7 vanishes ($\partial/\partial t\, n\langle R v_\varphi\rangle \rightarrow 0$). The externally applied torque $\langle S_{\mathrm{NBI}}\rangle$ is balanced by the three transport mechanisms, and their respective contributions cannot be identified uniquely.

By utilizing modulation and a time-dependent analysis, the rotation amplitude and phase profiles can be analyzed, effectively constraining the problem. The choice of the modulation frequency is crucial for a successful analysis. If the frequency is too high, the fast particle slowing-down time becomes larger than the modulation period. Consequently, the modulation amplitude cannot be clearly distinguished from noise and experimental uncertainties. Conversely, if the frequency is too low, the phase difference between the inner and outer core becomes too small to be detected beyond the noise and experimental uncertainties. The best frequency to use cannot be exactly predetermined without assumptions on the present transport and precise knowledge about the CXRS diagnostics and measurement characteristics.

For reduced voltage beams from beam box 2 of AUG, symmetric duty cycles with 3 and 5 Hz are found to provide the best modulation data. With 2 Hz modulation, the phase profiles are often too flat. With 7 and 10 Hz, the amplitude profiles are

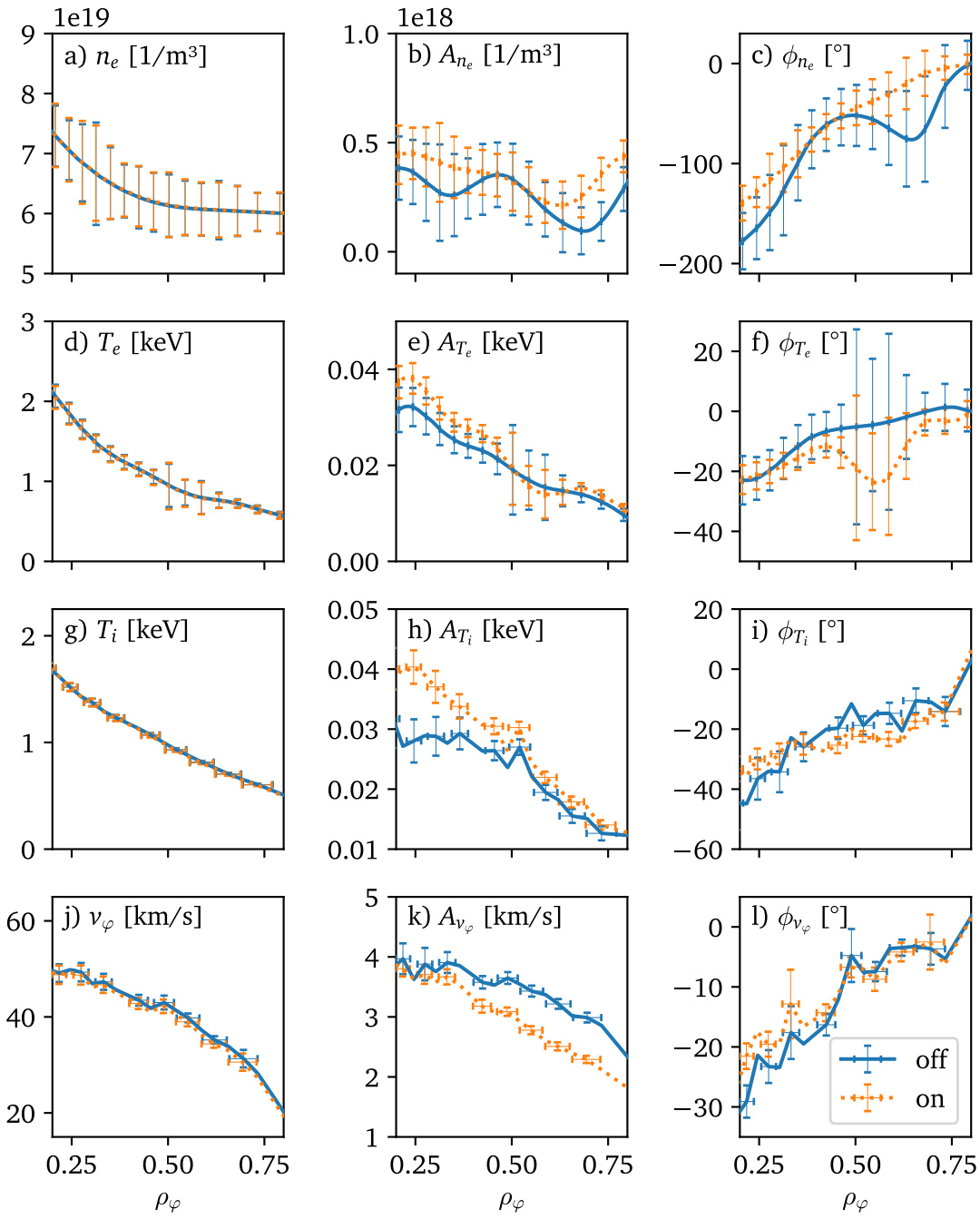

Figure 4.2: Steady-state (left column), amplitude (middle), and phase (right) profiles of the kinetic quantities of the reference discharge #40076 (off-axis modulation 2.0 – 4.2 s, on-axis modulation 4.2 – 6.4 s with $f_{\mathrm{mod}} = 5$ Hz).

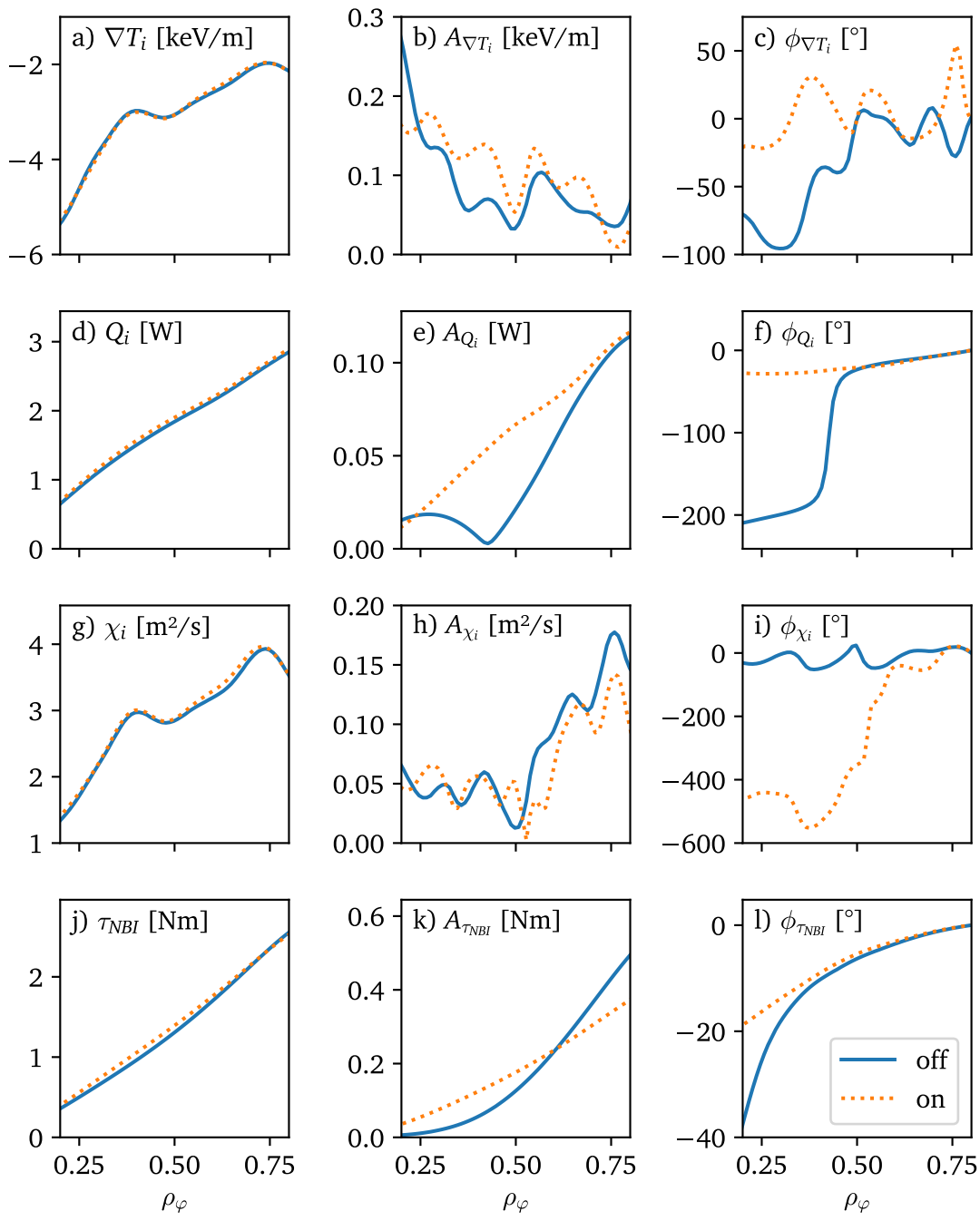

Figure 4.3: Steady-state (left column), amplitude (middle), and phase (right) profiles of the ion heating power (d-f) and torque (j-l) from TRANSP. From those, together with the temperature gradient (a-c), the power balance χ_i (g-i) can be calculated. The data is from the reference discharge #40076 (off-axis modulation 2.0 – 4.2 s, on-axis modulation 4.2 – 6.4 s with $f_{\mathrm{mod}} = 5$ Hz). Phase profiles are shown for completeness despite the numerical artifacts (jumps) introduced in the post-processing Fourier analysis due to points of no modulation (nearly zero amplitude), in particular in Panel (f) and (i).

too low. The exact voltage of the modulation beam can be optimized to slightly increase the modulation amplitude, but this brings the risk of a too large, undesired temperature perturbation, as the neutral beam injection not only applies torque to the plasma, but also transfers substantial heat. With the beam modulation, the heat flux to the ions and electrons is modulated, and the ion heat diffusivity, χ_i, is also observed to be perturbed.

For a better understanding of the radial distribution of the modulation, the time-averaged steady-state and the Fourier amplitude and phase profiles of n_e, Q_i, T_e, T_i, ∇T_i, and χ_i are shown in Figs. 4.2 and 4.3. The error bars on the Fourier profiles in this work are calculated via Regression of Gaussian Processes. While the experimental uncertainties on the `IDA` data represent a statistical uncertainty of the Bayesian inference and are used to approximate a Gaussian error, the uncertainty from the fitting of the CXRS data is, in fact, a Gaussian distributed error.

In these figures, values are shown for on- and off-axis modulation. This means that the modulation was either performed with sources 5/8 (on-axis) or source 6 (off-axis), see Fig. 3.4. As shown in the left-hand column of Fig. 4.2, Panels (d) and (g), the steady-state profiles are identical for both modulation sources. As visible in the middle column, the amplitude profiles of the modulation differ. The modulation of the temperatures, see Figs. 4.2(e) and 4.2(h), are higher for the on-axis modulation. While it is still within error bars for the modulation of T_e, it is significantly higher for T_i. Strong temperature modulation is not desired, as it brings the risk of modulating the background turbulence driving the transport. This suggests that off-axis modulation is the favorable scenario for analyzing momentum transport. Moreover, the modulation amplitude of the rotation, see Fig. 4.2(k) is higher for the off-axis modulation, which increases the signal-to-noise ratio, and the phase profile is slightly steeper, which is also advantageous.

These observations can be understood in terms of the heat and torque deposition profiles. Figures 4.3(d) and (j) show that the time-averaged ion heat flux Q_i and the torque from the NBI τ_{NBI} are nearly identical between the on- and off-axis modulation cases. The modulation of these quantities, see Panel (e) and (k), indicates that the modulation of the ion heat flux is larger for the on-axis modulation, and the peak of the torque profiles is located radially further outside for the off-axis modulation. The absolute values and the modulation of the ion temperature gradient and the ion heat diffusivity are very similar in both cases, see Panels (b) and (h), while the phase profiles are quite different, see Panels (c) and (i), consistent with the phase profiles of the ion heat diffusivity and the temperature gradient.

To gauge the relative effect of the modulation, the ratios of the amplitudes to their steady-state values are shown in Fig. 4.4 for the off-axis case. In Panel (a), where values for the kinetic profiles are shown, the modulation of the density is shown to be negligible. Consequently, the resulting modulated fueling effect appears to be small, and it is not expected to significantly alter the steady-state particle transport dynamics. This agrees with more detailed studies that quantified the effect of particle fueling from the beams at AUG [169] . Since the density remains constant during the modulation, changes in the plasma's angular momentum $L_\varphi = m_i n_i R v_\varphi$ are dominated by changes in the rotation velocity. This justifies modeling the toroidal rotation in the momentum transport analysis later on instead of the angular momentum, which is actually the physically conserved quantity.

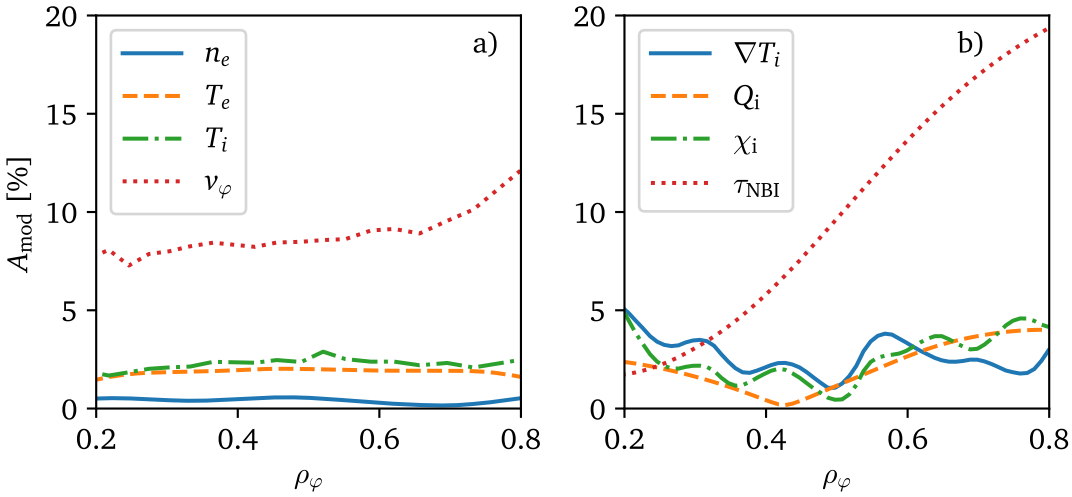

Figure 4.4: Relative modulation amplitudes for (a) kinetic profiles and (b) power balance quantities and NBI torque for #40076 (2.0 – 4.2 s, off-axis modulation).

The perturbation of the temperature is similar for electrons and ions. The modulation of the rotation is much stronger, up to 10 %. Panel (b) shows a strong modulation of the NBI torque. The modulation of the quantities involved in the calculation of the power balance is non-negligible and is on the order of a few percent. This makes it necessary to model the heat transport channel retaining its time dependence when calculating χ_i. This time dependence propagates into the momentum transport coefficients via Pr, mainly causing the temporal variation of χ_φ, V_c, and Π_Rs. These scalings are necessary to compensate for the changing turbulence intensity [80, 81]. In Section 4.3, the effects of neglecting the time dependences of the different terms in the momentum transport equation will be discussed. Possible higher harmonic Fourier component profiles are not relevant for this kind of analysis, as, with a symmetric duty cycle, the corresponding amplitude profiles are too low to be exploited.

Another possible pitfall of this kind of experiments could be the modulation of the equilibrium caused by the change in plasma pressure due to the modulation of the heating. To compensate for changes in the equilibrium, it is necessary to map all data from real space to flux-surface space. The equilibrium has further importance as it is a necessary ingredient for calculating flux surface averaged derivatives. In doing so, it is necessary to use a time-dependent equilibrium and to stay as consistent as possible in the use of the equilibrium in further analysis to avoid mismatches in the assumed underlying geometry.

As already introduced in Section 3.1, there are different levels of sophistication in the equilibrium reconstruction at AUG, in particular, the `IDE` and `EQH` equilibria. The effect of the modulation on the equilibria for the on- and the off-axis modulation is shown in Fig. 4.5. It is found that the modulation of the plasma volume, Panel (b), and the flux surface positions, Panel (f), is very weak, as expected from the comparably small modulation of the stored energy shown in Fig. 4.1(c). This justifies using a constant equilibrium in the `ASTRA` simulations, which significantly improves performance. Furthermore, a systematic deviation of the position of the magnetic axis is found for `IDE` and `EQH`, see Panel (c). This is expected, as `IDE`

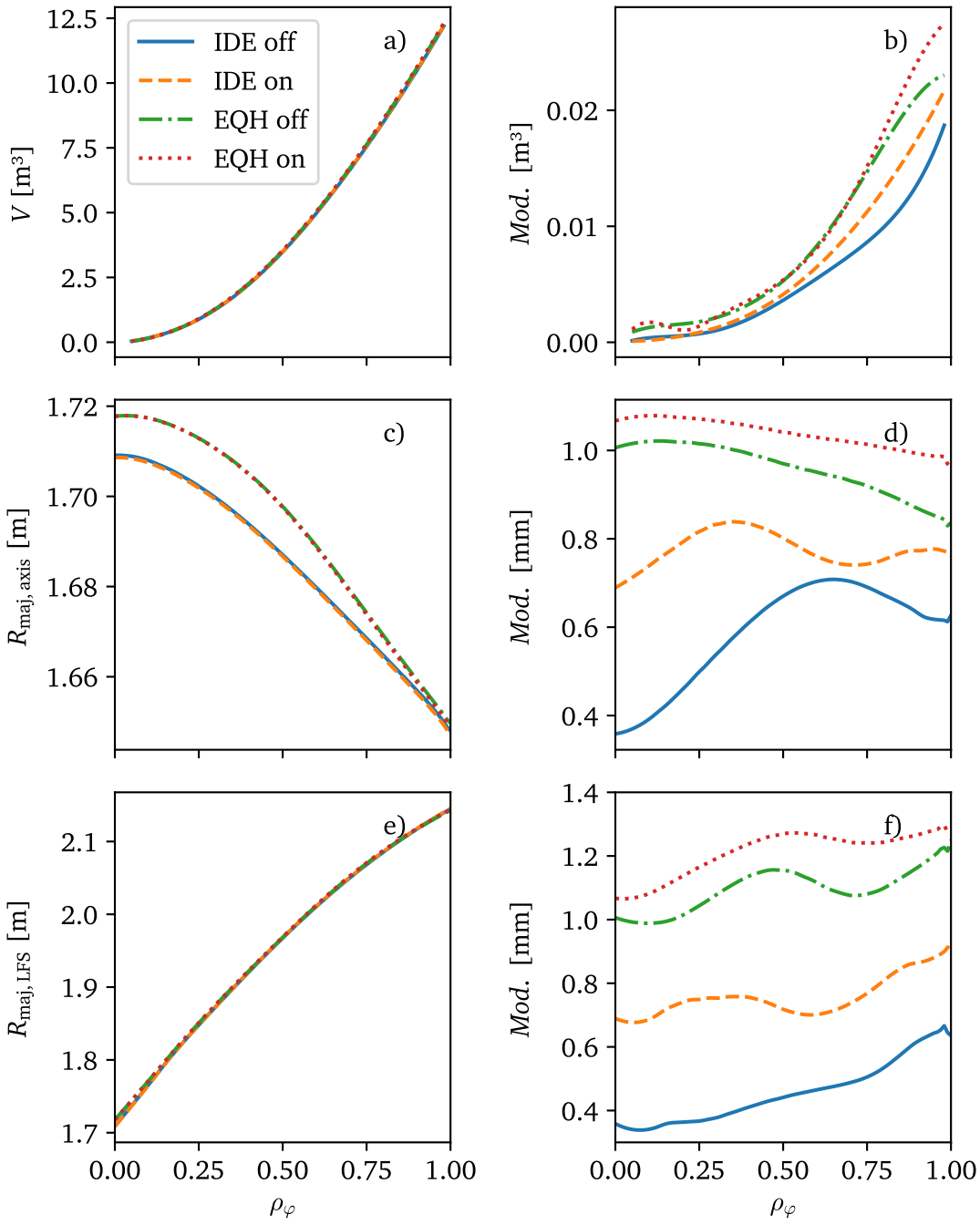

Figure 4.5: Comparison the the IDE and EQH equilibrium reconstruction for the reference discharge #40076 (off-axis modulation phase 2.0 – 4.2 s, on-axis modulation phase 4.2 – 6.4 s). Panel (a) shows the plasma volume, Panel (c) the center of each flux surface, and Panel (e) the radius of the corresponding flux surface on the low-field-side midplane. In the second column, the absolute modulation is shown. It is not possible to show relative values due to the volume approaching zero in the core. It is evident that there is minimal modulation in the volume. The position of the magnetic axis and the flux surface low-field-side radius is only barely modulated. A deviation of the geometric center of the flux surface between IDE and EQH in Panel (c) of up to 1 cm near the axis is observed.

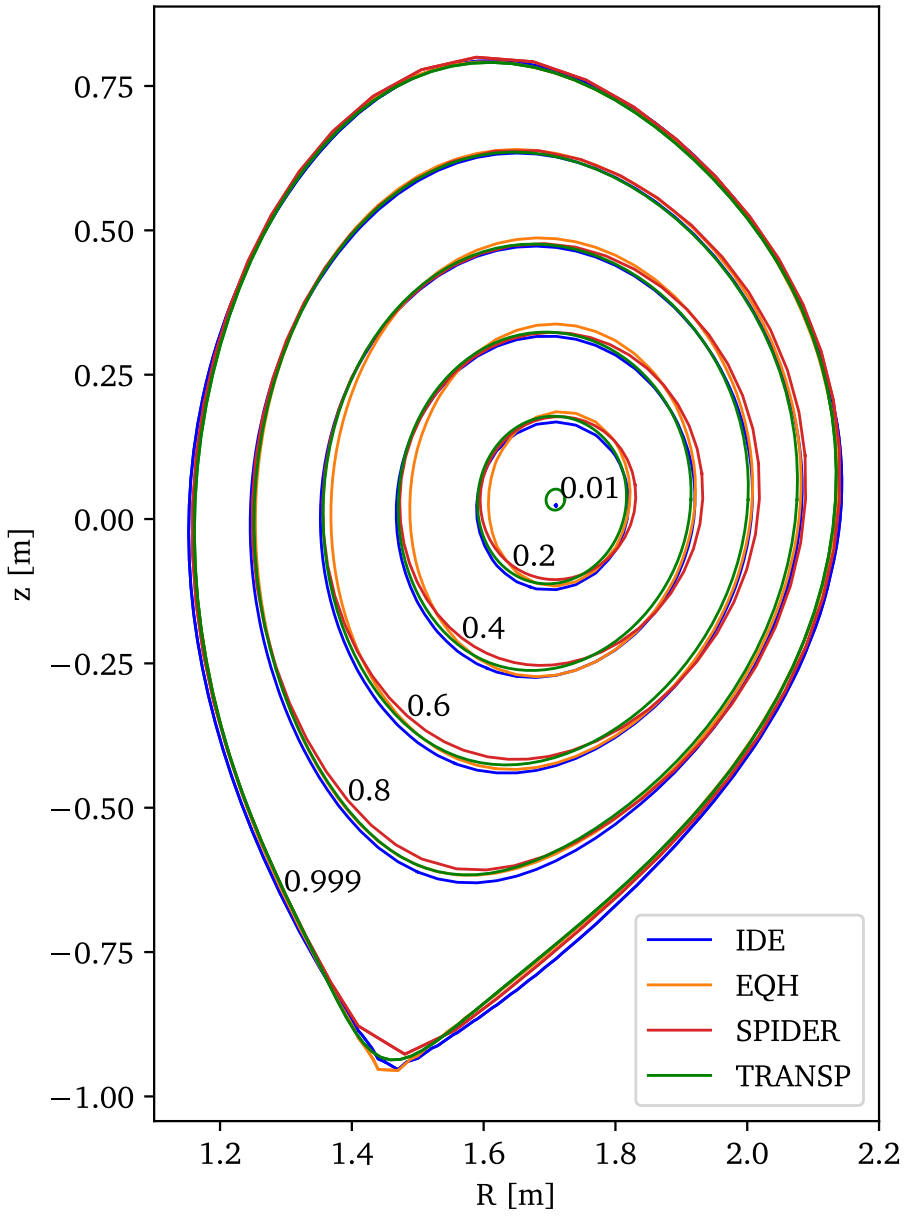

Figure 4.6: Flux surfaces for different values of ρ_φ (annotated in black) for different equilibrium reconstruction codes for the reference discharge #40076 (off-axis modulation phase 2.0 – 4.2 s). Shown is `IDE`, `EQH`, the equilibrium used by `TRANSP` and from the `SPIDER` code within `ASTRA`. The shape and enclosed area are very similar and agree within reconstruction uncertainties.

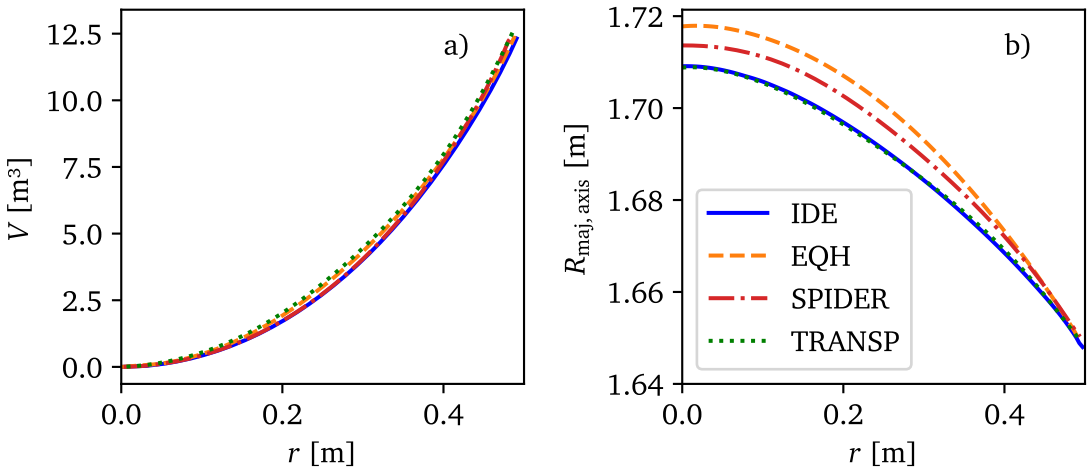

Figure 4.7: Comparison of the equilibrium reconstruction for the reference discharge #40076 (off-axis modulation phase 2.0 – 4.2 s). Shown is IDE, EQH, the equilibrium reconstructed by TRANSP and from the SPIDER code within ASTRA. On the horizontal axis, the averaged minor radius in the midplane is used.

includes effects of fast ions, is pressure-constrained, and solves the current diffusion law, which is not the case for the EQH equilibrium. Overall, these deviations in the innermost core could lead to differences in mapping the experimental kinetic profiles and calculating the derivatives.

The ASTRA equilibrium is calculated by the SPIDER code, which is unable to incorporate all of the advantageous effects of the IDE equilibrium [170]. It is, therefore, expected to be more similar to EQH. The equilibrium within TRANSP is calculated via the TEQ code, which is used as an inverse solver for a fixed boundary solution using the pressure and q profiles at an initial time point as input. It is pressure-constrained, includes the effects of fast ions onto the pressure, solves the current diffusion, and, therefore, is expected to be more similar to IDE.

As shown in Fig. 4.6, all codes reproduce the shape of the flux surfaces within reconstruction uncertainties. As shown in Fig. 4.7(a), the four codes calculate the same plasma volume, but differ slightly in the exact position of the center of the flux surfaces, see Panel (b) of the same figure. This agrees with the previous comparison of IDE and EQH. Overall, the deviations are considered to be within the reconstruction uncertainties [171, 172].

Although the differences among the reconstructions are minor in this scenario, deviations are expected to be more prominent in scenarios with a significant impact of the pressure constraint, e.g., with strong, localized ECRH. Within the used methodology, this would cause an inconsistency between the TRANSP equilibrium, which is the basis for the calculation of heat and torque fluxes, and the ASTRA equilibrium, which is used for solving the power balance and the momentum transport equation.

To not provoke a systematic mismatch between the mapping of the experimental data and the ASTRA modeling, in this work, it was decided to rely on the EQH equilibrium as input for all analysis steps and reconstruction codes. This makes the TRANSP equilibrium the only inconsistency. The ability to use an IDE-like equilib-

rium in ASTRA would be an essential improvement and would solve this inconsistency. However, it requires dedicated code development that could not be done in the framework of this thesis.

From these observations, without having performed any transport analysis, multiple conclusions can be drawn about how to set up an experimental scenario and an analysis methodology to provide beneficial conditions to extract momentum transport coefficients from NBI modulation experiments:

- The optimal modulation frequency needs to be low enough for the modulation amplitude to clearly emerge from the noise yet high enough for the phase profile to exhibit a noticeable phase shift over the analysis region outside of error bars. $f_{\mathrm{mod}} = 5$ Hz is the best compromise for AUG for the levels of diffusion studied in this work.
- The voltage of the modulation beams needs to be set to values that induce a modulation of the rotation of the order of 10 % of the steady-state value. The uncertainties on the amplitude profile should not be larger than 20 % of the absolute value. $U_{\mathrm{ex}} \approx 50$ kV (resulting in $P_{\mathrm{mod}} \approx 0.7$ MW) is found to be suitable.
- Rotation phase profiles with off-axis NBI modulation are steeper, and the amplitude profiles are higher, as desired. Furthermore, the temperature perturbation is larger with on-axis modulation. Perturbations of the heat transport channel are not desired and should be minimized, as they risk altering the background turbulence. To optimize the rotation modulation and to minimize the perturbation of the heat transport channel, off-axis modulation is preferred over on-axis modulation.
- The beam modulation affects both the heat and the momentum transport channel. Even when attempting to minimize the temperature perturbation and modulation of the turbulence amplitude, it cannot be avoided. This makes it necessary to model the transport channels with time-dependent transport coefficients.
- The mapping on the equilibrium has to be as consistent as possible for all involved quantities and steps in the analysis. Mapping from real space into flux surface space has to be performed based on a time-dependent equilibrium to compensate for possible changes or drifts. As ASTRA's equilibrium code SPIDER is not able to include pressure constraints, the entire analysis is performed based on the EQH equilibrium.

4.2 Momentum Transport Analysis Framework

The modeling of momentum transport involves multiple codes and analysis steps. In this Section, the flow of data and coupling of the codes is documented and discussed.

The first step, after the experimental data and equilibria are written, is to prepare the data for the TRANSP calculations to obtain heat and torque fluxes. This is done

by means of using the `trview` code [173]. The so-called *name list* sets the most important simulation properties and contains information about the configuration of heating sources and vessel geometry. Furthermore, information on the plasma profiles, the equilibrium, and the applied heating is provided with 10 ms time resolution as listed in Appendix A.1. The `TRANSP` run is started 300 – 500 ms before the time range of interest to give the calculation time to equilibrate. The entire calculation takes several hours. The `TRANSP` results were found to be very stable to variations in the input profiles, making the assessed fluxes rather robust quantities with respect to their use in the momentum transport analysis.

From the `TRANSP` calculation, several quantities are passed to `ASTRA` as input, see Appendix A.2. The most important inputs are the power densities onto the electrons and ions, the torque density from the beams, and the energy density of the fast ions. `ASTRA` is furthermore provided with the same kinetic profiles and equilibrium as `TRANSP` via the `trview` code. Finally, the toroidal rotation is provided to `ASTRA` directly from the shotfile database without any smoothing to preserve all possible time dependences. The measurement positions of the CXRS LOS are stored in real-space coordinates. As the plasma equilibrium can have slight variation during the considered time range, the mapping onto ρ_φ of the CXRS data can slightly vary. It was found to be necessary to interpolate the charge exchange T_i and v_φ onto a uniform and constant ρ_φ grid with the help of the equilibrium for every time frame of the CXRS data.

In addition to the experimental input, `ASTRA` requires an equation file, and it is necessary to prescribe the set of momentum transport coefficients. The equations are given in Sections 2.1 and 2.9. Within the simulation, which is performed on a 5 ms time base and takes several seconds, `ASTRA` initially reconstructs the equilibrium, solves the ion power balance to obtain the ion heat diffusivity, and then models the toroidal rotation based on the prescribed momentum transport coefficients and an experimental boundary condition of the rotation at $\rho_\varphi = 0.8$. The resulting modeled rotation is used to calculate the steady-state profile, as well as the amplitude and phase profile for the modulation frequency. These are then compared, in the given radial analysis range, with the experimental data by means of a χ^2_{red} error-weighted cost function:

$$\chi^2_{\text{red}} = \frac{1}{n-m} \sum_i \sum_j \frac{(O_{i,j} - C_{i,j})^2}{\sigma^2_{i,j}}. \tag{4.1}$$

Here, n is the number of observation data points (around 180), m the fitted parameters (8), i stands for the iteration over the steady-state, amplitude, and phase profiles of the toroidal rotation, $O_{i,j}$ are the experimentally measured values, $C_{i,j}$ the predicted values, and $\sigma_{i,j}$ are the absolute uncertainties on the experimental data. The weighting via the uncertainties balances the variation of absolute values from the experimental input profiles. No further weighting is applied. An important detail is that the experimental error bars undergo a validity check before they are utilized. In practice, an automated function examines the otherwise radially smooth steady-state, amplitude, and phase profiles for outliers. If such an outlier is identified, its corresponding error bar is artificially expanded such that a smooth fit of the profile would lie inside the error bars.

The radial analysis range is usually set to $\rho_\varphi = 0.2$ – 0.8 to avoid sawteeth instabilities in the core and effects of edge localized modes (ELM). Further boundary

conditions are to demand the Prandtl number and the pinch number be positive, as a negative diffusion is unphysical, and an outward pinch would contradict all established theory predictions for ITG and TEM dominated conditions [43, 48, 174]. The validity of the assumption on the pinch is discussed in the next Section.

It is crucial for successful modeling that the radial gradients of the steady-state, amplitude, and phase profiles at the boundary are smooth. Otherwise, `ASTRA` cannot properly adapt its boundary condition. This condition practically means that the boundary condition cannot be placed close to a transport barrier or the region strongly affected by ELM crashes, as no ELM-synchronization is applied in this work.

Different sets of momentum transport coefficients can be probed, and it is observed how they perform in reproducing the experimental data. The better the match, the smaller the χ^2_{red} value. With a suitable code framework, it is possible to iterate to find the set of transport coefficients that models the experimental data best.

Such an iteration is performed based on the *differential evolution* algorithm [175], included in the `scipy` Python package. This algorithm is capable of scanning a large parameter space to find global solutions. Finding the best solution for a standard NBI modulation experiment takes around 100,000 `ASTRA` runs and takes several days with suitable parallelization on a cluster. The final results are values for the 8 scalars, which are used to model the Prandtl number (2 scalars), the convective velocity (3 scalars), and the residual stress (3 scalars). Then, the ion heat diffusivity χ_i, the momentum diffusivity χ_φ, the Prandtl number, the pinch number, the effective intrinsic torque, and the modeled steady-state, amplitude, and phase profiles of the toroidal rotation can be extracted.

A modified version of this algorithm, written by the author, tracks, for all iterations, the probed sets of coefficients and the resulting χ^2_{red} values. After the best solution is found, this allows mapping out and plotting the scanned parameter space. By doing so, it is understood how the parameter space is shaped, i.e., if there are multiple minima, and how the transport coefficients can trade-off. Error bars on the assessed momentum transport coefficients can be reconstructed.

The reconstruction of error bars relies on the assumption that a variation of a factor 1.5 from the χ^2_{red} cost function corresponds to a variation of one standard deviation around the best solution. This can be motivated by considering the χ^2_{red} cost function for one parameter x in one dimension. Taylor expansion gives

$$\chi^2_{\text{red}} \sim 1 + a\,x^2 \tag{4.2}$$

around a symmetric optimum. The prefactor a corresponds to a Hess matrix value of $2a$. Based on this Hessian, the resulting absolute error one standard deviation away from the optimum is $1/\sqrt{2a}$. Using this value in Eq. 4.2 gives $\chi^2_{\text{red}} \approx 1.5$ for the 1σ environment around the optimum. For the problem studied herein, the calculation of the Hess matrix is computationally too expensive. Therefore, this χ^2_{red}-variation approach is the method of choice for the error analysis in this work. An important sanity check is to ensure that the error bars on the modeled rotation profiles roughly agree in size with the experimental uncertainties. Overall, this approach to calculate the error bars is comparable to the error estimate of the Bayesian Inference of the Integrated Data Analysis, where a deviation of 1 from the initial χ^2_{red} is used.

In addition to the experimental momentum transport analysis, the GKW code is used to give a theoretical prediction for the Prandtl and pinch numbers. These calculations are performed as discussed in Section 2.10. The experimental input is taken directly from the shotfile database to maintain full control over input quantities. Consistency with the input to TRANSP and ASTRA is manually verified.

The results from TRANSP, GKW, and the ASTRA modeling are stored in a *NBI modulation database* from where they can be accessed with a *NBI modulation browser*. This browser allows plotting of the modeling results and testing of possible parameter scalings. A flow chart of all involved codes and Python routines is presented in Fig. A.1 in Appendix A.3, together with a description of the involved Python functions.

Despite the fact that this rather detailed documentation of the methodology is given in the context of the AUG infrastructure by its coupling to the shotfile database, the methodology is capable of relying on only a TRANSP run. All data, which in this version is taken from the shotfile database, is then replaced by the TRANSP output. With small changes to the ASTRA input files, the codes developed here can be utilized to analyze NBI modulation experiments from other tokamaks.

4.3 Analysis of the Reference Discharge

In this Section, the momentum transport analysis framework is applied to the reference discharge #40076 (2.0 – 4.2 s, off-axis modulation), introduced in Section 4.1. The workflow is performed as documented in the previous Section, and the results are discussed in detail.

Experimental Momentum Transport Modeling

The results of the ASTRA modeling are shown in Fig. 4.8. There, the experimental data is shown in brown solid lines and the modeling in green dashed lines. The experimental data is matched to high accuracy by the modeling. The apparent "noise" on the time trace in Panel (d) stems from the lack of temporal smoothing applied to the boundary condition of the rotation and the experimental ion temperature and density profiles in the simulation. Despite these fluctuations, the modulation of rotation can be clearly observed.

The associated transport coefficients are shown in Fig. 4.9. The Prandtl number is of order unity, see Panel (a). This agrees with theory predictions and earlier results [45, 70, 176–179]. Furthermore, the Prandtl number increases clearly over the radius. In Panel (b), the resulting momentum diffusion coefficient is shown, which also monotonically increases over the radius.

The assessed pinch number, see Panel (c), is rather low in the core and increases towards the edge. It is important to mention that the convective term also includes possible contributions from particle convection. This, however, is not critical, as the gyrokinetic predictions, which are later compared to the experimental results,

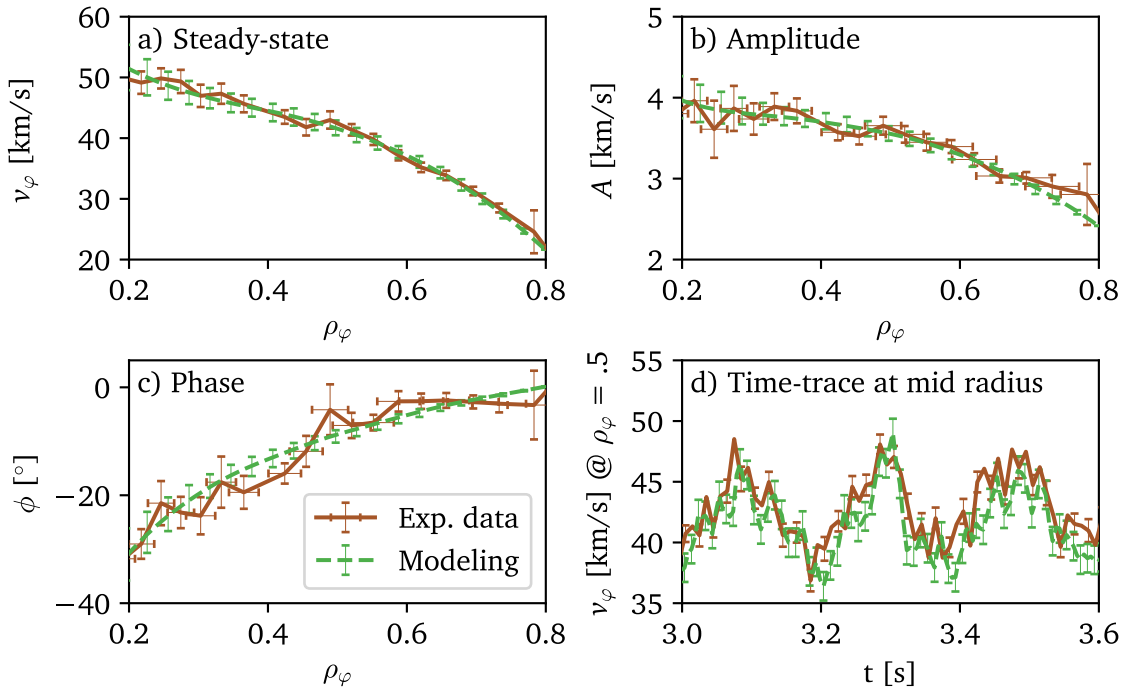

Figure 4.8: Experimental data and modeling of the reference discharge #40076 (2.0 – 4.2 s, off-axis modulation).

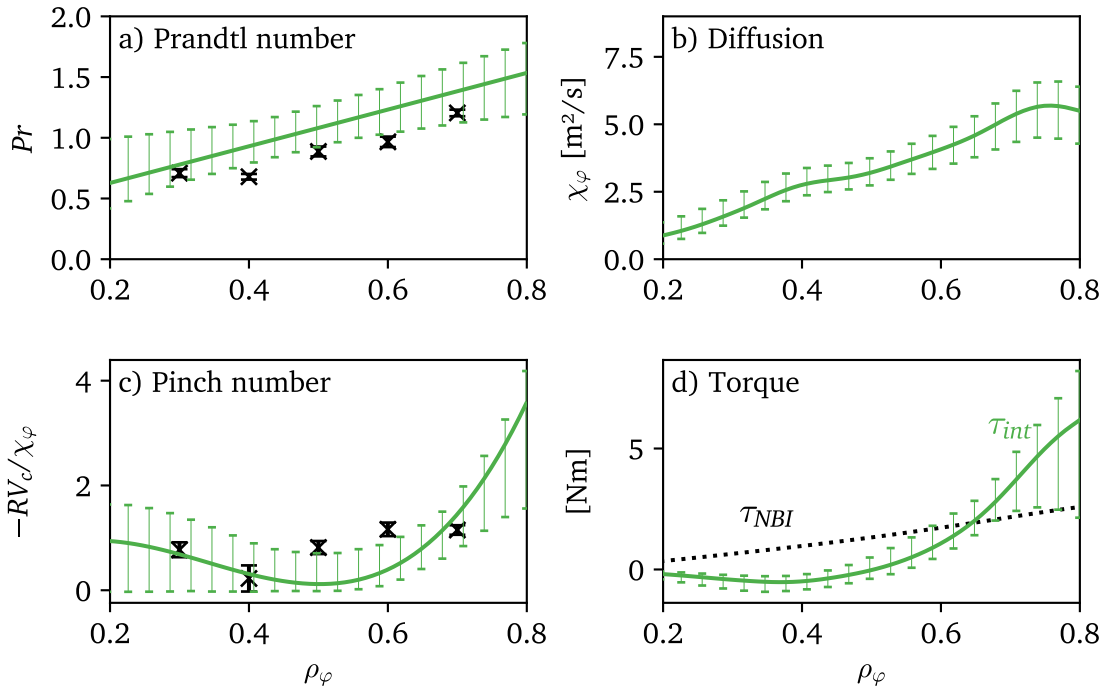

Figure 4.9: Transport coefficient assessed for the reference discharge #40076 (2.0 – 4.2 s). Panel (d) shows the intrinsic torque (green) in comparison to the torque from the NBI (black, dotted). The black symbols with small "error bars" show the GKW prediction. The "error bars" show the variation of the prediction over the analyzed time window due to the NBI modulation, which is small.

also include the particle flux contributions. Furthermore, the core particle flux is expected to be small in these scenarios [169].

The evaluated intrinsic torque is shown in Panel (d) in green, revealing a near-zero value in the core and a strong, edge-localized, co-current-directed intrinsic torque that is crucial for accurately reproducing the experimental data. The shape and size agree well with previous observations from balanced beam experiments in the DIII-D tokamak [180, 181]. Notably, unlike those studies, this approach obtains the intrinsic torque while accounting for its interplay with diffusion and convection. Furthermore, this analysis reveals that an intrinsic torque in the outer core, together with inward convection and diffusion, induces an effective co-current intrinsic rotation in the inner core despite the negligible or even counter-current-directed intrinsic torque found at that location. This emphasizes the important role of the interaction of the transport coefficients in setting the rotation profile shapes.

The reference discharge presented here is a repetition of the discharge #34027, 1.8 – 3.8 s, analyzed in a previous publication by the author [157], albeit with the modification of using off-axis beam modulation at a frequency of 5 Hz (instead of 3 Hz on-axis modulation). Interestingly, the evaluated transport coefficients show good agreement with those determined in the prior publication. This observation highlights the robustness of the applied methodology, which now has more flexibility compared to the previous study, in which the Prandtl number was fixed to gyrokinetic predictions, the pinch was prescribed to scale with the density gradient and the shear, and the residual stress was not included consistently in the modeling.

Comparison of the Individual Flux Components

Figure 4.10(a) shows the resultant momentum fluxes for the reference discharge to gauge their relative strength. The diffusive flux is mainly balanced by the NBI torque and intrinsic momentum flux. The sum of the fluxes, represented by the black symbols, is zero for the entire radius, leading to stable profiles over time. In other words, the initial values of each sinusoidal modulation remain unchanged, and no underlying drifts are observed within the modeling time span. This balance highlights the consistency of the modeling results, which is noteworthy because, at each modeling time step, the sum of fluxes can potentially be non-zero. Importantly, this balance is not artificially imposed or enforced, but naturally emerges as a result of model optimization. In Panel (b), the modulation amplitudes of the corresponding fluxes are depicted. The effect of the perturbation is most pronounced towards the outer core, yet it remains noticeable within the plasma core, especially for the diffusion. The NBI torque flux exhibits the most substantial modulation relative to its time-averaged values.

In Fig. 4.10(c), the phase shifts of the fluxes are plotted shifted to zero at $\rho_\varphi = 0.8$. The diffusive flux has a much stronger phase shift over the fitting domain compared, for example, with the convective flux. This is caused by the scaling of the diffusive flux with the rotation gradient. The rotation gradient is observed to have a larger phase shift than the rotation itself (which multiplies the convective flux). This likely arises from the differing time scales of the involved mechanisms.

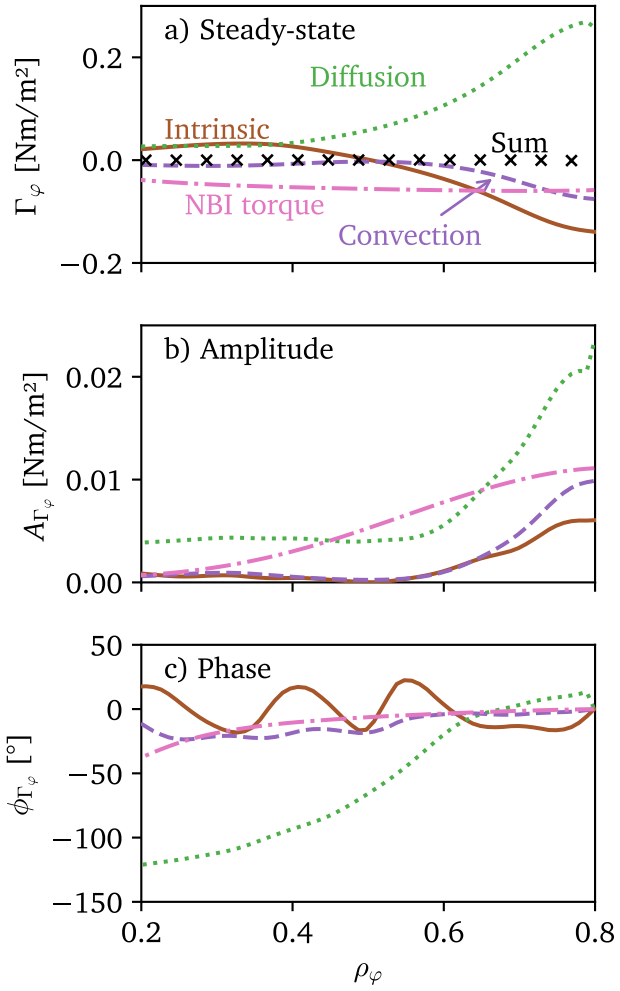

Figure 4.10: In Panel (a), a comparison of the calculated contributions to the total momentum flux originating from different transport mechanisms and sources is presented for the reference discharge #40076 (2.0 – 4.2 s). A negative value marks an inward-directed flux, resulting in co-current rotation. The symbols represent the sum of all four components. In Panel (b), the modulation amplitude of the fluxes is shown. The phase profiles are shown in Panel (c).

When switching on the modulating beam, an instantaneous $\mathbf{j} \times \mathbf{B}$-torque acts on the plasma, elevating the overall rotation profiles and the connected convective momentum flux. Subsequently, the collisional torque, together with transport, initiates a peaking of the rotation profiles on a delayed time scale. The different behavior of collisional and $\mathbf{j} \times \mathbf{B}$-torque is shown in Fig. 4.11. In the left column, the time-averaged torque density profiles are shown for both mechanisms. As seen in Panel (c), the $\mathbf{j} \times \mathbf{B}$-torque per volume is much more broadly deposited than the collisional torque, see Panel (a). From the phase profiles in the right column, the significantly higher phase shift that the collisional torque undergoes between the core and the edge (Panel b), compared to the instantaneous effect of the $\mathbf{j} \times \mathbf{B}$-torque (small phase shift, see Panel d), is seen.

Examining Fig. 4.10(c) further, it is found that the convective flux and the torque flux from the beams are mainly in phase. The time dependence of the convective flux is caused by the scaling of the convective velocity V_c with χ_φ and with the rotation. The intrinsic flux has multiple time dependences: it scales with χ_φ and the sound speed c_s. The ion sound speed scales with $\sqrt{T_e + 3\,T_i}$, and both tem-

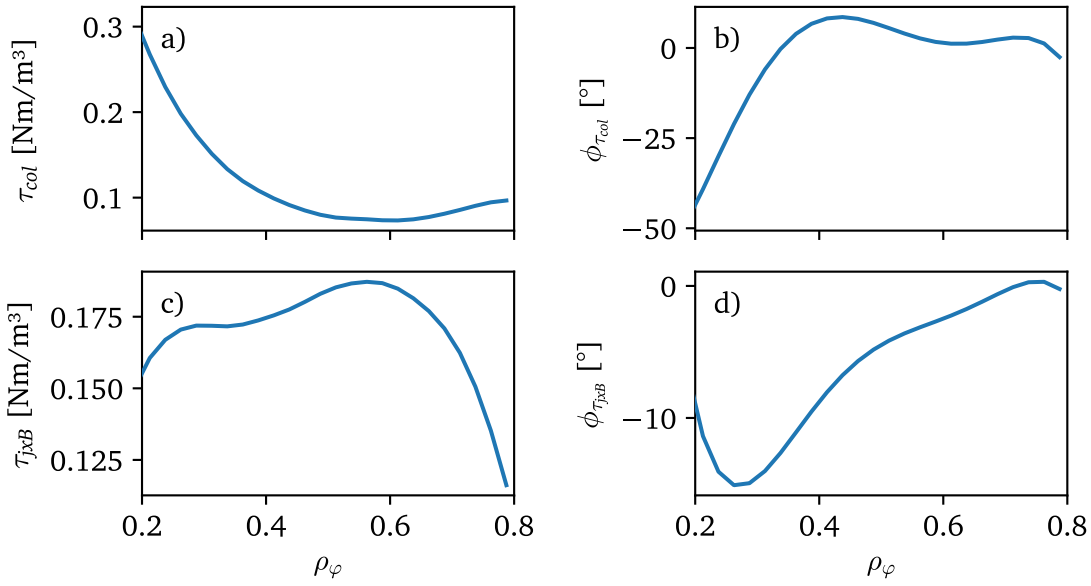

Figure 4.11: Results from the TRANSP calculation for #40076 (2.0 – 4.2 s). In Panel (a), the time-averaged profile of the collisional torque density is shown. In Panel (c), the corresponding profile for the $\mathbf{j} \times \mathbf{B}$-torque is shown. In Panel (b) and (d), the phase profiles are shown. The collisional torque peaks near the plasma center, and the $\mathbf{j} \times \mathbf{B}$-torque acts much faster in the core compared to the collisional torque.

peratures are slightly modulated. These different contributions result in a rather complex modulation that is not straightforward to disentangle. Overall, since diffusion represents the most influential individual momentum flux and exhibits a significant phase delay, it has a substantial influence on the modeling of rotation phase profiles.

Examination of the Parameter Space

The global error analysis is an important feature of this methodology. It not only results in the error bars shown on the modeling and the assessed transport coefficients, but also provides insights into the shape of the parameter space encompassing the interactions among the three transport mechanisms. In Figure 4.12, the logarithm of the cost function, $\log\left(\chi^2_{\text{red}}\right)$, around mid-radius ($\rho_\varphi = 0.6$) is depicted as a function of two of the three transport coefficients, while the third remains fixed at the optimal solution. The Figures in the second row are zoom-in versions of those in the first one.

The plots in the left column show a blue, valley-like structure of acceptable solutions and, here, a range of Prandtl and pinch number values that adequately replicate the experimental data, resulting in the modeling uncertainties, are shown. Most likely, there exist trade-off effects between the outward diffusion and the inward convection. If the fitting assumption of positive pinch number were invalid, the scan of the parameter space would exhibit a solution tied to the boundary. As seen, this is not the case.

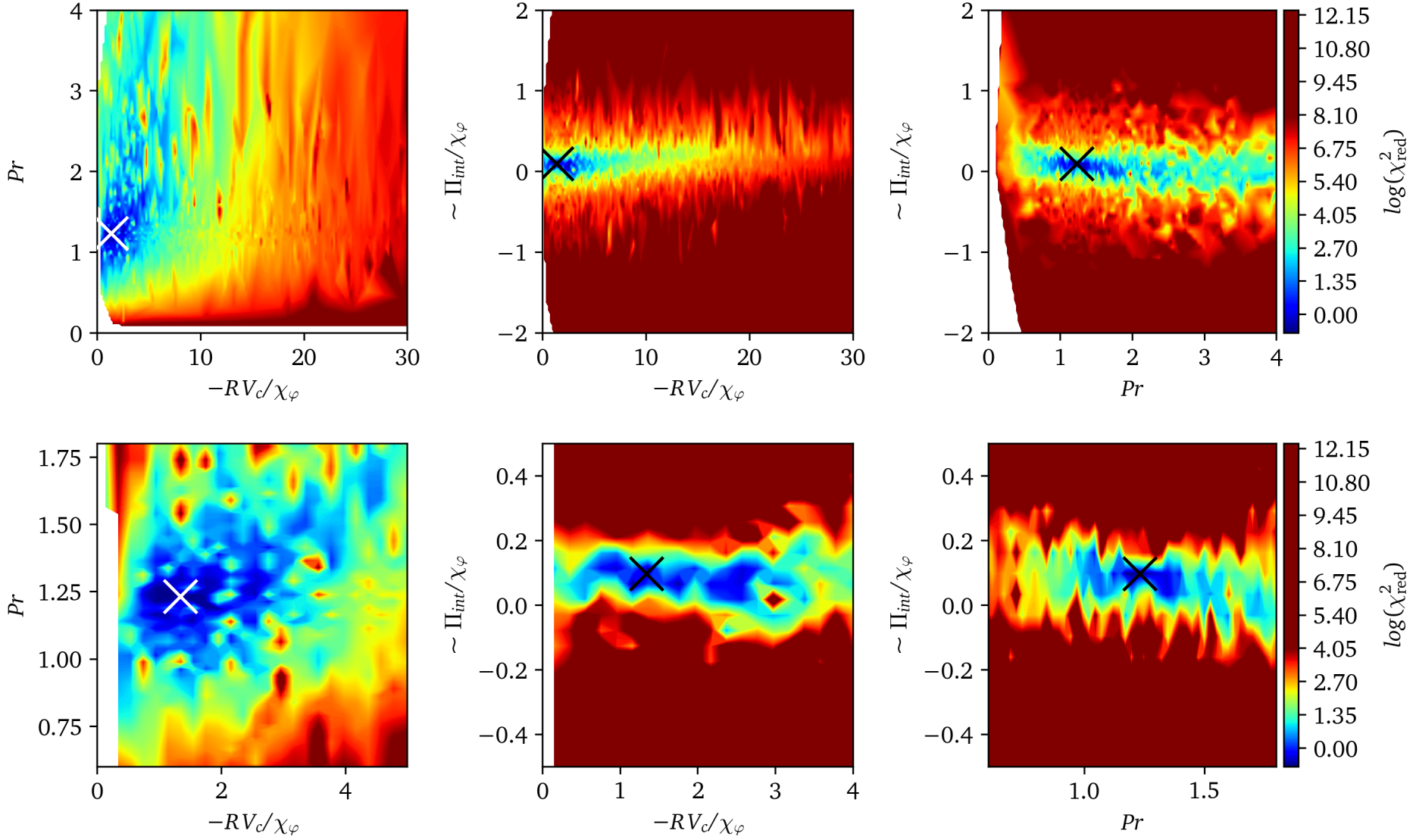

Figure 4.12: Logarithmic cost function value depending on fitted parameters at $\rho_\varphi = 0.6$ for the reference discharge #40076 (2.0 – 4.2 s). The cross marks the best solution. Plots in the second row are zoomed-in versions with adapted color bars.

In the middle column, a similar valley structure is seen. Here, the variation of the cost function depending on the pinch number and the residual stress number is shown. Both are normalized with χ_φ, and, therefore, not fully orthogonal. This results in trade-off effects and a corresponding uncertainty. This uncertainty is further amplified by the potential balance between inward convection and co-current intrinsic torque for larger radii. As a result, the error bars shown on the modeling and transport coefficients are composed of the uncertainties from the experimental rotation data as well as methodological uncertainties. A similar picture is shown for the residual stress number and the Prandtl number in the right column.

Remarkably, the contour plots reveal a single, well-defined best solution marked with a cross. There are no indications of multiple global minima. This underscores the robustness of the methodology and gives confidence in the obtained results.

Temporal Stability of the Transport Coefficients

The experimentally assessed transport coefficients are compared to gyrokinetic predictions, as introduced in Section 2.10. For the reference case, these calculations were performed for 10 randomly selected time points in the analyzed time span, covering the full variation of input profiles in the modulation cycle. This includes time points when the modulating beam was both activated and deactivated. The obtained averages are depicted in Fig. 4.9 as marked by crosses and are within the error bars of the experimental results. The error bars associated with these black data points represent the standard deviation among the gyrokinetic calculation from the randomly sampled time points. Additionally, a separate calculation employing time-averaged profiles yielded consistent outcomes, underscoring the stability of these results. These calculations show the Prandtl number and pinch number are not expected to change due to the modulation. Similar calculations for on-axis modulation agree.

The question of whether the Prandtl and pinch numbers remain constant is crucial for the successful modeling of the modulation experiment. If the modulation were to perturb the background turbulence to such an extent that it could not be compensated for using the observed variation of the ion heat diffusivity, stable values for the Prandtl and pinch numbers could not be derived, leaving the fitting problem underconstrained. As demonstrated, for these discharges, the modulations of temperatures and the rotation were small, and, consequently, it is possible to compensate for the perturbation of turbulence amplitude by including χ_i.

For the perturbation of the rotation, there is no reason to expect that the Prandtl or pinch numbers depend strongly upon the measured modulation of the rotation nor its gradients, as their effect on turbulence is weak compared with that from gradients in density and temperature. This has been demonstrated, for example, by Casson [182] for the Prandtl number. In that work, Fig. 5.5 shows the dependence of the Prandtl number on the normalized rotation gradient u'. In the experimental data studied in this work, u' varies between 0.2 – 1.5 depending on discharge and radial position. The effect of the modulation is only between 10 – 15 % of the absolute value of u' for all cases and radial positions. When comparing these numbers to the figure in Casson's work, the changes during the modulation are too small to affect the transport coefficients significantly. A similar plot is shown

in [76], see purple curve in Fig. 14. The author assumes that this also applies to the ratio of the convective velocity to the momentum diffusivity (pinch number) and the intrinsic torque. This assumption is supported by the significant difference in magnitude between the gyrokinetically calculated growth rates and the $\mathbf{E} \times \mathbf{B}$-shearing rates in the cases under investigation. Hence, a modulation of 10 – 15 % in the absolute value of u', directly affecting the shearing rate, is considered to have minimal to no influence on the turbulence state.

In order to validate the prediction of constant transport coefficients, the experimental rotation data was modeled using a time-dependent Prandtl number. However, this attempt did not lead to satisfying modeling results, as the problem was evidently underconstrained as the model had too many degrees of freedom. The approach of disentangling the modulation effects on the heat and momentum transport channels also contradicts the fundamental concept of the Prandtl number, which relies on the assumption of the similarity between ion heat and momentum diffusivities.

Benchmark of Simplified Transport Models

Given that this work is the first to include a time-dependent intrinsic torque in the modeling process, it becomes valuable to explore the impact of excluding the intrinsic torque or its time dependence. Such an investigation is important as the majority of prior momentum transport studies used one or both of these simplifications. To address this, three distinct numerical experiments are conducted using the same experimental data set of the reference discharge.

First, only constant diffusion and convection are used in the modeling, and the intrinsic torque is omitted. This results in very flat phase profiles and very high amplitude profiles (not shown in Fig. 4.13 to enhance clarity). Overall, the regressed fit leads to a strong reduction in the Prandtl number and diffusivity. Consequently, the pinch is significantly reduced to balance, reaching extremely low, unrealistic values and even nearing zero across large parts of the radius. The corresponding increase in cost-function value and decrease in modeling accuracy is evident. Together with prior theoretical arguments [80, 81, 183], this emphasizes the necessity to use time-dependent transport coefficients.

Second, time-dependent diffusion and convection are included in the modeling while still disregarding the intrinsic torque. This analysis is depicted by the dotted orange lines in Figure 4.13(a-c). The solution with time-dependent intrinsic torque, demonstrated earlier to closely match the experimental values, is indicated by the solid green lines. Modeling without intrinsic torque leads to an underestimation of the steady-state rotation profile up to $\rho_\varphi = 0.4$. This shows the absence of co-current intrinsic rotation needed to model the data correctly. In reality, based on fit-quality criteria, this would not have been accepted as a modeling solution, as $\chi^2_{red} \approx 5$. The Prandtl and pinch numbers are illustrated in Panels (d) and (e) by the dotted dark-purple lines. Neglecting the intrinsic torque causes the Prandtl number profile to flatten and decrease while the pinch number is slightly reduced. However, neglecting the co-current intrinsic rotation cannot be fully replicated by convection alone, as this would increase the modeled amplitude profile even further. To balance this, diffusion decreases to restore the steady-state rotation.

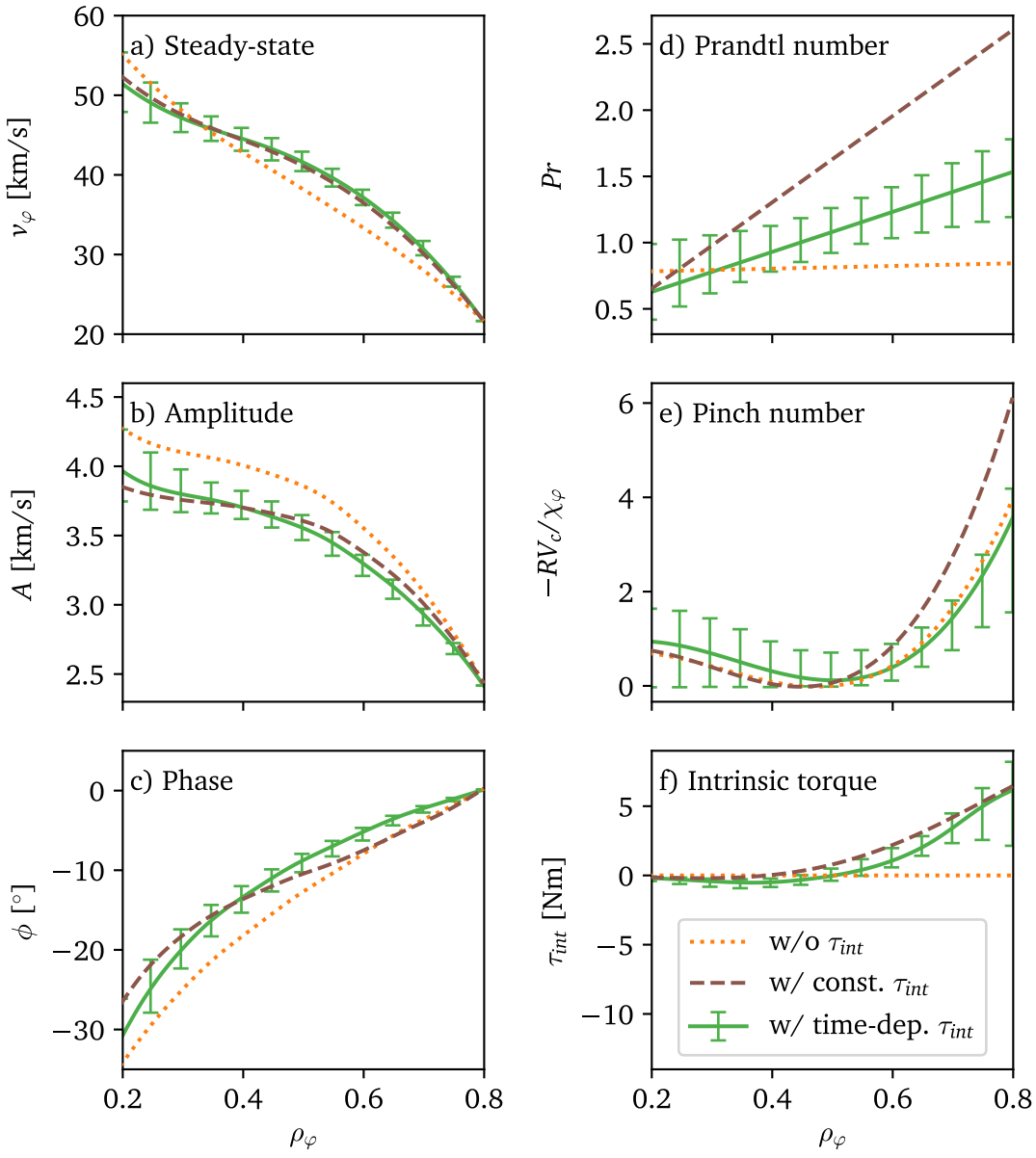

Figure 4.13: Various modeling approaches are explored for the reference discharge #40076 (2.0 – 4.2 s). The modeling with time-dependent intrinsic torque agrees well with the experimental data, as shown in Fig. 4.8. Therefore, in this plot, the experimental data is omitted for the sake of clarity.

Third, a radially varying intrinsic torque, remaining constant over time, is used in the model. The outcome of the regression is presented using dashed brown lines. While superior to the modeling without any intrinsic torque, this model still exhibits differences in both amplitude and phase profiles, with the latter exceeding experimental uncertainties. The corresponding cost-function value is more than twice that with time-dependent intrinsic torque ($\chi^2_{\mathrm{red}} \approx 2.1$), resulting in modeled profiles outside of experimental uncertainties. The Prandtl number is significantly changed. Modeling with a constant intrinsic torque yields similar profiles for the pinch number and intrinsic torque, albeit slightly higher. These discrepancies are primarily pronounced towards the outer plasma core, where the impact of temporal dependences, particularly for a more edge-localized intrinsic torque, is most prominent, see Figure 4.10(b). The overestimation of Prandtl and pinch numbers likely stems from the absence of temporal dependence in the co-current intrinsic torque. By neglecting its time dependence, the amplitude profile is lowered. Consequently, the convection, compensating for this effect, becomes larger, generating overly steep phase profiles. This forces the Prandtl number to increase, flattening the phase profile once again, in line with the observation. Ultimately, the constant intrinsic torque must grow larger to counteract the increased diffusion, as illustrated in Panel (f). Although employing a constant intrinsic torque yields improvements over scenarios without any intrinsic torque, it remains inferior to modeling encompassing all temporal dependences. Also, from a theoretical standpoint, there are strong arguments to include time dependences in the residual stress to compensate for the modulating turbulence amplitude [51, 80, 81].

Motivated by previous studies, such as by Tala *et al.* [178], it is plausible that neglecting the intrinsic torque or its time dependence contributed to a systematic distortion of the assessed transport coefficients and to their mismatch with gyrokinetic predictions. These numerical experiments with simplified models were conducted for several other AUG discharges with NBI modulation (#29216 2.0 – 4.5 s, #34042 6.1 – 7.4 s, #39015 7.0 – 9.3 s, #41551 6.4 – 7.6 s) covering a range of plasma parameters (as discussed in Chapter 7).

These numerical experiments underscore that modeling retaining time dependences in all transport coefficients provides the most accurate reproduction of the experimental data and, consequently, is the preferred approach in this study.

Edge Localized Nature of the Intrinsic Torque

The modeling carried out for the reference discharge clearly indicates that the best match with the experimental rotation modulation data is achieved with an intrinsic torque profile that peaks towards the outer edge of the fitting domain. It is speculated that this intrinsic torque is mainly edge localized and results from effects in the pedestal penetrating into the core. However, it is important to note that in this work, routinely, the simulation boundary is defined at $\rho_\varphi = 0.8$, which corresponds to $\rho_\psi \approx 0.88$. Consequently, it is not possible to draw conclusions about the plasma pedestal region from these results. In order to investigate whether an edge-localized intrinsic torque is sufficient to explain the results, a further numerical experiment is conducted.

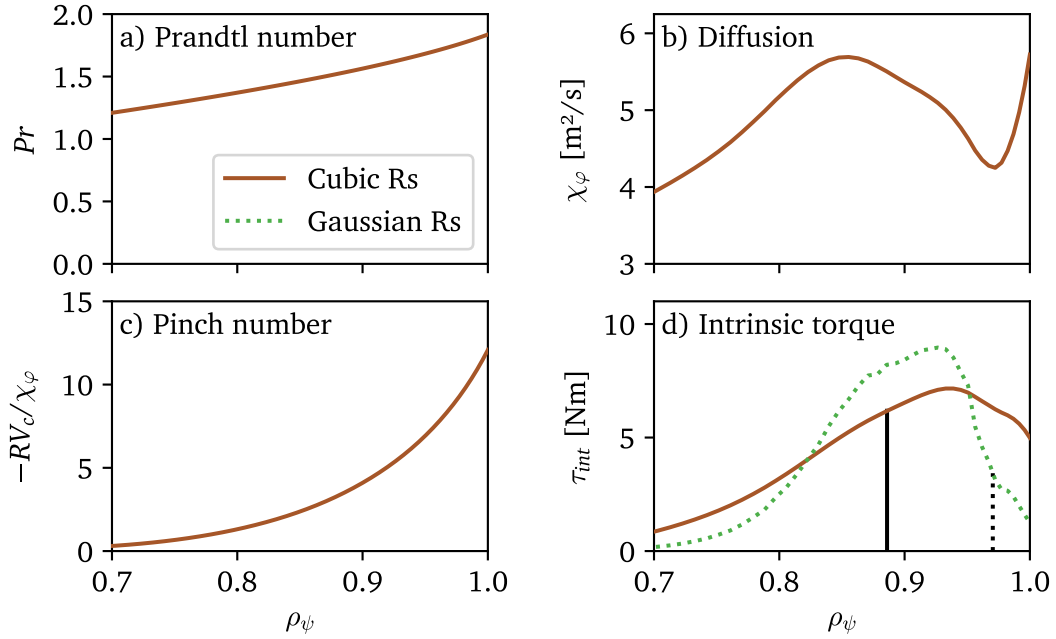

Figure 4.14: Numerical experiments to explore the edge localized nature of the evaluated intrinsic torque. In contrast to the original fitting where the boundary is around $\rho_\psi \approx 0.88$, this modified simulation set the boundary at $\rho_\psi \approx 0.97$, as indicated by vertical lines (full line for the cubic, dotted for the Gaussian model). A peak of the intrinsic torque emerges around $\rho_\psi \approx 0.93$.

A simulation is performed with the modeling boundary extended to $\rho_\psi = 0.97$. The residual stress in the model (before the cubic polynomial $g(\rho_\varphi)$ in Eq. 2.28) is replaced with a single Gaussian-shaped profile. The parameters of this Gaussian profile, including its position, width, and amplitude, are kept free. The diffusion and convection are extrapolated from the initial solution and held constant to isolate the effect of the modeled residual stress. The edge values of the Prandtl number, diffusion, and pinch number resulting from this model are depicted in Fig. 4.14(a)-(c). The corresponding intrinsic torque, displayed in Panel (d) as a green dotted line, shows a peak near the top of the pedestal at $\rho_\psi \approx 0.93$. For comparison, the extrapolated values from the cubic residual stress model are also provided. The core steady-state rotation, phase, and amplitude profiles (not shown) are well reproduced by using this alternative residual stress model.

This proves the validity of a Gaussian residual stress profile as an alternative solution. It further shows that momentum transport in the core is likely influenced by physics effects emerging from the plasma edge. However, it also reveals that the presented methodology cannot uniquely determine the radial distribution of this torque in the plasma edge. Notably, the required integrated values are quite similar, indicating that the technique has provided valuable insights into the magnitude of such a torque. It is important to mention that the plotted intrinsic torque does not appear as a symmetrical Gaussian, as the scaling with χ_φ in Eq. 2.28 is applied. Performing this exercise for other discharges is not always feasible, as the phase profiles at the edge are usually not smooth enough due to the ELM dynamics, which prevents the radial boundary of the analysis from being set that far outside.

4.4 Summary

This work is based on NBI modulation experiments. Through modulation of the beam torque, the toroidal rotation is modulated, and Fourier analysis is employed to distinguish the three contributions to the transport equation based on their temporal characteristics. However, this modulation introduces the potential risk of undesired temperature perturbations, resulting in a modulation of the turbulence intensity. To account for this perturbation, it is crucial to retain time dependences in all transport channels. Nevertheless, the temperature perturbation must be minimized to avoid altering the background turbulence above a level that can be compensated by including the scaling of the momentum transport coefficients with χ_i.

Several essential conditions for the successful setup and analysis of NBI modulation experiments are deduced. For ASDEX Upgrade, it is determined that off-axis modulation experiments using a lower-power beam ($P_{\text{mod}} = 0.7$ MW) at a modulation frequency of 5 Hz offer the most favorable conditions for the analysis. Throughout the analysis, it is crucial to ensure a coherent equilibrium reconstruction in all relevant steps to not cause inconsistencies in the mapping of experimental data and in calculating gradients. The equilibrium, however, is found not to change significantly during the modulation.

The momentum transport analysis relies on `TRANSP` runs, which provide the heat and torque fluxes from the heating sources. `ASTRA` is employed to solve the heat and momentum transport equation and to model the toroidal rotation. This is done based on an experimental boundary condition at the edge and a set of prescribed transport coefficients. A global minimization routine was implemented to iterate over a range of transport parameters, seeking the best fit of the modeled rotation to the experimental data. The global error analysis derives error bars on the modeling results. All outcomes are stored in a database.

The analysis of the reference discharge shows that the experimental rotation data can be modeled with high accuracy. The Prandtl number is determined to be of order unity, and it increases across the radial profile. Both the Prandtl and pinch numbers agree within error bars with the gyrokinetic predictions. The intrinsic torque is observed to increase towards the plasma edge and acts in the co-current direction. Numerical experiments demonstrate that it is likely to peak in the plasma edge and that this edge-localized torque is able to penetrate into the core. The error analysis shows that the obtained solution indeed represents a global minimum.

Both theoretical predictions and experimental data lead to the conclusion that the pinch and the Prandtl numbers likely remain constant during the modulation, indicating that the scaling of the diffusivity and convective velocity with χ_i was able to compensate for the induced cross-channel perturbation. However, the diffusivity, convective velocity, and intrinsic torque themselves are subjected to modulation. By conducting numerical experiments that exclude time dependences in the various transport mechanisms, it becomes evident that this omission leads to discrepancies with gyrokinetic predictions and overall worse modeling results. This underscores the need to retain time dependences to accurately extract momentum transport coefficients from NBI modulation experiments.

Chapter 5

Isotope Comparison

"Same, same, but different!?"

— Meritj

This work aims to validate the theory for a reliable application of models to future fusion devices. While present-day fusion research devices usually operate in H or D, future reactor operation is foreseen to operate with D and T fuelling mixtures. For a non-nuclear phase of ITER, He was also discussed to avoid neutron production. Some investigations of the mass and isotope effects on momentum confinement have been carried out [184, 185], but all publications on the local effects of momentum transport investigated D plasmas [177–181, 186–197]. However, the understanding of the mass and isotope dependence of momentum transport mechanisms is important for application of models to future devices. To this end, a pair of an H and D discharges was created and compared to investigate possible isotope effects. A key condition of such a comparison is a match of the dimensionless parameters governing the transport coefficients. In particular, the heat transport needs to be matched, as this can significantly impact the momentum transport analysis via the Prandtl number. Parts of this Chapter are the subject of publication [165].

5.1 Experimental Scenario

To isolate the possible effects of an isotope dependence between an H and D discharge, a special scenario has to be created in which all parameters that are expected to scale or interact with momentum transport are similar. The D reference discharge #40076 from 2.0 – 4.2 s, introduced in Chapter 4, was chosen as a starting point for the scenario development of the H discharge.

Comparable heating power was applied, $P_{tot}^{H} = 5.2$ MW and $P_{tot}^{D} = 6.6$ MW, resulting in plasma stored energies of $W_{MHD}^{H} = 0.30$ MJ and $W_{MHD}^{D} = 0.36$ MJ. While the fraction of the main isotope was $\approx$ 95 % in H, it was $\approx$ 100 % in D. To improve the quality of the CXRS measurements in H, N was puffed with $\Gamma^{N} \approx 0.35 \times 10^{21}$ atoms/s, yielding $Z_{\text{eff}}^{H} \approx 1.38$. This was not necessary in the D

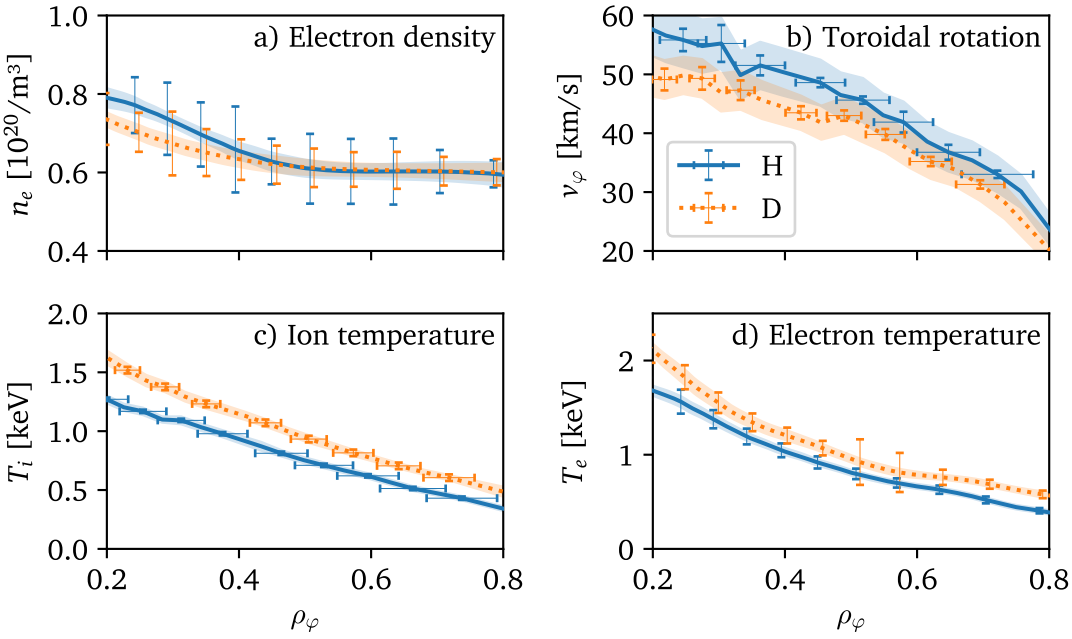

Figure 5.1: Core kinetic profiles of the compared H (#41550) and D (#40076) discharges. The error bars show the statistical uncertainty of the data reconstruction, and the band structures reflect the standard deviation over the analyzed time windows for each radial point, showing the stability of the corresponding quantity.

discharge, where the intrinsic B was sufficient for the CXRS measurements. In D, $Z^D_{\text{eff}} \approx 1.2$ with the main gas flux set to a value of $\Gamma^D \approx 1 \times 10^{22}$ atoms/s. To match the pedestal top density of the D discharge in H, the H gas puff was set to $\Gamma^H \approx 2 \times 10^{22}$ atoms/s, as previous experiments have shown that, in general, a significantly higher gas flux is required in H due to increased particle transport in the pedestal [198, 199]. The pedestal and core densities were matched within uncertainties, see Fig. 5.1(a).

As explained in Section 4.1, NBI modulation is used to assess the momentum transport coefficients. In these discharges, modulation of a single off-axis oriented source with reduced power ($P^H_{mod} \approx 1.1$ MW and $P^D_{mod} \approx 0.7$ MW) was a good compromise to provide a clear rotation modulation, while keeping the induced perturbations small. Indeed, the modulations of the kinetic profiles were measured to be relatively small, e.g. the electron density ≈ 0.5 % at mid-radius in both cases, the T_e (T_i) at mid-radius $\approx 2(3)$ % and $\approx 4(4)$ % for D and H, respectively, while the stored energy, W_{MHD}, varied by ≈ 5 % (D) and ≈ 7 % (H). The modulation of the toroidal velocity v_φ was ≈ 8.5 % (D) and ≈ 10 % (H). There are no drifts of these modulating quantities. Therefore, it is feasible to calculate and compare time-averaged, steady-state kinetic profiles (Fig. 5.1), torques, and heat fluxes (Fig. 5.2).

To avoid impurity accumulation, ≈ 0.6 MW on-axis ECRH was applied in both discharges [200, 201]. For D, 4.8 MW of steady NBI background heating was used with an extraction voltage of $U^D_{ex} = 53$ keV. In order to match the applied torque and the heat fluxes, the `TRANSP` code was used to determine the precise NBI settings for the H discharge. This was motivated by the different beam species used and by previous works on the isotope dependence of heat transport [184, 185,

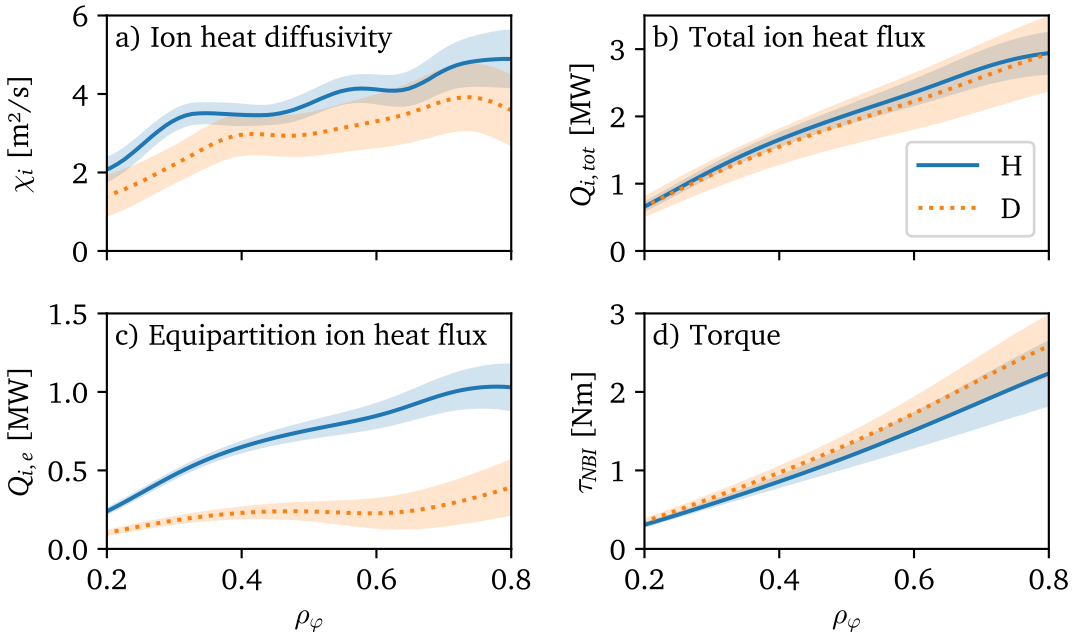

Figure 5.2: (a) Ion heat diffusivity from ASTRA calculations, (b) the total ion heat flux, (c) the electron-to-ion equipartition flux, and (d) the total applied torque from TRANSP calculations. The band structures show the standard deviation caused by the modulation on top of the averaged profile of the H (#41550) and D (#40076) discharge.

202–205]. There, stronger ion heat fluxes were observed in H than in D when the same total heating power is applied, resulting from the strong mass dependence of the equipartition term [206–208]. Also, for the discharges studied herein, the heating of the ions via collisions with the electrons was found to be a significant part of the ion heating in H in contrast to the D discharge, see Fig. 5.2(c). As a consequence, the higher total ion heating in H compared to D for matched NBI power results in a larger apparent ion heat diffusivity χ_i if the gradients are matched. Interestingly, when Q_i is matched instead of the NBI power, the overall transport behavior becomes similar between the two species. Based on the scenario development with TRANSP, 3.4 MW of NBI were used in the H discharge with two full voltage beams from NBI box 1 ($U^D_{ex,1} = 53$ keV) with H as the beam species. A reduced voltage beam from box 2 ($U^D_{ex,2} = 63$ keV) was used for the modulation.

The scenario development was successful, and comparable surface integrated ion heat fluxes were achieved, see Fig. 5.2(b). As similar temperature gradients were measured, see Fig. 5.3(b), and comparable densities were reached, see Fig. 5.1(a), similar ion heat diffusivities in the core of the plasma are obtained, see Fig. 5.2(b), in both discharges. This is consistent with earlier works [206–208] and was the aim of the scenario development to clearly distinguish the isotope effects of the different transport channels in this comparison. The electron heat transport channel has no influence on the analysis and was, therefore, not prioritized in the scenario optimization, but was matched within $\approx$ 20 % at mid-radius. The torque applied on the plasma was successfully matched, see Fig. 5.2(d).

The torques were applied to plasmas with comparable density, see Fig. 5.1(a), but the time-averaged, steady-state toroidal velocity is slightly higher for H, see Fig. 5.1(b). For the same external torque, a two times higher velocity for H would

be expected due to the mass difference. This is not observed, partly as the torque in H is slightly smaller, see Fig. 5.2(d), and the density is slightly higher inside $\rho_\varphi < 0.4$, see Fig. 5.1(a). Both result in a reduced rotation. As discussed later, the remaining difference is caused by small variations in the momentum transport coefficients.

Temperatures are slightly lower in the H discharge, see Figs. 5.1(c) and 5.1(d). This is partly caused by the pedestal confinement degradation in H due to the increased inter ELM transport with lower mass [208] despite comparable heat fluxes. This causes lower pedestal ion temperatures in the H discharge, this is shown in Figs. 5.4(b) and 5.4(c). In Fig. 5.4, the T_i data of the edge CXRS was shifted 15 mm radially inwards for the H discharge to match the region of steepest gradients with respect to the T_e data from the Thomson scattering diagnostics. In the used coordinate, ρ_ψ, this corresponds to a value of 0.02. This adjustment is necessary due to minor inaccuracies in the equilibrium reconstruction process, which impact the relative positioning of diagnostic measurements taken at different toroidal and poloidal locations [209]. Likewise, in the case of the D discharge, a 10 mm radial inward shift of the T_i data was applied, equivalent to a shift of 0.015 in ρ_ψ. Given the shallow gradients in these discharges, there remains some level of uncertainty associated with the relative alignment. Despite reaching similar pedestal top densities, see Fig. 5.1(a), the shapes of the density pedestal profiles are different, see Fig. 5.4(a). The ion pressure profiles in the pedestal are higher for D and have steeper gradients, see Figs. 5.4(d) and 5.4(h). The error bars presented on gradients are assessed through Gaussian process regression, employing the statistical uncertainties of the experimental profiles in Panels (a-d) to approximate Gaussian errors. For the error bars of the pressure, see Fig. 5.4(d), analytical error propagation is employed. In the kinetic profiles, the band structures represent the standard deviation over time at each radial position. Notably, given that the standard deviation is comparable with, or even smaller than, the uncertainties linked to the kinetic profiles, the propagation of uncertainties also functions as an indicator of the stability of the provided profiles.

In the discussed discharges, measurements of the radial electric field E_r were not available, but the E_r-well in the pedestal can be inferred via the diamagnetic term in the force balance, see [210, 211]. The shown pressure gradient profiles suggest, therefore, a deeper E_r-well for the D case, with stronger E_r gradients generating higher $\mathbf{E} \times \mathbf{B}$-velocity shear. This, likely, enhances edge turbulence suppression [31] and, possibly, the $\mathbf{E} \times \mathbf{B}$-driven intrinsic torque [76].

To isolate a possible isotope dependence of the momentum transport coefficients, dimensionless parameters need to match [212]. Therefore, as a next step, the most relevant dimensionless parameters are compared, see Fig. 5.3. Similar to Fig. 5.4, the error bars depicted on gradients in this figure are obtained through the regression of Gaussian processes, with the Gaussian errors approximated using the statistical uncertainties of the input profiles. For the remaining dimensionless parameters, the error bars arise from analytical uncertainty propagation. In Panel (a), the logarithmic density gradients are shown. They are within uncertainties due to the large uncertainties on the density profiles, see Fig. 5.1(a). However, the peaking in the inner core is slightly stronger for H. The effect of this difference on the momentum transport will be discussed later, together with the gyrokinetic results. The ion temperature gradient plays a key role in the calculation of the power balance ion heat diffusivity. It is reasonably well matched at most radii,

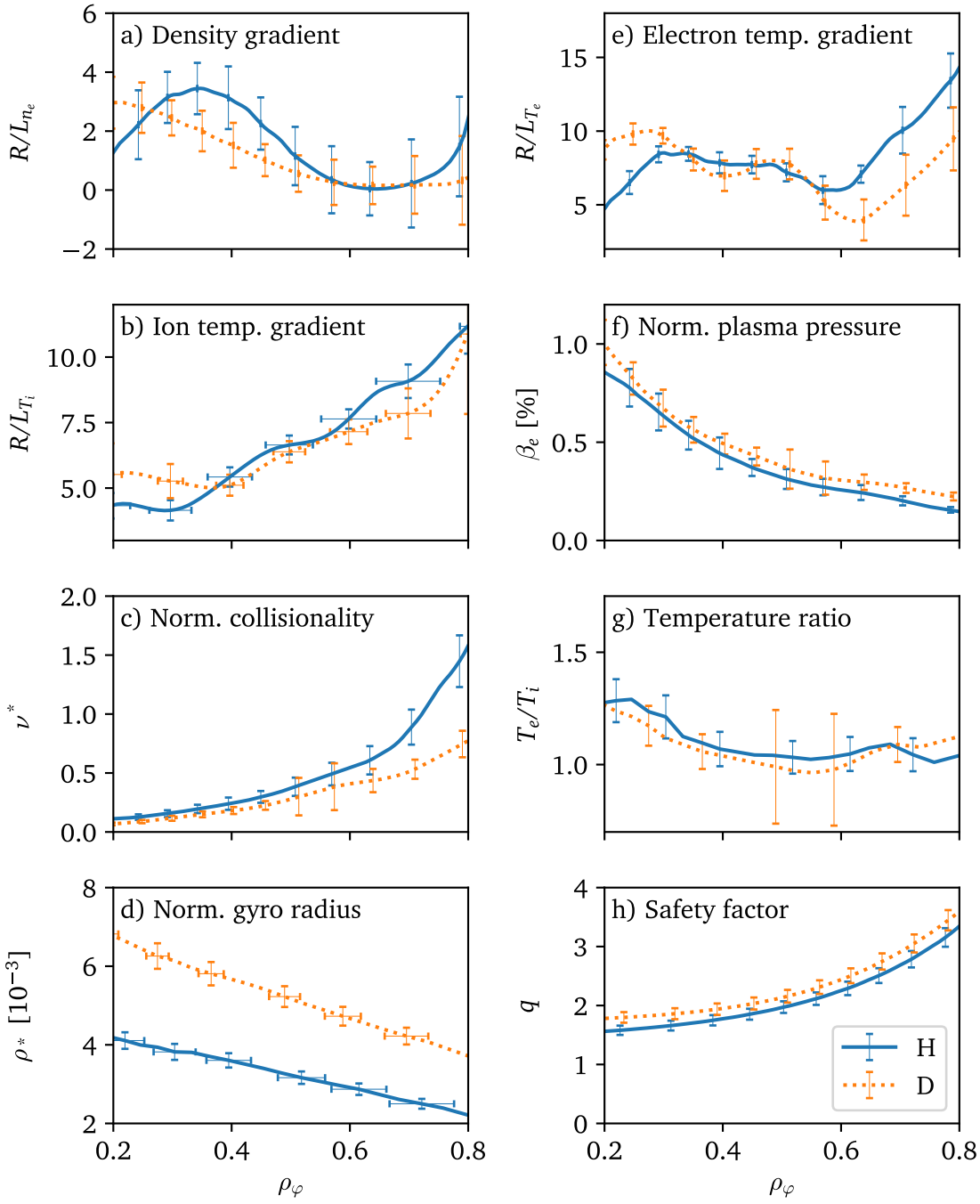

Figure 5.3: Comparison of dimensionless parameters of the H (#41550) and D (#40076) discharge in the plasma core.

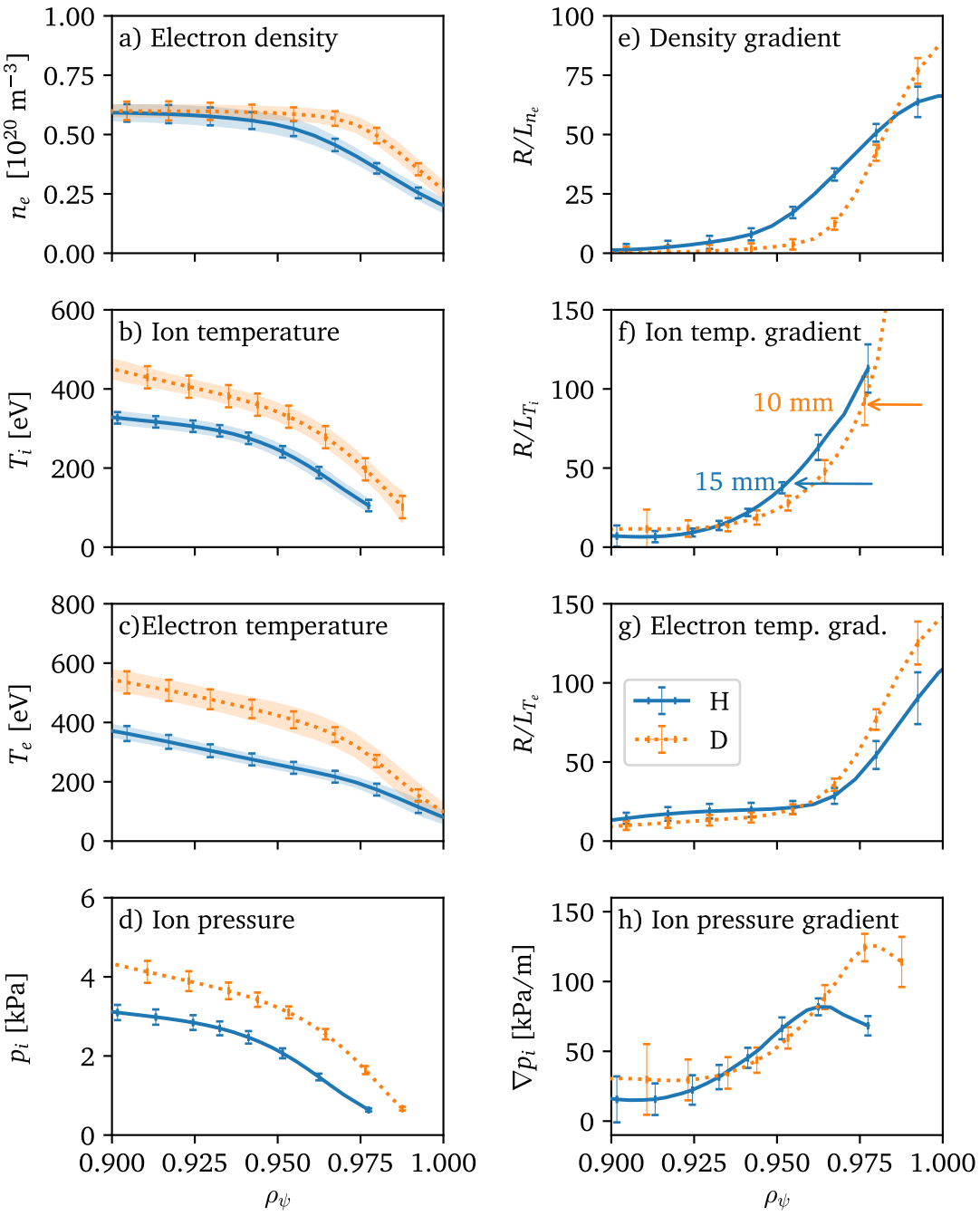

Figure 5.4: Comparison of pedestal profiles of the H (#41550) and D (#40076) discharge. ρ_ψ is chosen as a radial coordinate because it is defined outside the last closed flux surface and resolves the flux surfaces better. The arrows in Panel (f) show the shift of the T_i data to match the steepest region of the Thompson scattering T_e data. The standard deviation of the kinetic profiles over time is shown with band structures.

see Fig. 5.3(b), some difference exists towards the outer core. The collisionality $\nu_* \sim n_e/T_e^2$ is similar inside of $\rho_\varphi < 0.6$, see Fig. 5.3(c). The differences for larger radii emerge from lower T_e in the H discharge.

The normalized gyroradius, see Fig. 5.3(d), is defined as $\rho_* = \rho_i/a = \sqrt{m_i T_i}/eBa$ with a the minor radius, ρ_i the ion Larmor radius, and the electron charge e. As expected, due to the smaller ion mass m_i and lower T_i, ρ_* is found to be lower for H. For a matched ρ_*, the magnetic field and the plasma current would have been modified to not significantly change the q profile. This would have made a match of the density even more complex. Therefore, it was decided to accept a difference in ρ^* to achieve comparable densities and q profiles, as no dependence of momentum diffusion or convection upon the normalized gyroradius is expected. The intrinsic torque, however, is predicted to depend weakly on ρ^* [50, 51].

The electron temperature gradients, see Fig. 5.3(e), are matched within uncertainties inside between $0.3 < \rho_\varphi < 0.6$, whereas, outside this region, a slight difference is found. The normalized plasma pressure $\beta_e \sim n_e T_e/B^2$ is well matched, see Fig. 5.3(f), and the magnetic safety factor q is very similar due to the identical equilibrium, see Fig. 5.3(h). The temperature ratio T_e/T_i, which influences the turbulence regime, agrees well, see Fig. 5.3(g), and has rather large uncertainties around mid-radius from the electron temperature profiles.

The developed H scenario, together with the D reference discharge, offers an interesting data set: most of the relevant parameters governing transport and turbulence agree in the plasma core within experimental uncertainties. The experiment was designed in a way that the ion heat transport, which influences the analysis via the Prandtl number, is nearly identical. Applying the momentum transport analysis framework to this data should make it feasible to isolate a mass dependence, if present.

5.2 Experimental Results

For both discharges, the modeling reproduced the experimental steady-state, amplitude, and phase profiles. This is shown in Fig. 4.8 for the D reference discharge and in Fig. 5.5 for the H discharge. In both figures, the experimental data is shown by brown solid lines, and the modeling is shown by green dashed lines.

The assessed transport coefficients are compared in Fig. 5.6. The profiles of the Prandtl number are found to be nearly identical, see Fig. 5.6(a). As the ion heat diffusivities were matched, see Fig. 5.2(a), the momentum diffusivities of both discharges are very similar, see Fig. 5.6(b). The profiles of the assessed pinch numbers are shown in Fig. 5.6(c). They mostly match within uncertainties. Slightly higher values in the inner core are observed for the H discharge. These values may be connected with differences in density and temperature gradients, as shown in Figs. 5.3(a), (b), and (e). This would agree with previous predictions from theory, e.g., the scaling of the pinch number with density and temperature gradients [48]. For these specific discharges, the parameter dependences will be discussed further in Section 5.3 together with a comparison to gyrokinetic calculations.

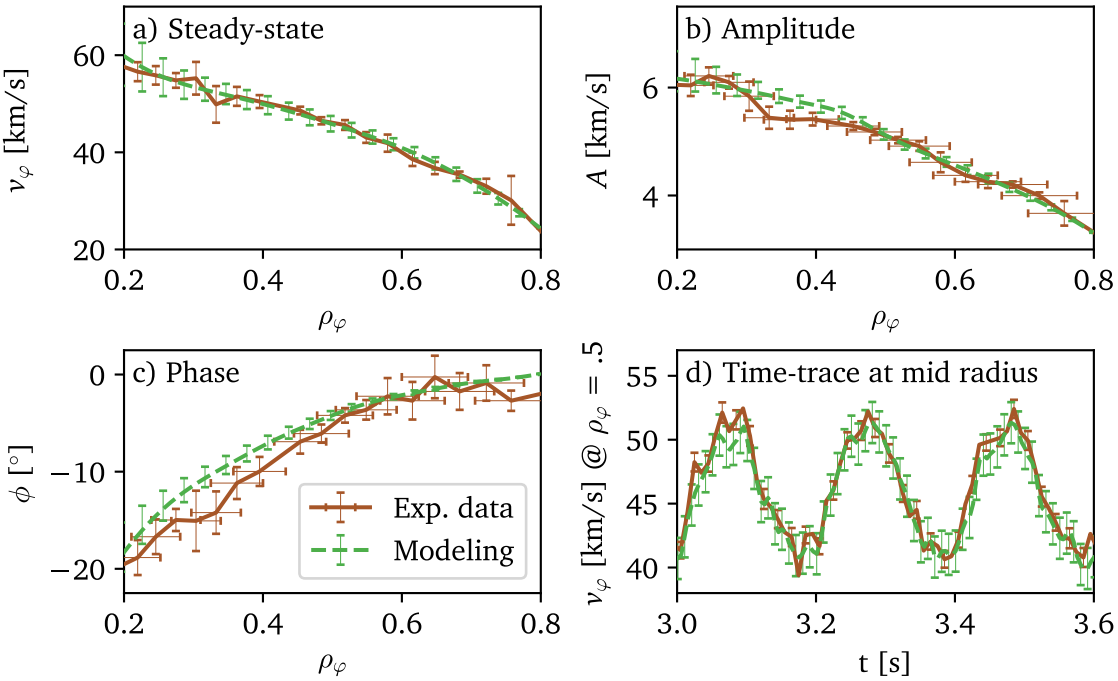

Figure 5.5: Modeling of the H comparison discharge #41550 (1.8 – 4.2 s).

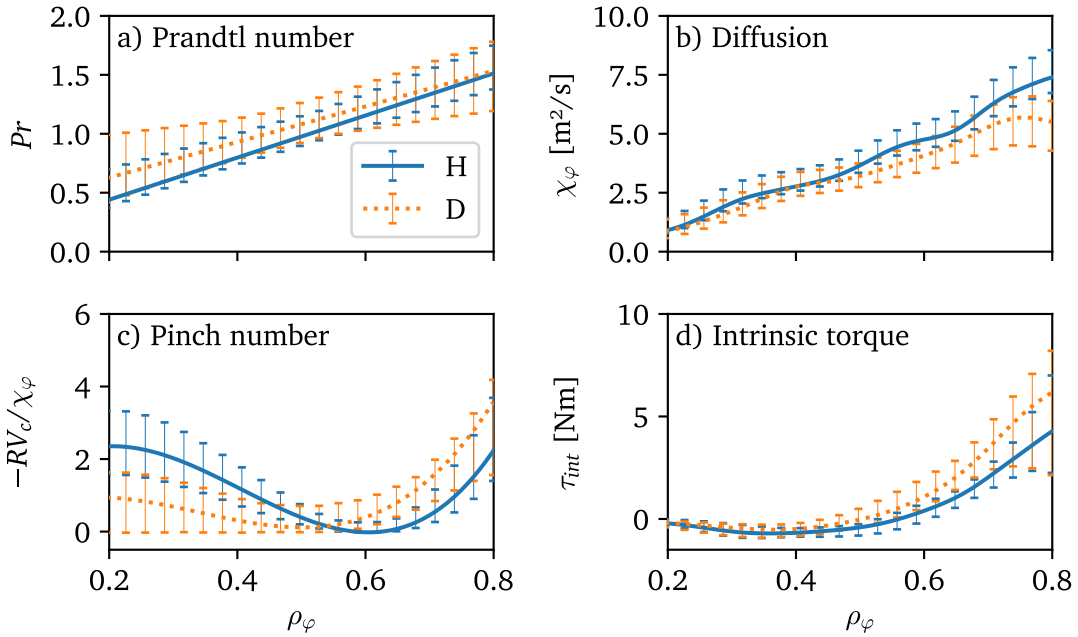

Figure 5.6: Comparison of the assessed transport coefficients of the H (#41550) and D (#40076) discharge.

The intrinsic torque profiles match within uncertainties, see Fig. 5.6(d). In the inner plasma core, a very small counter-current intrinsic torque is found. Towards the outer core, a strong, co-current intrinsic torque is needed to model the experimental data correctly. The shape and magnitude of the intrinsic torque values towards the edge are consistent with results from the DIII-D tokamak [181]. The slightly stronger intrinsic torque towards the plasma edge in the D discharge correlates with the pedestal pressure gradient, see Fig. 5.4(h). The theory background of this effect was introduced already in Chapter 2.7 and a possible scaling will be discussed further in Chapter 7.3. These two cases are insufficient to draw firm conclusions, as other parameters such as ρ_* and ν_*, see Figs. 5.3(c) and (d), also differ in this radial region.

These results clarify further why the H discharge does not exhibit a rotation twice as high as the D discharge, as expected due to the lower ion mass. As already mentioned, torques, see Fig. 5.2(d), and density, see Fig. 5.1(d), play a role, but also the assessed slightly lower intrinsic torque and pinch and the slightly higher diffusion in the outer core in H contribute to why the H rotation is only ≈ 20 % higher than in the D case. This highlights the sensitivity of the rotation profiles to edge transport phenomena, such as the inward convection of an edge-localized intrinsic torque that enhances the overall rotation profiles. It serves as a good demonstration of the crucial role played by edge intrinsic torque in predicting the rotation profiles of future machines.

Altogether, this analysis inferred similar core momentum transport coefficients for the matched discharges. This suggests that there is no fundamental isotope dependence present in the inner plasma core.

5.3 Comparison to Theory

The experimental results are compared to gyrokinetic predictions, which were performed, as explained in Section 2.10, with input profiles averaged over the analyzed time window. All calculations converged to unstable modes. The fastest-growing instabilities were found to be ion temperature gradient (ITG) for most of the radial points. An exception was the innermost radial point for H that was found to exhibit a negative mode frequency in the electron drift direction, indicating the presence of trapped electron modes (TEM).

For both isotopes, the gyrokinetic predictions agree with the experimental analysis mostly within uncertainties, which reflect one standard deviation around the best experimental solution. For the Prandtl numbers, see Figs. 5.7(a) and 5.8(a), the experimentally assessed values are slightly higher compared to the theory prediction. The asymmetric shape of the experimental error bars results from the constraints of a positive Prandtl and pinch number even for smaller radii outside the fitting domain, as mentioned in Section 4.2. For the Prandtl number, in particular, lower solutions would have been accepted in the radial range considered. This is not reflected in the shown error bars, but could be modified in future works.

For the pinch numbers, see Figs. 5.7(b) and 5.8(b), it is possible to theoretically reproduce the differences found experimentally in the inner core, where the pinch

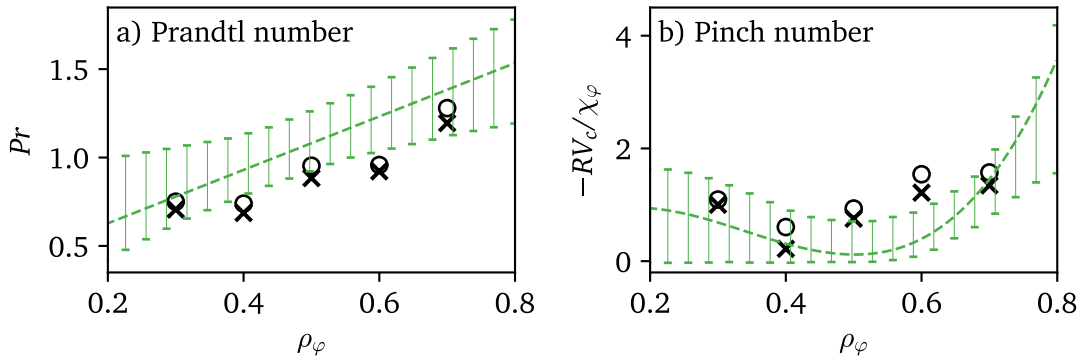

Figure 5.7: Gyrokinetic predictions (black crosses) and experimental modeling (green dashed line) for the D discharge #40076. Furthermore, gyrokinetic calculations from a numerical experiment in which the H mass ratio, instead of the D mass ratio, was used, are shown by circles. This shows the predicted effect of the isotope dependence, which is clearly smaller than the experimental uncertainties.

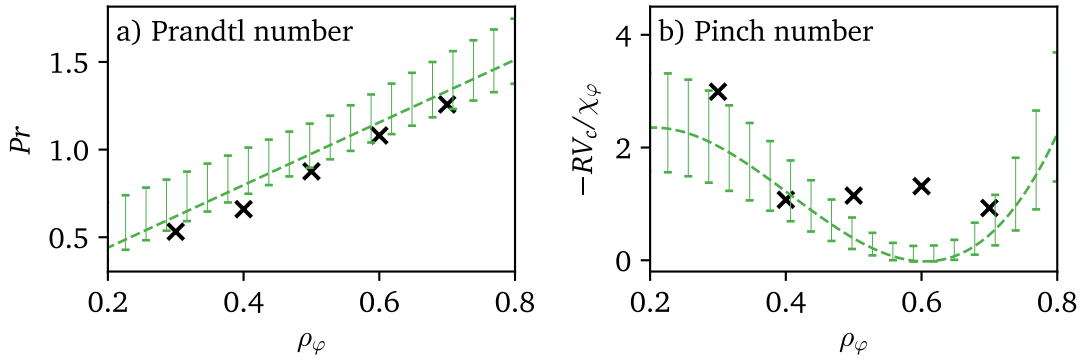

Figure 5.8: Gyrokinetic prediction (black crosses) and experimental modeling (green dashed line) for the H discharge #41550. Error bars on the Prandtl number are asymmetric as smaller Pr would have led to negative Pr for smaller radii due to the linear assumption on the Pr. Hence, lower solutions were rejected in the fitting. However, within the fitting domain, slightly lower solutions would have been an acceptable solution.

number was measured to be higher in H compared with D, see Fig. 5.6(c). The agreement of this detail between theory and experiment is encouraging. The gyrokinetic prediction for the innermost radial position ($\rho_\varphi = 0.3$) of the D discharge is $-RV_c/\chi_\varphi \approx 1$. For the H case, this position is found to be TEM dominated with $-RV_c/\chi_\varphi \approx 3$. To understand these differences, first, the input parameters for the gyrokinetic calculations are compared. They show small differences in the temperature and density gradients for the innermost radial point. While for D, $R/L_{T_e} = 10$ and $R/L_{T_i} = 6.0$, for H $R/L_{T_e} = 8.5$ and $R/L_{T_i} = 4.15$. This is also shown in Figs. 5.3(b) and 5.3(e). Furthermore, for D $R/L_{n_e} = 2.4$, while for H $R/L_{n_e} = 3.2$, see Fig. 5.3(a).

To separate the effect of the input parameters on the gyrokinetic calculations, three numerical experiments were performed. The gyrokinetic calculations for the innermost radial point of the H discharge were repeated, replacing the temperature gradients, the density gradients, and finally both, with the respective values used in the calculation of the D discharge. The first numerical experiment shows that the TEM found in the H case is temperature gradient driven, as after replacing the temperature gradients, the results indicate an ITG mode. This significantly impacts the predicted pinch number: $-RV_c/\chi_\varphi \approx 1.1$, moving it very close to the D result. The second experiment, where only the density gradient was replaced, still predicted a weak TEM with a pinch number of $-RV_c/\chi_\varphi \approx 1.9$. Lastly, in the third experiment, replacing all three gradients, the pinch number was predicted as $-RV_c/\chi_\varphi \approx 0.93$, close to the value from the D case. This demonstrates that the differences between the H and the D discharge observed and predicted result from gradients and are not emerging from isotope effects. A further observation is the stability of the Prandtl number in these numerical experiments, suggesting that the Prandtl number does not strongly depend on the gradients. This will be discussed further in the following Chapters.

An absence of a strong isotope effect can also be motivated: Starting from a simple gyrokinetic picture, collisions are neglected, and the electrons have no mass and instantaneously follow the ions. The adiabatic electrons can react immediately to fluctuations in the parallel electric pressure. The corresponding gyrokinetic equations are normalized to the ion mass. From this normalization, it is concluded, for example, that the diffusivity follows a gyro-Bohm scaling $\chi_{GB} \sim \sqrt{m_i}$ [213]. The mass dependence of the gyro-Bohm scaling is modified when electrons are treated kinetically, as then the electron-to-ion mass is taken into account. Including collisions further breaks the gyro-Bohm scaling, as the electron-to-ion mass ratio influences the calculation of the parallel wave function. The gyro-Bohm dependence is less and less recovered with increased realism of the gyrokinetic formalism.

As collisions and kinetic electrons are included in the calculation of these predictions, it is expected that differences found in the predictions for both isotopes mainly result from differences in the input gradients and that mass effects themselves are weak. To demonstrate this, another numerical experiment was performed. The D calculation was repeated with the H electron-to-ion mass ratio. The corresponding Prandtl and pinch numbers are shown in Fig. 5.7 in circles and tend to be slightly higher than the calculations with the D mass ratio. However, this effect is significantly smaller than the experimental uncertainties and, therefore, would not be resolvable. This effectively demonstrates that no significant isotope dependence in the momentum diffusion or convection from a theoretical perspective is expected.

5.4 Summary

An H discharge, with ion heat fluxes, neutral beam torque, and most dimensionless parameters comparable to the D reference discharge was created, resulting in similar heat transport and gradient lengths. In the absence of a strong isotope effect, the momentum transport coefficients of both discharges are expected to be similar.

This expectation is confirmed by the experiment as the obtained transport coefficients are within uncertainties for both isotopes. This, furthermore, agrees with gyrokinetic predictions, supposing a weak mass dependence, smaller than typical experimental uncertainties. The remaining differences in the assessed transport coefficients are understood in terms of variations in the discharge kinetic profiles.

These results provide confidence that the present theoretical models can be used to provide reliable predictions of the momentum transport in future machines. The good agreement between experimental results and theory predictions is a promising starting point for further investigations in this work.

Chapter 6

Theory Predictions

"Midway upon the journey of this thesis,
I found myself within a forest dark, For the
straightforward pathway had been lost."

— after Dante Alighieri, Inferno

Local, linear gyrokinetic calculations, as introduced in Section 2.10, are capable of predicting the Prandtl and pinch numbers. In this Chapter, their theoretical parameter dependences are investigated. Then, the Stoltzfus-Dueck model is used to predict the edge intrinsic torque.

6.1 Gyrokinetic Parameter Scans

Theoretical approaches have the advantage that parameter dependences can be clearly separated, whereas for experiment-based data, often many variables are cross-correlated. This possibility is now used to investigate the dependences of the Prandtl and pinch numbers.

Gyrokinetic Waltz Standard Case

First, the so-called *GA* or *Waltz* gyrokinetic standard case is studied. This was the starting point for many previous works in the context of momentum transport research [45, 48, 77, 214]. The Waltz standard case uses the gyrokinetic input parameters presented in Tab. 6.1. Further, important assumptions are $T_i = T_e$ (if not varied), $R/L_{n_i} = R/L_{n_e}$, and $R/L_{T_e} = R/L_{T_i}$. The mass ratio of D is used, $m_e/m_D = 0.00027$. To neglect electromagnetic effects, it is set $\beta_{\text{ref}} = 0.0003$. Furthermore, an analytical *s-alpha* equilibrium (as this allows q, s and ϵ to be changed independently) is utilized, and collisions are neglected. Moreover, only one mode with $k_y\rho_i = 0.3\sqrt{2}$ is studied, which usually represents the fastest-growing mode of the instabilities in the plasma core (ITG). Additionally, in Tab. 6.1, the input parameters of an adapted standard case are shown, which is more representative

Quantity	Waltz std. case	Adapted std. case
R/L_n	3	1.2
R/L_T	9	5.7
q	2	2.27
s	1	0.8
ϵ	0.16	0.16

Table 6.1: Input parameters for the standard cases used for isolated parameter scans via gyrokinetic calculations.

of the database of experimental data studied in this work. They mainly differ in the density and temperature gradients.

For the following parameter scans, only a single parameter was varied, and the others were left constant at the values given in Tab. 6.1. The results are shown in Figs. 6.1 and 6.2 for the Waltz standard case as blue crosses and the adapted standard case as orange points. The range of variation was adapted to the values seen in the experimental data studied in this work to gauge the relative influence of the different parameters.

First, the growth rate γ and the mode frequency ω_r are addressed in Fig. 6.1. The growth rate of the instability increases with increasing R/L_T, ϵ, f_{Tr}, R/L_{n_e}, and T_e/T_i. For the shear in Fig. 6.1(i), a stabilizing effect for larger values is visible. Furthermore, there is a clear offset of the growth rates between the Waltz and the adapted standard case due to the differences in R/L_T.

The mode frequency clearly increases with increasing R/L_T, see Fig. 6.1(b), because the ITG mode is driven by the temperature gradient. ω_r decreases with increasing density gradient, see Fig. 6.1(f), probably due to an increased role of TEMs. The density gradient causes the largest variation of the mode frequency and is responsible for most of the offset in the mode frequency seen between the Waltz and the adapted standard case in Figs. 6.1(b), 6.1(d), 6.1(h), and 6.1(j). An exception is Fig. 6.1(f), the mode frequency depending on R/L_{n_e}, where the offset is caused by the difference in R/L_T. For the scan of ϵ and f_{Tr}, Fig. 6.1(d) shows a non-monotonic behavior for the adapted standard case, the origin of this effect is not immediately clear. It is speculated that for higher R/L_T (as in the Waltz case), ITG is the dominant turbulent regime, and the increase of the trapped particle fraction has a weaker effect. This stands in contrast to the situation at lower R/L_T values (as the adapted case), where the increased trapped particle fraction destabilizes TEM, reducing the frequency of the modes. T_e/T_i also shows some influence, see Fig. 6.1(g), with larger growth rates for larger values of the temperature ratio. This is expected from theory, as the temperature ratio destabilizes ITG: for the same initial density fluctuation, the feedback loop via the potential fluctuation is reinforced proportional to T_e/T_i. While ω_r shows no clear trend for the variation of T_e/T_i for the adapted case, it tends to increase for the Waltz case, see Fig. 6.1(h). This is expected, as ITG is destabilized with increasing temperature ratio. For the shear scan, a TEM is observed for low values of the Waltz case and a saturation of ω_r for larger values, see Fig. 6.1(j).

Now, the dependences of the Prandtl and pinch numbers are studied. For the variation of R/L_T, the Waltz and the adapted standard case give very similar results for the Prandtl and pinch numbers. The trend is that the Prandtl number, see

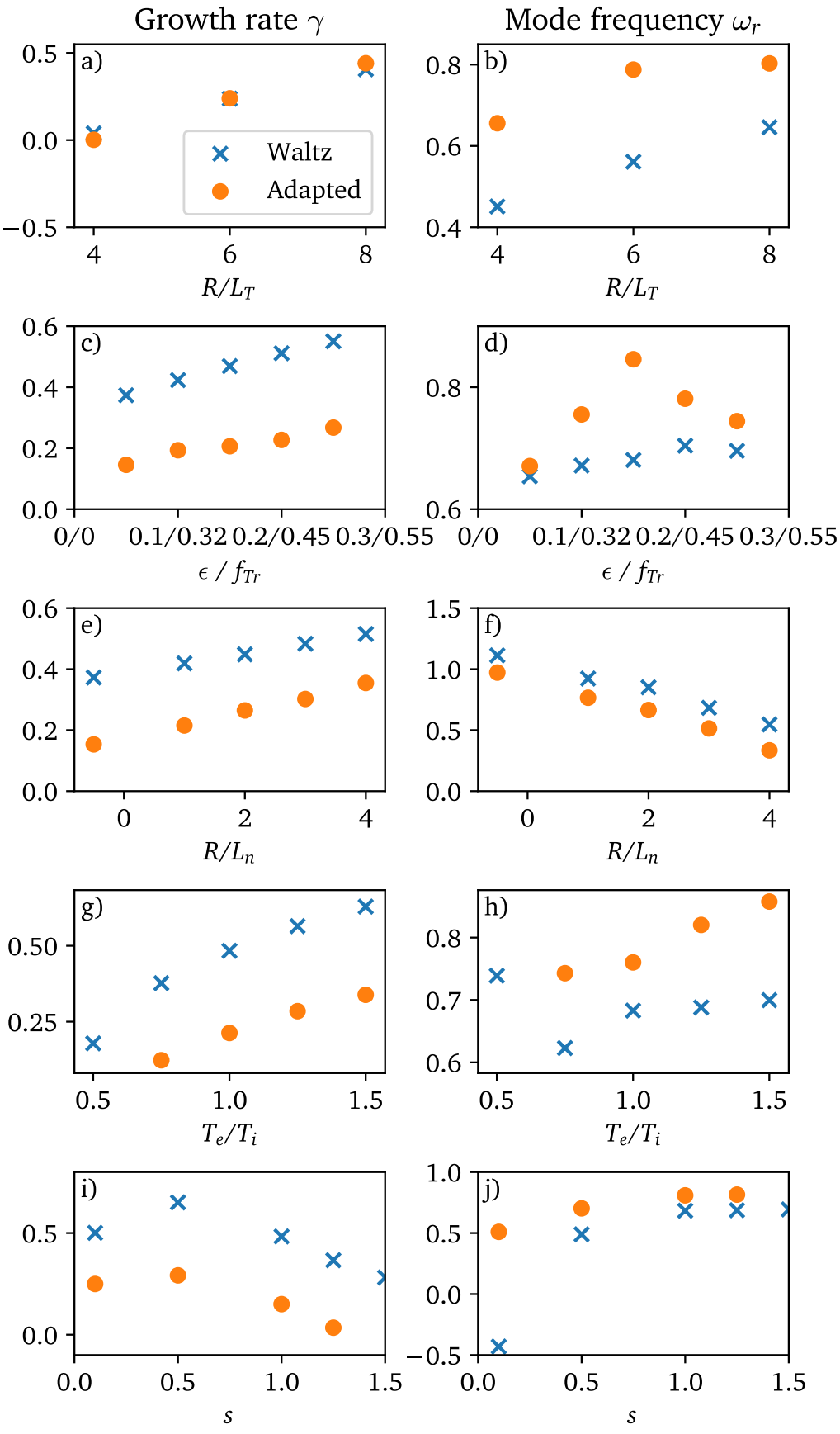

Figure 6.1: Gyrokinetic parameter scans, based on the Waltz standard case and its adaption as shown in Tab. 6.1. Growth rates are in [1/s] and the mode frequencies in $[v_{\text{therm}}/R]$.

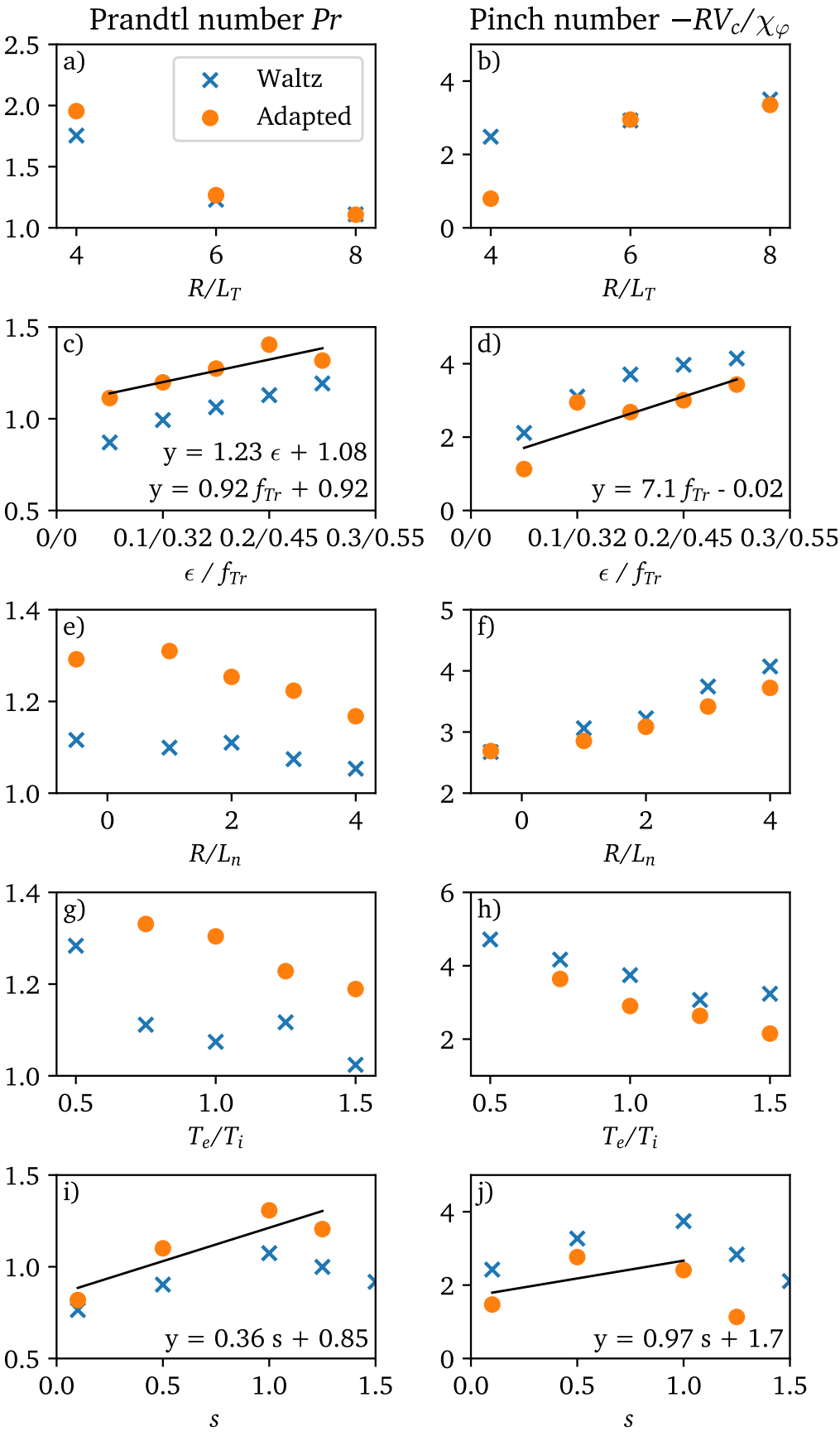

Figure 6.2: Gyrokinetic parameter scans, based on the Waltz standard case and its adaption as shown in Tab. 6.1. Linear fits to the adapted case are shown as black lines.

Fig. 6.2(a), decreases with increasing gradient, i.e., the ion heat diffusivity scales more strongly with R/L_T than the momentum diffusivity. The pinch number, see Panel (b), increases with increasing temperature gradient as the gradients increase the asymmetry of the eigenfunction. The lowest R/L_T point tested for the adapted standard case reveals a rather low pinch number, most likely due to the lower values of R/L_{n_e} in the adapted case compared to the Waltz case. In contrast, the Waltz case, which has a higher pinch number for this temperature gradient value, shows a higher pinch number. As the Waltz case has a stronger temperature gradient than the adapted standard case, the Prandtl numbers in the following are found to be consistently lower, and the pinch numbers are consistently higher for the Waltz case.

Figure 6.4(c) shows a clear increase of the Prandtl number with ϵ, which is a proxy for the trapped particle fraction $f_{\text{Tr}} \approx \sqrt{2\epsilon}$. The same is seen for the pinch number in Panel (d). The linear fit suggests that the pinch would vanish for $f_{\text{Tr}} \to 0$. Please mind the non-linear x-axis for f_{Tr} in the shown plot. This is expected from earlier works on this topic [77] and can be connected to compensation effects through a finite $k_\parallel$ mentioned earlier when discussing the properties of the Coriolis pinch (see Section 2.6).

The Prandtl number is only slightly modified by the scan in the density gradient, as shown in Panel (e). It slightly decreases with increasing gradient. In a linear gyrokinetic calculation, no statements can be made about the absolute values of the diffusive fluxes, therefore, the exact origin of this trend cannot be identified. The corresponding pinch number increases with the density gradient, as expected from earlier works [43].

The temperature ratio does not strongly modify the Prandtl number. There is a slight trend of the Prandtl number to decrease with increasing T_e/T_i, as shown in Panel (g). The pinch number, see Panel (h), decreases with increasing temperature ratio.

Finally, the scaling with the shear is shown. Both the Prandtl, see Panel (i), and the pinch number, see Panel (j), exhibit a non-monotonic behavior, increasing at lower shear and then decreasing at higher. There seems to be a stabilizing effect of the shear on the modes, as seen in Fig. 6.1(i), where the growth rates of the corresponding calculations are shown. However, there is no universal pattern for all calculations, how the growth rate and the mode frequency exactly propagate into the calculation of the Prandtl and pinch number.

To summarize these simplified parameter scans, the Prandtl number is expected to scale most strongly with R/L_T, s, and ϵ. The pinch number seems to vanish for $f_{\text{Tr}} \approx \sqrt{2\epsilon} \to 0$ and shows clear dependences on all studied quantities. High values for s can decrease the Prandtl and the pinch number.

The shown results are in good agreement with earlier work by Peeters *et al.* [48] and Strintzi *et al.* [45] on the parameter dependences of the pinch and Prandtl numbers, respectively. This is expected, as they were based on the same gyrokinetic standard case. As an important addition, these scans show that their results are also valid for the slight variation of the adapted standard case, which is more representative of the database studied later on in this work.

More Realistic Gyrokinetic Calculations

An important limitation of these standard cases is the rather large number of applied simplifications. This concerns, in particular, the analytical equilibrium, neglect of collisions and electromagnetic effects, and the assumptions on equality of temperatures and their gradients. For isolated parameter scans, the use of an analytical equilibrium is necessary, as it is not possible to vary s, q, and ϵ independently in the input parameters with an experimental equilibrium from a numerical reconstruction. It is, however, feasible to test the influence of the temperature gradient, the density gradient, and the temperature ratio.

This was done, including all of the effects which were neglected in the previous scans. To increase the degree of realism, experimental profiles were taken as a basis, namely from the reference discharge #40076, 2.0 – 4.2 s at $\rho_\varphi = 0.7$. This position was chosen due to its strong gradients to balance possible stabilizing effects in the scans. The precise input parameters are shown in Tab. 6.2. A variety of $k_y\rho_i$ were tested, as documented in Section 2.10. For comparability to the simplified scans, in Figs. 6.3 and 6.4, only the values for the same $k_y\rho_i = 0.3\sqrt{2}$ are shown. However, the results of the spectrum-averaged Prandtl and pinch numbers are found to be very close to these scans, indicating that the chosen $k_y\rho_i$ is a representative test case, and the assessed scalings can be compared later to spectrum averaged results.

Looking at growth rates and mode frequencies, see Fig. 6.3, it is found, in agreement with the result of the simplified parameter scan, that increasing R/L_{n_e}, T_e/T_i, and R/L_{T_i} increases the growth rate of the instability. In further agreement with the results of the simplified scan, the mode frequencies decrease with increasing density gradient, see Fig. 6.3b. The increase of ω_r with T_e/T_i is now more pronounced, see Fig. 6.3(d). Similar results are obtained for the temperature gradient, increasing R/L_{T_i} yields increasing ω_r, see Fig. 6.3(f). No separate scan for the electron temperature gradient was performed, as this study focuses on the ITG regime. A comparable work was performed for TEM in [174].

The resulting Prandtl and pinch numbers of the more realistic parameter scans are shown in Fig. 6.4. For the scan of the density gradient, it is concluded that the density gradient influences the Prandtl number, although the absolute change is not large, as shown in Panel (a). This is comparable to the simplified scan, although the scaling was less clear there. In addition, a linear scaling of the pinch number is seen in Fig. 6.4(b), which is significantly stronger than in the simplified scan. Both effects could be connected with stronger TEMs with increasing density gradient. The Prandtl number has a positive correlation with the temperature ratio, as shown in Panel (c), which is opposite to the trend previously observed for the simplified scan. The pinch number correlation also differs from the simplified scan, at least for low T_e/T_i, as shown in Panel (d). The overall variation of the pinch number is smaller for the scan of T_e/T_i compared to the dependence on the density gradient. The disagreement between the Prandtl and pinch numbers assessed from the simplified and more realistic scan stands in contrast to similar trends in growth rates and mode frequencies, as shown in Figs. 6.3(c) and 6.3(d), compared with Figs. 6.1(g) and (h). In general, as shown later in this Chapter, the dependence of the transport coefficients on the logarithmic density gradient can be understood from the fact that momentum transport reflects the deformation of

Quantity	Value
Z_{eff}	1.26
m_e/m_p	0.00027
n_e [10^{19} m^{-3}]	0.6
R/L_{T_i}	7.42
R/L_{T_e}	6.9
R/L_{n_e}	0.19
T_e/T_i	0.94
ϵ	0.22
s	1.54
q	3.04

Table 6.2: Experimental input parameters for the gyrokinetic calculation of the reference discharge #40076, 2.0 – 4.2 s at $\rho_\varphi = 0.7$.

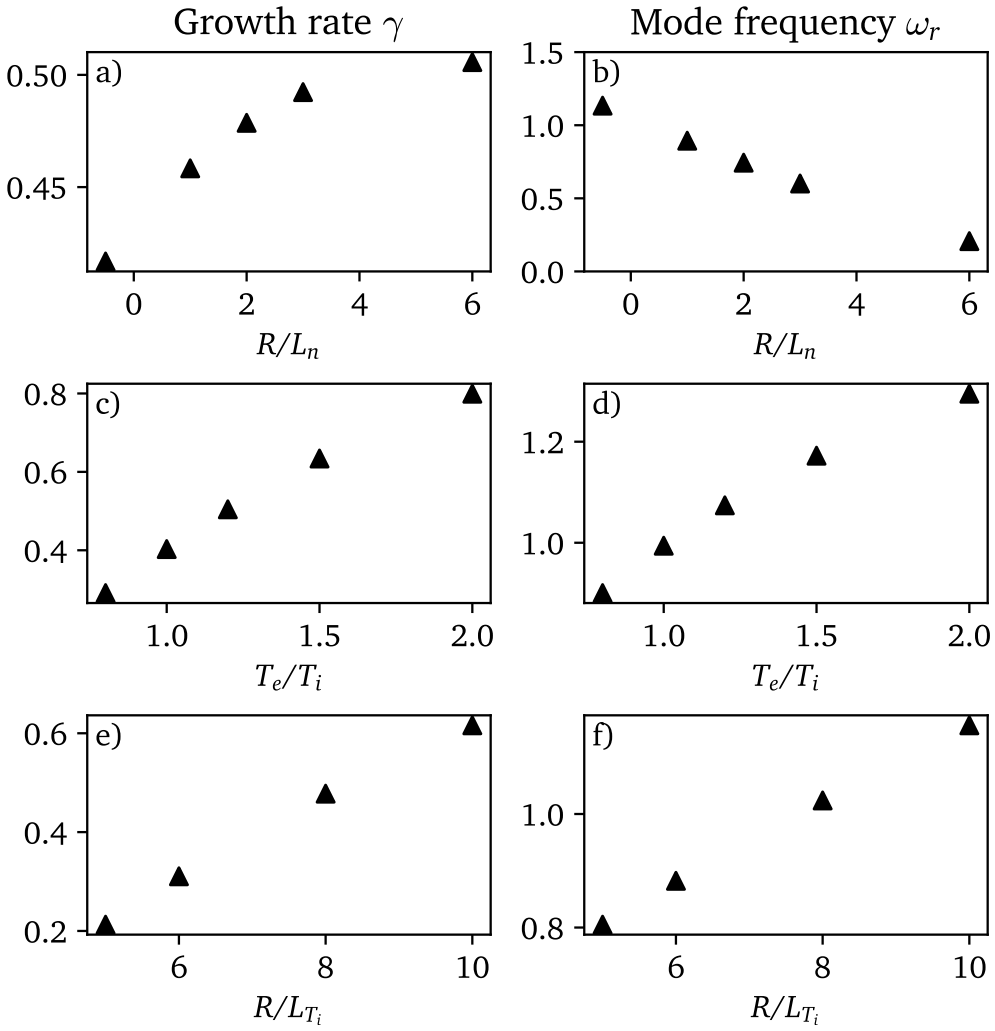

Figure 6.3: Gyrokinetic parameter scans based on experimental values (see Tab. 6.2) with more physical effects included. Growth rates are in [1/s] and the mode frequencies in $[v_{\text{therm}}/R]$.

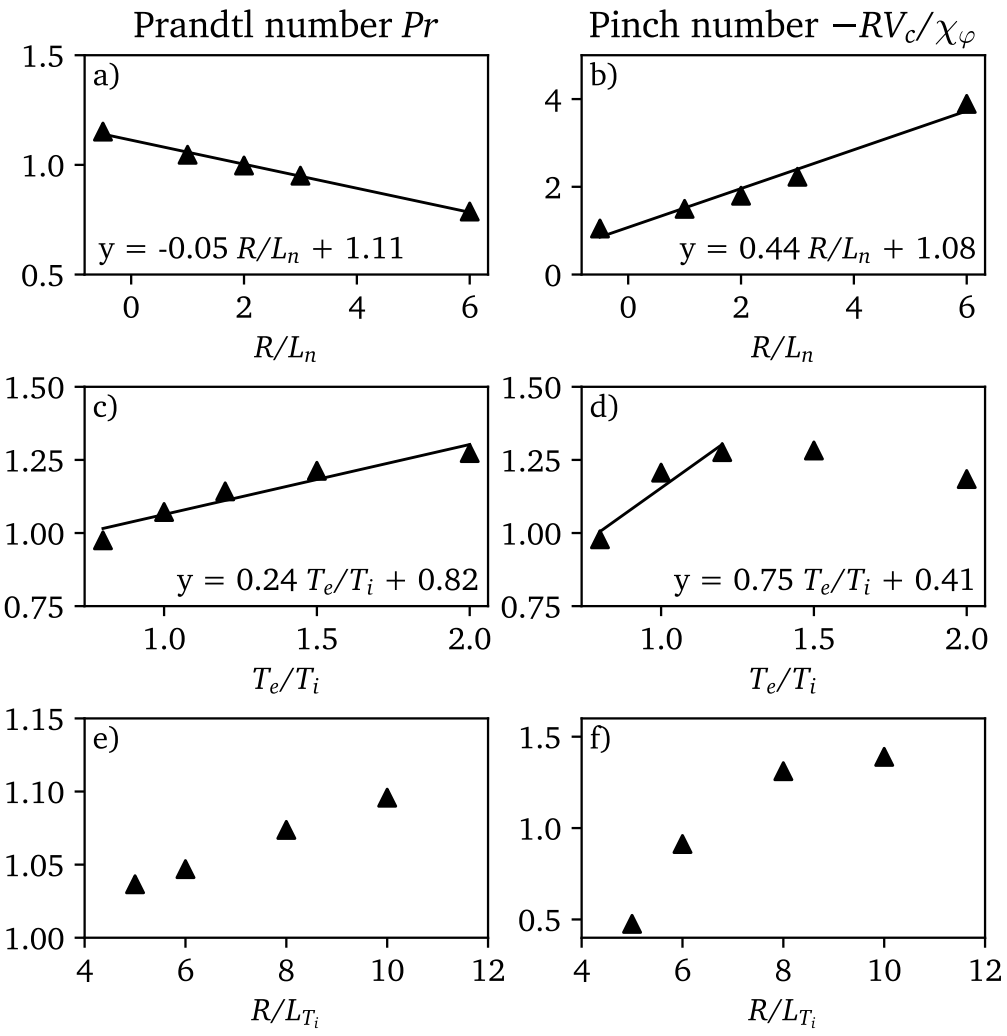

Figure 6.4: Gyrokinetic parameter scans based on experimental values (see Tab. 6.2) with more physical effects included. Growth rates are in [1/s] and the mode frequencies in $[v_{\text{therm}}/R]$.

the perturbed distribution function in the parallel velocity and the eigenfunction along the field line. As shown in Panel (e), no significant scaling of the Prandtl number with the ion temperature gradient is found. The pinch number, see Panel (f), increases slightly, as already seen before in the simplified scans.

In the next Section, a database of gyrokinetic simulations of real experiments will be compared to the scans presented in this Section. For these comparisons, realistic scans of R/L_{T_i}, R/L_{n_e}, and T_e/T_i are used, while the simplified ones for ϵ, f_{Tr}, and s were kept. Together, these parameter scans brought the following insights:

- a vanishing pinch number for $f_{\text{Tr}} \to 0$,
- strong scaling of the pinch number with R/L_{n_e},
- weak scaling of the pinch number with R/L_{T_i} and T_e/T_i,
- strong scaling of the Prandtl number with ϵ, f_{Tr} and T_e/T_i,
- weak scaling of the Prandtl number with $-R/L_{n_e}$, and
- a non-monotonic dependence of the Prandtl and pinch numbers on s.

6.2 Gyrokinetic Database Approach

In this Section, parameter dependences of the gyrokinetically predicted Prandtl and pinch numbers will be assessed via regression of scaling laws to a database of gyrokinetic calculations relying on realistic, experimental input data, including more realistic physics effects like, for example, finite β and finite collisionality which were neglected in the Waltz standard case. A variety of $k_y\rho_i$ was tested, precisely as documented in Sec. 2.10, and spectrum averaged values for Prandtl and pinch numbers are calculated.

Using a database of experimental data to create the gyrokinetic database has advantages and disadvantages. On the upside, it is possible to trust the consistency of the used data to be physical and that the obtained predictions are at a realistic point in parameter space. On the downside, cross-correlations of the gyrokinetic input parameters can be very large, up to the point where it is not feasible to separate the real, physical dependences causing a certain observed effect.

In the following, experimental input from a database of 29 discharges is used for gyrokinetic calculations. The list of discharges is given in Appendix B.1. For every discharge, gyrokinetic calculations were performed for $\rho_\varphi = 0.3$, 0.4, 0.5, 0.6, 0.7, as described in Section 2.10. Table 6.3 shows the maxima and minima of parameter space spanned by these gyrokinetic predictions. The median of this database corresponds to the values used for the adapted standard case studied in the Section before.

The calculation of the Pearson correlation coefficient between these input parameters allows the quantification of cross-correlations. The cross-correlation matrix is shown in Fig. 6.5. A first cluster of correlation exists between s, q, ϵ, and f_{Tr}. The experimental collisionality ν_* is also correlated with this first cluster to some degree. Furthermore, a second cluster is found, anti-correlated to the first one, with R/L_{n_e} and β_{ref}, with strong cross-correlation between themselves. The normalized gradients R/L_{T_e} and R/L_{T_i} and the temperature ratio T_e/T_i are more independent, but they also have cross-correlations with other quantities. These cross-correlations bring the risk of increased uncertainties in the regression of scaling laws due to possible trade-off effects.

Quantity	min	max	median
q	1.111	4.504	2.289
s	0.080	2.461	0.902
ϵ	0.096	0.237	0.165
T_e/T_i	0.858	2.731	1.112
R/L_{T_e}	-0.758	12.639	8.074
R/L_{T_i}	1.856	8.511	5.650
R/L_{n_e}	-0.426	6.546	1.244
β_{ref}	0.001	0.015	0.004

Table 6.3: Parameter space spanned by the database of experimental input data for gyrokinetic predictions.

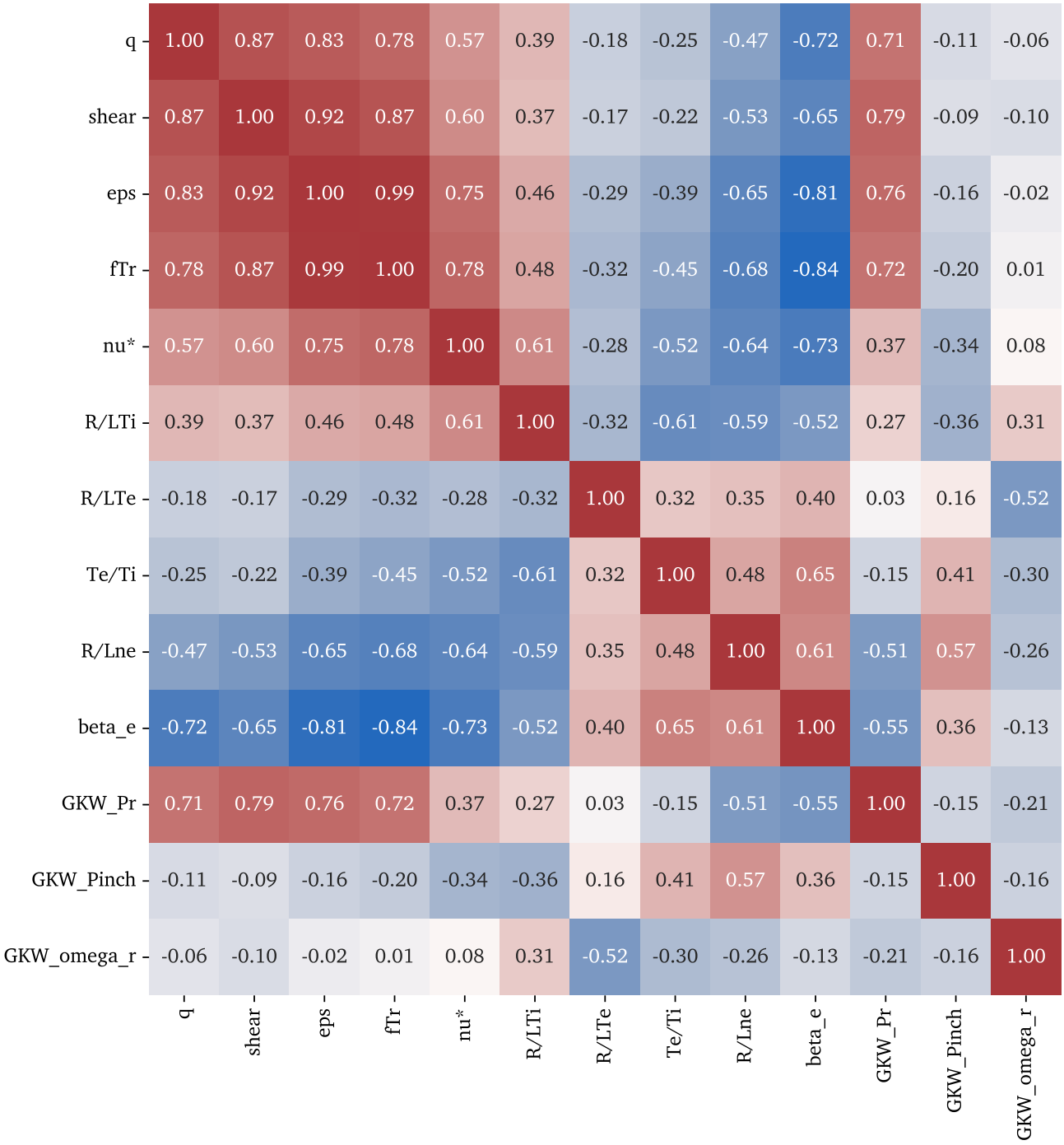

Figure 6.5: Pearson correlation coefficients for the input to the database of gyrokinetic calculations. Red colors correspond to 1 (suggesting strong correlation), and blue to -1 (suggesting strong anti-correlation).

Prandtl Number

Referring back to the isolated parameter scans in Sec. 6.1, dependences of Pr in this database on ϵ (f_{Tr}), s, T_e/T_i, and $-R/L_{n_e}$ are expected. The cross-correlation matrix in Fig. 6.5 shows clearly that the strongest correlations of Pr are with s, ϵ, f_{Tr} and anti-correlation with R/L_{n_e}. Indeed, using all of them in the regression of a linear scaling law yields good agreement and a root mean square error between gyrokinetic prediction and regression of $\texttt{RMSE} = 17.4$ %. The regressed scaling law reads as

$$Pr_{\text{reg}} = 1.265\,\epsilon + 0.244\,s + 0.083\,T_e/T_i - 0.033\,R/L_{n_e} + 0.503. \tag{6.1}$$

The statistical relevance is calculated by multiplying the regression coefficient with the standard deviation of the scaling parameter. This value can then be divided by the standard deviation of the regressed quantity to estimate the extent to which the variation in the scaling parameter contributes to the observed changes in the regressed quantity [215]. The variation in Eq. 6.1 is caused to 20 % by ϵ, to 55 % by s, and only to a minor degree by T_e/T_i and R/L_{n_e}.

In Tab. 6.4, the scaling coefficients (third column, "Db. reg. I") are compared to the results obtained from the linear fits to the scans (see Figs. 6.2 and 6.4). The trends of the isolated parameter scans are qualitatively recovered. Due to the non-monotonic dependences to the shear, only the linear increase of the Prandtl number with shear was used for comparison, see Fig. 6.2(i). It is possible to include, in future work, also a component s^2 or $(T_e/T_i)^2$, as done in Strintzi *et al.* [45], to compensate for the non-monotonic behavior.

An included uncertainty calculation of the scaling coefficients has also been done. This relies on mapping out possible solutions up to a variation of 1.5 of the underlying χ^2 cost function, corresponding to one standard deviation for a Gaussian error distribution. The uncertainties are shown in Tab. 6.4 next to the scaling values in the third column. They are much larger than the absolute values of the fitted coefficients due to the strong cross-correlation of the used fitting parameters. Obviously, fewer parameters need to be selected for the regression to lower the uncertainties.

Therefore, in the following, single order parameters to regress the Prandtl number are tested. The calculation of correlation coefficients suggests a strong correlation of the predicted Prandtl numbers with s, ϵ, or f_{Tr}. In a linear regression with s, the following scaling law is found:

$$Pr_{reg} \approx (0.34 \pm 0.18)\,s + (0.66 \pm 0.22). \tag{6.2}$$

The resulting regression has a root mean squared error of $\texttt{RMSE} \approx 17.8$ %. This scaling agrees quantitatively with the increase of Pr with s seen in the isolated parameter scans, see Fig. 6.2(i). In those scans, however, a decrease of Pr for $s > 1$ was observed (around $\rho_\varphi = 0.5$ – 0.6 for most of the studied discharges herein), which is not observed when looking at the predictions of entire radial profiles included in the gyrokinetic database. For these simulations, Pr always increases monotonically with radius. An example of such a radial Pr profile can be seen in Fig. 5.7. This makes the exact physics mechanisms behind the scaling with the shear questionable. The author speculates that the shear, by cross-correlations, is a surrogate for other quantities in the regression and that the good regression, with

Quantity	Isolated scan	Db. reg. I Eq. 6.1	Db. reg. II Eq. 6.2	Db. reg. III 6.4
ϵ	1.23	1 ± 8		4.8 ± 2.9
s	0.36	0.2 ± 0.4	0.34 ± 0.18	
T_e/T_i	0.24	0.1 ± 0.4		
R/L_{n_e}	-0.05	-0.03 ± 0.1		
RMSE		17.7 %	17.8 %	18.8 %

Table 6.4: Comparison of coefficients for a linear scaling law for Pr, assessed from the isolated parameter scans in Section 6.1 and based on the database regression.

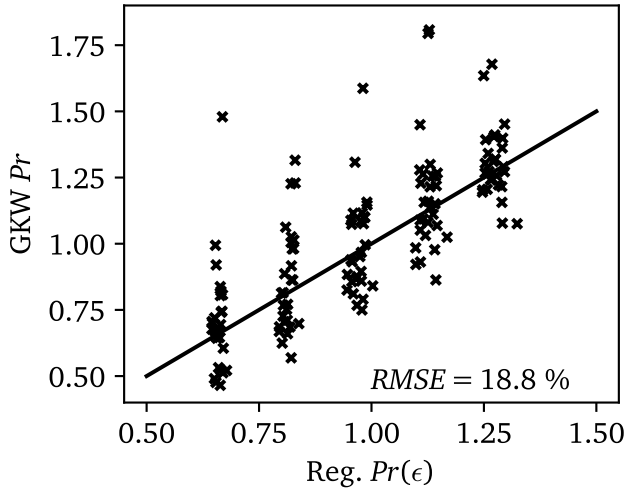

Figure 6.6: Regressed Prandtl numbers from Eq. 6.4, a scaling with ϵ versus the GKW prediction. Unity is shown as a black line.

respect to the observations from the isolated parameter scans, does not represent a real physical relationship.

A much clearer picture is obtained by regressing the Pr with f_{Tr} or ϵ. They also show a correlation with Pr in the database and in the isolated parameter scans. Most importantly, Pr monotonically increased with them, see Fig. 6.2(c). A scaling law regression yields

$$Pr_{\text{reg}} = (3.4 \pm 2.3)\, f_{\text{Tr}} - (0.8 \pm 1.2) \tag{6.3}$$

and

$$Pr_{\text{reg}} = (4.8 \pm 2.9)\, \epsilon + (0.2 \pm 0.5) \tag{6.4}$$

with RMSE $\approx$ 18.8 %. The scaling with ϵ is shown in Fig. 6.6. The first formula implicates that Pr would become negative for low f_{Tr}, which is unphysical and results from the non-linear relation of f_{Tr} to ϵ, which is, in fact, the input to GKW. A linear fit cannot account for this, leading to the negative offset.

Both scaling laws, Eq. 6.3 and 6.4, can be compared to the isolated parameter scans, see Figs. 6.2(c) and 6.2(i), and in Tab. 6.4 in the fourth and fifth columns ("Db. reg. II/III"). The slope of the ϵ scaling is much steeper in the database regression. This observation could serve as an indicator that the scaling laws, in fact, reflect a combination of multiple effects from cross-correlations.

It was found that there is no clear dependence of Pr on the dominant mode frequency. The same holds for the growth rates.

In summary, the results of the isolated parameter scans were quantitatively reproduced using the database approach. The strongest empirical ordering parameters for Pr were found to be s, ϵ, or f_{Tr}. It is shown that ϵ is the most physical and robust quantity for a scaling of Pr.

These results agree with earlier works, which were, however, performed with simplified gyrokinetic calculations. Peeters *et al.* [59, Fig. 5] found only very weak dependences of Pr on R/L_n, s, q, and R/L_T via linear gyrokinetic calculations. Also Strintzi *et al.* [45, Fig. 2] found the inverse local aspect ratio ϵ to be the strongest scaling parameter of the Prandtl number, but there were also dependences on the temperature gradients identified, which are not seen in this work.

Pinch Number

From the isolated scans, a strong scaling of the pinch number with R/L_{n_e} and possible scalings with R/L_{T_i}, s, and T_e/T_i is expected. The cross-correlation matrix of the database suggests weaker correlation with T_e/T_i ($p = 0.41$) and R/L_{n_e} ($p = 0.57$) and very weak anti-correlation with R/L_{T_i} ($p = -0.36$), see Fig. 6.5.

All these quantities can be used together in a scaling law, but it is noticed that the influence of the R/L_{T_i} is very small. Likely, cross-correlations render the use of R/L_{T_i} unnecessary. This contribution can be neglected without loss of quality:

$$-RV_c/\chi_{\varphi_{\mathrm{reg}}} = 0.34\,T_e/T_i + 0.4\,R/L_{n_e} + 0.32\,s - 0.12. \tag{6.5}$$

The variation is caused to 65 % by R/L_{n_e}, s and T_e/T_i play a subordinated role. This suggests that R/L_{n_e} is the strongest order parameter. The quality of this regression is by far worse, compared to those obtained for the Prandtl number, the $\mathtt{RMSE} \approx 46.7$ %. Again, the uncertainties are rather large, as shown in Tab. 6.5 in the third column ("Db. reg. I"). The large uncertainties also result from the overall worse quality of the regression, as a variation of 1.5 in the χ^2 cost function is mapped out around the best solution to calculate the uncertainties.

In Tab. 6.5, the coefficients are compared to those obtained in the isolated parameter scans. The scaling coefficients show similar values, but uncertainties are large. For the fit to the parameter scan of T_e/T_i and s, see Figs. 6.4(d) and 6.2(j), only the linear increase was used, as most of the input data lies in this parameter range. Of course, for both effects, in future work, a quadratic term can be included in the scaling to reflect the non-monotonic behavior.

To decrease the uncertainties, components are systematically removed. Doing so for the shear dependence results in

$$-RV_c/\chi_{\varphi_{\mathrm{reg}}} = (0.6 \pm 0.5)\,T_e/T_i + (0.3 \pm 0.4)\,R/L_{n_e}, \tag{6.6}$$

which gives $\mathtt{RMSE} \approx 49.6$ %. The result of the regression agrees with the isolated parameter scans within uncertainties (see Tab. 6.5, fourth column, "Db. reg. II").

Quantity	Isolated scan	Db. reg. I Eq. 6.5	Db. reg. II Eq. 6.6	Db. reg. III Eq. 6.7	Db. reg. IV Eq. 6.8
T_e/T_i	0.75	0.34 ± 1.2	0.6 ± 0.5		
R/L_{n_e}	0.44	0.40 ± 0.4	0.3 ± 0.4	0.50 ± 0.2	0.34 ± 0.7
s	0.97	0.32 ± 0.7		0.44 ± 0.4	
RMSE		46.7 %	49.6 %	47.6 %	49.6 %

Table 6.5: Comparison of coefficients for a linear scaling law for the pinch number, assessed from the isolated parameter scans in Section 6.1 (second column) and based on the database regression. For the isolated scans, fits to the more realistic calculations were chosen where possible, while for s, the simplified scan was used. Without significant loss of quality, the scaling can be reduced to one parameter.

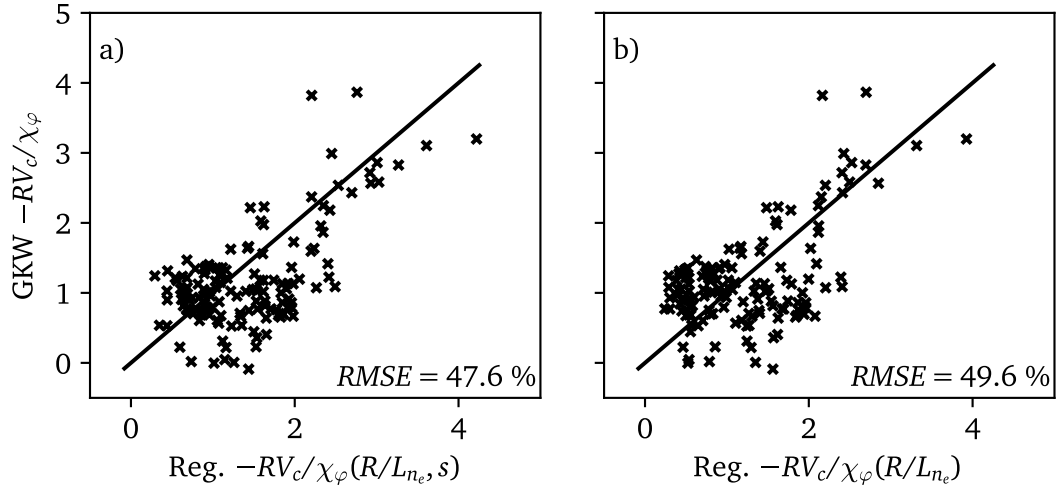

Figure 6.7: Regressed pinch numbers versus the GKW prediction. In Panel (a), the regression from Eq. 6.7 is shown, consisting of a scaling with R/L_{n_e} and s. In Panel (b), from Eq. 6.8, a linear scaling with R/L_{n_e}. Unity is shown as a black line.

Alternatively, it is possible to use only s and R/L_{n_e}:

$$-RV_c/\chi_{\varphi\text{reg}} = (0.44 \pm 0.4)\, s + (0.5 \pm 0.2)\, R/L_{n_e}, \tag{6.7}$$

with a better RMSE $\approx$ 47.6 %. A comparison of the regression with the gyrokinetic value is shown in Fig. 6.7(a). The variation of the regressed quantity is caused to a larger degree by R/L_{n_e}, consistent with results obtained earlier in this Section. Again, the influence of the shear is lower in the database regression compared to the isolated parameter scans, probably due to the non-monotonic dependence (see Tab. 6.5, fourth column, "Db. reg. III").

In order to find the best single order parameter, different scalings were tested. When using only one scaling parameter (together with a constant), clearly, a scaling with R/L_{n_e} is the best and results in

$$-RV_c/\chi_{\varphi\text{reg}} = (0.34 \pm 0.3)\, R/L_{n_e} + (0.7 \pm 0.6), \tag{6.8}$$

with an RMSE $=$ 49.6 %, which is not that much worse than the regression with s before (cp. Eq. 6.7), as now a constant is used. This constant was neglected in the regression before because it caused large uncertainties. The regression using

R/L_{n_e} shows good agreement, within uncertainties, with the linear fit obtained from the isolated parameter scan, $y = 0.44\,x + 1.04$, as shown in Fig. 6.4(b). This agreement is consistent and stable across all regressions conducted. The comparison between the regression and gyrokinetic values is illustrated in Fig. 6.7(b).

For the assessed scaling laws, it is feasible to enforce that the pinch vanishes for $f_{\text{Tr}} \to 0$ via a scaling ansatz

$$-RV_c/\chi_{\varphi_{\text{reg}}} = f_{\text{Tr}} \cdot (...).$$

This gives:

$$-RV_c/\chi_{\varphi_{\text{reg}}} = f_{\text{Tr}} \cdot (1.501\,T_e/T_i + 0.708\,R/L_{n_e})$$
$$-RV_c/\chi_{\varphi_{\text{reg}}} = f_{\text{Tr}} \cdot (0.834\,s + 1.302\,R/L_{n_e})$$
$$-RV_c/\chi_{\varphi_{\text{reg}}} = f_{\text{Tr}} \cdot (0.92\,R/L_{n_e} + 1.55)$$

with RMSE values of $\approx$ 50 %. These values are slightly worse than those obtained without the boundary condition on the pinch to vanish for $f_{\text{Tr}} \to 0$. The main effect of this additional scaling is that the other coefficients increase to balance the $f_{\text{Tr}} < 1$. Better agreement with the scalings from the isolated parameter scans is not observed. From the regression of the database, there is no clear argument for a fundamental scaling with f_{Tr}, or it is hidden.

It is found that there is no clear trend in how the pinch number relates to the frequency of the fastest-growing mode.

These results suggest that the pinch number mainly depends on the density gradient and the shear. The density gradient emerges as the only parameter that can serve as a robust ordering parameter, with a consistently stable scaling factor of $\approx$ 0.3 – 0.5 observed across all tested scenarios. Furthermore, the results of the database regression are in qualitative agreement with the isolated parameter scans.

In comparison with earlier works, the dominant role of the density gradient is reproduced. Peeters *et al.* [43] studied the parameter dependence of the pinch number via a gyrofluid code and found R/L_{n_e} to be the strongest scaling parameter. They also identified the non-monotonic influence of s and observed only a small influence of R/L_{T_i}. In their work with a simple, analytical fluid model, they derived $-RV_c/\chi_\varphi = 4 + R/L_{n_e}$ for the dependence of the pinch number on the density gradient. It is much stronger than assessed in this work as their approach neglects the parallel dynamics. Studies of the gyrokinetic Waltz standard case by Peeter *et al.* [48, Fig. 7] later showed that this scaling is reduced in agreement with the calculations presented here.

In a study conducted by Weisen et al. [197], the dependences of the gyrokinetically assessed pinch number were investigated using an experimental database of JET data. In that publication, a linear scaling law is regressed to the pinch number, see Eq. 4 there. Remarkably, the coefficient obtained for the influence of the density gradient on the pinch number aligns quantitatively with the coefficients derived from the isolated parameter scans and the database regression performed in this study. By employing the same combination of parameters (R/L_{n_e}, f_{Tr}, q, R/L_{T_e}, and s) as identified in the JET database, a regression of the current

database yielded comparable results with an approximate RMSE of 46.8%, similar to the best results shown in Table 6.5. This indicates that the JET parameters exhibit consistency with the gyrokinetic database constructed for AUG. Despite employing many more regression parameters, they do not significantly improve upon the quality of the regression.

6.3 Interpretation of the Gyrokinetic Results

Discussing the physical mechanisms driving these results entails an examination of the deformation of the eigenfunction. To illustrate this approach and to interpret the most important results shown in this Chapter, a comparison of the eigenfunctions of the electric potentials for the scans in R/L_{n_e}, ϵ and s is provided in the following.

The dependence of the pinch on the density gradient arises as a direct consequence of the coupling of density, temperature, and parallel velocity perturbation, see Eqs. 12, 13, and 14 derived in the fluid picture in [78]. It even manifests when neglecting any contribution to the flux coming from the development of a finite parallel wavenumber, as demonstrated with an analytical fluid model in [43]. In Fig. 6.8, three potential eigenfunctions of the aforementioned isolated parameter scan are shown. In Panel (b), the deformation of the potential function is shown, especially for the convective term and in the presence of a strong density gradient (dash-dotted green line). To quantify the effect of the deformation, it is feasible to calculate an eigenfunction weighted-averaged value for $k_\parallel$. From the general definition of the parallel wavenumber, an averaged value over the eigenfunction of the complex electrostatic potential perturbation along the field line is computed with the following formula:

$$\bar{k}_\parallel = \frac{1}{qR}\,\mathrm{Im}\left[\int \overline{\phi}\,\frac{\mathrm{d}\phi}{\mathrm{d}\theta}\,\mathrm{d}\theta\right] / \left[\int \overline{\phi}\,\mathrm{d}\theta\right], \tag{6.9}$$

with ϕ the complex solution of the potential eigenfunction and its complex conjugate $\overline{\phi}$. For a completely symmetric eigenfunction around $\theta = 0$ (low-field-side midplane), this formula provides a zero averaged parallel wavenumber, as expected.

The values for this quantity for the scan of the density gradient are shown in Fig. 6.9(a) (for the calculation of the diffusive term) and Fig. 6.9(b) (for the convective term). The scans for the Waltz standard case (blue crosses), the adapted standard case (orange circles), and the scans with more realistic gyrokinetic calculations (black triangles) are shown. All three cases agree in their trends: for the calculation of the diffusive fluxes, see Panel (a), the value of $\bar{k}_\parallel$ depends only weakly on R/L_{n_e}, as observed for Pr in the isolated parameter scans, see Figs. 6.2(e) and 6.4(a).

For the calculation of the convective fluxes, Panel (b), the value of $\bar{k}_\parallel$ decreases with increasing R/L_{n_e}. In [77, 78], the coupled set of equations for the temperature, density, and parallel velocity perturbation is derived in an analytical fluid model. In these works, the contribution from a finite parallel wavenumber is in-

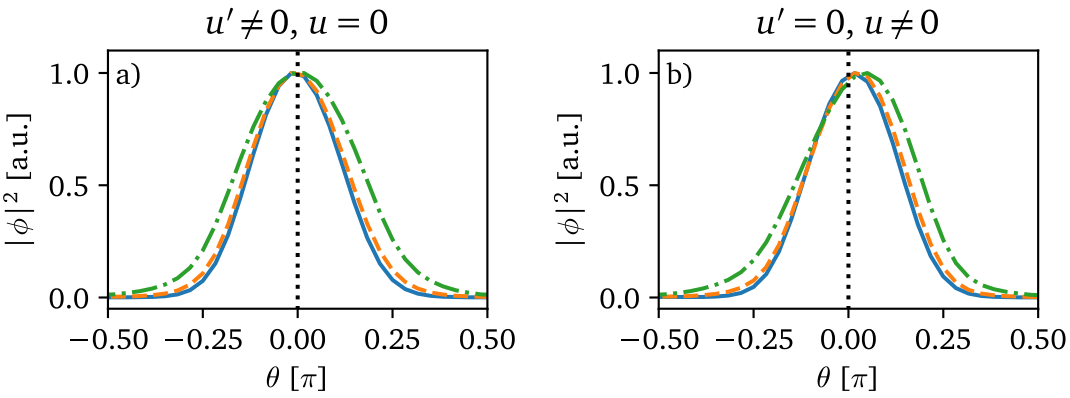

Figure 6.8: Deformation of the potential eigenfunction for different density gradients. Solid blue line for $R/L_{n_e} = 1$, dashed orange line for $R/L_{n_e} = 3$, and dash-dotted green line for $R/L_{n_e} = 6$. In Panel (a), the result from the calculation of the diffusive fluxes is shown. In Panel (b), the corresponding calculation for the convective fluxes is shown. Clearly, a strong effect of a large density gradient on the eigenfunction is visible for the calculation of the convective term. On the x-axis, the poloidal angle θ along the field line is used in multiples of π.

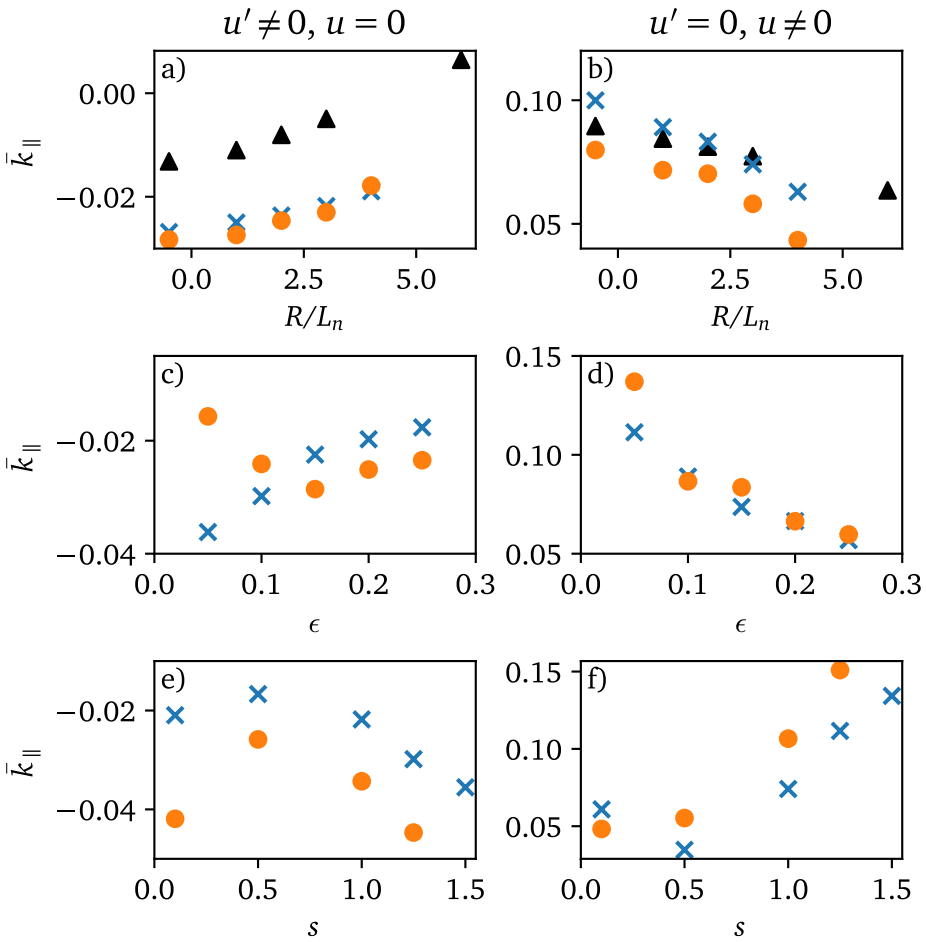

Figure 6.9: Averaged $\bar{k}_\parallel$ (see Eq. 6.9) for the gyrokinetic calculations of the diffusive terms (left column) and convective terms (right column) for the parameter scans of the density gradient, inverse aspect ratio, and shear. Blue crosses mark the Waltz standard case, orange circles for the adapted standard case, and the black triangle is from the scan with more realistic gyrokinetic simulations, as discussed before in Section 6.1.

cluded. In the coupled equation for the density perturbation,

$$\hat{\omega}^* \hat{n} + ... + \frac{2A}{ZA_i} \left[2\hat{u} - \frac{1}{2} \frac{ZA_i}{A} \hat{k}_\parallel \right] \hat{v}_\parallel = \left[\frac{R}{L_n} - 2 \right] \frac{\hat{\phi} T_e}{T_i}, \tag{6.10}$$

the second term on the l.h.s is the Coriolis term with the normalized toroidal velocity $\hat{u}$, the normalized parallel wave vector $\hat{k}_\parallel = k_\parallel v_{\text{th,i}}/\omega_{\text{D}}$ (with the drift frequency ω_{D}), the normalized, perturbed, parallel velocity $\hat{v}_\parallel$, the mode frequency $\hat{\omega}^*$, the normalized density $\hat{n}$, and the perturbed vector potential A. The second term in the brackets on the left-hand side is the additional contribution from the parallel wave vector, modifying the Coriolis pinch. Excluding the parallel dynamics and, thus, this additional term leads to an overestimation of the pinch [79]. The Coriolis pinch is weakened by positive values of $\bar{k}_\parallel$. Such positive values are found in the gyrokinetic calculations, see, e.g., Fig. 6.9(b). From the same figure, it is found that the larger the density gradient, the smaller the correction from the parallel dynamics, as values are decreasing. Together, these observations of the density gradient scan agree with earlier results [43, 45, 48].

The interpretation of the scans in ϵ for the pinch is more complicated, as the deformation of the eigenfunction is introduced entirely via the parallel dynamics. Again, a look at the left-hand side of Eq. 6.10 gives insights. For a certain deformation of the potential eigenfunction, $\hat{k}_\parallel$ can take values such that the terms in the brackets vanish, resulting in zero pinch. This compensation effect from the large fraction of passing particles in the limit of low trapped particles fraction ($\epsilon \to 0$) near the axis was discussed for the pinch in [77] and was recovered in gyrokinetic calculations in this work. It is shown in Panel 6.9(d), how $\bar{k}_\parallel$, and consequently the second term in the bracket on the left-hand side, increases for smaller ϵ for both the Waltz and the adapted standard case, resulting in the compensation. This behavior was also confirmed in the isolated parameter scans, see Fig. 6.2(d).

Furthermore, in this work, a strong scaling of the Prandtl number with ϵ was found, see Fig. 6.2(c) and in the database regression, Fig. 6.6. This can be explained along similar lines as the compensation effect of the pinch number. As seen from [78, Eq. 13], the coupled equation for the parallel velocity perturbation is:

$$\hat{\omega}^* \hat{T} + ... = \left[\hat{u}' - 2\hat{u} + \frac{1}{2} \frac{ZA_i}{A} \hat{k}_\parallel \right] \frac{\hat{\phi} T_e}{T_i}. \tag{6.11}$$

Here, it is speculated that the diffusive flux (via $\hat{u}'$, the gradient of the normalized toroidal velocity) could be affected by such a compensation effect for negative values of $\hat{k}_\parallel$. However, it will not vanish for the same values as the pinch. Therefore, an identical behavior for $\epsilon \to 0$ is not expected. As seen from Fig. 6.9(c), there is the tendency of more negative $\bar{k}_\parallel$ for smaller ϵ. The lowest point of the parameter scan with the adapted standard case, however, is an outlier. Such low values of $\epsilon < 0.1$, however, are not relevant for this study, which focuses for the gyrokinetic database on $\rho_\varphi > 0.3$, corresponding to $\epsilon > 0.1$. Altogether, it is speculated that an effect similar to the compensation effect of the pinch due to the passing particles also affects the Prandtl number via the diffusive momentum flux and influences its scaling with ϵ. As a caveat, the variation of $\bar{k}_\parallel$ with ϵ is weaker than for the calculation of the convective fluxes, see Panel (d). This suggests that the compensation effect on the Prandtl number is weaker than for the pinch.

It is also possible to interpret the observed scaling of the pinch and Prandtl number with the shear in this formalism. The changed $\bar{k}_{\|}$ enters Eq. 6.10 and 6.11 and modifies the resulting momentum flux. It is shown in Figs. 6.9(e) and 6.9(f) that the impact of shear on $\bar{k}_{\|}$ is much more pronounced in the calculations for the convective fluxes than for the diffusive fluxes.

For the calculation of the convective fluxes, see Fig. 6.9(f), it is understood that for low shear values, the values for $\bar{k}_{\|}$ remain constant, for values above $s > 0.5$, they grow. This agrees with the trend seen for the parameter scans, Fig. 6.2(j), where the pinch number was found to decrease for larger shear values. It is observed that larger $k_{\|}$ values yield lower pinch number values. This agrees with the trend observed for the ϵ scan as discussed above along the lines of Eq. 6.10. For the diffusive fluxes, a non-monotonic behavior is recovered, as already observed for the scaling of the Pr with s, see Fig. 6.2(i), but its absolute variation is much smaller than for the values from the calculation of the diffusive fluxes.

It is concluded from the analysis of the eigenfunction deformation and the resulting parallel wavenumbers that the observed scaling of the pinch with the density gradient and the shear can be interpreted consistently with previous results. Furthermore, it is speculated that the fundamental dependence of Pr on ϵ is explained by a similar compensation effect as for the pinch.

6.4 Edge Intrinsic Torque Predictions

The theoretical prediction of the residual stress and the resulting intrinsic torque would require the knowledge of second-order derivatives of the kinetic profiles and global, non-linear gyrokinetic calculations. The experimental uncertainties on the second-order derivatives are usually too large to give trustworthy results, and global gyrokinetic calculations are computationally too expensive for a database approach.

While these approaches have been applied to model the confined region, the analytical Stoltzfus-Dueck model, as presented in Section 2.7, focuses on the edge region of the confined plasma out to the scrape-off layer and results in a boundary condition for the intrinsic torque between the core and the edge. For the discharges studied for the gyrokinetic database, see Appendix B.1, this model was used to predict the pedestal top intrinsic torque, which will be compared to the experimental intrinsic torque results in the outer core at $\rho_\varphi \approx 0.7 - 0.8$ in the next Chapter. The pedestal top is approximately at $\rho_\varphi = 0.88$ in these discharges, and the decay length of the turbulence was calculated via L_{T_e} at $\rho_\varphi \approx 0.955$. In Fig. 6.10, the corresponding profiles are shown. The mentioned radial positions are shown as vertical, dotted lines. The following predictions and scalings were found to be stable under variation of both positions.

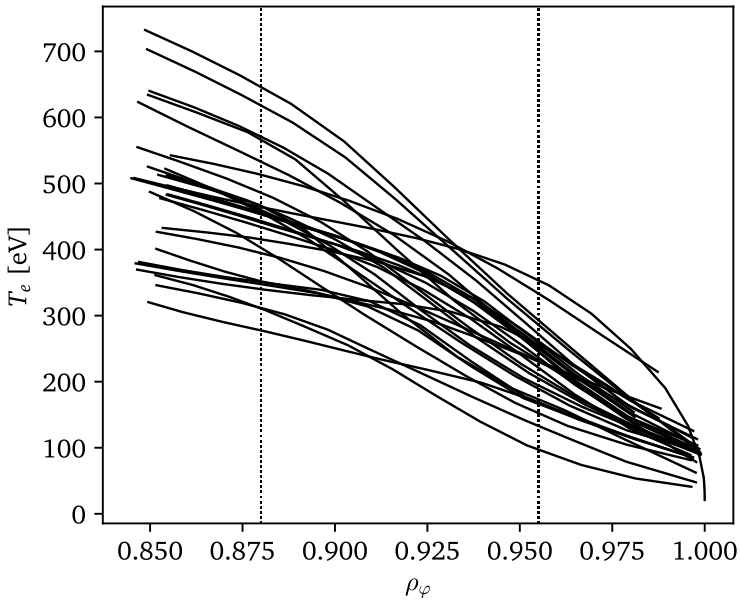

Figure 6.10: Electron temperature pedestal profiles of the analyzed discharges for the calculation of the Stoltzfus-Dueck intrinsic torque. The vertical lines show the assumed pedestal top position ($\rho_\varphi \approx 0.88$, left line) and the location of steepest gradients ($\rho_\varphi \approx 0.955$, right line). This is a good assumption for most of the cases. Discharges are listed in Appendix B.1.

Quantity	min	max
$Q_{i,\text{top}}$ [MW]	1.6	5.0
$1/L_{T_e,\text{ped}}$ [1/m]	28	65
$f_{\text{Tr,top}}$	0.64	0.67
q_{top}	3.2	4.6
$\bar{R}_X$	-0.70	-0.62
B_φ [T]	-2.5	-2.48

Table 6.6: Variation of the input parameters for the calculation of the Stoltzfus-Dueck intrinsic torque for the discharges listed in Appendix B.1.

Equation 2.27 shows that the intrinsic torque predicted by the Stoltzfus-Dueck model scales with f_{Tr}, the trapped particle fraction, $\bar{R}_X$, the normalized major radius of the X-point, q, the effective safety factor, B_φ, the toroidal magnetic field, Q_i, the pedestal ion heat flux, and L_ϕ, the turbulence decay length, which, in the Stoltzfus-Dueck model, is approximated by L_{T_e}. Within the database studied, the variations in f_{Tr}, q, and B_φ are small, see Tab. 6.6. Therefore, it is expected that the variation in Q_i and L_{T_e} will have the strongest impact on the predicted intrinsic torque.

The calculated $\tau_{\text{int,SD}}$ varies between 0 and 6 Nm at the pedestal top, which is quite sizable. In the experiment, this effect should be visible, as it is of the order of the steady-state value of NBI torque, which was found to vary between 2.2 and 7.9 Nm at the pedestal top within this data set. The results will be discussed in the next Chapter, together with the experimental results.

6.5 Summary

In earlier works, isolated parameter scans via gyrokinetic calculations were the basis of scalings of the Prandtl [45] and pinch numbers [43, 48]. In this Chapter, it is found that these results, relying on gyrokinetic standard cases, do not always hold when more realistic gyrokinetic calculations are used in the simulations, e.g., with collisions, the use of realistic equilibria, and with fewer assumptions on the equality of temperatures and their gradients. Scans connected to the kinetic profiles are affected by such simplifications and should be performed under more realistic conditions. These isolated parameter scans indicate that trends in growth rates and mode frequencies do not directly translate to trends in Prandtl and pinch numbers, but they suggest a large number of possible parameter dependences.

The assessed dependences are compared with database regressions and correlation matrices. This database consists of gyrokinetic calculations with experimental inputs. The main parameter dependences are found to be quantitatively consistent with the isolated scans. The Prandtl number exhibits its most pronounced dependence on dynamics related to trapped particles. The most physical and robust ordering parameter is identified as the inverse aspect ratio ϵ. An examination of the decrease in diffusive momentum flux with a smaller trapped particle fraction is carried out by analyzing the deformation of the potential eigenfunction. A compensational effect of the passing particles is observed that balances the parallel mode structure. This is similar to what was previously found for the pinch.

The best ordering parameter for the pinch number is the logarithmic density gradient R/L_{n_e}. A detailed analysis of the deformation of the potential eigenfunction explains this dependence in line with previous work on the Coriolis pinch together with the parallel dynamics.

An important limitation of these results is the correlation of the parameters in the studied database and the limits of the parameter space covered. In general, care has to be taken when interpreting simple scaling laws regressed to databases, which are purely empirical correlations. The main results given here, however, are also consistent with the dedicated parameter scans, which reveal the underlying physics behavior.

Lastly, a prediction for the pedestal top intrinsic torque via the Stoltzfus-Dueck model is calculated. Within the studied experimental database, it is expected that among the various input parameters of that model, most variation results from Q_i at the pedestal top and L_{T_e} in the steepest region of the pedestal. The ordering character of these quantities can be tested on the experimental results.

Chapter 7

Experimental Results

"In theory, there is no difference between theory and practice – in practice there is."

— Yogi Berra

This Chapter presents the experimental analysis results of a small database of discharges, and the parameter dependences of the transport coefficients are compared to theoretical predictions. An outlook on a reduced momentum transport model for the core is given. These results are then discussed in the context of previous research. Some of the analysis results of this Chapter have already been published in [166].

7.1 Analyzed Data Set

The database of NBI modulation experiments performed at AUG encompasses around 80 discharges. Many of them, however, were done in very special conditions, which are challenging for the analysis. Discharges that are part of a ρ_* study for an inter-machine comparison with JET have, for example, large sawteeth inversion radii and suffer from modes. Other discharges meant to extend the performed isotope comparison to helium have insufficient CXRS signal. Experiments with ECRH and ICRH modulation are challenging due to a large perturbation of the heat transport. Aside from these special discharges, the database has 50 phases from 29 discharges. 18 of these phases were performed with modulation frequencies of 7 and 10 Hz, which is not optimal for the analysis, as explained in Section 4.1. Furthermore, 9 phases with $P_{ECRH} > 1$ MW were excluded to focus this study mainly on ITG-dominated discharges. These discharges are left for future work.

The analysis of discharges with flat rotation phase profiles often results in large error bars on the modeled transport coefficients. Another effect of such flat phase profiles is that fitting without an intrinsic torque is already sufficient to model the data, as the phase profile cannot give a meaningful constraint to the parameters. In such cases, no unique solution from the analysis can be obtained. This affected

Quantity	min	max
ν_*	0.1	0.9
q	1.5	4.1
s	0.15	2.4
ϵ	0.1	0.24
f_{Tr}	0.44	0.63
T_e/T_i	0.96	1.24
R/L_{T_e}	2.26	12.0
R/L_{T_i}	3.71	10.04
R/L_{n_e}	-0.18	3.83
β_e	0.001	0.007
ρ_*	0.003	0.008
n_e [10^{19} m^{-3}]	4.03	7.29
Q_e/Q_i	0.16	1.1

Table 7.1: Parameter space spanned by the experimental data points

6 phases in the database, which were excluded. From the remaining 17 phases, the modeling of 9 phases did not reproduce the experimental data properly, potentially indicating that the present model is not flexible enough to sufficiently represent the transport in these plasmas, making these cases interesting targets for future study. A possible reason could be MHD effects, steep gradients, or transport barriers.

This leaves this study with only 8 phases to be compared, as listed in Tab. B.2 in the Appendix, and the strong reduction shows the major challenges this kind of analysis faces. Such a limited data set does not allow for a detailed assessment of scaling laws. Rather, main order parameters can be compared to the theoretical predictions. As diffusive and convective coefficients are local quantities, their values at multiple radial positions can be sampled, e.g., ρ_φ =[0.3,0.4,0.5,0.6,0.7]. This results in 40 data points, which span the parameter space listed in Tab. 7.1. The variation in parameter space is similar to the one investigated in the previous Chapter, with the exception that the values for R/L_{n_e}, T_e/T_i and β_e do not reach as high values due to the limitation $P_{ECRH} < 1$ MW. Aside from this restriction, the experimental findings should be comparable to the theoretical predictions and should agree if there are no fundamental deviations.

7.2 Modeling Results

In Fig. 7.1, the experimental (brown) and modeled (green) steady-state (column a), amplitude (column b), and phase profiles (column c) of the toroidal rotation are shown for the 8 plasmas studied in this Chapter. The transport coefficients are shown in column (d)-(g) with the gyrokinetic predictions as black points.

The first three columns show that the modeling reproduces the experimental data with high accuracy and within uncertainties. For the steady-state profiles, variation in the peak values is observed, being the largest for discharges (1), (3), and (6). As shown in Tab. B.2, for (1), the high rotation can be attributed to the high NBI power and, consequently, the torque applied. For (3), a relatively low ex-

perimental diffusivity is observed, contributing to the peaked steady-state profile. For (6), the NBI power is remarkably low, but the intrinsic torque is positive over the entire analysis domain, contributing to the peaked profiles. Interestingly, the steady-state rotation profiles have different curvatures: most are slightly concave. Slightly convex shapes are observed for discharges (3) and (6), in which no ECRH power was applied. This indicates a relation between heating mixtures and transport mechanisms. The observation of hollow or even negative rotation profiles concomitant with strong ECRH is known from earlier works and will be discussed later.

For the amplitude profiles in column (b), the already discussed behavior of higher amplitudes for lower modulation frequencies is observed, e.g., for discharge (8) with $f_{\text{mod}} = 2$ Hz. Together with the low modulation frequencies come flat phase profiles, see column (c) for discharge (8). Generally, the same behavior holds for discharge (6) with $f_{\text{mod}} = 3$ Hz. Although also discharge (7) is performed with $f_{\text{mod}} = 3$ Hz, the amplitude stays rather small, and the phase shift between the inner and outer edge of the fitting domain is of the order of the other discharges performed with $f_{\text{mod}} = 5$ Hz. There seems to be different transport present in this discharge, indicated by the flat experimental Prandtl number profile.

For the Prandtl numbers (column d), it is seen that nearly all of the discharges reveal an increasing Prandtl number with increasing radius. Except for 2 discharges, (3) and (7), the gyrokinetic predictions reproduce the experimental analysis over the whole measured radius. For those discharges, prediction and measurement recover a factor of two variation between the inner and outer core. The resulting diffusion profiles are shown in column (e). All of them monotonically increase with radius. The lowest values are obtained for (3), which has the lowest overall heating power of ≈ 2.75 MW and, consequently, smallest values for the power balance $\chi_i \sim Q_i$.

Remarkably, the gyrokinetic predictions follow the assessed pinch numbers (column f) closely. There are distinctive variations, e.g., for the inner core in discharge (1) with a peaked profile or discharge (6) with a very flat pinch number.

In column (g), the intrinsic torque profiles are shown. They are flat in the inner core and steepen towards the outer core, being co-current directed there. While for some discharges, e.g. (5), the profiles are very peaked towards the outer core, for other discharges, e.g. (3) and (8), the profiles stay rather flat or even tend to roll over. However, the error bars are often very large for the outermost radial position.

It becomes evident that the formation of the rotation profiles is the result of a highly entangled interaction of the externally applied torque and the transport mechanisms.

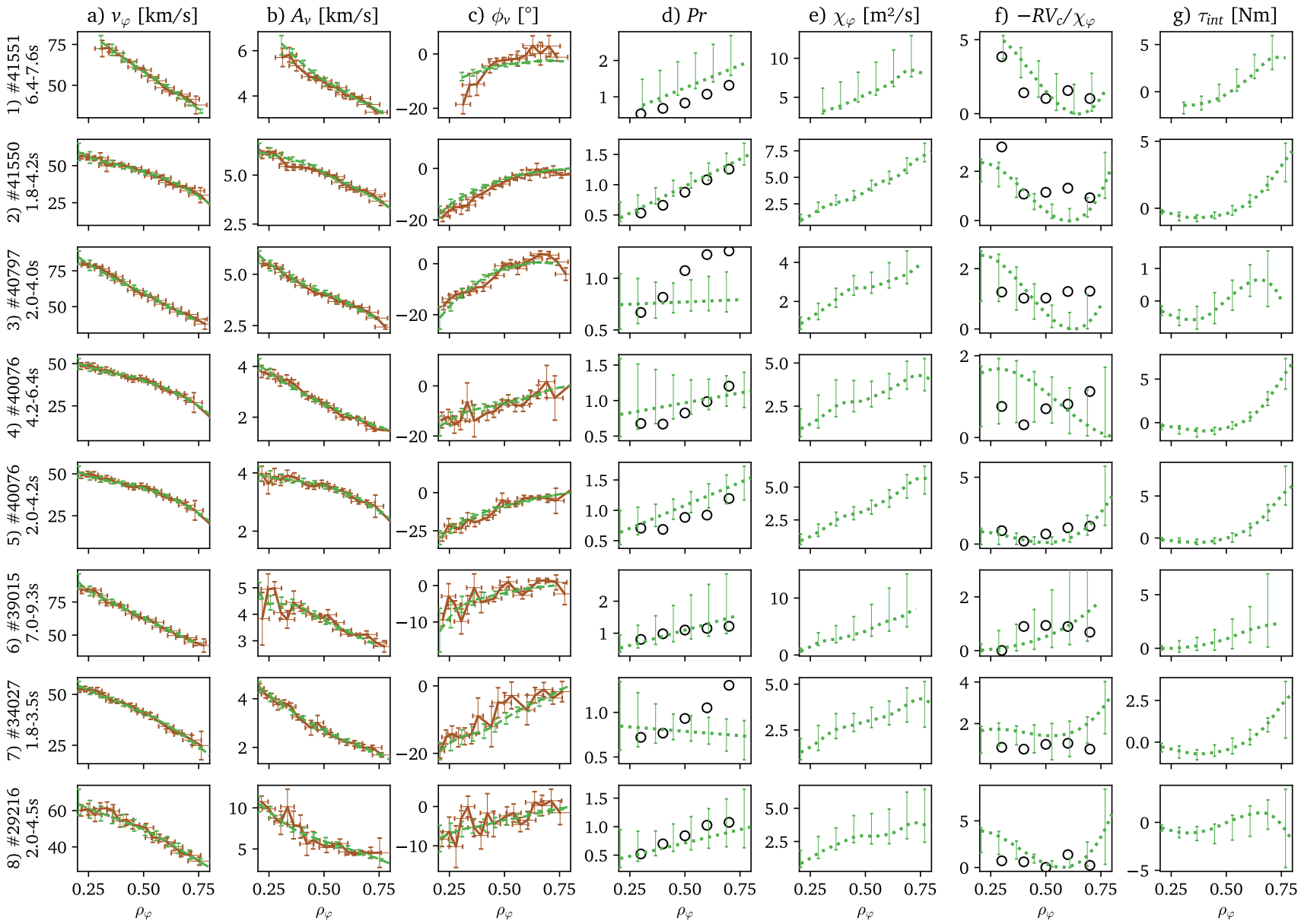

Figure 7.1: Experimental (brown) and modeled (green) steady-state, amplitude, and phase profiles in the left three columns. In the four columns on the right, the experimentally assessed transport coefficients (green) are plotted versus the gyrokinetic prediction (black).

7.3 Parameter Scalings

The following Section discusses the experimental parameter dependences of the various transport mechanisms and compares them to the theoretical results.

Prandtl Number

Theoretical predictions in the previous Chapter suggested the local inverse aspect ratio (as a proxy for the trapped particle fraction) as the Prandtl number's strongest ordering parameter. Also, in the experimental analysis, the inverse aspect ratio is found to be the best order parameter. Linear fitting leads to

$$Pr_{reg} = (3.4 \pm 2.9)\,\epsilon + (0.4 \pm 0.5) \tag{7.1}$$

with $\texttt{RMSE} = 20$ % and $\chi^2_{\text{red}} \approx 0.85$. The uncertainty given on the scaling parameters corresponds to a variation of 1.5 in the use cost function value. No weighting with the experimental uncertainties was used in this fitting, as the asymmetry of the error bars could not be reflected properly. In Fig. 7.2, the experimentally assessed Prandtl numbers are plotted over the inverse aspect ratio. The experimental fit from Eq. 7.1 is shown with a green dashed line. For clarity, uncertainties are not plotted for all data points. Instead, a representative one corresponding to the average of the data set is shown. The linear fits are within uncertainties for most points. Remarkably, the scaling law assessed from the gyrokinetic database (see Eq. 6.4), which is shown as a solid black line, agrees in its trend and size with the experimental results. It was impossible to significantly reduce the scatter by including additional quantities, e.g., q, q_{95}, or T_e/T_i in the scaling. The lowest points mainly result from discharges (3) and (7), with a flat Prandtl number profile measured. As indicated by the shown error bar and the χ^2_{red}, including further regression parameters would, most likely, result in over-fitting.

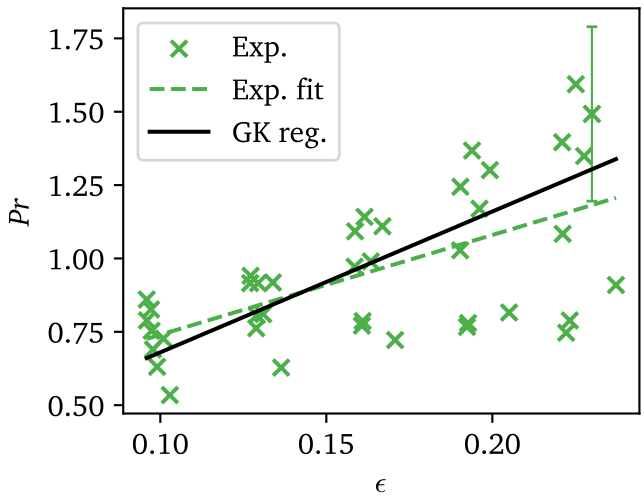

Figure 7.2: Experimentally assessed Prandtl numbers plotted over the inverse aspect ratio. The fit of the experimental data (see Eq. 7.1) is shown as a dashed green line, the regression obtained from the gyrokinetic database (see Eq. 6.4) as a black solid line. The error bars shown correspond to the average error bar of the data set.

Similar results are obtained using f_{Tr} as an order parameter, as ϵ is a proxy for the trapped particle fraction. In this experimental analysis, R/L_{T_i}, ν_*, and s also order the data, but with higher RMSE values. From the insights of the previous Chapter, it is assumed that this ordering is rather caused by experimental cross-correlations, as these quantities are mostly monotonically increasing over the radius.

Momentum Diffusion

As the momentum diffusion scales with the Prandtl number and the ion heat diffusivity, parameter dependences of both can be recovered for the momentum diffusivity. Strongest correlations exist between the momentum diffusion and radially, monotonically increasing quantities such as ϵ or f_{Tr}. This is expected due to the dependence on the Prandtl number. Also, the normalized collisionality ν_* is highly correlated with the diffusion coefficient, most likely due to its monotonically increasing shape over radius. It cannot order the results locally. Also, a correlation with the quantities from the ion power balance is observed, such as Q_i, ∇T_i, or R/L_{T_i}, as expected. The logarithmic density gradient plays a special role, as it is a key quantity for the growth rates of the ITG modes. No correlation was found on the heating powers, Q_e/Q_i or the temperature ratio T_e/T_i, but, especially for the latter parameter, the variation is small within the data set.

Plotting the assessed diffusion coefficients over the growth rates from the gyrokinetic calculations is more insightful. As shown in Fig. 7.3, the experimentally assessed momentum diffusion scales with the growth rate of the fastest-growing mode and, thus, its instability. These observations align with the basic understanding of turbulent transport, see Eq. 2.11, which connects the growth rate with the turbulent diffusion coefficient. It is, however, remarkable that a comparison of the theoretically predicted turbulence properties and the experimentally assessed diffusion values is that clear. No clear correlation with the mode frequencies is present.

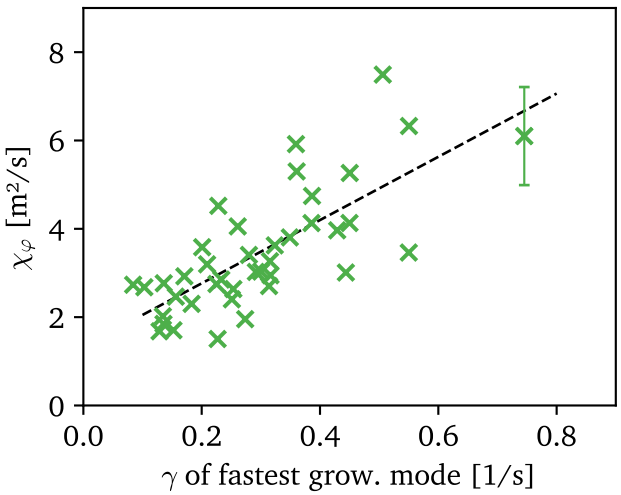

Figure 7.3: Experimentally assessed momentum diffusion plotted over the growth rate. Fit to guide the eye. The error bars shown correspond to the average error bar of the data set.

Pinch Number

The theoretical predictions in the previous Chapter suggested many possible parameter dependences of the pinch number. The most prominent were T_e/T_i, R/L_{n_e}, and s. No correlation of the pinch number on T_e/T_i was found in the experimental data, possibly due to the limited variation. Rather, the logarithmic density gradient was observed to be the best single order parameter in agreement with the theoretical prediction. The largest variation of the density gradient within the studied data set is found for $\rho_\varphi = 0.35$. For this radial position, the predicted and measured pinch numbers are plotted versus R/L_{n_e} in Fig. 7.4. It is shown that the pinch number increases with the density gradient, which, in fact, can order the pinch number locally. Linear fits are plotted as a dashed line (experimental data) and a solid line (gyrokinetic prediction) to guide the eye. Both trends agree qualitatively. Including further parameters does not significantly reduce the scatter, i.e., no ordering was observed, e.g., by q, q_{95}, s, I_p, or T_e/T_i. This is also shown in the figure, in which different symbols were used for $I_p = 0.6$ MA (triangles) and $I_p = 0.8$ MA (squares), and no grouping is found.

Motivated by this scaling, the available data set was used to regress simple scaling laws. The best regression of the experimental pinch number with R/L_{n_e} is given by

$$-RV_c/\chi_{\varphi\text{reg}} = (0.6 \pm 0.46)\, R/L_{n_e} + (0.4 \pm 0.8), \tag{7.2}$$

with RMSE $\approx$ 69 %. The assessed dependence is stronger in the experiment, compared with the theory, $(0.34 \pm 0.3)\, R/L_{n_e} + (0.7 \pm 0.6)$, but the overall trend is recovered. The regression can be improved when replacing the constant by s,

$$-RV_c/\chi_{\varphi\text{reg}} = (0.7 \pm 0.3)\, R/L_{n_e} + (0.44 \pm 0.5)\, s, \tag{7.3}$$

with RMSE $\approx$ 63 %. This RMSE is worse than the one from ordering the gyrokinetically predicted pinch numbers. As $\chi^2_{\text{red}} \approx 1.2$, the regression is reasonable with respect to the uncertainties, and including a larger number of regression parameters is not advised to avoid over-fitting.

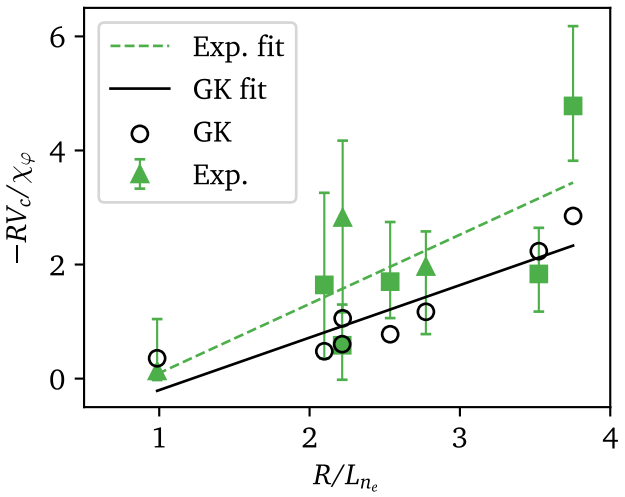

Figure 7.4: Experimental and theoretical pinch number values plotted versus the logarithmic density gradient at $\rho_\varphi = 0.35$. Linear, unweighted fits are included to guide the eye. The upward triangles depict discharges with $I_p = 0.6$ MA, the squares those with $I_p = 0.8$ MA.

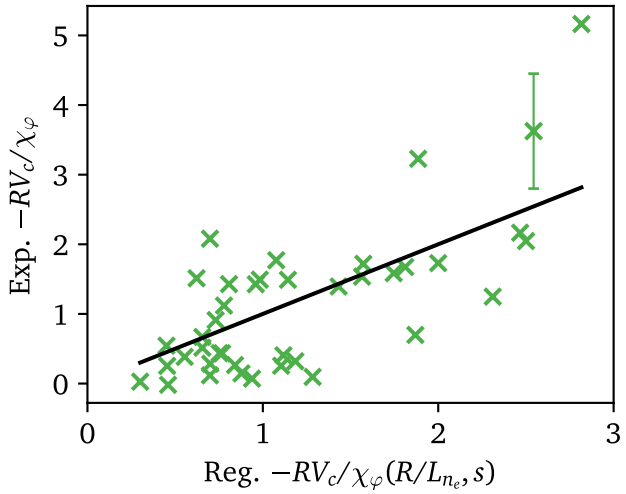

Figure 7.5: Experimentally assessed Pinch numbers plotted over the regression with R/L_{n_e} and s. The solid line shows unity. The error bars shown correspond to the average error bar of the data set.

The variation of the regressed value is caused by 78 % by the variation in the density gradient. Figure 7.5 shows the experimental values plotted against the regressed ones from Eq. 7.3. The solid black line shows unity.

The values of this scaling law agree within uncertainties with the theoretical predictions, $(0.5 \pm 0.2)\, R/L_{n_e} + (0.44 \pm 0.4)\, s$, but the experimental dependence on the density gradients is slightly stronger. Within the studied data set, no stronger order parameters were found. The beneficial effect of including the shear does not contradict the previous observation that the local ordering at $\rho_\varphi = 0.35$ cannot be improved with including q or q_{95}, as q and s peak towards the edge and, thus, play a minor role at smaller radii. Furthermore, at this radial position, there is only a very small variation among the q and s values within the studied data set.

Core Intrinsic Torque

For the local intrinsic torque in the inner plasma core ($\rho_\varphi = 0.3$ – 0.6), deriving parameter dependences is complicated, as the overall variation of the values is small. The values assessed are between -0.5 to 1.0 Nm at mid-radius and are of the size of the NBI torque, which is between 1.2 to 1.9 Nm at mid-radius for the studied discharges.

Due to the simple shape prescribed for the residual stress, its value mainly increases between $\rho_\varphi = 0.3$ – 0.6 for all analyzed cases. This results in strong correlations, e.g., with s, ν_*, or p_i, which also have a monotonic shape in this radial region. None of these quantities can clearly order the assessed intrinsic torque locally, and neither can R/L_{p_i}. In contrast, it is interesting that the case with co-current intrinsic torque in the core, #39015, has the lowest R/L_{n_e} values at that location. In contrast, #41551, which has the steepest core density gradient, reveals the strongest counter-current intrinsic torque. This is shown in Fig. 7.6, with the density gradient in Panel (a) and the intrinsic torque values in Panel (b).

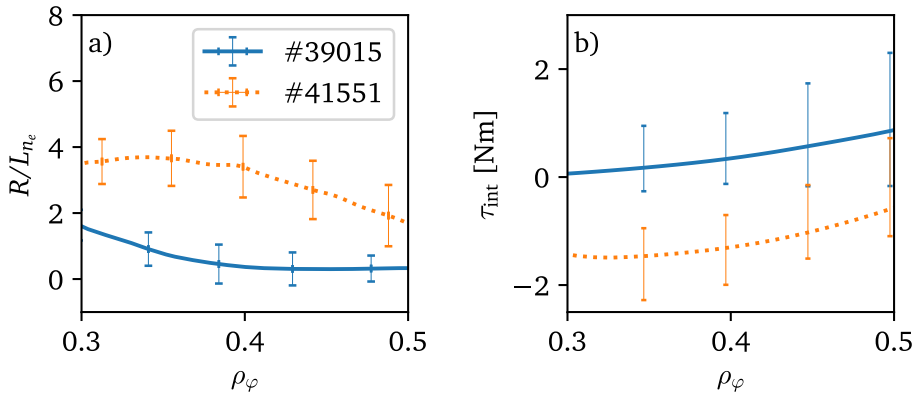

Figure 7.6: The local core intrinsic torque (Panel b) for two discharges with the most variation in the logarithmic density gradients (Panel a).

The fastest-growing mode frequency was calculated via GKW, and the frequency of the mode with the strongest growth rate was sampled. No spectral averaging was applied. This frequency does not show a monotonic behavior over radius. Furthermore, no strong correlation exists between ω_r and the previously mentioned quantities or their gradients. Interestingly, the measured co- and counter-current acting core intrinsic torque can be well organized as a function of the fastest-growing mode number. This is shown in Fig. 7.7(a). This is interpreted as two sign reversals of the local residual stress flux exist, one taking place as the plasma transitions from TEM to a mixed regime and the other as ITGs become more dominant. Stronger TEM-dominated cases are needed for a more conclusive picture and were not available for this study. A comparison of Panels (a) and (b) shows that the co-current intrinsic torque is found for flat density profiles, while peaked density gradients are found in the transition regime together with counter-current intrinsic torque. A regression of the core intrinsic torque values with the logarithmic density gradient results in $\chi^2_{\text{red}} \approx 0.57$, which is a good value. Overall, this connects these observations to the rotation reversals seen in LOC-SOC transitions, see [195] as discussed later. The relation of the density gradient and the dominant mode frequency was observed before by Fable *et al.* [216].

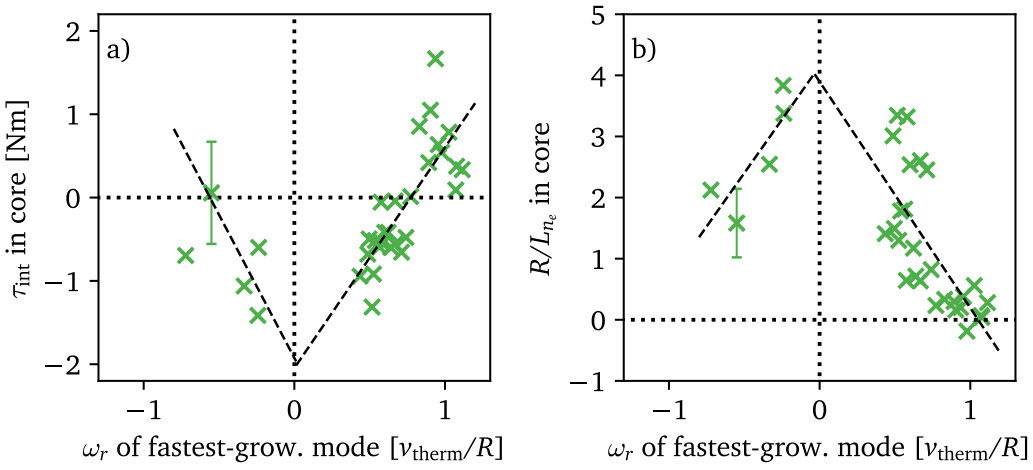

Figure 7.7: The local core intrinsic torque (Panel a) and the experimental logarithmic density gradient (Panel b) plotted over the frequency of the fastest-growing mode. Fits to guide the eye. The error bars shown correspond to the average error bar of the data set.

Aside from the scaling with R/L_{n_e}, the ordering characteristics of several parameters were tested. It became clear that the TEM-dominated data points feature small R/L_{T_i} and large R/L_{T_e} values. For the ITG-dominated and mixed cases, R/L_{T_i} was able to order the core intrinsic torque, but failed to order the TEM-dominated cases, resulting in $\chi^2_{\text{red}} \approx 0.76$, which is worse than the ordering by the logarithmic density gradient. Of course, there exists experimental cross-correlation between R/L_{T_i} and R/L_{n_e}. R/L_{p_i}, R/L_{T_e}, u', and T_e/T_i were not able to order the core intrinsic torque or the calculated ω_r. Corresponding plots are shown in the Appendix, see Fig. B.1.

The effect of a sign reversal cannot be explained by intrinsic torque generation from $\mathbf{E} \times \mathbf{B}$-shearing effects. Furthermore, the up-down asymmetry is negligible. Therefore, the intrinsic torque is most likely generated by higher-order contributions in ρ_*, such as profile shearing and turbulence intensity gradients. Due to their large error bars, it is not possible to reliably test the correlation of second-order derivatives with the experimental results.

Edge Intrinsic Torque

The intrinsic torque at the edge of the fitting domain ($\rho_\varphi \approx 0.7$) cannot be ordered by ω_r or R/L_{n_e}. Therefore, a large number of possible order parameters were tested. The discharge #39015 was excluded as it had too large uncertainties at this radial position to give a meaningful contribution. This results in seven data points to assess possible orderings, allowing only the test of single parameters.

For an overview of possible scalings, cross-correlation matrices were calculated. Strong cross-correlation is found between T_i, ∇T_i, Q_i, p_i, and ∇p_i, not only at $\rho_\varphi = 0.7$, but also with their value in the steepest region of the pedestal around $\rho_\varphi \approx 0.95$. All of these quantities show correlation with the experimentally measured intrinsic torque at $\rho_\varphi = 0.7$.

As a first check, the popular *Rice scaling* [187, 217, 218] was tested, which links the intrinsic rotation with the plasma stored energy and the current as $\Delta v_\varphi \sim W_p/I_p$. As already discussed, the variation in I_p is very small in this data set. W_p ordered the assessed intrinsic torque with a $\texttt{RMSE} \approx 40$ % and $\chi^2_{\text{red}} \approx 1.2$. ∇T_i was able to order the intrinsic torque with a $\texttt{RMSE} \approx 47$ % and $\chi^2_{\text{red}} \approx 1.4$. Of course, this comparison is very limited as the Rice scaling concerns an effective intrinsic rotation, while in this work, the intrinsic torque is extracted.

Further exploration of the experimentally measured values shows that the local ion pressure gradient $-\nabla p_i$ is the best order parameter. This is shown in Fig. 7.8(a). The linear fit (dashed line) is within the experimental uncertainties, and the corresponding RMSE value is 23 %. The $\chi^2_{\text{red}} \approx 0.25$, which is a good value for a single parameter regression. Panel (b) shows that for the experimentally measured values, the ion pressure gradient in the steepest region is also a sufficient order parameter. The corresponding linear fit is still within error bars with slightly worse $\chi^2_{\text{red}} \approx 0.73$ and $\texttt{RMSE} = 28$ %. It is important to mention that the momentum diffusion scales the residual stress and does not exhibit a local ordering with the pressure or its gradient. Hence, the observed trends are not a result of cross-correlation. It is concluded from these two plots that the experimental

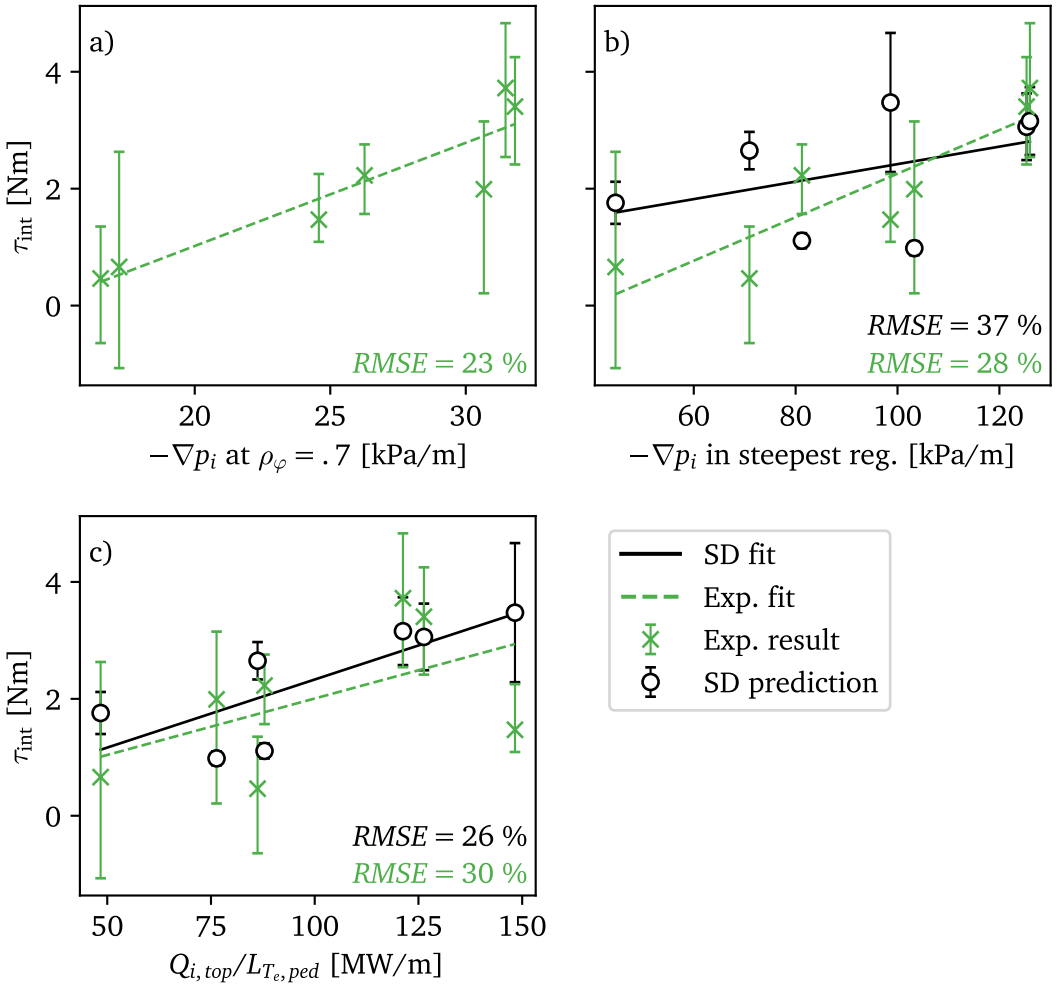

Figure 7.8: The experimentally measured intrinsic torque and the pedestal top intrinsic torque prediction by the Stoltzfus-Dueck model plotted versus various quantities. Linear fits are added to guide the eye. RMSE values for the linear fits are given in the corresponding color. In Panel (a), the theory prediction was not plotted for clarity as it revealed no insightful ordering.

values can be ordered by the local and steepest ion pressure gradient, which are cross-correlated within this data set. As the overall variation of the values is not large compared to the size of the error bars, it is not possible to clearly favor one of them over the other.

The excellent ordering of the experimental results with the pressure gradient motivates the interpretation that ∇p_i is a proxy for the radial electric field E_r, in this respect, a measure for the $\mathbf{E} \times \mathbf{B}$-shearing. Hence, the good ordering of the edge intrinsic torque with the pressure gradient is also consistent with the idea of $\mathbf{E} \times \mathbf{B}$-driven residual stress [76, 84] as the dominant mechanisms creating co-current intrinsic torque.

In Panel (b), the prediction of the Stoltzfus-Dueck (SD) model is also plotted. Here, the comparison of an edge-generated intrinsic torque prediction with the experimentally assessed values in the outer core is appropriate, as both are local quantities, and strong discontinuities in the profile of the intrinsic torque over small radial regions are not expected in the absence of strong variation of background gradients. In the plot, the assigned error bars on the SD prediction show

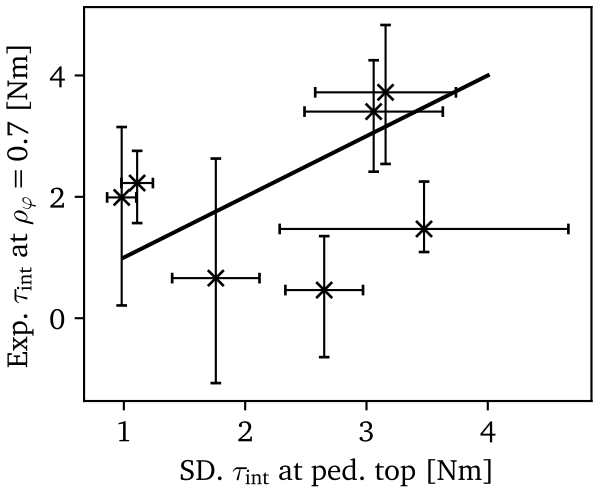

Figure 7.9: The intrinsic torque at the pedestal top predicted by the Stoltzfus-Dueck model versus the experimentally measured intrinsic torque at $\rho_\varphi = 0.7$. Unity is shown as a black line.

the standard deviation over time during the analyzed time frame as a measure of stability. Plotting this prediction over the pressure gradient in the steepest region orders the upper five points, while the lower two do not follow this trend. These two points are H discharges, and as the SD intrinsic torque has a $\tau_{\text{int,SD}} \sim A_i/Z_i$ dependence, they are only half as large. This mass dependence emerges from the fact that the loss of a heavier counter-current rotating ion makes a larger co-current torque in the SD model. These points would align with the other points and the experimental trend if this mass dependence were neglected. A worse ordering holds for plotting the SD in Panel (a), which was not done for clarity. This suggests that the mechanism observed in the experiment could differ from the one modeled by Stoltzfus-Dueck.

In the previous Chapter, it was discussed that for the studied data set, the main variation of the Stoltzfus-Dueck prediction is caused by Q_i/L_{T_e}. This motivates plotting the experimental results over this quantity, as shown in Panel (c). A fit through the experimental values also gives a reasonable $\texttt{RMSE} = 30$ %, which is not as good as the ordering by the local pressure gradient. However, as shown, the linear fits agree in magnitude, size, and trend.

Prediction and measurement are directly compared in Fig. 7.9. Concerning the size of the experimental uncertainties and the modulation of the Stoltzfus-Dueck prediction, it is impossible to confirm or reject the Stoltzfus-Dueck model. Furthermore, this data set is not ideal for validation purposes due to the limited variation in the other parameters, such as the X-point position. The H cases are predicted to be outliers by the SD model, which is not seen in the experiment. It is speculated that any edge intrinsic torque model scaling with the pressure gradient might have produced similar results.

7.4 Perspectives for a Reduced Transport Model

The scaling laws assessed in this work can be utilized to construct a reduced model for the prediction of rotation in the plasma core. The scalings for the Prandtl and pinch numbers from the regression of the gyrokinetic database cover a larger parameter space and were confirmed by the experimental results. Therefore, as a starting point for a reduced model, these scalings are taken such that

$$\chi_\varphi = (4.8\,\epsilon + 0.2)\,\chi_i \text{ and} \tag{7.4}$$

$$V_c = -\frac{\chi_\varphi}{R}\,(0.5\,R/L_{n_e} + 0.44\,s), \tag{7.5}$$

see Eq. 6.4 and 6.7 from Chapter 6.2. From the experimental investigations of the intrinsic torque, it is understood that the intrinsic torque in the core shows a clear dependence on the logarithmic density gradient, which reveals the strongest variation in the studied data set at $\rho_\varphi \approx 0.35$. At $\rho_\varphi \approx 0.7$, the intrinsic torque scales most clearly with the local pressure gradient. Within this work, the residual stress was modeled as

$$\Pi_{\text{Rs}} = m_i n_i\,\chi_\varphi\,c_s\,g(\rho_\varphi)$$

and from the experimental data set studied in this Chapter, the values of $g(\rho_\varphi)$ can be approximated as a quadratic polynomial without a constant part (for continuity in zero), such that

$$g(0.35) = 0.068 \cdot R/L_{n_e} - 0.048 \tag{7.6}$$

and

$$g(0.7) \approx 0.0057\,\text{[m/kPa]} \cdot \nabla p_i + 0.024. \tag{7.7}$$

Equation 7.6 allows, consciously, for a sign change in the intrinsic torque, which takes place for values lower than $R/L_{n_e} \approx 0.7$. The constant part in the second equation does not contribute to a sign change, but rather compensates for the effects not scaling with the pressure gradient at this radial position. From Eq. 7.7, a sign change would happen at $-\nabla p_i < 5$ kPa m^{-1}, which is much below the experimental values seen at this radial position, so it is assumed that the contribution of the intrinsic torque at this radial position is always co-current. The values of $g(\rho_\varphi)$ are interpolated due to a cubic implementation of this function. As done for the entire modeling in this work, the torque from the NBI is provided via `TRANSP`. Furthermore, the experimental boundary condition for the rotation is set at $\rho_\varphi \approx 0.8$. This model is only thought to approximate experimental data at AUG in the studied parameter space. While the gyrokinetic scaling laws, Eq. 7.4 and 7.5, are non-AUG specific, a proper normalization of the intrinsic torque scaling is subject to future work. The necessity of this normalization for the extrapolation of the intrinsic torque is discussed in the next Section. The exact implementation of the reduced model in the `ASTRA` code is documented in Appendix A.2.

As a first validation, the predictions of this reduced model are tested on the reference discharge #40076, 2.0 – 4.2 s. This gives quite reasonable results as shown in Fig. 7.10. In Panel (a)-(c), the steady-state, amplitude, and phase profiles are shown, and the reduced model is close to the error bars of the optimized solution. The Prandtl number (Panel d) and the intrinsic torque (Panel f) are spot on, while the pinch number is matched nearly within the error bars. In the following analysis, however, the focus will be on the reconstruction quality of the steady-state profiles rather than the transient dynamics.

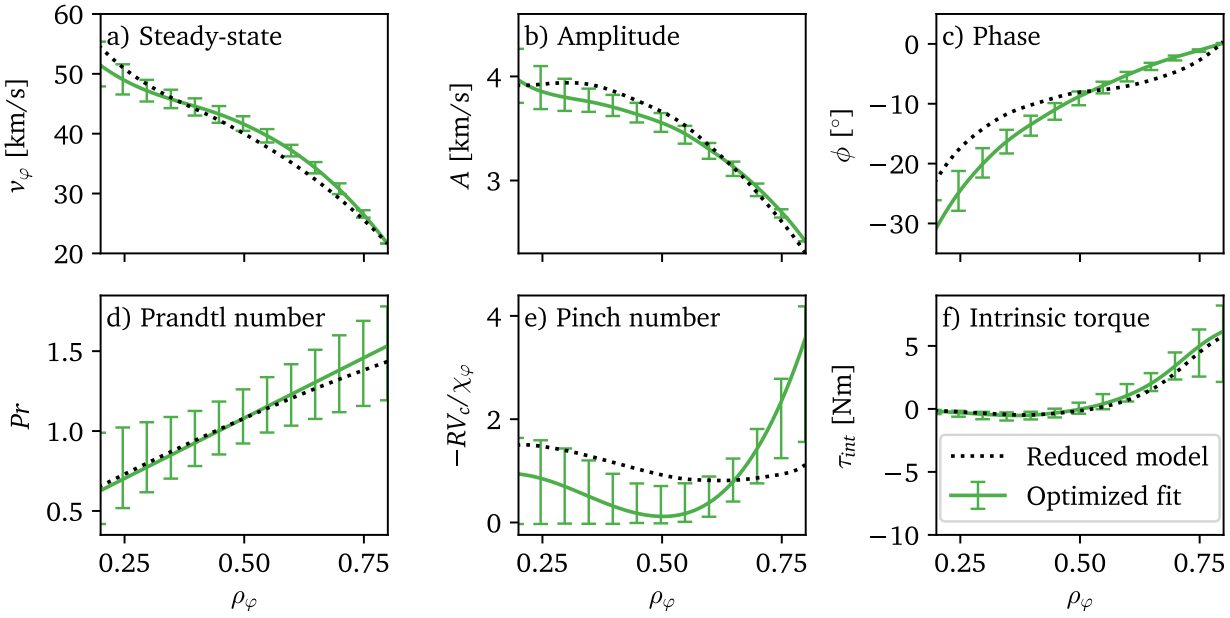

Figure 7.10: Comparison of the optimized modeling for the reference discharge (#40076, 2.0 – 4.2 s) compared with the solution based on the reduced model.

As a next step of validation, the reduced model is tested on the gyrokinetic database studied in Section 6.2, which was the basis for the regression of the Prandtl and pinch number. This allows, in particular, the simple intrinsic torque model to be studied, which was not assessed from the gyrokinetic database, but from experimental values. Figure 7.11(a) shows the reduced model solution plotted versus the measured toroidal rotation. In different colors and symbols, values are shown for several radial positions. As expected, the reconstruction quality decreases the further the prediction is made from the boundary ($\rho_\varphi \approx 0.8$). Several points are slightly underpredicted. This could have to do with the observed trend of slightly smaller Prandtl numbers in the experimental regression, see Eq. 7.1, or slightly higher values for the pinch number in the experimental regression, see Eq. 7.3. Overall, the RMSE is ≈ 7 %, which is a great value for such a simple model. This suggests that the reduced model is, in fact, capable of reproducing the most important features of the intrinsic torque.

After this successful validation, the reduced model is now applied to a database of H-mode discharges, which were not part of the investigations in this work. This includes experiments in helium, a large number of discharges with 2 and 10 Hz modulation, current and heating scans, and JET identity discharges for a ρ_* comparison. Discharges with strong mode activities are still rejected. Altogether, this makes a data set with 85 plasma phases. The parametric variation in this test data set is much larger than the gyrokinetic data set from which the scalings were obtained, not only in the engineering parameters, but also in the local quantities, see Tab. 7.2. Therefore, this data set is an excellent test bed to understand if the assessed scaling laws catch the most important mechanisms over a wider range of parameter space.

This is shown in Fig. 7.11(b). Most modeled values group around the unity line in black. Despite only plotting the steady-state values here, the results were temporally stable. The RMSE ≈ 9.6 % is comparable to that for the gyrokinetic database,

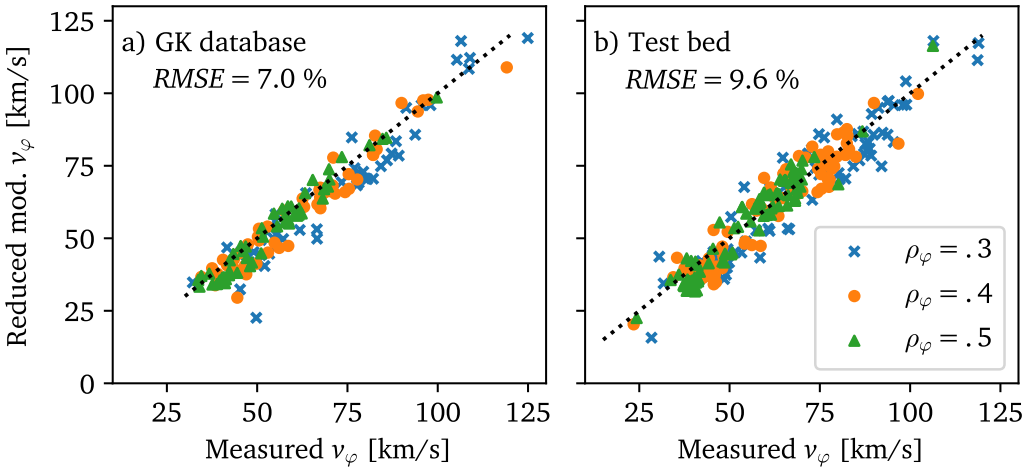

Figure 7.11: Comparison of the experimentally measured toroidal rotation (x-axis) with the results from the reduced modeling (y-axis) for multiple radii. In Panel (a), the modeling of the gyrokinetic database is shown, which was used to assess the scaling laws. Panel (b) shows the results for an entirely different data set of H-mode discharges with the parametric variation shown in Tab. 7.2. In both plots, unity is shown as a black dotted line.

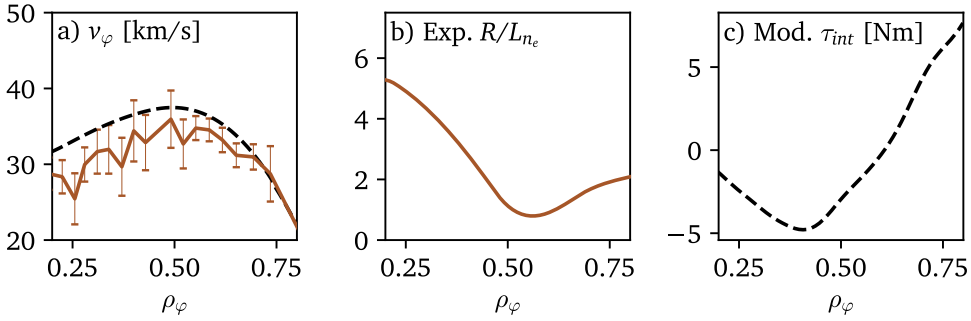

Figure 7.12: (a) Comparison of hollow experimentally measured toroidal rotation (brown) with reduced modeling (black, dashed) for #29216 (5.5 – 7.0 s, $P_{\mathrm{ECRH}} = 3.4$ MW). In Panel (b), it is shown that a large logarithmic density gradient translates into a strong counter-current intrinsic torque in the inner core (Panel c).

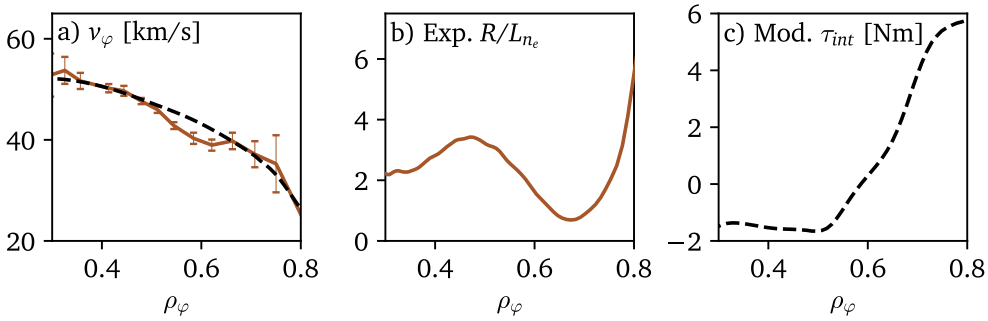

Figure 7.13: (a) Comparison of a non-hollow experimentally measured toroidal rotation (brown) with reduced modeling (black, dashed) for #39014 (4.5 – 6.8 s, off-axis $P_{\mathrm{ECRH}} = 3.8$ MW). Values below $\rho_\varphi < 0.3$ are neglected due to mode activity.

Quantity	min	max
ν_*	0.015	2.26
q	0.88	5.2
T_e/T_i	0.65	2.4
R/L_{T_e}	0.12	11.9
R/L_{T_i}	2.4	12.89
R/L_{n_e}	-0.3	6.27
β_e	0.001	0.017
ρ_*	0.004	0.013
n_e [10^{19} m^{-3}]	3.74	9.91
P_{NBI} [MW]	2.3	11.05
P_{ECRH} [MW]	0	5
I_p [MA]	0.4	1.2
B_φ [T]	1.8	2.7

Table 7.2: Parameter space spanned by the additional 85 data points used as a test bed for the reduced modeling. The comparison for the modeling of these data points to the experiment is shown in Fig. 7.11(b). Local quantities were mapped in the plasma core between $\rho_\varphi = 0.3$ – 0.7.

and points are uniformly distributed around the unity line. It is found that the deviation between modeled and measured values increases with distance from the boundary, RMSE $\approx$ 10.5 % for $\rho_\varphi = 0.3$, RMSE $\approx$ 9.0 % for $\rho_\varphi = 0.4$, and RMSE $\approx$ 6.7 % for $\rho_\varphi = 0.5$. The boundary condition varies in this data set between 15 – 40 km/s, while the modeling reaches values up to 120 km/s. This shows that the reproduced variation within the data set is not entirely caused by the variation of the boundary. The simple model is capable of reproducing the most important transport mechanisms for all three transport channels and can give a meaningful estimate for the steady-state rotation profiles as long as a reliable boundary condition at the edge of the core is provided.

In the following, the discharge #29216 (5.5 – 7.0 s) is studied, which exhibits hollow rotation profiles. This case was, so far, difficult to analyze due to the large uncertainties associated with the experimental data. In this discharge, dominant ECRH was applied, $P_{\text{ECRH}} \approx 3.4$ MW and $P_{\text{NBI}} \approx 3.0$ MW, to study a possible sign reversal of the intrinsic torque. The reduced model, which scales the intrinsic torque with the density gradient in the core and with the pressure gradient at the edge, can reproduce this sign reversal and the hollow rotation profiles. This is shown in Fig. 7.12(a), in which the experimental data is shown in brown with error bars, and the modeling is shown as a black dashed line and is within experimental uncertainties for most radial positions. The experimental density profile in Panel (b) shows large values in the inner core, and the intrinsic torque, Panel (c), is modeled via Eq. 7.6 to be strongly counter-current in the inner core. Gyrokinetic calculations suggest a mixed turbulence regime for the inner core in this discharge and, therefore, this sign reversal can be attributed to the high density gradient branch of Fig. 7.7. The reproduction of the hollow profiles was also found for a similar discharge #29217.

For comparison, another discharge is shown in Fig. 7.13, with comparably high $P_{\text{ECRH}} = 3.8$ MW, but off-axis ECRH deposition. As shown in Panel (b), the logarithmic density gradient stays much lower in the inner core, and, therefore, so does the modeled intrinsic torque. This reproduces the rotation profile, Panel (a), which is not hollow. The peaking of the density gradient is more towards mid-

radius due to the off-axis ECRH. There is a corresponding dip in the steady-state rotation profile, which is, of course, not reproduced by the model, which interpolates between the scaling laws at $\rho_\varphi = 0.35$ and 0.7. Here, it is necessary to resolve the radial dependence of R/L_{n_e}.

This shows that a simple, reduced model, which features the most important momentum transport mechanisms, can also contribute to the understanding and interpretation of more complicated experimental scenarios, which are not directly accessible in the analysis.

As possible next steps to improve the performance of such a reduced model, it is considered to substitute the time-consuming TRANSP calculations, for instance, with the RABBIT code [148], which has been successfully integrated into the ASTRA suite. Additionally, different scaling laws examined in this study could be benchmarked. Implementing it in the FENIX flight simulator [219, 220] presents a potential application for scenario development and real-time control. Since CXRS analysis of edge rotation is notably simpler than that of the core, it is, in principle, possible to provide real-time boundary values for edge rotation to the control system, while core values can be approximated using a reduced model.

Furthermore, the integration of this model into the integrated modeling suite IMEP [105–107] is a consequent next step, allowing for validation on other machines such as AUG, JET, Alcator C-Mod, based on the data set from [107], provided that a suitable normalization of the intrinsic torque is established. An unresolved aspect for modeling without any experimental data remains the boundary condition for edge rotation. In this context, intrinsic rotation predictions by Stoltzfus-Dueck, as demonstrated in [104], could be evaluated.

7.5 Discussion

This Section discusses the experimental results in light of previous experimental and theoretical work.

The Prandtl number is found to be on the order of unity, in agreement with earlier experimental and theoretical results [45, 96, 174, 178, 197, 221–224]. Its radial dependence has rarely been resolved in experimental analysis. In experimental works at JET by Tala *et al.* [178] and Mantica *et al.* [179], it was found to increase over radius, in agreement with this study. However, the experimentally assessed Prandtl number was often significantly larger than the corresponding gyrokinetic prediction, most likely due to a missing intrinsic torque in such investigations. The work from Strintzi *et al.* predicted that the Prandtl number depends weakly on s or R/L_{T_i}. Also experimental work at JET by Tala *et al.* [178] has shown constant Pr during parameter scans of q, R/L_{n_e}, and ν_*. A study at JT-60U [193] came to similar conclusions, but discovered a dependence of Pr on β_N. An inter-machine comparison [225] suggested larger Prandtl numbers for larger machines.

Aside from the inherited dependences from the ion heat diffusivity via the Prandtl number, the momentum diffusion was found to depend most clearly on the strength of the turbulence. The correlation of the diffusivity with collisionality, as found at

DIII-D in [180], could not be demonstrated, potentially due to cross-correlations in the data set.

The ordering of the pinch with the density gradient is in agreement with earlier experimental results, e.g., by Tala *et al.*, who found the scaling of the pinch number with the density gradient in experiments at the JET tokamak [178]. This agrees with inter-machine comparisons by Yoshida *et al.* [225] and by Tala *et al.* [221]. In the latter, the assessed pinch numbers, however, were larger than the theory prediction. Consequently, the linear scaling with the density gradient gave higher absolute values, disagreeing with the gyrokinetic prediction. These differences are probably caused by a distortion of the transport coefficients in their analysis due to the exclusion of the intrinsic torque and its time dependence. The discussed q dependence of the pinch, see [178, 221, 226], was not assessed due to the limited variation in current within the studied data set, but the scaling with s could be understood as a proxy for the q dependence. In [178, 227, 228], no or only marginal dependence of the pinch on the collisionality was found, agreeing with the results in this work. The scaling of the pinch on R/L_{n_e} and q was also found in a database study at JET, see [197].

While comparing the experimental steady-state profiles of the toroidal rotation in this work, it was found that discharges without ECRH show a more convex profile shape. The case without ECRH was the only studied phase with clearly co-current intrinsic torque in the inner core. The other discharges, with low ECRH power, exhibited slightly concave profiles. Similar effects of ECRH on the shape of the rotation profile were found earlier in experiments at DIII-D [186], JT-60U [193], and AUG [195, 229]. In this work, the effect seems weak, most likely as P_{ECRH} was relatively small in this study. No discharges with a sign reversal of the rotation were analyzed. The author speculates that such sign reversal happens for scenarios with strong counter-current intrinsic torque in the core, combined with low external torque, inward momentum pinch, and edge intrinsic torque. However, more strongly TEM-dominated plasmas with clearly hollow rotation profiles must be studied to draw firm conclusions.

A theoretical study from AUG [230] suggests a clear dependence of the residual stress on the density gradient R/L_{n_e}. To some degree, this dependence was reproduced by the two discharges with the lowest/highest density gradients, showing the most co/counter-current core intrinsic torque. The curvature of the density profiles, found in [121] to have an important role in forming the residual stress, has large experimental error bars and remains an open point of experimental validation. Furthermore, global, non-linear gyrokinetic calculations from Grierson *et al.* investigated the transition from flat to hollow toroidal rotation with increased ECRH power due to the modified ion temperature gradient [124]. This dependence, to a certain extent, is recovered by this analysis.

Similar observations of the relationships between the density gradient, the dominant mode frequency, and the effect on the intrinsic rotation were found by McDermott *et al.* [195], who studied the intrinsic torque behavior across the LOC-SOC transition (linear ohmic confinement - saturated ohmic confinement). In that work, two sign reversals of the intrinsic rotation were found. A first, in TEM or a mixed regime, from co- to counter-current intrinsic rotation due to changes in the density gradient. Then, a second reversal back to the co-current intrinsic rotation in ITG with lowered density gradient profiles. Furthermore, it was concluded that

the sign reversal of the intrinsic torque does not depend on the LOC-SOC transition per se but on the simultaneous change of the kinetic profiles. This is analogous to the results on the core intrinsic torque found in this work.

It was found already in previous works [181] that the intrinsic torque mechanisms in the inner and outer core can decouple and are, most likely, dominated by different mechanisms. The dependences of the intrinsic torque and residual stress in the inner plasma core are an open point of discussion in the community. Advanced studies, e.g., like [181, 227], could not draw a firm conclusion about its parameter dependences. In agreement with this work, the core intrinsic torque was very small. Furthermore, it became more strongly counter-current with increased ECRH [181]. As already discussed by McDermott *et al.* [195], most likely, this sign reversal is not caused by a change of the turbulence regime itself, but rather correlated to changes of the profile shearing, as indicated by the analysis results in this work.

For the edge intrinsic torque, several empirical models and scalings have been explored in previous works, for example, the famous Rice scaling. In a follow-up publication [188], Rice *et al.* found ordering of the intrinsic rotation by the edge ion temperature gradient. Similar results were obtained on other fusion experiments, for example, NSTX [231], and LHD [232], where strong correlations of the intrinsic torque with the ion temperature gradient were identified, as well as at DIII-D, where scaling of the intrinsic rotation with the ion temperature in the pedestal was observed [95]. Both the Rice scaling and the dependence on the edge ion temperature gradient were recovered in this work. This is expected due to the common cross-correlation of the stored energy, the ion temperature gradient, and the pressure gradients at the edge. Still, they showed inferior ordering characteristics than the pressure gradient. The caveat here is that those studies often focused on the net intrinsic rotation, which can include the interacting effects of all transport mechanisms. In contrast, this work discusses the isolated effects on the residual stress induced torque.

Experiments in the DIII-D tokamak with balanced beams allow to zero toroidal rotation. In such a zero rotation scenario, the diffusive and convective components of the transport vanish, and the intrinsic torque can be calculated from the net beam torque [181, 191, 227]. The assessed intrinsic torque profiles agree in size and shape with the results of this work, with small negative counter-current intrinsic torque in the inner core and stronger co-current intrinsic torque towards the plasma edge. Their work showed an ordering of the edge intrinsic torque at $\rho_\varphi = 0.8$ with the pedestal pressure gradient in agreement with the results of this work [181, 227]. The authors draw the same conclusion as in this work, that the pressure gradient, especially in the absence of the toroidal and poloidal terms of the E_r force balance, as in their experiments, is a proxy for the $\mathbf{E} \times \mathbf{B}$-shearing, which produces residual stress. In their work, however, a mismatch between the experimentally measured Reynolds Stress and the measured intrinsic torque remained. Therefore, the authors concluded that ion orbit losses could be contributing to the intrinsic torque in this radial region. This would somewhat explain the correlations seen here with the Stoltzfus-Dueck model. A similar scaling of the intrinsic toroidal rotation with the pressure gradient was also observed at JT-60U by Yoshida *et al.* [233].

In contrast to earlier work, herein, no scaling laws for the intrinsic torque are given

as they would invite the expectation of universal applicability. Previous scalings have been done using dimensional parameters. They are not extrapolatable to other machines or parameter ranges. The proper normalization of the intrinsic torque for such an extrapolation was discussed in [226, 228, 234], but it has not been resolved. Another open question that this work has not studied is the ρ_* dependence of the intrinsic torque, as the variation of ρ_* is relatively limited within the studied data set. The observed variation is dominated by its dependence on the ion temperature, $\rho_* \sim \sqrt{T_i}$. It is, therefore, not straightforward to decouple this from the previously mentioned scalings with the first and second order derivatives. In several experimental works, the dependence of the intrinsic rotation/torque on ρ_* has been discussed [226, 228, 234], but with differing approaches to the applied normalization of their torques. The disentanglement of such scans from other parameter dependences remains crucial and unsolved. As the variation of ρ_* is very limited in a tokamak, inter-machine comparisons are required.

7.6 Summary

The analysis of the experimental data shows a number of practical difficulties, and the methodology in its current form is susceptible to strong temperature perturbations and modes. It is not applicable in strong TEM-dominated regimes. The top priority for successful experimental analysis is to avoid overly flat phase profiles.

A detailed comparison of the experimental steady-state, amplitude, and phase profiles confirms the already discussed effects of the modulation frequencies. Furthermore, it shows the influence of the applied heating mixtures on the formation of the rotation profiles: More concave steady-state profiles are observed for cases without ECRH. The gyrokinetic predictions for the Prandtl and pinch numbers follow the experimental results well within uncertainties for most cases. The Prandtl number increases monotonically over the radius for nearly all discharges. The intrinsic torque profiles are flat in the inner core and become strong, co-current towards the edge of the fitting domain.

An investigation of the parametric dependences shows that the local inverse aspect ratio is the Prandtl number's most robust order parameter in the experimental analysis. A linear fit gives values for $Pr(\epsilon)$, similar to those of the theory predictions, validating that result. No second order parameter is found that significantly reduces the remaining scatter between the fit and the data points.

As expected, parameter dependences from the Prandtl number and the ion heat diffusivity are recovered for the experimental momentum diffusivity. Furthermore, a clear correlation between the experimentally assessed momentum diffusion and the gyrokinetically calculated growth rates is found, consistent with the basic understanding of turbulent transport.

For the pinch number, the logarithmic density gradient is observed to be the best order parameter. This result aligns with theory prediction and earlier works. A regression with the density gradient and the shear yields results similar to those obtained from regressing the gyrokinetic database. Therefore, for the convective transport, the theoretical predictions can be validated for these plasmas.

The intrinsic torque in the inner and outer core is dominated by different mechanisms, resulting in a certain decoupling. The results for the inner core suggest a scaling with the density gradient. Studying the dominant turbulence regimes reveals two sign reversals, one from dominant TEM with flat density profiles to a mixed regime with peaked density profiles and another from the mixed regime to strong ITG modes with flat density profiles. A correlation to the applied ECRH power is found. This is analogous to earlier works on the LOC-SOC transition, the influence of the ECRH on the rotation profile, and theoretical works on the effects of profile shearing. It is concluded that the intrinsic torque in this radial domain is mainly generated by profile shearing effects of higher order in ρ_*.

At the edge of the fitting domain, the pressure gradient is found to order the assessed intrinsic torque values. They are co-current directed without any indication of a sign reversal. This suggests that linear effects in ρ_*, connected to the $\mathbf{E} \times \mathbf{B}$-shearing, could be responsible, which cannot induce a sign reversal of the intrinsic torque in this scenario. The analytical Stoltzfus-Dueck model is compared to the experimental results. While the main parameter dependences from the Stoltzfus-Dueck model could be used to order the experimental data, a direct comparison of prediction and measurement does not result in a thorough validation.

A reduced momentum transport model based on gyrokinetic scalings for the Prandtl and pinch numbers, together with experimental scalings for the intrinsic torque, is constructed and implemented in ASTRA. It is shown that this simple model not only reproduces the transport coefficients obtained for the reference plasma, but can also model the rotation profiles of the discharges from the gyrokinetic database. This shows that the intrinsic torque scaling assessed from only a few discharges is relatively robust. As a next step, the reduced model is applied to a data set with sizeable parametric variation, which was not used so far in this work. Also, for these independent cases, the rotation profiles are correctly predicted, which is a clear indication that the model catches the most important transport contributions. This is, to the author's knowledge, the first reduced and validated momentum transport model available for the core. Such a model finds future applications in integrated modeling and for real-time control. The boundary condition remains an important and critical open question for future work.

While many of these results agree with earlier experimental and theoretical works, this is the first time such a coherent picture of this transport channel is presented for the core plasma. While for the Prandtl and the pinch number, the presented results align with earlier works, for the intrinsic torque, the precise parameter dependences are still under discussion.

Chapter 8

Summary and Outlook

"Ask me what I learned from all those years..."
— Taylor Swift, Karma, Midnights

In this work, a methodology was implemented that is capable of unambiguously, separately, and concomitantly determining the contribution of diffusion, convection, and residual stress to momentum transport within the plasma core. The analysis is based on experiments with neutral beam modulation, which results in heating and torque perturbations. While the torque perturbations are used to infer the transport coefficients by analyzing the Fourier amplitude and phase profiles, the temperature perturbation is an undesired side effect. It is found that it is crucial to scale the momentum transport coefficients with the experimental ion heat diffusivity to compensate for the modulated turbulence amplitude.

The transport analysis is based on the `TRANSP` and `NUBEAM` codes to assess the torque from the neutral beams and the ion heat flux that serves as input to the `ASTRA` code. An analytical momentum transport model is implemented in the `ASTRA` code, together with an experimental boundary condition at the outer edge of the fitting domain. `ASTRA` solves the momentum transport equation and can predict the toroidal rotation based on a set of prescribed transport coefficients in the transport model. A statistical minimization algorithm is used to iterate on the transport coefficients to fit the `ASTRA` prediction to the experimentally measured rotation data. Statistical error analysis calculates uncertainties in the modeling and allows insights into the topology of the spanned parameter range. It is found that the methodology can assess a global and unique minimum, increasing the confidence in the fitting results.

Successful analysis requires high-quality experimental data that exhibits sufficiently steep phase profiles and the absence of strong MHD activity. These requirements limit the number and the kind of plasmas that were analyzed in this work. However, the modeled rotation agrees with the experimental data with high accuracy for the analyzed data set. The determined values for the Prandtl and the pinch numbers agree within uncertainties with gyrokinetic predictions. This resolves a long-standing mismatch of theory and experiment for these transport channels, reported in earlier works. Numerical experiments with simplified transport models show that such a mismatch can be caused by a distortion of the transport

coefficients due to neglecting the residual stress and the time dependences in the modeling. Furthermore, only with time-dependent residual stress is the modeling of the experimental data possible within the experimental uncertainties.

The first application of this methodology was to analyze the isotope dependence of the momentum transport channel. To separate the effects of the isotope dependence on the heat and momentum transport channel, a special scenario was designed in which the heat transport between an H and a D plasma were matched. Furthermore, most of the dimensionless parameters agree. This should isolate a possible isotope dependence of the momentum transport channel. Theory calculations predict a negligible isotope effect, and the experimental analysis reproduces this. The remaining differences are caused by parametric variations in the kinetic profiles.

The study of these parameter dependences of the momentum transport coefficients was first focused on theory predictions by gyrokinetic calculations. Isolated parameter scans are carried out. In these calculations, different physics effects are consciously activated and deactivated. It is shown that many previous theoretical works used oversimplified models that neglected important effects, such as collisions. In addition to the isolated parameter scans, a database of gyrokinetic calculations based on experimental data was constructed. The isolated parameter scans are used to understand which trends in the database resulted from experimental cross-correlation and which are of a physical nature.

It is possible to show that the Prandtl number depends on the inverse aspect ratio as a proxy for the dynamics connected with the trapped particles. A compensational effect of the passing particles is suggested based on the coupled equations for the perturbed density, parallel velocity, and temperature. For the pinch number, a strong dependence on the logarithmic density gradient is seen, as expected from the basic principle of the Coriolis pinch. Also, the magnetic shear contributes to the pinch. Lastly, the Stoltzfus-Dueck model for the pedestal top intrinsic torque is implemented to provide a theory comparison for the intrinsic torque.

Then, the experimental results are used to understand the validity of these theory predictions. For the Prandtl and pinch numbers, the assessed parameter dependences align in trend and size with the theory predictions. Corresponding scaling laws agree within uncertainties. The intrinsic torque is flat in the inner core, becoming increasingly strong and co-current directed towards the plasma edge. Different underlying mechanisms likely drive the torque in the inner and outer core. The logarithmic density gradient is found to order the experimental results in the inner core. Strong density gradients occur together with counter-current intrinsic torque, while co-current-directed intrinsic torque is measured for flat density gradients, consistent with previous observations of intrinsic rotation behavior. These results can be connected to the effects of profile shearing and turbulence intensity gradients.

At the outer edge of the fitting domain, the pressure gradient orders the experimental data best. $\mathbf{E} \times \mathbf{B}$-shearing effects in the pedestal are responsible for this. The Stoltzfus-Dueck model reproduces the trends seen in the data to a certain degree, scaling with the gradients in the steepest edge regions. However, the different dependences of the Stoltzfus-Dueck model are not thoroughly investigated, not allowing for detailed validation. Overall, the assessed trends of the intrin-

sic torque align with the expectations from previous theoretical work. However, for real validation, non-linear global gyrokinetic calculations would be required, which are beyond the scope of this work and cannot be applied in such a database approach.

A discussion of these results in light of earlier theoretical and experimental work shows overall agreement for the parameter dependences of the Prandtl and the pinch number. At the same time, this is the first work to validate the theoretical predictions quantitatively. The study of the intrinsic torque shows that previously suggested parameter scalings can be confirmed, but a conclusive picture unifying the observations from multiple experiments is still missing.

Finally, the validated scaling laws for the Prandtl and the pinch number and the experimental scalings for the intrinsic torque are used to construct a first validated and reduced transport model to show the potential for integrated modeling approaches. It is possible to successfully reproduce experimental rotation data for many discharges with large parametric variations, which were not part of the analysis in this work, including discharges with hollow rotation profiles. This is a great success for such a simple transport model.

The next development steps of the reduced model would be to refine the parameter dependences and implement it in integrated modeling approaches. This could lead to first, physics-based predictions of the rotation profiles of future machines. The boundary condition, set in this work at $\rho_\varphi = 0.8$, needs to be replaced. Here, major future work on the theoretical and the experimental side remains. A starting point to understand the momentum transport in the outer core could be to use the presented methodology in small-ELM scenarios or in L-mode, where the experimental boundary condition can be set further outside. Such data already exists for the KSTAR and JET tokamak and should allow for a better understanding of the core-edge coupling of this transport channel.

For a future machine, strong rotation profiles are beneficial for plasma stability. In general, the assessed dependence of the intrinsic torque on the pressure gradient is favorable, but, of course, this is limited by the peeling-ballooning stability. Furthermore, the ρ_* dependence of the intrinsic torque and its proper normalization is still unclear. Existing data for an identity discharge in dimensionless parameters from AUG, JET, and KSTAR could be used in an inter-machine comparison to study this dependence.

A machine like ITER could obtain elevated rotation profiles through flat density profiles in the inner core to avoid counter-current intrinsic torque. This is, of course, not beneficial for the fusion gain. Rather, steep gradients towards the edge are attractive for giving a substantial inward pinch and an edge-localized, co-current intrinsic torque. An essential limitation of this work is the restriction to very moderate levels of ECRH. Indeed, more experiments with mixed or even TEM-dominated turbulence regimes need to be analyzed. This poses challenges for this methodology, and improvements in the modeling are likely required to expand the experimental validation to stronger ECRH-dominated plasmas. The author proposes decoupling the momentum transport solver from `ASTRA` or implementing more efficient optimization algorithms for fast iteration over the transport coefficients. More detailed models or Bayesian inference can then be used with more radial spline points, accounting for steep changes in the profiles of the transport

coefficients likely to happen for the very local deposition of the ECRH. Additional effort is needed to ensure consistent use of the equilibria throughout the various analysis steps. It is recommended that a systematic study of potential deviations in equilibrium reconstructions be conducted, particularly in discharges featuring strong ECRH. Improving ASTRA's capability to use the IDE equilibrium would address the existing discrepancy. Furthermore, the basic assumption to compensate for the changed turbulence intensity via the ion heat diffusivity has to be revisited when going to an electron-channel-dominated turbulence regime. For a more compact, spherical tokamak line, the kinetic ballooning mode turbulence regime or different mixed turbulence regimes are relevant. Theoretical and experimental work could focus here on the MAST-U tokamak.

The NBI modulation database constructed at AUG also contains experiments with ECRH and ICRH modulation that pose challenges in momentum transport analysis. They could be used to further understand the interaction of the heat and the momentum transport channel. From such results, it could be understood better how to separate these channels in such an analysis. As a possible extension to the study of the isotope dependence, helium data exists that matches the discharges used in the isotope comparison in this work. This is an interesting data set, as the available data allows for directly measuring the main ion rotation.

As a side effect of this work's experimental efforts, many failed power scans with NBI modulation exist in which MHD modes were detected and found to modify the rotation profiles. These experiments could allow insight into how such a mode influences and interacts with the momentum transport channel.

To conclude, the author suggests focusing future research on the ρ_* dependence of the intrinsic torque, investigating more TEM-dominated turbulence regimes, and implementing and validating corresponding reduced models. Significant and crucial work remains to assess and validate the momentum transport in the plasma edge, interacting strongly with the core transport mechanisms. This method can be a starting point for such investigations, particularly in ELM-free regimes.

Appendix A

Numerical Inputs

A.1 TRANSP

The following experimental input is given to TRANSP by means of ASCII files with a time resolution of 10 ms (unless not stated otherwise):

- Effective charge Z_{eff}, calculated from the bremsstrahlung via the CEZ, could also be taken from the IDZ shotfile directly
- Toroidal rotation Ω, as measured by CEZ and CMZ diagnostic, radially smoothed
- Ion temperature T_i, taken from CEZ and CMZ, radially smoothed
- Electron temperature T_e, taken from IDA, radially smoothed
- Electron density n_e, taken from IDA, radially smoothed
- Fourier moment decomposition of the last closed flux surface to prescribe the equilibrium, taken from EQH for the initial time point
- Safety factor q, calculated from the EQH shotfile, for the equilibrium reconstruction for the initial time point
- Toroidal magnetic field B_φ on the magnetic axis, obtained from the FPC shotfile
- Plasma current I_p, from the FPC shotfile
- Loop voltages u_{loop}, taken from the TOT shotfile, calculated via the FPG measurements
- ECRH power P_{ECRH} for every source, time traces taken from the ECS shotfile
- toroidal and poloidal angle for every ECRH source, time traces taken from the ECS shotfile
- NBI power P_{NBI}, time traces for every beam from the NIS shotfile

A.2 ASTRA

The experimental inputs to the ASTRA simulation are linked via the so-called exp-file, and via the log-file, a set of momentum transport coefficients is prescribed. By starting the ASTRA simulation, the equ-file is parsed. From the TRANSP calculation, the following outputs are used as input to ASTRA by means of ASCII files:

- Power density onto the ions P_i, a sum of: total ion heating (IHEAT), electron to ion heat flux (QIE), ion heating by convection and friction from rotation (QROT), fast ion thermalization power (PBTH), minus net loss due to charge exchange (PONET), minus ion gain (GAINI)
- Power density onto the electrons P_e, sum of: total electron heating (EHEAT), minus electron to ion heat flux (QIE), minus neutral ionization work (PION), minus radiated power (PRAD), minus electron gain (GAINE)
- Torque density (TQIN)
- Fast particle energy density parallel and perpendicular (UFASTPA and UFASTPP)
- Radiated power P_{rad} (PRAD)
- To enforce consistency of the ASTRA input with the TRANSP input: safety factor (Q), electron density and temperature (NE and TE), ion temperature (TI), effective charge (ZEFFI)
- To compare to the power balance calculation from ASTRA, but not necessarily needed: electron and ion heat diffusivity (CONDE and CONDI)

Additionally, the following data is given from the shotfile database via the trview code:

- Last closed flux surface boundary in R and z coordinates
- Plasma current I_p and toroidal magnetic field B_φ
- Main ion charge and mass numbers A_i and Z_i

The experimental toroidal rotation data v_φ is taken directly from the shotfile database and postprocessed manually.

The ASTRA equations for the reduced transport model are given below:

```
CAR62 = abs(-625*QITOT/GRAD(TIX)/NI/G11)+0.001; !chi_i
CAR63 = (4.8*AMETR/RTOR+0.2); !Prandtl number
XUPAR = CAR63*CAR62; !chi_phi
CNPAR = -XUPAR/RTOR*(0.5*RTOR/LNE+0.44*SHEAR); !V_c

CAR42 = NE*TI*11604.25*1.38*10**(-4); !pi
CAR43 = -GRAD(CAR42); !-grad(pi) in kPa/m
CAR48 = RTOR/LNE;
```

```
CMHD3 = 0.068*CAR48(AFX(0.35))-0.048; !value of g(rhot=0.35)
CMHD4 = -(0.0057*CAR43(AFX(0.7))+0.024); !value g(rhot=0.7)
CMHD1 = 10/7*(4*CMHD3-CMHD4); !b for g=ax^2+bx
CMHD2 = -200/49*(2*CMHD3-CMHD4); !b for g=ax^2+bx
RUPFR = MRHO*XUPAR*RTOR*CS/ABC*(CMHD1*XRHO+CMHD2*XRHO*XRHO)*G11/VRS;
!Rs scaled by g(rhot)
```

A.3 Workflow

In Fig. A.1, the flow of data is depicted. The main Python functions are:

- `get.py`: prepares all used input data from the shotfile database in a uniform format together with their uncertainties
- `fourier_analysis.py`: a shared library that performs the Fourier analysis in all needed code instances
- `error_validity.py`: function to perform validity checks for the error bars from non-smooth profiles
- `trview_cmdline.py`: a non-GUI version of the `trview` code
- `ASTRA_prepare.py`: merges all necessary data to prepare the input for an `ASTRA` run
- `ASTRA_fit_parallel.py`: wrapper to run and iterate on `ASTRA` runs and derive the experimental momentum transport coefficients together with their uncertainties. Includes all steps in the red, dashed rectangle.
- `ASTRA_read_mult.py`: plotting functions comparing `ASTRA` runs and experimental data
- `ASTRA_read_errors.py`: plotting functions to compare results of the momentum transport analysis and experimental data. Includes functions to map the scanned parameter space.
- `GKW_perform.py`: writes input for `CHEASE` and `GKW`, supervises the calculation and analyzes the results. Includes plotting functions to compare to the experimental momentum transport analysis.
- `scaling_law_fitting.py`: provides a flexible library to fit scaling laws

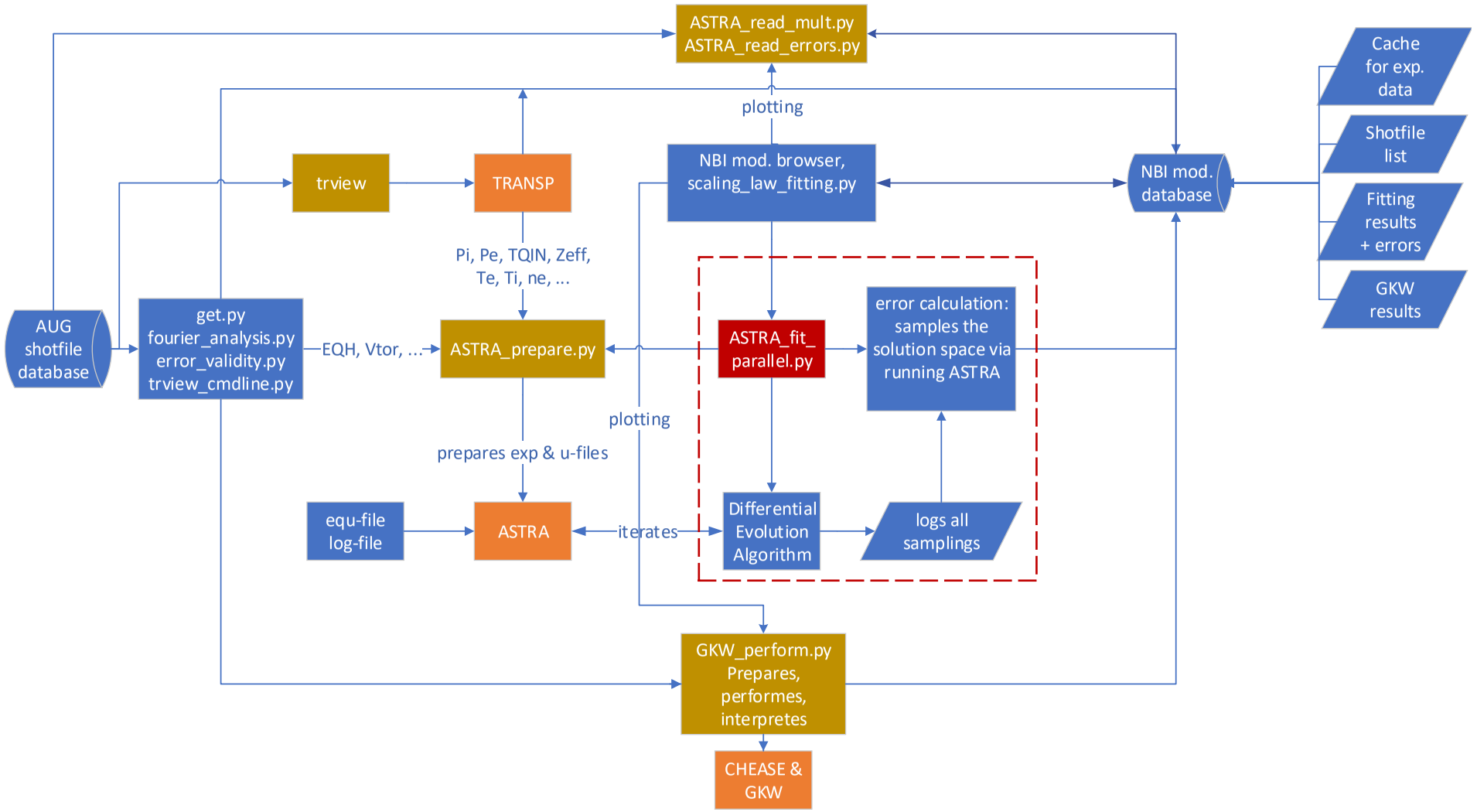

Figure A.1: Flow of data within the analysis framework. In orange, the major codes are shown. Dark yellow marks routines that prepare input data. In red, the experimental momentum transport analysis is marked. All functions can be started and controlled from the *NBI modulation browser*.

Appendix B

Additional Material

B.1 Tables

Analyzed Discharges for Gyrokinetic Database

Discharge #	t_{Begin} [s]	t_{End} [s]	f_{mod} [Hz]	I_p [MA]	P_{NBI} [MW]	P_{ECRH} [MW]
41551	6.4	7.6	5	0.8	6.73	0.78
41550	1.8	4.2	5	0.8	4.01	0.78
40797	4.2	6.0	5	0.6	2.74	2.91
40797	2.0	4.0	5	0.6	2.75	0.0
40076	4.2	6.4	5	0.8	5.21	0.61
40076	2.0	4.2	5	0.8	5.22	0.64
39333	7.16	9.16	3	0.6	2.86	4.98
39018	5.5	6.83	3	0.6	8.97	1.59
39016	5.5	7.83	3	0.6	6.65	0.81
39016	2.17	5.5	3	0.6	6.66	0.84
39015	7.0	9.34	3	0.6	2.89	0.0
39015	4.5	6.83	3	0.6	2.89	2.4
39015	2.33	4.33	3	0.6	2.9	5.2
39014	7.0	9.34	3	0.6	2.88	2.35
39014	4.5	6.83	3	0.6	2.86	3.82
39014	2.33	4.33	3	0.6	2.88	5.21
39013	3.0	4.33	3	0.6	2.78	5.24
34042	6.12	7.4	7	0.8	5.2	0.59
34042	1.83	3.5	3	0.8	5.33	0.61
34027	6.48	7.48	7	0.8	5.21	0.57
34027	1.83	3.5	3	0.8	5.35	0.61
30393	2.29	2.99	10	1.1	10.31	1.81
29230	1.9	3.9	2	0.8	5.32	0.57
29217	5.69	6.99	10	0.6	3.01	3.41
29216	1.99	4.49	2	0.6	3.01	0.58
28043	4.4	7.0	10	0.7	4.33	0.48
28043	1.89	4.4	2	0.7	4.36	0.5
26270	2.1	3.9	10	0.7	3.05	0.82
26235	4.5	6.9	10	0.7	6.65	0.0

Table B.1: List of discharges used for the database approach in Chapter 6.

Analyzed Discharges for Experimental Analysis

Discharge #	t_{Begin} [s]	t_{End} [s]	f_{mod} [Hz]	I_p [MA]	P_{NBI} [MW]	P_{ECRH} [MW]
(1) 41551	6.4	7.6	5	0.8	6.73	0.78
(2) 41550	1.8	4.2	5	0.8	4.01	0.78
(3) 40797	2.0	4.0	5	0.6	2.75	0.0
(4) 40076	4.2	6.4	5	0.8	5.21	0.61
(5) 40076	2.0	4.2	5	0.8	5.22	0.64
(6) 39015	7.0	9.34	3	0.6	2.89	0.0
(7) 34027	1.83	3.5	3	0.8	5.35	0.61
(8) 29216	1.99	4.49	2	0.6	3.01	0.58

Table B.2: List of discharges analyzed in Chapter 7.

B.2 Figures

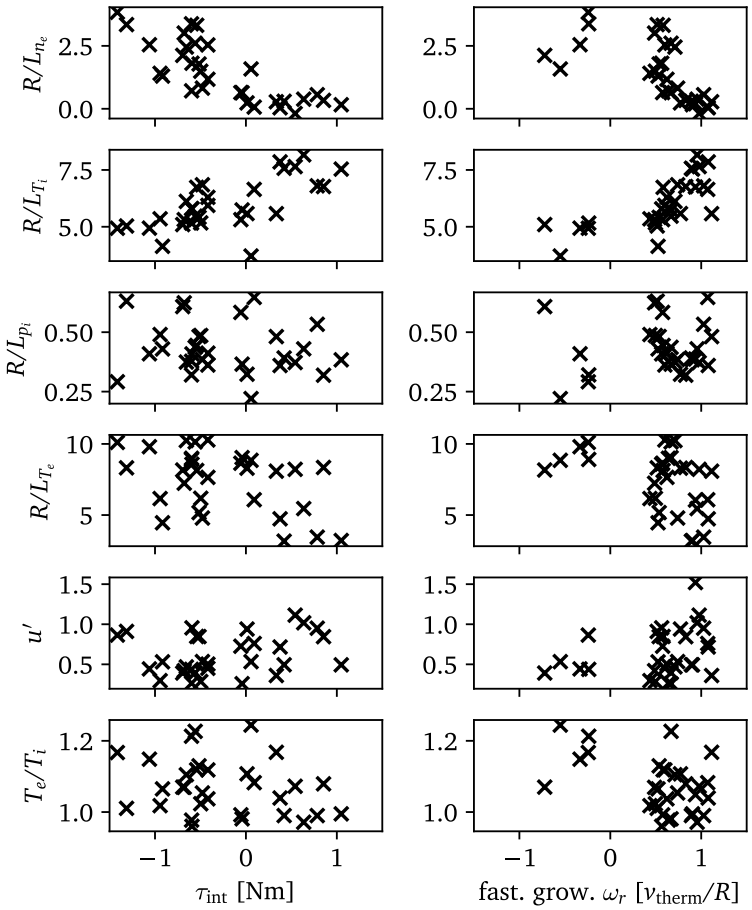

Figure B.1: Core intrinsic torque values $\rho_\varphi = 0.3 - 0.6$ and corresponding ω_r from GKW plotted versus various dimensionless parameters for the discharges from Tab. B.2.

Bibliography

[1] F. Wagner. “Fusion energy”. In: *MRS Energy & Sustainability* 5.1 (2018). DOI: 10.1557/mre.2018.8. URL: https://doi.org/10.1557/mre.2018.8.

[2] *Climate Change 2013: The Physical Science Basis. Contribution of Working Group I to the Fifth Assessment Report of the Intergovernmental Panel on Climate Change*. Cambridge University Press, 2013, p. 1535. ISBN: ISBN 978-1-107-66182-0. DOI: 10.1017/CBO9781107415324. URL: www.climatechange2013.org.

[3] T. Hamacher and A. M. Bradshaw. “Fusion as a future power source: recent achievements and prospects”. In: *18th World Energy Congress* (2001). URL: https://fire.pppl.gov/energy_eu_wec01.pdf.

[4] R. Dux. *Vorlesungsskript Plasmaphysik und Fusionsforschung II*. Universität Augsburg, 2010.

[5] J. P. Freidberg. *Plasma Physics and Fusion Energy*. Cambridge University Press, 2008. ISBN: 978-1-139-46215-0.

[6] U. Stroth. *Plasmaphysik*. Springer Berlin Heidelberg, 2018. DOI: 10.1007/978-3-662-55236-0. URL: https://doi.org/10.1007/978-3-662-55236-0.

[7] А. Д. Сахаров. “Теория магнитного термоядерного реактора”. In: Физика плазмы и проблема 4.2 (1958). (A. D. Sacharov. "Theory of a magnetic thermonuclear reactor" in *Physics of Plasmas and their Problems* 4.2, by the Academy of Science of the USSR), p. 20.

[8] И. Е. Тамм. “Теория магнитного термоядерного реактора”. In: Физика плазмы и проблема 4.1 (1958). (I. E. Tamm. "Theory of a magnetic thermonuclear reactor" in *Physics of Plasmas and their Problems* 4.1, by the Academy of Science of the USSR), p. 31.

[9] Б. Б. Кадомцев. “От МТР до ИТЭР”. In: Успехи физических наук 166.5 (1996). (B. B. Kadomtsev. "From MTR to ITER" in *Advances in Physical Sciences* 166.5), pp. 449–458. DOI: 10.3367/ufnr.0166.199605b.0449. URL: https://doi.org/10.3367/ufnr.0166.199605b.0449.

[10] H. Grad and H. Rubin. “Hydromagnetic equilibria and force-free fields”. In: *Journal of Nuclear Energy (1954)* 7.3-4 (1958), pp. 284–285.

[11] V. D. Shafranov. “Plasma equilibrium in a magnetic field”. In: *Reviews of plasma physics* 2 (1966), p. 103.

[12] J. D. Lawson. “Some Criteria for a Power Producing Thermonuclear Reactor”. In: *Proceedings of the Physical Society. Section B* 70.1 (1957), pp. 6–10. DOI: 10.1088/0370-1301/70/1/303. URL: https://doi.org/10.1088%2F0370-1301%2F70%2F1%2F303.

[13] J. Wesson and D. J. Campbell. *Tokamaks*. OUP Oxford, 2011. ISBN: 978-0-199-59223-4.

[14] T. Görler et al. “The global version of the gyrokinetic turbulence code GENE”. In: *Journal of Computational Physics* 230.18 (2011), pp. 7053–7071. ISSN: 0021-9991. DOI: https://doi.org/10.1016/j.jcp.2011.05.034. URL: https://www.sciencedirect.com/science/article/pii/S0021999111003457.

[15] F. Jenko. “Auf dem Weg zu einem virtuellen Fusionsplasma”. In: (2018). [Accessed 17-10-2023]. DOI: 10.17617/1.65. URL: https://www.mpg.de/11812008.

[16] M. Bernert. “Analysis of the H-mode Density Limit in the ASDEX Upgrade Tokamak Using Bolometry”. PhD thesis. Ludwig-Maximilians-Universität München, 2013. URL: https://edoc.ub.uni-muenchen.de/16262.

[17] X. Garbet et al. “Physics of transport in tokamaks”. In: *Plasma Physics and Controlled Fusion* 46.12B (2004), B557–B574. DOI: 10.1088/0741-3335/46/12b/045. URL: https://doi.org/10.1088%2F0741-3335%2F46%2F12b%2F045.

[18] P. Mantica et al. “Progress and challenges in understanding core transport in tokamaks in support to ITER operations”. In: *Plasma Physics and Controlled Fusion* 62.1 (2019), p. 014021. DOI: 10.1088/1361-6587/ab5ae1. URL: https://doi.org/10.1088%2F1361-6587%2Fab5ae1.

[19] F. Ryter et al. “Experimental Characterization of the Electron Heat Transport in Low-Density ASDEX Upgrade Plasmas”. In: *Physical Review Letters* 86 (24 2001), pp. 5498–5501. DOI: 10.1103/PhysRevLett.86.5498. URL: https://link.aps.org/doi/10.1103/Phy%20sRevLett.86.5498.

[20] F. Ryter et al. “Electron heat transport in ASDEX Upgrade: experiment and modelling”. In: *Nuclear Fusion* 43.11 (2003), pp. 1396–1404. DOI: 10.1088/0029-5515/43/11/011. URL: https://doi.org/10.1088/0029-5515/43/11/011.

[21] F. Ryter et al. “Simultaneous analysis of ion and electron heat transport by power modulation in JET”. In: *Nuclear Fusion* 51.11 (2011), p. 113016. DOI: 10.1088/0029-5515/51/11/113016. URL: https://doi.org/10.1088/0029-5515/51/11/113016.

[22] F. Ryter et al. “Heat transport driven by the ion temperature gradient and electron temperature gradient instabilities in ASDEX Upgrade H-modes”. In: *Nuclear Fusion* 59.9 (2019), p. 096052. DOI: 10.1088/1741-4326/ab3061. URL: https://dx.doi.org/10.1088/1741-4326/ab3061.

[23] C. Angioni et al. “Particle transport in tokamak plasmas, theory and experiment”. In: *Plasma Physics and Controlled Fusion* 51.12 (2009), p. 124017. DOI: 10.1088/0741-3335/51/12/124017. URL: https://dx.doi.org/10.1088/0741-3335/51/12/124017.

[24] D. R. Baker et al. “Measurement of electron particle transport coefficients in different operational modes of DIII-D”. In: *Nuclear Fusion* 38.4 (1998), pp. 485–494. DOI: 10.1088/0029-5515/38/4/301. URL: https://doi.org/10.1088/0029-5515/38/4/301.

[25] K. W. Gentle et al. “Determination of particle transport coefficients in ASDEX by gas modulation”. In: *Nuclear Fusion* 32.2 (1992), pp. 217–237. DOI: 10.1088/0029-5515/32/2/i03. URL: https://doi.org/10.1088/0029-5515/32/2/i03.

[26] C. Angioni et al. “The impact of poloidal asymmetries on tungsten transport in the core of JET H-mode plasmas”. In: *Physics of Plasmas* 22.5 (2015), p. 055902. DOI: 10.1063/1.4919036. URL: https://doi.org/10.1063/1.4919036.

[27] F. J. Casson et al. “Theoretical description of heavy impurity transport and its application to the modelling of tungsten in JET and ASDEX upgrade”. In: *Plasma Physics and Controlled Fusion* 57.1 (2014), p. 014031. DOI: 10.1088/0741-3335/57/1/014031. URL: https://doi.org/10.1088/0741-3335/57/1/014031.

[28] F. J. Casson et al. “Validation of gyrokinetic modelling of light impurity transport including rotation in ASDEX Upgrade”. In: *Nuclear Fusion* 53.6 (2013), p. 063026. DOI: 10.1088/0029-5515/53/6/063026. URL: https://dx.doi.org/10.1088/0029-5515/53/6/063026.

[29] C. Angioni et al. “Analytic formulae for centrifugal effects on turbulent transport of trace impurities in tokamak plasmas”. In: *Physics of Plasmas* 19.12 (2012), p. 122311. DOI: 10.1063/1.4773051. URL: https://doi.org/10.1063/1.4773051.

[30] C. Angioni et al. “Tungsten transport in JET H-mode plasmas in hybrid scenario, experimental observations and modelling”. In: *Nuclear Fusion* 54.8 (2014), p. 083028. DOI: 10.1088/0029-5515/54/8/083028. URL: https://dx.doi.org/10.1088/0029-5515/54/8/083028.

[31] H. Biglari et al. “Influence of sheared poloidal rotation on edge turbulence”. In: *Physics of Fluids B: Plasma Physics* 2.1 (1990), pp. 1–4. DOI: 10.1063/1.859529. URL: https://doi.org/10.1063/1.859529.

[32] R. E. Waltz et al. “Advances in the simulation of toroidal gyro-Landau fluid model turbulence”. In: *Physics of Plasmas* 2.6 (1995), pp. 2408–2416. DOI: 10.1063/1.871264. URL: https://doi.org/10.1063/1.871264.

[33] T. S. Hahm. “Rotation shear induced fluctuation decorrelation in a toroidal plasma”. In: *Physics of Plasmas* 1.9 (1994), pp. 2940–2944. DOI: 10.1063/1.870534. URL: https://doi.org/10.1063/1.870534.

[34] T. S. Hahm and K. H. Burrell. “Flow shear induced fluctuation suppression in finite aspect ratio shaped tokamak plasma”. In: *Physics of Plasmas* 2.5 (1995), pp. 1648–1651. DOI: 10.1063/1.871313. URL: https://doi.org/10.1063/1.871313.

[35] K. H. Burrell. “Effects of E×B velocity shear and magnetic shear on turbulence and transport in magnetic confinement devices”. In: *Physics of Plasmas* 4.5 (1997), pp. 1499–1518. DOI: 10.1063/1.872367. URL: https://doi.org/10.1063/1.872367.

[36] P. W. Terry. “Suppression of turbulence and transport by sheared flow”. In: *Reviews of Modern Physics* 72 (1 2000), pp. 109–165. DOI: 10.1103/RevModPhys.72.109. URL: https://link.aps.org/doi/10.1103/RevModPhys.72.109.

[37] P. C. de Vries et al. “Survey of disruption causes at JET”. In: *Nuclear Fusion* 51.5 (2011), p. 053018. DOI: 10.1088/0029-5515/51/5/053018. URL: https://doi.org/10.1088/0029-5515/51/5/053018.

[38] P. A. Politzer et al. “Influence of toroidal rotation on transport and stability in hybrid scenario plasmas in DIII-D”. In: *Nuclear Fusion* 48.7 (2008), p. 075001. DOI: 10.1088/0029-5515/48/7/075001. URL: https://doi.org/10.1088/0029-5515/48/7/075001.

[39] R. J. Buttery et al. “Multimachine extrapolation of neoclassical tearing mode physics to ITER”. In: *Proceedings of 22nd IAEA Fusion Energy Conference* (2008). URL: https://infoscience.epfl.ch/record/135075/files/buttery_iaea_08.pdf.

[40] E. J. Strait et al. “Wall Stabilization of High Beta Tokamak Discharges in DIII-D”. In: *Physical Review Letters* 74 (13 1995), pp. 2483–2486. DOI: 10.1103/PhysRevLett.74.2483. URL: https://link.aps.org/doi/10.1103/PhysRevLett.74.2483.

[41] A. M. Garofalo et al. “Sustained Stabilization of the Resistive-Wall Mode by Plasma Rotation in the DIII-D Tokamak”. In: *Physical Review Letters* 89 (23 2002), p. 235001. DOI: 10.1103/PhysRevLett.89.235001. URL: https://link.aps.org/doi/10.1103/PhysRevLett.89.235001.

[42] H. Reimerdes et al. “Reduced Critical Rotation for Resistive-Wall Mode Stabilization in a Near-Axisymmetric Configuration”. In: *Physical Review Letters* 98 (5 2007), p. 055001. DOI: 10.1103/PhysRevLett.98.055001. URL: https://link.aps.org/doi/10.1103/PhysRevLett.98.055001.

[43] A. G. Peeters et al. “Toroidal Momentum Pinch Velocity due to the Coriolis Drift Effect on Small Scale Instabilities in a Toroidal Plasma”. In: *Physical Review Letters* 98.26 (2007), p. 265003. DOI: 10.1103/physrevlett.98.265003. URL: https://doi.org/10.1103/physrevlett.98.265003.

[44] T. S. Hahm et al. “Nonlinear gyrokinetic theory of toroidal momentum pinch”. In: *Physics of Plasmas* 14.7 (2007), p. 072302. ISSN: 1070-664X. DOI: 10.1063/1.2743642. URL: https://doi.org/10.1063/1.2743642.

[45] D. Strintzi et al. “The toroidal momentum diffusivity in a tokamak plasma: A comparison of fluid and kinetic calculations”. In: *Physics of Plasmas* 15.4 (2008), p. 044502. DOI: 10.1063/1.2907370. URL: https://doi.org/10.1063/1.2907370.

[46] T. S. Hahm et al. “Turbulent equipartition theory of toroidal momentum pinch”. In: *Physics of Plasmas* 15.5 (2008), p. 055902. ISSN: 1070-664X. DOI: 10.1063/1.2839293. URL: https://doi.org/10.1063/1.2839293.

[47] P. H. Diamond et al. “Physics of non-diffusive turbulent transport of momentum and the origins of spontaneous rotation in tokamaks”. In: *Nuclear Fusion* 49.4 (2009), p. 045002. DOI: 10.1088/0029-5515/49/4/045002. URL: https://doi.org/10.1088%2F0029-5515%2F49%2F4%2F045002.

[48] A. G. Peeters et al. “Overview of toroidal momentum transport”. In: *Nuclear Fusion* 51.9 (2011), p. 094027. DOI: 10.1088/0029-5515/51/9/094027. URL: https://doi.org/10.1088/0029-5515/51/9/094027.

[49] T. Stoltzfus-Dueck. “Transport-Driven Toroidal Rotation in the Tokamak Edge”. In: *Physical Review Letters* 108 (6 2012), p. 065002. DOI: 10.1103/PhysRevLett.108.065002. URL: https://link.aps.org/doi/10.1103/PhysRevLett.108.065002.

[50] Y. Camenen et al. “Transport of Parallel Momentum Induced by Current-Symmetry Breaking in Toroidal Plasmas”. In: *Physical Review Letters* 102 (12 2009), p. 125001. DOI: 10.1103/PhysRevLett.102.125001. URL: https://link.aps.org/doi/10.1103/PhysRevLett.102.125001.

[51] Y. Camenen et al. “Consequences of profile shearing on toroidal momentum transport”. In: *Nuclear Fusion* 51.7 (2011), p. 073039. DOI: 10.1088/0029-5515/51/7/073039. URL: https://doi.org/10.1088%2F0029-5515%2F51%2F7%2F073039.

[52] N. Holtkamp. “An overview of the ITER project”. In: *Fusion Engineering and Design* 82.5 (2007). Proceedings of the 24th Symposium on Fusion Technology, pp. 427–434. ISSN: 0920-3796. DOI: https://doi.org/10.1016/j.fusengdes.2007.03.029. URL: https://www.sciencedirect.com/science/article/pii/S0920379607001160.

[53] F. L. Hinton and R. D. Hazeltine. “Theory of plasma transport in toroidal confinement systems”. In: *Reviews of Modern Physics* 48 (2 1976), pp. 239–308. DOI: 10.1103/RevModPhys.48.239. URL: https://link.aps.org/doi/10.1103/RevModPhys.48.239.

[54] B. Scott and J. Smirnov. “Energetic consistency and momentum conservation in the gyrokinetic description of tokamak plasmas”. In: *Physics of Plasmas* 17.11 (2010), p. 112302. ISSN: 1070-664X. DOI: 10.1063/1.3507920. URL: https://doi.org/10.1063/1.3507920.

[55] A. Lebschy et al. “Measurement of the complete core plasma flow across the LOC–SOC transition at ASDEX Upgrade”. In: *Nuclear Fusion* 58.2 (2017), p. 026013. DOI: 10.1088/1741-4326/aa9c54. URL: https://dx.doi.org/10.1088/1741-4326/aa9c54.

[56] W. D. D’haeseleer et al. *Flux Coordinates and Magnetic Field Structure*. Springer Berlin Heidelberg, 1991. DOI: 10.1007/978-3-642-75595-8. URL: https://doi.org/10.1007/978-3-642-75595-8.

[57] P. Helander and D. J. Sigmar. *Collisional Transport in Magnetized Plasmas*. Cambridge Monographs on Plasma Physics. Cambridge University Press, 2002. ISBN: 9780521807982.

[58] G. Tardini. “Validation of theory based transport models in tokamak plasmas”. PhD thesis. Technische Universität München, 2003. URL: https://mediatum.ub.tum.de/603004.

[59] A. G. Peeters and C. Angioni. “Linear gyrokinetic calculations of toroidal momentum transport in a tokamak due to the ion temperature gradient mode”. In: *Physics of Plasmas* 12.7 (2005), p. 072515. DOI: 10.1063/1.1949608. URL: https://doi.org/10.1063/1.1949608.

[60] P. N. Guzdar et al. “Ion-temperature-gradient instability in toroidal plasmas”. In: *The Physics of Fluids* 26.3 (1983), pp. 673–677. ISSN: 0031-9171. DOI: 10.1063/1.864182. URL: https://doi.org/10.1063/1.864182.

[61] T. Dannert and F. Jenko. “Gyrokinetic simulation of collisionless trapped-electron mode turbulence”. In: *Physics of Plasmas* 12.7 (2005), p. 072309. ISSN: 1070-664X. DOI: 10.1063/1.1947447. URL: https://doi.org/10.1063/1.1947447.

[62] F. Ryter et al. “Experimental Study of Trapped-Electron-Mode Properties in Tokamaks: Threshold and Stabilization by Collisions”. In: *Physical Review Letters* 95 (8 2005), p. 085001. DOI: 10.1103/PhysRevLett.95.085001. URL: https://link.aps.org/doi/10.1103/PhysRevLett.95.085001.

[63] A. Scheinberg. *Ion temperature gradient instability*. [Accessed 17-10-2023]. 2016. URL: http://fusionwiki.ciemat.es/wiki/Ion_Temperature_Gradient_instability.

[64] R. G. Littlejohn. “Variational principles of guiding centre motion”. In: *Journal of Plasma Physics* 29.1 (1983), pp. 111–125. DOI: 10.1017/S002237780000060X.

[65] T. S. Hahm. “Nonlinear gyrokinetic equations for tokamak microturbulence”. In: *The Physics of Fluids* 31.9 (1988), pp. 2670–2673. ISSN: 0031-9171. DOI: 10.1063/1.866544. URL: https://doi.org/10.1063/1.866544.

[66] A. Brizard. “Nonlinear gyrokinetic Maxwell-Vlasov equations using magnetic coordinates”. In: *Journal of Plasma Physics* 41.3 (1989), pp. 541–559. DOI: 10.1017/S0022377800014070.

[67] H. Sugama. “Gyrokinetic field theory”. In: *Physics of Plasmas* 7.2 (2000), pp. 466–480. ISSN: 1070-664X. DOI: 10.1063/1.873832. URL: https://doi.org/10.1063/1.873832.

[68] A. G. Peeters et al. “The nonlinear gyro-kinetic flux tube code GKW”. In: *Computer Physics Communications* 180.12 (2009), pp. 2650–2672. ISSN: 0010-4655. DOI: https://doi.org/10.1016/j.cpc.2009.07.001. URL: http://www.sciencedirect.com/science/article/pii/S0010465509002112.

[69] C. Angioni et al. “Off-diagonal particle and toroidal momentum transport: a survey of experimental, theoretical and modelling aspects”. In: *Nuclear Fusion* 52.11 (2012), p. 114003. DOI: 10.1088/0029-5515/52/11/114003. URL: https://doi.org/10.1088%2F0029-5515%2F52%2F11%2F114003.

[70] N. Mattor and P. H. Diamond. “Momentum and thermal transport in neutral-beam-heated tokamaks”. In: *Physics of Fluids* 31.5 (1988), p. 1180. DOI: 10.1063/1.866747. URL: https://doi.org/10.1063/1.866747.

[71] R. E. Waltz et al. “Coupled ion temperature gradient and trapped electron mode to electron temperature gradient mode gyrokinetic simulationsa)”. In: *Physics of Plasmas* 14.5 (2007), p. 056116. ISSN: 1070-664X. DOI: 10.1063/1.2436851. URL: https://doi.org/10.1063/1.2436851.

[72] J. Weiland et al. “Symmetry breaking effects of toroidicity on toroidal momentum transport”. In: *Nuclear Fusion* 49.6 (2009), p. 065033. DOI: 10.1088/0029-5515/49/6/065033. URL: https://dx.doi.org/10.1088/0029-5515/49/6/065033.

[73] A. G. Peeters et al. “Toroidal momentum transport”. In: *Plasma Physics and Controlled Fusion* 48.12B (2006), B413. DOI: 10.1088/0741-3335/48/12B/S39. URL: https://dx.doi.org/10.1088/0741-3335/48/12B/S39.

[74] I. Holod and Z. Lin. “Gyrokinetic particle simulations of toroidal momentum transport”. In: *Physics of Plasmas* 15.9 (2008). 092302. ISSN: 1070-664X. DOI: 10.1063/1.2977769. URL: https://doi.org/10.1063/1.2977769.

[75] I. Holod and Z. Lin. “Effects of electron dynamics in toroidal momentum transport driven by ion temperature gradient turbulence”. In: *Plasma Physics and Controlled Fusion* 52.3 (2010), p. 035002. DOI: 10.1088/0741-3335/52/3/035002. URL: https://dx.doi.org/10.1088/0741-3335/52/3/035002.

[76] F. J. Casson et al. “Anomalous parallel momentum transport due to E×B flow shear in a tokamak plasma”. In: *Physics of Plasmas* 16.9 (2009), p. 092303. ISSN: 1070-664X. DOI: 10.1063/1.3227650. URL: https://doi.org/10.1063/1.3227650.

[77] A. G. Peeters et al. “The influence of the self-consistent mode structure on the Coriolis pinch effect”. In: *Physics of Plasmas* 16.6 (2009), p. 062311. DOI: 10.1063/1.3124133. URL: https://doi.org/10.1063/1.3124133.

[78] Y. Camenen et al. “Impact of the background toroidal rotation on particle and heat turbulent transport in tokamak plasmas”. In: *Physics of Plasmas* 16.1 (2009), p. 012503. ISSN: 1070-664X. DOI: 10.1063/1.3057356. URL: https://doi.org/10.1063/1.3057356.

[79] A. G. Peeters et al. “Influence of the centrifugal force and parallel dynamics on the toroidal momentum transport due to small scale turbulence in a tokamak”. In: *Physics of Plasmas* 16.4 (2009), p. 042310. DOI: 10.1063/1.3097263. URL: https://doi.org/10.1063/1%20.3097263.

[80] E. Fable. “A toroidal momentum transport equation for axisymmetric 1D transport codes”. In: *Plasma Physics and Controlled Fusion* 57.4 (2015), p. 045007. DOI: 10.1088/0741-3335/57/4/045007. URL: https://dx.doi.org/10.1088/0741-3335/57/4/045007.

[81] F. I. Parra and M. Barnes. “Intrinsic rotation in tokamaks: theory”. In: *Plasma Physics and Controlled Fusion* 57.4 (2015), p. 045002. DOI: 10.1088/0741-3335/57/4/045002. URL: https://dx.doi.org/10.1088/0741-3335/57/4/045002.

[82] E. Fable et al. “The role of the source versus the collisionality in predicting a reactor density profile as observed on ASDEX Upgrade discharges”. In: *Nuclear Fusion* 59.7 (2019), p. 076042. DOI: 10.1088/1741-4326/ab1f28. URL: https://dx.doi.org/10.1088/1741-4326/%20ab1f28.

[83] Y. Camenen et al. “Intrinsic rotation driven by the electrostatic turbulence in up-down asymmetric toroidal plasmas”. In: *Physics of Plasmas* 16.6 (2009). 062501. ISSN: 1070-664X. DOI: 10.1063/1.3138747. URL: https://doi.org/10.1063/1.3138747.

[84] G. M. Staebler et al. “New Paradigm for Suppression of Gyrokinetic Turbulence by Velocity Shear”. In: *Physical Review Letters* 110 (5 2013), p. 055003. DOI: 10.1103/PhysRevLett.110.055003. URL: https://link.aps.org/doi/10.1103/PhysR%20evLett.110.055003.

[85] R. E. Waltz et al. “Gyrokinetic simulation of momentum transport with residual stress from diamagnetic level velocity shears”. In: *Physics of Plasmas* 18.4 (2011). 042504. ISSN: 1070-664X. DOI: 10.1063/1.3579481. URL: https://doi.org/10.1063/1.3579481.

[86] R. R. Dominguez and G. M. Staebler. “Anomalous momentum transport from drift wave turbulence”. In: *Physics of Fluids B: Plasma Physics* 5.11 (1993), pp. 3876–3886. DOI: 10.1063/1.860610. URL: https://doi.org/10.1063/1.860610.

[87] X. Garbet et al. “Turbulence simulations of transport barriers with toroidal velocity”. In: *Physics of Plasmas* 9.9 (2002), pp. 3893–3905.

[88] Ö. D. Gürcan et al. “Intrinsic rotation and electric field shear”. In: *Physics of Plasmas* 14.4 (2007), p. 042306. DOI: 10.1063/1.2717891. URL: https://doi.org/10.1063/1.2717891.

[89] N. Fedorczak et al. “Dynamics of tilted eddies in a transversal flow at the edge of tokamak plasmas and the consequences for L–H transition”. In: *Plasma Physics and Controlled Fusion* 55.12 (2013), p. 124024. DOI: 10.1088/0741-3335/55/12/124024. URL: https://dx.doi.org/10.1088/0741-3335/55/12/124024.

[90] P. H. Diamond et al. “Transport of parallel momentum by collisionless drift wave turbulence”. In: *Physics of Plasmas* 15.1 (2008), p. 012303. DOI: 10.1063/1.2826436. URL: https://doi.org/10.1063/1%20.2826436.

[91] Ö. D. Gürcan et al. “A simple model of intrinsic rotation in high confinement regime tokamak plasmas”. In: *Physics of Plasmas* 17.3 (2010). 032509. ISSN: 1070-664X. DOI: 10.1063/1.3339909. URL: https://doi.org/10.1063/1.3339909.

[92] C. J. McDevitt et al. “Toroidal Rotation Driven by the Polarization Drift”. In: *Physical Review Letters* 103 (20 2009), p. 205003. DOI: 10.1103/PhysRevLett.103.205003. URL: https://link.aps.org/doi/10.1103/PhysRevLett.103.205003.

[93] C. J. McDevitt et al. “A novel mechanism for exciting intrinsic toroidal rotation”. In: *Physics of Plasmas* 16.5 (2009). 052302. ISSN: 1070-664X. DOI: 10.1063/1.3122048. URL: https://doi.org/10.1063/1.3122048.

[94] F. I. Parra and P. J. Catto. “Turbulent transport of toroidal angular momentum in low flow gyrokinetics”. In: *Plasma Physics and Controlled Fusion* 52.4 (2010), p. 045004. DOI: 10.1088/0741-3335/52/4/045004. URL: https://dx.doi.org/10.1088/0741-3335/52/4/045004.

[95] J. S. DeGrassie et al. “Intrinsic toroidal velocity near the edge of DIII-D H-mode plasmas”. In: *Nuclear Fusion* 49.8 (2009), p. 085020. DOI: 10.1088/0029-5515/49/8/085020. URL: https://dx.doi.org/10.1088/0029-5515/49/8/085020.

[96] P. C. de Vries et al. “Scaling of rotation and momentum confinement in JET plasmas”. In: *Nuclear Fusion* 48.6 (2008), p. 065006. DOI: 10.1088/0029-5515/48/6/065006. URL: https://doi.org/10.1088/0029-5515/48/6/065006.

[97] M. Honda et al. “Numerical analysis of the effect of fast-ion losses on plasma rotation in a tokamak with toroidal field ripple”. In: *Nuclear Fusion* 48.8 (2008), p. 085003. DOI: 10.1088/0029-5515/48/8/085003. URL: https://dx.doi.org/10.1088/0029-5515/48/8/085003.

[98] P. Monier-Garbet et al. “Effects of neutrals on plasma rotation in DIII-D”. In: *Nuclear Fusion* 37.3 (1997), p. 403. DOI: 10.1088/0029-5515/37/3/I09. URL: https://dx.doi.org/10.1088/0029-5515/37/3/I09.

[99] T. W. Versloot et al. “Momentum losses by charge exchange with neutral particles in H-mode discharges at JET”. In: *Plasma Physics and Controlled Fusion* 53.6 (2011), p. 065017. DOI: 10.1088/0741-3335/53/6/065017. URL: https://dx.doi.org/10.1088/0741-3335/53/6/065017.

[100] J. D. Callen. “Effects of 3D magnetic perturbations on toroidal plasmas”. In: *Nuclear Fusion* 51.9 (2011), p. 094026. DOI: 10.1088/0029-5515/51/9/094026. URL: https://dx.doi.org/10.1088/0029-5515/51/9/094026.

[101] K. C. Shaing et al. “Neoclassical plasma viscosity and transport processes in non-axisymmetric tori”. In: *Nuclear Fusion* 55.12 (2015), p. 125001. DOI: 10.1088/0029-5515/55/12/125001. URL: https://dx.doi.org/10.1088/0029-5515/55/12/125001.

[102] T. Stoltzfus-Dueck. “Tokamak-edge toroidal rotation due to inhomogeneous transport and geodesic curvaturea)”. In: *Physics of Plasmas* 19.5 (2012), p. 055908. ISSN: 1070-664X. DOI: 10.1063/1.4718335. URL: https://doi.org/10.1063/1.4718335.

[103] T. Stoltzfus-Dueck et al. “X-Point-Position-Dependent Intrinsic Toroidal Rotation in the Edge of the TCV Tokamak”. In: *Physical Review Letters* 114 (24 2015), p. 245001. DOI: 10.1103/PhysRevLett.114.245001. URL: https://link.aps.org/doi/10.1103/PhysRevLett.114.245001.

[104] T. Stoltzfus-Dueck et al. “X-point position dependence of edge intrinsic toroidal rotation on the Tokamak à Configuration Variable”. In: *Physics of Plasmas* 22.5 (2015), p. 056118. ISSN: 1070-664X. DOI: 10.1063/1.4921158. URL: https://doi.org/10.1063/1%20.4921158.

[105] T. Luda et al. “Integrated modeling of ASDEX Upgrade plasmas combining core, pedestal and scrape-off layer physics”. In: *Nuclear Fusion* 60.3 (2020), p. 036023. DOI: 10.1088/1741-4326/ab6c77. URL: https://dx.doi.org/10.1088/1741-4326/ab6c77.

[106] T. Luda et al. “Validation of a full-plasma integrated modeling approach on ASDEX Upgrade”. In: *Nuclear Fusion* 61.12 (2021), p. 126048. DOI: 10.1088/1741-4326/ac3293. URL: https://dx.doi.org/10.1088/1741-4326/ac3293.

[107] T. Luda et al. “Validation of IMEP on Alcator C-Mod and JET-ILW ELMy H-mode plasmas”. In: *Plasma Physics and Controlled Fusion* 65.3 (2023), p. 034001. DOI: 10.1088/1361-6587/acb011. URL: https://dx.doi.org/10.1088/1361-6587/acb011.

[108] K.-D. Zastrow et al. “Transfer rates of toroidal angular momentum during neutral beam injection”. In: *Nuclear Fusion* 38.2 (1998), p. 257. DOI: 10.1088/0029-5515/38/2/309. URL: https://dx.doi.org/10.1088/0029-5515/38/2/309.

[109] F. L. Hinton and J. A. Robertson. “Neoclassical dielectric property of a tokamak plasma”. In: *The Physics of Fluids* 27.5 (1984), pp. 1243–1247. ISSN: 0031-9171. DOI: 10.1063/1.864478. URL: https://doi.org/10.1063/1.864478.

[110] W. G. F. Core and K.-D. Zastrow. *Efficient Time Dependent Modelling of the Physics of NBI Heating in JET*. Tech. rep. JET Joint Undertaking, 1996. URL: https://scipub.euro-fusion.org/wp-content/uploads/2014/11/JETR96001.pdf.

[111] R. J. Goldston et al. "New techniques for calculating heat and particle source rates due to neutral beam injection in axisymmetric tokamaks". In: *Journal of Computational Physics* 43.1 (1981), pp. 61–78. ISSN: 0021-9991. DOI: https://doi.org/10.1016/0021-9991(81)90111-X. URL: https://www.sciencedirect.com/science/article/pii/002199918190111X.

[112] N. Asakura et al. "Toroidal rotation and ion heating during neutral beam injection in PBX-M". In: *Nuclear Fusion* 33.8 (1993), p. 1165. DOI: 10.1088/0029-5515/33/8/I06. URL: https://dx.doi.org/10.1088/0029-5515/33/8/I06.

[113] R. J. Hawryluk. "An Empirical Approach to Tokamak Transport". In: *Physics of Plasmas Close to Thermonuclear Conditions* (1981), pp. 19–46. DOI: 10.1016/b978-1-4832-8385-2.50009-1. URL: https://doi.org/10.1016/b978-1-4832-8385-2.50009-1.

[114] J. Breslau et al. "TRANSP". In: *Princeton Plasma Physics Laboratory (PPPL), Princeton, New Jersey, United States* (2018). DOI: 10.11578/DC.20180627.4. URL: https://www.osti.gov/doecode/biblio/12542.

[115] *TRANSP documentation*. [Accessed 17-10-2023]. URL: https://w3.pppl.gov/~pshare/help/transp.htm.

[116] E. Poli et al. "TORBEAM 2.0, a paraxial beam tracing code for electron-cyclotron beams in fusion plasmas for extended physics applications". In: *Computer Physics Communications* 225 (2018), pp. 36–46. DOI: 10.1016/j.cpc.2017.12.018. URL: https://doi.org/10.1016/j.cpc.2017.12.018.

[117] A. Pankin et al. "The tokamak Monte Carlo fast ion module NUBEAM in the National Transport Code Collaboration library". In: *Computer Physics Communications* 159.3 (2004), pp. 157–184. ISSN: 0010-4655. DOI: https://doi.org/10.1016/j.cpc.2003.11.002. URL: https://www.sciencedirect.com/science/article/pii/S0010465504001109.

[118] G. Pereverzev and P. N. Yushmanov. "ASTRA Automated System for TRansport Analysis in a Tokamak". In: *Max Planck Institute for Plasma Physics, Garching, Germany* (2002). URL: https://pure.mpg.de/rest/items/item_2138238/component/file_2138237/content.

[119] E. Fable et al. "Novel free-boundary equilibrium and transport solver with theory-based models and its validation against ASDEX Upgrade current ramp scenarios". In: *Plasma Physics and Controlled Fusion* 55.12 (2013), p. 124028. DOI: 10.1088/0741-3335/55/12/124028. URL: https://dx.doi.org/10.1088/0741-3335/55/12/124028.

[120] A. A. Ivanov et al. "New adaptive grid plasma evolution code SPIDER". In: *Proceedings of 32nd EPS Conference on Plasma Physics* 29 (2005), pp. 5–63.

[121] W. A. Hornsby et al. "Global gyrokinetic simulations of intrinsic rotation in ASDEX Upgrade Ohmic L-mode plasmas". In: *Nuclear Fusion* 58.5 (2018), p. 056008. DOI: 10.1088/1741-4326/aab22f. URL: https://doi.org/10.1088%2F1741-4326%2Faab22f.

[122] W. X. Wang et al. "Gyrokinetic Studies on Turbulence-Driven and Neoclassical Nondiffusive Toroidal-Momentum Transport and the Effect of Residual Fluctuations in Strong $E \times B$ Shear". In: *Physical Review Letters* 102 (3 2009), p. 035005. DOI: 10.1103/PhysRevLett.102.035005. URL: https://link.aps.org/doi/10.1103/PhysRevLett.102.035005.

[123] W. X. Wang et al. “Nonlinear flow generation by electrostatic turbulence in tokamaks”. In: *Physics of Plasmas* 17.7 (2010), p. 072511. DOI: 10.1063/1.3459096. URL: https://doi.org/10.1063/1.3459096.

[124] B. A. Grierson et al. “Main-Ion Intrinsic Toroidal Rotation Profile Driven by Residual Stress Torque from Ion Temperature Gradient Turbulence in the DIII-D Tokamak”. In: *Physical Review Letters* 118 (1 2017), p. 015002. DOI: 10.1103/PhysRevLett.118.015002. URL: https://link.aps.org/doi/10.1103/PhysRevLett.118.015002.

[125] B. Streibl et al. “Machine design, fueling, and heating in ASDEX Upgrade”. In: *Fusion Science and Technology* 44 (2003), pp. 578–592. DOI: 10.13182/FST03-A400. URL: https://www.tandfonline.com/doi/citedby/10.13182/FST03-A400.

[126] *ASDEX Upgrade Drawing Gallery*. [Accessed 17-10-2023]. 2023. URL: https://www.aug.ipp.mpg.de/aug/local/aug_only/AUG_Aufbau/Drawing_Gallery/index.htm.

[127] V. Rohde et al. “Comparison of boronization and siliconization in ASDEX Upgrade”. In: *Proceedings of 26th EPS Conference on Controlled Fusion and Plasma Physics* (1999). URL: https://pure.mpg.de/rest/items/item_2224142/component/file_3376481/content.

[128] W. E. Gordon. “Incoherent scattering of radio waves by free electrons with applications to space exploration by radar”. In: *Proceedings of the IRE* 46.11 (1958), pp. 1824–1829. URL: https://ieeexplore.ieee.org/abstract/document/4065300.

[129] K. L. Bowles. “Observation of Vertical-Incidence Scatter from the Ionosphere at 41 Mc/sec”. In: *Physical Review Letters* 1 (12 1958), pp. 454–455. DOI: 10.1103/PhysRevLett.1.454. URL: https://link.aps.org/doi/10.1103/PhysRevLett.1.454.

[130] D. H. Froula. *Plasma scattering of electromagnetic radiation*. Elsevier, 2011. ISBN: 978-0-12-374877-5.

[131] H. Murmann et al. “The Thomson scattering systems of the ASDEX upgrade tokamak”. In: *Review of Scientific Instruments* 63.10 (1992), pp. 4941–4943. DOI: 10.1063/1.1143504.

[132] B. Kurzan and H. D. Murmann. “Edge and core Thomson scattering systems and their calibration on the ASDEX Upgrade tokamak”. In: *Review of Scientific Instruments* 82.10 (2011), p. 103501. ISSN: 0034-6748. DOI: 10.1063/1.3643771. URL: https://doi.org/10.1063/1.3643771.

[133] H. J. Hartfuss et al. “Heterodyne methods in millimetre wave plasma diagnostics with applications to ECE, interferometry and reflectometry”. In: *Plasma Physics and Controlled Fusion* 39.11 (1997), p. 1693. DOI: 10.1088/0741-3335/39/11/001. URL: https://dx.doi.org/10.1088/0741-3335/39/11/001.

[134] N. A. Salmon. “First electron temperature edge measurements on the asdex upgrade tokamak using a heterodyne radiometer”. In: *International Journal of Infrared and Millimeter Waves* 15.1 (1994), pp. 53–60. DOI: 10.1007/bf02265876. URL: https://doi.org/10.1007/bf02265876.

[135] S. K. Rathgeber et al. “Estimation of edge electron temperature profiles via forward modelling of the electron cyclotron radiation transport at ASDEX Upgrade”. In: *Plasma Physics and Controlled Fusion* 55.2 (2012), p. 025004. DOI: 10.1088/0741-3335/55/2/025004. URL: https://dx.doi.org/10.1088/0741-3335/55/2/025004.

[136] E. Wolfrum et al. “Fast lithium-beam spectroscopy of tokamak edge plasmas”. In: *Review of Scientific Instruments* 64.8 (1993), pp. 2285–2292. ISSN: 0034-6748. DOI: 10.1063/1.1144460. URL: https://doi.org/10.1063/1.1144460.

[137] K. McCormick et al. “Edge density measurements with a fast Li beam probe in tokamak and stellarator experiments”. In: *Fusion Engineering and Design* 34-35 (1997). Fusion Plasma Diagnostics, pp. 125–134. ISSN: 0920-3796. DOI: https://doi.org/10.1016/S0920-3796(96)00685-0. URL: https://www.sciencedirect.com/science/article/pii/S0920379696006850.

[138] J. Schweinzer et al. “Reconstruction of plasma edge density profiles from Li I (2s-2p) emission profiles”. In: *Plasma Physics and Controlled Fusion* 34.7 (1992), p. 1173. DOI: 10.1088/0741-3335/34/7/001. URL: https://dx.doi.org/10.1088/0741-3335/34/7/001.

[139] M. Willensdorfer et al. “Improved chopping of a lithium beam for plasma edge diagnostic at ASDEX Upgrade”. In: *Review of Scientific Instruments* 83.2 (2012), p. 023501. ISSN: 0034-6748. DOI: 10.1063/1.3682003. URL: https://doi.org/10.1063/1.3682003.

[140] R. Fischer et al. “Probabilistic lithium beam data analysis”. In: *Plasma Physics and Controlled Fusion* 50.8 (2008), p. 085009. DOI: 10.1088/0741-3335/50/8/085009. URL: https://doi.org/10.1088%5C%2F0741-3335%5C%2F50%5C%2F8%5C%2F085009.

[141] A. Mlynek et al. “Design of a digital multiradian phase detector and its application in fusion plasma interferometry”. In: *Review of Scientific Instruments* 81.3 (2010), p. 033507. ISSN: 0034-6748. DOI: 10.1063/1.3340944. URL: https://doi.org/10.1063/1.3340944.

[142] A. Lebschy. “Experimental characterization of the core plasma flow at the ASDEX Upgrade tokamak”. PhD thesis. Technische Universität München, 2018. URL: https://mediatum.ub.tum.de/1428276.

[143] R. Fischer et al. “Integrated Data Analysis of Profile Diagnostics at ASDEX Upgrade”. In: *Fusion Science and Technology* 58.2 (2010), pp. 675–684. DOI: 10.13182/FST10-110. URL: https://doi.org/10.13182/FST10-110.

[144] P. J. McCarthy et al. “The CLISTE interpretive equilibrium code”. In: *IPP Report* 5.85 (1999). URL: https://hdl.handle.net/11858/00-001M-0000-0027-6025-9.

[145] P. J. McCarthy. “Analytical solutions to the Grad–Shafranov equation for tokamak equilibrium with dissimilar source functions”. In: *Physics of Plasmas* 6.9 (1999), pp. 3554–3560. ISSN: 1070-664X. DOI: 10.1063/1.873630. URL: https://doi.org/10.1063/1.873630.

[146] M. G. Dunne et al. “Measurement of neoclassically predicted edge current density at ASDEX Upgrade”. In: *Nuclear Fusion* 52.12 (2012), p. 123014. DOI: 10.1088/0029-5515/52/12/123014. URL: https://doi.org/10.1088/0029-5515/52/12/123014.

[147] R. Fischer et al. “Coupling of the flux diffusion equation with the equilibrium reconstruction at ASDEX Upgrade”. In: *Fusion Science and Technology* 69.2 (2016), pp. 526–536. DOI: 10.13182/FST15-185. URL: https://doi.org/10.13182/FST15-185.

[148] M. Weiland et al. “RABBIT: Real-time simulation of the NBI fast-ion distribution”. In: *Nuclear Fusion* 58.8 (2018), p. 082032. DOI: 10.1088/1741-4326/aabf0f. URL: https://doi.org/10.1088/1741-4326/aabf0f.

[149] R. J. Fonck et al. “Determination of plasma-ion velocity distribution via charge-exchange recombination spectroscopy”. In: *Physical Review A* 29 (6 1984), pp. 3288–3309. DOI: 10.1103/PhysRevA.29.3288. URL: https://link.aps.org/doi/10.1103/PhysRevA.29.3288.

[150] R. C. Isler. “An overview of charge-exchange spectroscopy as a plasma diagnostic”. In: *Plasma Physics and Controlled Fusion* 36.2 (1994), p. 171. DOI: 10.1088/0741-3335/36/2/001. URL: https://dx.doi.org/10.1088/0741-3335/36/2/001.

[151] *OPEN-ADAS*. https://open.adas.ac.uk/. [Accessed 17-10-2023].

[152] J. D. Huba. *NRL plasma Formulary*. Naval Research Laboratory, 2009. URL: https://apps.dtic.mil/sti/citations/tr/ADA499299.

[153] M. Cavedon. “The role of the radial electric field in the development of the edge transport barrier in the ASDEX Upgrade tokamak”. PhD thesis. Technische Universität München, 2016. URL: https://mediatum.ub.tum.de/1295389.

[154] Y. B. Kim et al. “Neoclassical poloidal and toroidal rotation in tokamaks”. In: *Physics of Fluids B: Plasma Physics* 3.8 (1991), pp. 2050–2060. DOI: 10.1063/1.859671. URL: https://doi.org/10.1063/1.859671.

[155] E. Viezzer et al. “Evidence for the neoclassical nature of the radial electric field in the edge transport barrier of ASDEX Upgrade”. In: *Nuclear Fusion* 54.1 (2013), p. 012003. DOI: 10.1088/0029-5515/54/1/012003. URL: https://dx.doi.org/10.1088/0029-5515/54/1/012003.

[156] A. G. Peeters. “Reduced charge state equations that describe Pfirsch Schlüter impurity transport in tokamak plasma”. In: *Physics of Plasmas* 7.1 (2000), pp. 268–275. ISSN: 1070-664X. DOI: 10.1063/1.873812. URL: https://doi.org/10.1063/1.873812.

[157] C. F. B. Zimmermann et al. “Analysis and modelling of momentum transport based on NBI modulation experiments at ASDEX Upgrade”. In: *Plasma Physics and Controlled Fusion* 64.5 (2022), p. 055020. DOI: 10.1088/1361-6587/ac5ae8. URL: https://doi.org/10.1088/1361-6587/ac5ae8.

[158] R. M. McDermott et al. “Evaluation of impurity densities from charge exchange recombination spectroscopy measurements at ASDEX Upgrade”. In: *Plasma Physics and Controlled Fusion* 60.9 (2018), p. 095007. DOI: 10.1088/1361-6587/aad256. URL: https://doi.org/10.1088/1361-6587/aad256.

[159] R. M. McDermott et al. “Extensions to the charge exchange recombination spectroscopy diagnostic suite at ASDEX Upgrade”. In: *Review of Scientific Instruments* 88.7 (2017). DOI: 10.1063/1.4993131. URL: https://doi.org/10.1063/1.4993131.

[160] E. Viezzer et al. “High-resolution charge exchange measurements at ASDEX Upgrade”. In: *Review of Scientific Instruments* 83.10 (2012), p. 103501. DOI: 10.1063/1.4755810. URL: https://doi.org/10.1063/1.4755810.

[161] M. Cavedon et al. “A fast edge charge exchange recombination spectroscopy system at the ASDEX Upgrade tokamak”. In: *Review of Scientific Instruments* 88.4 (2017), p. 043103. ISSN: 0034-6748. DOI: 10.1063/1.4979801. URL: https://doi.org/10.1063/1.4979801.

[162] A. D. Whiteford et al. [Accessed 17-10-2023]. 2007. URL: https://www.adas.ac.uk/notes/adas_r07-01.pdf.

[163] P. Zeeman. “VII. Doublets and triplets in the spectrum produced by external magnetic forces”. In: *The London, Edinburgh, and Dublin Philosophical Magazine and Journal of Science* 44.266 (1897), pp. 55–60.

[164] P. Zeeman. “XXXII. On the influence of magnetism on the nature of the light emitted by a substance”. In: *The London, Edinburgh, and Dublin Philosophical Magazine and Journal of Science* 43.262 (1897), pp. 226–239.

[165] C. F. B. Zimmermann et al. “Comparison of momentum transport in matched hydrogen and deuterium H-mode plasmas in ASDEX Upgrade”. In: *Nuclear Fusion* 63.12 (2023), p. 126006. DOI: 10.1088/1741-4326/acf387. URL: https://dx.doi.org/10.1088/1741-4326/acf387.

[166] C. F. B. Zimmermann et al. “Experimental determination of the three components of toroidal momentum transport in the core of a tokamak plasma”. In: *Nuclear Fusion* (2023). URL: http://iopscience.iop.org/article/10.1088/1741-4326/ad0489.

[167] N. J. Lopes Cardozo. “Perturbative transport studies in fusion plasmas”. In: *Plasma Physics and Controlled Fusion* 37.8 (1995), pp. 799–852. DOI: 10.1088/0741-3335/37/8/001. URL: https://doi.org/10.1088/0741-3335/37/8/001.

[168] P. Mantica and F. Ryter. “Perturbative studies of turbulent transport in fusion plasmas”. In: *C. R. Physique* 7.6 (2006), pp. 634–649. ISSN: 1631-0705. DOI: https://doi.org/10.1016/j.crhy.2006.06.004. URL: https://www.sciencedirect.com/science/article/pii/S1631070506001162.

[169] E. Fable et al. “The role of the source versus the collisionality in predicting a reactor density profile as observed on ASDEX Upgrade discharges”. In: *Nuclear Fusion* 59.7 (2019), p. 076042. DOI: 10.1088/1741-4326/ab1f28. URL: https://dx.doi.org/10.1088/1741-4326/ab1f28.

[170] E. Fable (Max-Planck-Institut für Plasmaphysik, Garching). Private communication. 2023.

[171] R. Fischer et al. “Estimation and Uncertainties of Profiles and Equilibria for Fusion Modeling Codes”. In: *Fusion Science and Technology* 76.8 (2020), pp. 879–893. DOI: 10.1080/15361055.2020.1820794. URL: https://doi.org/10.1080/15361055.2020.1820794.

[172] M. Dunne (Max-Planck-Institut für Plasmaphysik, Garching). Private communication. 2023.

[173] G. Tardini et al. “A package to bridge experimental data in magnetic nuclear fusion to modelling workflows for heating and transport”. In: *Computer Physics Communications* (2023, to be submitted).

[174] N. Kluy et al. “Linear gyrokinetic calculations of toroidal momentum transport in the presence of trapped electron modes in tokamak plasmas”. In: *Physics of Plasmas* 16.12 (2009), p. 122302. ISSN: 1070-664X. DOI: 10.1063/1.3271411. URL: https://doi.org/10.1063/1.3271411.

[175] R. Storn and K. Price. In: *Journal of Global Optimization* 11.4 (1997), pp. 341–359. DOI: 10.1023/a:1008202821328. URL: https://doi.org/10.1023/a:1008202821328.

[176] J. Weiland et al. “Progress on anomalous transport in tokamaks, drift waves and nonlinear structures”. In: *Plasma Physics and Controlled Fusion* 49.5A (2007), A45–A57. DOI: 10.1088/0741-3335/49/5a/s04. URL: https://doi.org/10.1088/0741-3335/49/5a/s04.

[177] G. Tardini et al. “Angular momentum studies with NBI modulation in JET”. In: *Nuclear Fusion* 49.8 (2009), p. 085010. DOI: 10.1088/0029-5515/49/8/085010. URL: https://doi.org/10.1088/0029-5515/49/8/085010.

[178] T. Tala et al. “Parametric dependencies of momentum pinch and Prandtl number in JET”. In: *Nuclear Fusion* 51.12 (2011), p. 123002. DOI: 10.1088/0029-5515/51/12/123002. URL: https://doi.org/10.1088%2F0029-5515%2F51%2F12%2F123002.

[179] P. Mantica et al. “Perturbative studies of toroidal momentum transport using neutral beam injection modulation in the Joint European Torus: Experimental results, analysis methodology, and first principles modeling”. In: *Physics of Plasmas* 17.9 (2010), p. 092505. DOI: 10.1063/1.3480640.

[180] W. M. Solomon et al. “Advances in understanding the generation and evolution of the toroidal rotation profile on DIII-D”. In: *Nuclear Fusion* 49.8 (2009), p. 085005. DOI: 10.1088/0029-5515/49/8/085005. URL: https://doi.org/10.1088/0029-5515/49/8/085005.

[181] W. M. Solomon et al. “Characterization of intrinsic rotation drive on DIII-D”. In: *Nuclear Fusion* 51.7 (2011), p. 073010. DOI: 10.1088/0029-5515/51/7/073010. URL: https://doi.org/10.1088/0029-5515/51/7/073010.

[182] F. J. Casson. “Turbulent transport in rotating tokamak plasmas”. PhD thesis. University of Warwick, 2011. URL: https://wrap.warwick.ac.uk/36765/.

[183] S. M. Yang et al. “Perturbative studies of toroidal momentum transport in KSTAR H-mode and the effect of ion temperature perturbation”. In: *Nuclear Fusion* 58.6 (2018), p. 066008. DOI: 10.1088/1741-4326/aab90e. URL: https://doi.org/10.1088%2F1741-4326%2Faab90e.

[184] H. Weisen et al. “Isotope dependence of energy, momentum and particle confinement in tokamaks”. In: *Journal of Plasma Physics* 86.5 (2020). DOI: 10.1017/s0022377820000781. URL: https://doi.org/10.1017/s0022377820000781.

[185] M. Bessenrodt-Weberpals et al. “The isotope effect in ASDEX”. In: *Nuclear Fusion* 33.8 (1993), p. 1205. DOI: 10.1088/0029-5515/33/8/I09. URL: https://dx.doi.org/10.1088/0029-5515/33/8/I09.

[186] J. S. deGrassie et al. “Toroidal rotation in DIII-D in electron cyclotron heating and Ohmic H-mode discharges”. In: *Physics of Plasmas* 11.9 (2004), pp. 4323–4331. ISSN: 1070-664X. DOI: 10.1063/1.1778751. URL: https://doi.org/10.1063/1.1778751.

[187] J. E. Rice et al. “Spontaneous core toroidal rotation in Alcator C-Mod L-mode, H-mode and ITB plasmas”. In: *Plasma Physics and Controlled Fusion* 50.12 (2008), p. 124042. DOI: 10.1088/0741-3335/50/12/124042. URL: https://doi.org/10.1088/0741-3335/50/12/124042.

[188] J. E. Rice et al. “Edge Temperature Gradient as Intrinsic Rotation Drive in Alcator C-Mod Tokamak Plasmas”. In: *Physical Review Letters* 106 (21 2011), p. 215001. DOI: 10.1103/PhysRevLett.106.215001. URL: https://link.aps.org/doi/10.1103/PhysRevLett.106.215001.

[189] T. Tala et al. “Toroidal and poloidal momentum transport studies in tokamaks”. In: *Plasma Physics and Controlled Fusion* 49.12B (2007), B291–B302. DOI: 10.1088/0741-3335/49/12b/s27. URL: https://doi.org/10.1088%2F0741-3335%2F49%2F12b%2Fs27.

[190] J. S. deGrassie et al. “Intrinsic rotation in DIII-Da)”. In: *Physics of Plasmas* 14.5 (2007), p. 056115. ISSN: 1070-664X. DOI: 10.1063/1.2539055. URL: https://doi.org/10.1063/1.2539055.

[191] W. M. Solomon et al. “Momentum confinement at low torque”. In: *Plasma Physics and Controlled Fusion* 49.12B (2007), B313. DOI: 10.1088/0741-3335/49/12B/S29. URL: https://dx.doi.org/10.1088/0741-3335/49/12B/S29.

[192] M. Yoshida et al. “Momentum transport and plasma rotation profile in toroidal direction in JT-60U L-mode plasmas”. In: *Nuclear Fusion* 47.8 (2007), pp. 856–863. DOI: 10.1088/0029-5515/47/8/017. URL: https://doi.org/10.1088%2F0029-5515%2F47%2F8%2F017.

[193] M. Yoshida et al. “Characteristics of momentum transport in JT-60U H-mode plasmas”. In: *Nuclear Fusion* 49.11 (2009), p. 115028. DOI: 10.1088/0029-5515/49/11/115028. URL: https://doi.org/10.1088/0029-5515/49/11/115028.

[194] M. Yoshida et al. “Core and edge toroidal rotation study in JT-60U”. In: *Nuclear Fusion* 52.2 (2012), p. 023024. DOI: 10.1088/0029-5515/52/2/023024. URL: https://dx.doi.org/10.1088/0029-5515/52/2/023024.

[195] R. M. McDermott et al. “Core intrinsic rotation behaviour in ASDEX Upgrade Ohmic L-mode plasmas”. In: *Nuclear Fusion* 54.4 (2014), p. 043009. DOI: 10.1088/0029-5515/54/4/043009. URL: https://doi.org/10.1088%2F0029-5515%2F54%2F4%2F043009.

[196] R. M. McDermott et al. “Effect of electron cyclotron resonance heating (ECRH) on toroidal rotation in ASDEX Upgrade H-mode discharges”. In: *Plasma Physics and Controlled Fusion* 53.3 (2011), p. 035007. DOI: 10.1088/0741-3335/53/3/035007. URL: https://dx.doi.org/10.1088/0741-3335/53/3/035007.

[197] H. Weisen et al. “Identification of the ubiquitous Coriolis momentum pinch in JET tokamak plasmas”. In: *Nuclear Fusion* 52.4 (2012), p. 042001. DOI: 10.1088/0029-5515/52/4/042001. URL: https://doi.org/10.1088%2F0029-5515%2F52%2F4%2F042001.

[198] F. M. Laggner et al. “Pedestal structure and inter-ELM evolution for different main ion species in ASDEX Upgrade”. In: *Physics of Plasmas* 24.5 (2017), p. 056105. DOI: 10.1063/1.4977461. URL: https://doi.org/10.1063/1.4977461.

[199] E. Viezzer et al. “Ion heat transport dynamics during edge localized mode cycles at ASDEX Upgrade”. In: *Nuclear Fusion* 58.2 (2018), p. 026031. DOI: 10.1088/1741-4326/aaa22f. URL: https://doi.org/10.1088/1741-4326/aaa22f.

[200] C. Angioni et al. “A comparison of the impact of central ECRH and central ICRH on the tungsten behaviour in ASDEX Upgrade H-mode plasmas”. In: *Nuclear Fusion* 57.5 (2017), p. 056015. DOI: 10.1088/1741-4326/aa6453. URL: https://doi.org/10.1088/1741-4326/aa6453.

[201] J. Stober et al. “Dependence of particle transport on heating profiles in ASDEX Upgrade”. In: *Nuclear Fusion* 43.10 (2003), pp. 1265–1271. DOI: 10.1088/0029-5515/43/10/030. URL: https://doi.org/10.1088/0029-5515/43/10/030.

[202] J. G. Cordey et al. “Plasma confinement in JET H mode plasmas with H, D, DT and T isotopes”. In: *Nuclear Fusion* 39.3 (1999), p. 301. DOI: 10.1088/0029-5515/39/3/301. URL: https://dx.doi.org/10.1088/0029-5515/39/3/301.

[203] M. L. Watkins and the JET Team. “Physics of high performance JET plasmas in DT”. In: *Nuclear Fusion* 39.9Y (1999), p. 1227.

[204] C. F. Maggi et al. “Isotope effects on L-H threshold and confinement in tokamak plasmas”. In: *Plasma Physics and Controlled Fusion* 60.1 (2018), p. 014045. DOI: 10.1088/1361-6587/aa9901. URL: https://dx.doi.org/10.1088/1361-6587/aa9901.

[205] C. F. Maggi et al. “Isotope identity experiments in JET-ILW with H and D L-mode plasmas”. In: *Nuclear Fusion* 59.7 (2019), p. 076028. DOI: 10.1088/1741-4326/ab1ccd. URL: https://dx.doi.org/10.1088/1741-4326/ab1ccd.

[206] P. A. Schneider et al. “Explaining the isotope effect on heat transport in L-mode with the collisional electron-ion energy exchange”. In: *Nuclear Fusion* 57.6 (2017), p. 066003. DOI: 10.1088/1741-4326/aa65b3. URL: https://doi.org/10.1088/1741-4326/aa65b3.

[207] P. A. Schneider et al. “The dependence of confinement on the isotope mass in the core and the edge of AUG and JET-ILW H-mode plasmas”. In: *Nuclear Fusion* 62.2 (2022), p. 026014. DOI: 10.1088/1741-4326/ac3e82. URL: https://dx.doi.org/10.1088/1741-4326/ac3e82.

[208] P. A. Schneider et al. “Overview of the isotope effects in the ASDEX Upgrade tokamak”. In: *Plasma Physics and Controlled Fusion* 63.6 (2021), p. 064006. DOI: 10.1088/1361-6587/abf540. URL: https://dx.doi.org/10.1088/1361-6587/abf540.

[209] E. Viezzer et al. “High-accuracy characterization of the edge radial electric field at ASDEX Upgrade”. In: *Nuclear Fusion* 53.5 (2013), p. 053005. DOI: 10.1088/0029-5515/53/5/053005. URL: https://dx.doi.org/10.1088/0029-5515/53/5/053005.

[210] E. Viezzer et al. “Parameter dependence of the radial electric field in the edge pedestal of hydrogen, deuterium and helium plasmas”. In: *Plasma Physics and Controlled Fusion* 56.7 (2014), p. 075018. DOI: 10.1088/0741-3335/56/7/075018. URL: https://dx.doi.org/10.1088/0741-3335/56/7/075018.

[211] R. M. McDermott et al. “Edge radial electric field structure and its connections to H-mode confinement in Alcator C-Mod plasmas”. In: *Physics of Plasmas* 16.5 (2009), p. 056103. DOI: 10.1063/1.3080721. URL: https://doi.org/10.1063/1.3080721.

[212] C. C. Petty et al. “Experimental constraints on transport from dimensionless parameter scaling studies”. In: *Physics of Plasmas* 5.5 (1998), pp. 1695–1702. DOI: 10.1063/1.872838. URL: https://doi.org/10.1063/1.872838.

[213] I. Pusztai et al. “Isotope mass and charge effects in tokamak plasmas”. In: *Physics of Plasmas* 18.12 (2011), p. 122501. DOI: 10.1063/1.3663844. URL: https://doi.org/10.1063/1.3663844.

[214] R. E. Waltz et al. “A gyro-Landau-fluid transport model”. In: *Physics of Plasmas* 4.7 (1997), pp. 2482–2496. ISSN: 1070-664X. DOI: 10.1063/1.872228. URL: https://doi.org/10.1063/1.872228.

[215] O. J. W. F. Kardaun. *Classical methods of statistics*. Berlin, Germany: Springer, 2004.

[216] E. Fable et al. “The role of ion and electron electrostatic turbulence in characterizing stationary particle transport in the core of tokamak plasmas”. In: *Plasma Physics and Controlled Fusion* 52.1 (2009), p. 015007. DOI: 10.1088/0741-3335/52/1/015007. URL: https://dx.doi.org/10.1088/0741-3335/52/1/015007.

[217] J. E. Rice et al. “Central impurity toroidal rotation in ICRF heated Alcator C-Mod plasmas”. In: *Nuclear Fusion* 39.9 (1999), p. 1175. DOI: 10.1088/0029-5515/39/9/310. URL: https://dx.doi.org/10.1088/0029-5515/39/9/310.

[218] J. E. Rice et al. “Inter-machine comparison of intrinsic toroidal rotation in tokamaks”. In: *Nuclear Fusion* 47.11 (2007), pp. 1618–1624. DOI: 10.1088/0029-5515/47/11/025. URL: https://doi.org/10.1088/0029-5515/47/11/025.

[219] F. Janky et al. “ASDEX Upgrade flight simulator development”. In: *Fusion Engineering and Design* 146 (2019). SI:SOFT-30, pp. 1926–1929. ISSN: 0920-3796. DOI: https://doi.org/10.1016/j.fusengdes.2019.03.067. URL: https://www.sciencedirect.com/science/article/pii/S0920379619303886.

[220] F. Janky et al. “Validation of the Fenix ASDEX Upgrade flight simulator”. In: *Fusion Engineering and Design* 163 (2021), p. 112126. ISSN: 0920-3796. DOI: https://doi.org/10.1016/j.fusengdes.2020.112126. URL: https://www.sciencedirect.com/science/article/pii/S0920379620306748.

[221] T. Tala et al. “Tokamak Experiments to Study the Parametric Dependences of Momentum Transport”. In: *Proceedings of 24th IAEA Fusion Energy Conference* (2012). URL: https://scipub.euro-fusion.org/wp-content/uploads/2014/11/EFDC120613.pdf.

[222] P. C. de Vries et al. “Plasma rotation and momentum transport studies at JET”. In: *Plasma Physics and Controlled Fusion* 48.12 (2006), pp. 1693–1708. DOI: 10.1088/0741-3335/48/12/001. URL: https://doi.org/10.1088/0741-3335/48/12/001.

[223] J. S. deGrassie et al. “Toroidal rotation in neutral beam heated discharges in DIII-D”. In: *Nuclear Fusion* 43.2 (2003), p. 142. DOI: 10.1088/0029-5515/43/2/307. URL: https://dx.doi.org/10.1088/0029-5515/43/2/307.

[224] S. D. Scott et al. “Local measurements of correlated momentum and heat transport in the TFTR tokamak”. In: *Physical Review Letters* 64 (5 1990), pp. 531–534. DOI: 10.1103/PhysRevLett.64.531. URL: https://link.aps.org/doi/10.1103/PhysRevLett.64.531.

[225] M. Yoshida et al. “Momentum transport studies from multi-machine comparisons”. In: *Nuclear Fusion* 52.12 (2012), p. 123005. DOI: 10.1088/0029-5515/52/12/123005. URL: https://dx.doi.org/10.1088/0029-5515/52/12/123005.

[226] T. Tala et al. “Multi-machine experiments to study the parametric dependences of momentum transport and intrinsic torque”. In: *Proceedings of 43rd EPS Conference on Plasma Physics* (2016). URL: https://pure.mpg.de/rest/items/item_2353276/component/file_3319023/content.

[227] W. M. Solomon et al. “Mechanisms for generating toroidal rotation in tokamaks without external momentum input”. In: *Physics of Plasmas* 17.5 (2010), p. 056108. DOI: 10.1063/1.3328521. URL: https://doi.org/10.1063/1.3328521.

[228] C. Chrystal et al. “Dependence of intrinsic torque and momentum confinement on normalized gyroradius and collisionality in the DIII-D tokamak”. In: *Physics of Plasmas* 24.4 (2017), p. 042501. DOI: 10.1063/1.4978563. URL: https://doi.org/10.1063/1.4978563.

[229] R. M. McDermott et al. “Core momentum and particle transport studies in the ASDEX Upgrade tokamak”. In: *Plasma Physics and Controlled Fusion* 53.12 (2011), p. 124013. DOI: 10.1088/0741-3335/53/12/124013. URL: https://dx.doi.org/10.1088/0741-3335/53/12/124013.

[230] C. Angioni et al. “Intrinsic Toroidal Rotation, Density Peaking, and Turbulence Regimes in the Core of Tokamak Plasmas”. In: *Physical Review Letters* 107 (21 2011), p. 215003. DOI: 10.1103/PhysRevLett.107.215003. URL: https://link.aps.org/doi/10.1103/PhysRevLett.107.215003.

[231] J.-K. Park et al. “Intrinsic rotation generation in NSTX ohmic H-mode plasmas”. In: *Nuclear Fusion* 53.6 (2013), p. 063012. DOI: 10.1088/0029-5515/53/6/063012. URL: https://dx.doi.org/10.1088/0029-5515/53/6/063012.

[232] K. Ida et al. “Spontaneous toroidal rotation driven by the off-diagonal term of momentum and heat transport in the plasma with the ion internal transport barrier in LHD”. In: *Nuclear Fusion* 50.6 (2010), p. 064007. DOI: 10.1088/0029-5515/50/6/064007. URL: https://dx.doi.org/10.1088/0029-5515/50/6/064007.

[233] M. Yoshida et al. “Role of Pressure Gradient on Intrinsic Toroidal Rotation in Tokamak Plasmas”. In: *Physical Review Letters* 100 (10 2008), p. 105002. DOI: 10.1103/PhysRevLett.100.105002. URL: https://link.aps.org/doi/10.1103/PhysRevLett.100.105002.

[234] J. E. Rice et al. “Dimensionless parameter scaling of intrinsic torque in C-Mod enhanced confinement plasmas”. In: *Nuclear Fusion* 61.2 (2021), p. 026013. DOI: 10.1088/1741-4326/abcb26. URL: https://doi.org/10.1088/1741-4326/abcb26.

Acknowledgements

"It was the best of times,
it was the worst of times..."

— Charles Dickens, A Tale of Two Cities

It finally happens that I have to write these lines. Unbelievable. *Apathetic stare*

Many people, friends, and colleagues have been by my side for four years since I arrived at AUG. I am not sure if all of you know what it means to me to work with you on this incredible project, but as it is likely that I will forget someone, a first thanks goes to the entire ASDEX and TOK Team, with all the helpful technicians and experts around.

Several colleagues were just always very, very supportive, such as Alexander Bock (for support with Python at the very beginning and for correction reading), Rainer Fischer (sorry for getting on your nerves with my special EQH-IDA editions and thank you for correction reading), Matthias Willensdorfer (for your care and the motivation for our PRL attempt), Biggy Perey (being there when I lost my keys and representing the Sozialwerk with its beautiful mountain cabin Forschersruh which significantly contributed to the sucess of this work) and Gabi Dörsch (for handling the official things uncomplicated), Louis Giannone (EQR was a great help for inter-shot analysis), Branka Vanovac and Tim Happel (for your support with my negative triangularity hobby), Philip Schneider (explaining me heat transport), Michael Griener (for the support on redesigning the lab course experiment), Marc Maraschek (for telling me a lot about modes and being in the control room for inter-shot analysis) and, finally, Athina Kappatou (with who I have been the first time in the torus, I will never forget this!).

Furthermore, Oleg Samoylov (мой самый лучший товарищ), Christian Schuster (for all the discussion about our methodologies), Tautvydas Maceina (for all the deep talk in the years of the PhD when I was not stressed out), Nina Schwarz (for the awareness and the nice work together as representatives), Brando Rettino (for going to all the external meetings as a representative and for your honest and open way of meeting people), Marco Muraca (for having a very down-to-earth, common sense), Sergei Makarov (for his enthusiastic way of discussing my results), Michael Bergmann (for helping with my special IDA editions, thousand questions, and your motivation in the last months), Jan-Paul Koschinsky (the best left-over of my BA thesis and the fun work on the neutron stuff), Marion Smedberg (for talking about this faith thing and inviting me to the 09 o'clock Angelus), and Antonello Zito (for being an incredible role model for fighting until the end).

All the friendly faces from the 11:30 lunch group: Sebastian Hörmann (with his incredible knowledge of physics and his down-to-earth German accent), Felix Klossek (for his always relaxed attitude), Joey Kalis (for his jokes and being the subject of great gossip), Manuel Herschel (who could/should be my cousin; we would have had a good fight when we were kids), Jonas Puchmayr (for answering all my stupid theory questions, sorry and thank you for this), David Kulla (for his inspiration on food, a healthy way of life and his efforts on making fusion happen), Magdalena Bauer (to make me feel that we are still in Bavaria) and Raphael Schramm (who accompanied this work since the very first hour in the L6 southside office, always contributed with a good portion of Galgenhumor and his skills in disabling the fire-alarm system in Daniel's office for the Feuerzangenbowle).

I want to thank Dirk Hartmann, Johannes-Peter Kallmeyer, and Simppa Äkäslompolo, who made it possible for me to engage in this research field. Furthermore, Hartmut Zohm and Jörg Stober for the motivation and the great lecture at LMU, which brought me to IPP Garching, especially Thomas Pütterich as the academic supervisor of the first part of this project, who contributed to the scenario development and always had good ideas how to proceed. To Arne Kallenbach, who was always very generous with contingency shots and believed in this work from a very early point on. To Daniel Fajardo and Teobaldo Luda for the helpful discussions about integrated modeling and their code snippets and support on the Stoltzfus-Dueck model. To the CXRS diagnostic group: Ralph Dux (for your calm and uncomplicated way of handling the official things), the expertise from Sevilla, in particular Pilar Cano Megias (for loving Taylor as much as I do and always being very motivating with your positive attitude), and Marco Cavedon (for his helpful discussion on fitting algorithms). To Elisabeth Wolfrum, who was always very supportive when certain decisions had to be made, for the advice on personal and professional questions and for the correction reading.

A big thanks goes to Michaela Mayer for being a great support in the frustrating months of this work, I am grateful that you were there and made IPP a better place. To Tabea Gleiter, who always took away my anxiety with her optimistic attitude and who is one of the most reliable people I have met so far. Dear Tabea, I am glad we had this time as PhDs in the same group together, I will not forget about this. To Daniel Wendler, who always had a good intuition on the essential questions of life, for suffering together in the last weeks of our thesis, I will not forget the Feuerzangenbowle in your office. To Johannes Illerhaus for his more mature view on things, for helping me understand myself better, and for ensuring a continuous flow of coffee.

To Francesco Sciortino, who had an incredible impact on this project by showing me what it means to become active and how to engage in research projects, and who inspires me with his own work. I am very proud to know you and grateful for your company, inspiration, and advice until now, and I am excited to see where our projects take us. For sure: to a better future.

To Ulrike Plank, who helped me make the right decisions in the right moments from the beginning of this PhD. We had an incredible time, unexpected emotional fights, and lovely reconciliations in our shared office. I will always smile when I think about all the discussions, the shared passion for music and culture, and the great feedback and answers you gave me on science and life. I will really miss you, Uli!

This project would not have been possible without the great support of my co-authors/colleagues, who started this project roughly a decade before I got involved. First, Giovanni Tardini for his help with TRANSP and ASTRA, Emiliano Fable for his support in setting up the momentum transport modeling in ASTRA, Yann Camenen for his helpful feedback and the GKW development, and Timothy Stoltzfus-Dueck for the support when we were fighting with the referees. Further, Antti Salmi (for his ideas on the numerical details) and Anu Kirjasuo (for giving me hope that this project continues), as well as Tuomas Tala being my scientific counsel and "supervising" this thesis from abroad with good ideas, to focus on the relevant milestones and his great intuition in the control room.

To Basil Duval, who destroyed every single draft with at least 30 comments per page (from where did you take all this time!?), significantly improving the style and the rigorousity of this work and the corresponding publications. I have really appreciated this support and your often criticizing, sometimes positive, but always honest and constructive feedback.

To Clemente Angioni, who was an incredible support to dip into the world of gyrokinetic theory, running GKW, and for correction reading the theory-related parts of this work. You were always there for my easy-minded questions, for which you always took an incredible amount of time. This work was significantly improved by your advice on interpreting the results. And I really enjoyed watching the astonishing way how an excellent theoretician approaches physics. I have learned a lot, even though I doubt I will ever come to the level of understanding you have for physics.

To Ulrich Stroth as my academic supervisor, who was supportive from the very first days until the last weeks with helpful corrections to make the thesis more understandable. I have always enjoyed your experienced and calm way of approaching questions and decisions, and I have benefited from your intuition and guidance through this project. I am grateful for the freedom, trust, and support you gave, which enabled me to learn how to manage such a large project.

Neben den vielen Kollegen, die auf ihre ganz eigene Art und Weise dazu beigetragen haben, diese Arbeit zu vollbringen, haben viele liebe Menschen im Hintergrund auf mich aufgepasst und Wache gehalten. Zuerst denke ich da an meinen besten Freund Leon, der nie aufgehört hat, mir auf die Schulter zu klopfen, der da war während dieser Jahre, während diesen tagelangen Fahrten in Richtung Osten, der mein Stein ist, auf den ich bauen kann, wenn die Welt untergeht und dafür, dass das ganze Abenteuer weshalb ich Physik studiert habe auch an dir hing. Ich wünsch mir von Herzen, dass wir noch einmal zurück können in die verlorene Zeit, in unser verlorenes Land. Ich denke an meine liebe Katja in Sankt Petersburg, deren Freundschaft durch all die Wirren dieser Jahre mir gezeigt hat, dass nicht alles falsch war. Florian, der mit seiner fachlichen Exzellenz, seinem Fleiß und seiner Menschlichkeit mir immer ein Vorbild war. Zhuo und Emmie, du kleiner Schatz, der du noch gar nicht weißt, was das hier alles bedeutet, zu den ich immer kommen konnte, wenn es nicht mehr ging. Meinen Lieblings-„Ossis" Peter, Daniel und Charlotte, die diesen ganzen Weg von Anbeginn meines kläglichen Physiker-Daseins begleitet haben und die immer voll Respekt, Zuversicht und Unterstützung waren. Ebenso an die „Münchner Familie" Laura, Linus, Lucia, Eberhard, Chari, Cordula, Isabella, Tryphon und Jutta, die mich wie eine Familie aufgenommen haben, unverdient wie eh und je. Und der kleine Kasimir, der uns

leider in den letzten Monaten nicht mehr schnurrend und kratzend zur Seite stehen konnte. Ebenso denk ich an die Halle-Gang, Anni und Basti, Jessi und Krister, ebenso wie Rene, der genau genommen schon viel länger an Bord ist, die mich sofort adoptiert hatten.

Ich denke an meine Familie, von der ich hoffe, sie mit Stolz zu erfüllen: meinen Eltern Gerd und Diane, die mir immer Vorbilder waren. Mein Vater, der mich (auch durch seine Liebe zum Raumschiff Enterprise und zu Western-Filmen) motiviert hat, Forscher und Entdecker zu werden und immer einen Schritt weiterzugehen. Meine Mutter, die mich mit ihrer endlosen Liebe und Menschlichkeit inspiriert hat, das Entdeckertum mit etwas zutiefst Gutem zu verbinden. Meine kleine Schwester Cora, die mir schon längst ein Vorbild ist, weil sie kämpfen kann wie zwei, und es wahrscheinlich gar nicht weiß. Und meiner Oma Elisabeth, die immer stolz war, immer Fragen gestellt hat, mich motiviert hat, es noch ein bisschen besser zu machen und leider diesen Lebensabschnitt nicht mehr erleben durfte.

Und natürlich dir, Anaïs, die du das alles ausgehalten hast, mich 1001 Mal wieder zurechtgerückt hast, und für dein aussichtsloses Unterfangen, auf meine Gesundheit zu achten. Die du selten die Geduld verloren hast, wenn ich mich hin und hergewälzt habe abends im Bett, weil es eigentlich zu viel war und ich getrieben war. Die ganzen Höhen und Tiefen, die langen Nächte, als wir das PRL versucht haben, aber vor allem bin ich dir dankbar für die gemeinsamen Auszeiten und deine wunderbare Art, uns ein Zuhause zu basteln. Ich weiß gar nicht, wo ich da anfangen soll, aber nun wissen wir es, was es bedeutet, solch ein Projekt zu stemmen und ich bin gespannt, was wir uns als nächstes vornehmen.

An incredible thank from the bottom of my heart goes to my supervisor, Rachael McDermott. I could write a long paragraph about what it means to me to be your student, but no words describe how thankful I am. I will always remember what you taught me: to be honest, self-critical, respectful, caring, and rigorous. For your patience and belief that I could manage this, even when I was sitting in your office with tears in my eyes. You always motivated me to not give up, to continue to find a way to solve the problems, well, until it worked out finally. All the help on our paper drafts, the presentations, and the immense support you have put into correcting my thesis despite you having many more critical things on your plate now. Only through your help has this thesis become the best and most valuable thing I have done in my life so far. Dear Rachael, I sincerely hope that you are fine with what I have done and that I have met the expectations you placed in me when you gave me this project four years ago. I am proud and thankful that I was your student and that I learned from you what it means to be a scientist. I will never forget these intense years.

Abschließend möchte ich der Studienstiftung des deutschen Volkes meinen tief empfundenen Dank aussprechen, deren großzügige Unterstützung während meines gesamten akademischen Weges immens war und unschätzbare Möglichkeiten bot, sich vollkommen auf die Aufgaben in diesem Lebensabschnitt einzulassen. Ich hoffe, das in mich gesetzte Vertrauen während dieses Jahrzehnts erfüllt zu haben und der Erwartung an meine „Leistung, Initiative und Verantwortung“, bis an diesen Punkt und darüber hinaus in Zukunft, gerecht zu werden.